

DISS.ETH NO. 29175

# Influences of snow microstructure on the Arctic sea ice energy budget

A thesis submitted to attain the degree of  
DOCTOR OF SCIENCES  
(Dr. sc. ETH Zurich)

Presented by  
Amy R. Macfarlane  
MSc(Res) University of Sheffield  
born on 20.07.1994

**Accepted on the recommendation of**  
Prof. Dr Martin Schroth  
Dr Martin Schneebeli  
Dr Melinda Webster  
Prof. Dr Andrea Carminati

2023

# Acknowledgements

This work was only possible due to the incredible support I have received over the last few years.

Firstly, I would like to thank Martin Schneebeli for giving me this opportunity, guiding me and trusting me with the responsibilities throughout this PhD. I'll never forget the excitement of seeing saline snow with the  $\mu$ -CT during our north pole exchange! Thank you for all the inspiring discussions and for believing I could do this PhD.

Thank you to Martin Schroth for the support, for agreeing to be my supervisor in the first place and for always being contactable. Thanks to my committee for all the support over the past few years and for helping guide this project. Thank you to everyone in the SLF office: Ruschle for all the writing help, the discussions and for being an amazing role model. Henning for all the invaluable contributions, Kavitha, Anna, Benni and the rest of the snow physics team for the inspiring weekly discussions.

Thank you to Jessica for the bike-ski-camp-ski-bike adventures, the infinite supply of frozen banana bread and the infectious laughter, to Melin the famous swimming unicorn and all the beautiful running trips, and Océane for leading the way across Lac Léman. You three have been there for me over the past few years, and I couldn't have done this without you! In addition, I want to thank Giulia (for smuggling cheese across borders, always being there for a sunny lap around the lake and showing me the way up Tromsdalstinden), Christian, Nati (and Archie), Tine, Celia (and Henry), Sophia for all the runs, the delicious dinners, the illegal langlauf and cheesy evenings. Thank you to Jaggi, Vincent, Bertrand, and Ben for the runs and the cycle rides and Leo, Tiziano, Moein, and David for all the office energy. Thank you to all my office mates over the years: Carolin, Hagen (for the best espressos in Davos), Mareike, Marie, Neige, Sabine, Lucille, Lars, Michael, and everyone at SLF, who helped make such an incredible time skiing, running and biking around the Davos mountains.

I would like to thank my family: my Mum and Dad for supporting me in all aspects of my life, particularly for taking time out of your holidays to help me chop wood. I could not have completed my PhD without this! To my sister, Harriet, for never failing to cheer me up. To Delphin for inspiring me to dream big, taking me on my first winter camping, and so many other adventures. I am always amazed to see what you achieve, and I look forward to all the upcoming adventures. Thank you to the Ballingers for being the best little family, never failing to send a birthday card on time, and entertaining my mountain hiking ideas.

Thank you to Fran for changing my life with tea, slacklining, and hiking evenings at Stillberg, rolling down the ski slopes with me, and being there for me ever since. To Hazel, for all the parallel PhD motivation, I cannot wait to see your defence and to celebrate with you on a long sunny cycle. Thank you to Amy for bringing sunshine and sparkles into my life and all the visits to Davos and camping trips in Italy. To Luke for helping me channel my inner Hof and Callum and Imogen for helping look for Norwegian moose. Thank you to the swans and the cygnet: Daisy, Ettie, Lotty, Jo, Katherine, Beth, Fiona, Lucy, Sophie, and Alice. I couldn't have done this without your support.

A considerable part of this PhD was my time spent on the MOSAiC expedition. Alongside all the logistics and crew support, I want to thank the ice team, David, Gena, Steven, Saga,

Robert, and Steffi, from Leg 3. From Leg 4, I would like to thank everyone at the ice coffee hours, particularly Maddie, Marcel and Melinda, for their continued support throughout my PhD. Thank you, Nico, Adrien, and David at APECS, for being a fantastic group of people to work with. Finally, the incredibly supportive and inspiring sustainable science group: Maddie, Radiance, Verena, and Linda, for fighting the fights that are worth fighting.

My Frauenkirch adventures were possible thanks to the Blasers and, of course, Toasti.

Written in loving memory of Adrien.

This work was funded by:

WSL Institute for Snow and Avalanche Research SLF. WSL\_201812N1678. Funder ID: <http://dx.doi.org/10.13039/501100015742>.

Swiss Polar Institute (SPI reference DIRCR-2018-003). Funder ID: <http://dx.doi.org/10.13039/501100015594>.

European Union's Horizon 2020 research and innovation program projects ARICE (grant 730965) for berth fees associated with the participation of the DEARice project.

Data sets used in this manuscript were produced as part of the international Multidisciplinary drifting Observatory for the Study of the Arctic Climate (MOSAiC) with the tag MOSAiC20192020 and the Project\_ID: AWI\_PS122\_00. We thank all people involved in the expedition of the Research Vessel Polarstern [1] during MOSAiC in 2019–2020 as listed in [2]. I want to thank Scanco Medical AG for lending and supporting the use of the MicroCT90 throughout the MOSAiC expedition.

# Abstract

Sea ice plays a critical role in the Arctic by providing habitats, buttressing tidewater glaciers, stabilising ocean currents and regulating the Earth's climate by reflecting solar radiation, all of which can have a ripple effect on global weather patterns. The Arctic is experiencing unprecedented change, and warming of the Arctic is occurring faster than the rest of the planet. About half of the sea ice area in the Arctic has been lost since satellite monitoring began 40 years ago, and the region now contains predominantly younger sea ice. One consequence of the diminishing sea ice is increased precipitation (more snow in the winter season and more rain events in the summer), which has unknown implications for the energy budget of the Arctic sea ice system. To improve the modelling and monitoring of Arctic sea ice and reduce uncertainties in predictions, we first need to understand internal processes occurring in the snow that influence energy budget components.

While the inaccessibility of this region means there is a lack of ground-truth measurements, in 2019–2020, an expedition to the Arctic (the MOSAiC expedition) opened opportunities for scientists to conduct a year-long interdisciplinary study on the Arctic sea ice. This thesis focuses on the influence of snow microstructure on energy exchanges through data collected during this year-long expedition. We outline the importance of snow in the Arctic sea ice system whilst conducting a process study using in-situ data to better understand energy exchanges.

One component of the energy budget is the ground heat flux: the transfer of heat through the snow on sea ice. Thermal conductivity and resistance of the snow cover are the main parameters influencing heat transfer and sea ice growth during winter. Various measurements and parametrisations of thermal properties exist, but an assessment of the entire seasonal evolution of thermal conductivity and snow resistance is hitherto lacking. Using the comprehensive snow data set from the MOSAiC expedition, we have evaluated for the first time the seasonal evolution of the snow's thermal conductivity and thermal resistance on different ice ages (leads, first and second-year ice) and topographic features (ridges). We found that seasonality is not a prominent feature of thermal conductivity, and there is an overestimation of thermal conductivity in large-scale climate models. We suggest testing alternative values of thermal conductivity (measured in situ using X-ray microcomputer tomography) and that sea ice models treat level and ridged ice separately (we found approximately three times higher thermal resistance on ridges). We confirm that the spatial variability of the snow cover is vertically and horizontally large.

The insulative properties of the snow result in high-temperature gradients through the high-Arctic snowpack. These extreme temperature gradients produce large vapour fluxes in the snowpack. Our isotopic analysis changes the discourse of the origin of snow on sea ice. We no longer think of the snow as purely "atmospherically sourced", as our analysis revealed "ocean sourced" snow (a result of sublimation of the sea ice surface) is also present across the Arctic sea ice contributing to 28 % of the snow cover. This finding has identified sources of uncertainty in precipitation estimates (when comparing modelled precipitation to snow water equivalent measured in situ), the heat transfer through the ice and snow (a highly-conductive material is being replaced by a highly-insulating material), and the snow's chemical composition (a better understanding of the source of sea salt aerosols and the contribution of a snowpack molecular iodine source to Arctic ozone destruction). This new understanding and the suggestion to include

vapour flux in large-scale sea ice models have the opportunity to reduce major uncertainties in sea ice modelling.

In summer, the snow melts away to reveal another porous structure originating from melting sea ice: the surface scattering layer (SSL). The SSL effectively backscatters solar radiation and keeps the surface albedo of melting ice relatively high compared to the ice with the SSL manually removed. Albedo measurements provide information on how the SSL partitioned incoming shortwave radiation (i.e. how much radiation is absorbed, reflected and transmitted). This information is pivotal to improving climate model parameterisations of sea ice melt. However, the relationship between the physical and optical properties of the SSL is still poorly constrained. Until now, radiative transfer models have been the only way to infer the microstructure of the SSL. This thesis documents the unmeasured microstructural properties of melting sea ice and related this to the optical properties. We show that the SSL has a highly anisotropic, coarse, and porous structure, with a small optical diameter and density at the surface, increasing with depth. The SSL regenerates as the melting surface ablates, maintaining some aspects of its microstructure throughout the melt season. This study tested current radiative transfer models, typically used for snow, and their ability to model the albedo of the SSL. Compared to in situ albedo measurements, the radiative transfer model produced a 10 to 15 % overestimation of the reflectance at 850 nm. This is likely due to either 1) spatial variability at the meter scale is relevant and unaccounted for in the model or 2) an alternative modelling approach is needed using either a ray-tracing approach or using a model that considers anisotropy as opposed to estimating the structure as spheres in discrete layers.

# Résumé

La banquise joue un rôle essentiel dans l'Arctique en fournissant des habitats, en soutenant les glaciers de marée, en stabilisant les courants océaniques et en régulant le climat de la Terre via le réfléchissement du rayonnement solaire, et tous ces mécanismes peuvent influencer à leur tour les régimes météorologiques mondiaux. L'Arctique connaît des changements sans précédent, et le réchauffement de l'Arctique est plus rapide que celui du reste de la planète. Environ la moitié de la superficie de la banquise dans l'Arctique a été perdue depuis le début de la surveillance par satellite il y a 40 ans, et la région contient maintenant principalement de la banquise plus jeune. L'une des conséquences de la diminution de la banquise est l'augmentation des précipitations (davantage de neige en hiver et de pluies en été), ce qui a des répercussions inconnues sur le bilan énergétique du système de banquise arctique. Pour améliorer la modélisation et la surveillance de la banquise arctique et réduire l'incertitude des prévisions, nous devons d'abord comprendre les processus internes qui se produisent au niveau de la neige et qui influencent les composantes du bilan énergétique.

Alors que l'inaccessibilité de cette région explique en partie le manque de mesures sur le terrain, en 2019–2020, l'expédition MOSAiC a permis de mener une étude interdisciplinaire d'un an sur la banquise arctique. Cette thèse se concentre sur l'influence de la microstructure de la neige/SSL sur les échanges énergétiques à travers les données collectées pendant cette expédition d'un an. Nous soulignons l'importance de la neige dans le système de la banquise arctique et menons une étude des processus affectant les échanges d'énergie à partir des données in-situ étape de base si l'on veut améliorer la surveillance et la modélisation de l'Arctique.

L'une des composantes du bilan énergétique est le flux thermique, autrement dit le transfert de chaleur à travers la neige présente sur la banquise. Ce transfert de chaleur (conductivité thermique) et la résistance de la couverture neigeuse sont les principaux paramètres influençant la croissance de la banquise en hiver.

Les mesures et paramétrages des propriétés thermiques ont fait l'objet de nombreuses études, mais une évaluation de l'évolution saisonnière complète de la conductivité thermique et de la résistance de la neige fait jusqu'à présent défaut. En utilisant la totalité des données collectées durant l'expédition MOSAiC, nous avons évalué pour la première fois l'évolution saisonnière de la conductivité thermique et de la résistance thermique de la neige, et ce sur des banquises d'âge varié (chenaux, glace de première et deuxième année) et en tenant compte du relief (crêtes). Nous avons constaté que les valeurs actuelles de la conductivité thermique utilisées dans les modèles climatiques à grande échelle peuvent être surestimées. Nous suggérons d'autres valeurs de conductivité thermique (mesurées in situ à l'aide de la tomographie au rayons X assistée par ordinateur) et proposons que la modélisation de la banquise différencie les crêtes du reste de la banquise (nous avons trouvé une résistance thermique environ trois fois plus élevée sur les crêtes). Nous confirmons que la variabilité spatiale de la couverture neigeuse est importante verticalement et horizontalement.

Les propriétés isolantes de la neige entraînent des gradients de température élevés dans le manteau neigeux de l'Arctique. Nous avons découvert que les gradients de température extrêmes produisent d'importants flux de vapeur dans le manteau neigeux. Cette nouvelle compréhension grâce à l'analyse isotopique change le discours sur l'origine de la neige sur la banquise. Nous ne

pensons plus que la neige est purement « d'origine atmosphérique », car notre analyse a révélé que la neige « d'origine océanique » (provenant de la sublimation de la surface de la banquise) contribue à 28 % de la couverture neigeuse. Cette découverte a permis d'identifier une source de sous-estimation des précipitations (par rapport à l'équivalent en eau de la neige mesuré in situ), le transfert de chaleur à travers la glace et la neige (car un matériau hautement conducteur est remplacé par un matériau hautement isolant), et la composition chimique de la neige sur la banquise (grâce à une meilleure compréhension de la source des aérosols de sel marin et de la contribution d'une source d'iode moléculaire du manteau neigeux à la destruction de l'ozone arctique). Cette nouvelle compréhension et notre suggestion d'inclure les flux de vapeur dans la modélisation à grande échelle de la banquise permettraient de réduire des incertitudes majeures dans la modélisation de la banquise.

En été, la neige fond pour révéler une autre structure poreuse provenant de la fonte de la banquise: « surface scattering layer » (SSL). La SSL renvoie efficacement le rayonnement solaire et maintient l'albédo de surface de la banquise qui fond à un niveau relativement élevé par rapport à la banquise dont la SSL a été retirée manuellement. Les mesures de l'albédo fournissent des informations sur la façon dont le rayonnement de courte longueur d'onde entrant est distribué par la SSL et ont été essentielles pour améliorer les paramétrages des modèles climatiques. Cependant, la relation entre les propriétés physiques et optiques de la SSL est encore mal définie. Jusqu'à présent, les modèles de transfert radiatif ont été la seule façon de déduire la microstructure de la SSL. Nous avons documenté les propriétés microstructurelles non mesurées de la banquise fondante et les avons reliées aux propriétés optiques. Nous montrons que la SSL a une structure très anisotrope, grossière et poreuse, avec un petit diamètre optique et une faible densité à la surface et qui augmente avec la profondeur. Lorsque la surface fond, la SSL se régénère, conservant certains aspects de sa microstructure tout au long de la saison de fonte. Cette étude a testé les modèles de transfert radiatif actuels, généralement utilisés pour la neige, et leur capacité à modéliser l'albédo de la SSL. Comparé aux mesures in situ de l'albédo, le modèle de transfert radiatif a produit une surestimation de 10 à 15 % de la réflectance à 850 nm. Cela est probablement dû au fait que 1) la variabilité spatiale à l'échelle du mètre est pertinente et non prise en compte dans le modèle ou 2) une autre approche de modélisation est nécessaire en utilisant soit une approche de traçage de rayons au lieu de résoudre explicitement l'équation du transfert radiatif, soit un modèle qui prend en compte l'anisotropie au lieu d'estimer la structure comme des sphères dans des couches discrètes.

# Zusammenfassung

Meereis spielt in der Arktis eine entscheidende Rolle. Es bietet Lebensraum, unterstützt die Gezeitengletscher, stabilisiert die Meeresströmungen und durch die Reflexion der Sonnenstrahlung wird das Erdklima reguliert. Das wirkt sich unter anderem auf die globalen Wettermuster aus. Gegenwärtig ist die Arktis einem beispiellosen Wandel unterworfen, und sie erwärmt sich schneller als der Rest der Erde. Seit dem Beginn der Satellitenmessungen vor 40 Jahren ist etwa die Hälfte der Meereisfläche in der Arktis verschwunden, und das Meereis hat sich stark verjüngt. Dadurch hat sich der Niederschlag verstärkt (mehr Schnee im Winter und mehr Regen im Sommer). Allerdings die Auswirkungen auf den Energiehaushalt des arktischen Meereissystems weitgehend unbekannt. Eine verbesserte Modellierung und Überwachung des arktischen Meereis und verringerte Unsicherheiten bei Vorhersagen bedingen ein besseres Verständnis der internen Prozesse im Schnee, welche die verschiedenen Komponenten des Energiehaushalts stark beeinflussen.

Durch die Unzugänglichkeit dieser Region fehlt es an verlässlichen Messungen. 2019–2020 eröffnete die MOSAiC-Expedition den Wissenschaftlern die Möglichkeit eine einjährige interdisziplinäre Studie im arktischen Meereis durchzuführen. Diese Arbeit konzentriert sich auf den Einfluss der Mikrostruktur von Schnee und Schmelzschicht auf den Energieaustausch basierend auf den Daten, die während dieser einjährigen Expedition gesammelt wurden. Wir zeigen mittels Prozessstudien die Bedeutung des Schnees für den Energiehaushalt auf, und machen damit einen ersten Schritt für eine verbesserte Überwachung und Modellierung.

Ein Element der Strahlungsbilanz ist der Bodenwärmestrom, hier die Übertragung von Wärme durch den Schnee auf das Meereis. Wärmeleitfähigkeit und Wärmewiderstand der Schneedecke sind die wichtigsten Parameter, die das Wachstum des Meereises im Winter beeinflussen. Es gibt verschiedene Messungen und Parametrisierungen der thermischen Eigenschaften, aber die saisonale Entwicklung von Wärmeleitfähigkeit und -widerstand fehlt. Mit dem umfassenden Schneedatensatz der MOSAiC-Expedition konnten wir erstmals die jahreszeitliche Entwicklung der Wärmeleitfähigkeit und des Wärmewiderstands auf verschiedenen Eistypen (Rinnen, ein- und zweijährigem Eis) und topographischen Merkmalen (Presseisrücken) auswerten. Wir haben herausgefunden, dass die derzeit angenommenen Werte der Wärmeleitfähigkeit, welche in grossmasstäblichen Klimamodellen verwendet werden, möglicherweise zu hoch sind. Unsere neuen Messungen, die auf der mit Röntgen-Computertomographie gemessenen Mikrostruktur beruhen, ergeben deutlich niedrigere Werte. Presseisrücken haben einen bis zu dreimal höheren Wärmewiderstand, und sollten deshalb gesondert von flachem Eis behandelt werden. In allen Messungen zeigte sich, dass die vertikale und horizontale Variabilität sehr gross ist.

Der isolierende Schnee führt in der hocharktischen Schneedecke zu hohen Temperaturgradienten. Diese hohen Temperaturgradienten erzeugen in der Schneedecke einen grossen Dampfdruck. Mittels der Analyse der stabilen Wasserisotope konnten wir ein neues Verständnis über den Ursprung des Schnees auf dem Meereis gewinnen. Wir können den Schnee nicht mehr als rein atmosphärischen Schnee betrachten, denn unsere Analyse hat gezeigt, dass auch Schnee aus dem Ozean, welcher durch Sublimation der Meereisoberfläche entsteht, auf dem arktischen Meereis vorhanden ist und 28% der Schneedecke ausmacht. Mit dieser Erkenntnis findet sich eine Ursache für die Unterschätzung des Niederschlags (beim Vergleich mit dem in situ gemessenen Schneewasseräquivalent), für die Änderung der Wärmeübertragung durch Eis und Schnee



(ein gut leitendes Material wird durch ein isolierendes Material ersetzt) und die chemische Zusammensetzung des Schnees auf dem Meereis (durch ein besseres Verständnis der Quelle von Meersalzaerosolen und damit einer molekularen Jodquelle, welche das arktische Ozon reduziert) aufgezeigt. Diese neuen Erkenntnisse zur Schneemetamorphose sollten grosse Unsicherheiten bei der Meereismodellierung verringern.

Im Sommer schmilzt der Schnee und gibt danach die schmelzende Eisschicht frei, welche aber durch die hohe Kristallinität porös bleibt. Diese Schmelzschicht heisst englisch "surface scattering layer (SSL)", was sich mit Oberflächenstreuung übersetzen lässt. Die SSL streut ähnlich wie Schnee die Sonnenstrahlung zurück und behält die Albedo des schmelzenden Eises vergleichsweise hoch im Vergleich zu Meereis, bei welchem die SSL manuell entfernt wurde. Spektrale Albedo-Messungen zeigen, wie die kurzwellige Strahlung durch die SSL aufgeteilt wird, womit die Parametrisierung von Klimamodellen wesentlich verbessert wird. Die Beziehung zwischen den physikalischen und optischen Eigenschaften der SSL ist jedoch immer noch nicht ausreichend geklärt. Bis jetzt wurden Strahlungstransportmodelle mittels empirischer Parameter für die SSL angepasst. Wir haben die bisher nicht gemessenen mikrostrukturellen Eigenschaften des schmelzenden Meereises gemessen und diese mit den optischen Eigenschaften in Beziehung gesetzt. Wir konnten zeigen, dass die SSL eine stark anisotrope, grobe und poröse Struktur hat, mit einem kleinem optischen Durchmesser und einer geringen Dichte an der Oberfläche, welche mit der Tiefe zunimmt. Das schmelzende Eis regeneriert die SSL und behält die meisten Eigenschaften ihrer Mikrostruktur während der gesamten Schmelzperiode bei. Wir verglichen ein aktuelles Strahlungstransportmodell für Schnee auf seine Fähigkeit die Albedo der SSL zu modellieren. Im Vergleich zu den Albedo-Messungen vor Ort ergab das Strahlungstransfermodell eine um 10 bis 15% zu hohe Reflexion bei 850 nm. Dies ist wahrscheinlich darauf zurückzuführen, dass entweder die räumliche Variabilität auf der Meterskala relevant ist und im Modell nicht berücksichtigt wird oder ein alternativer Modellierungsansatz erforderlich ist. Dazu könnte ein Ray-Tracing-Ansatz unter Berücksichtigung der genauen Geometrie anstelle des Strahlungstransfermodell mit einer idealisierten, auf Kugeln beruhenden, Struktur in Frage kommen.

# Contents

<b>Acknowledgements</b>	<b>iv</b>
<b>Abstract</b>	<b>vi</b>
<b>Résumé</b>	<b>viii</b>
<b>Zusammenfassung</b>	<b>x</b>
<b>1 Introduction</b>	<b>1</b>
1.1 The Arctic energy budget . . . . .	2
1.1.1 Ground heat flux . . . . .	3
1.1.2 Latent heat . . . . .	4
1.1.3 Net surface radiation . . . . .	4
1.2 Spatial heterogeneity and temporal changes of snow on sea ice . . . . .	6
1.3 Scope of the thesis . . . . .	9
1.3.1 Research gap . . . . .	9
1.3.2 Outline . . . . .	9
<b>2 Measuring snow on Arctic sea ice</b>	<b>13</b>
2.1 Background & Summary . . . . .	14
2.2 Methods . . . . .	14
2.2.1 In situ measurements . . . . .	25
2.2.2 Ship-based measurements . . . . .	28
2.2.3 Shore-based lab measurements . . . . .	28
2.2.4 Sampling strategy . . . . .	28
2.3 Data Records . . . . .	30
2.3.1 Overview of datasets . . . . .	30
2.3.2 Parameter coverage . . . . .	32
2.4 Technical Validation . . . . .	32
2.5 Conclusion . . . . .	35
<b>3 Thermal conductivity of snow on Arctic sea ice</b>	<b>37</b>
3.1 Introduction . . . . .	38

3.2	Data and methods . . . . .	39
3.2.1	MOSAIC expedition . . . . .	39
3.2.2	$\mu$ -CT Samples . . . . .	39
3.2.3	SMP profiles . . . . .	42
3.2.4	Density profiles . . . . .	43
3.2.5	Atmospheric data . . . . .	44
3.3	Results . . . . .	44
3.3.1	Direct numerical simulations using FEM . . . . .	44
3.3.2	Parametrisations of thermal conductivity . . . . .	45
3.3.3	Spatial heterogeneity and temporal changes . . . . .	46
3.4	Discussion . . . . .	50
3.4.1	Assessing existing parametrisations . . . . .	50
3.4.2	Spatial heterogeneity . . . . .	51
3.4.3	Temporal change . . . . .	52
3.5	Conclusions . . . . .	53
<b>4</b>	<b>Ocean-sourced snow on Arctic sea ice</b>	<b>55</b>
4.1	Introduction . . . . .	56
4.2	Methods . . . . .	57
4.2.1	The MOSAiC expedition . . . . .	57
4.2.2	Stable water isotope and snow salinity profiles . . . . .	57
4.3	Results . . . . .	58
4.3.1	Stable water isotopes as a tracer . . . . .	58
4.3.2	Salinity and d-excess as tracers . . . . .	61
4.3.3	The rate of the sea ice sublimation . . . . .	63
4.4	Discussion . . . . .	64
4.4.1	Precipitation estimates . . . . .	65
4.4.2	Heat transfer . . . . .	65
4.4.3	Sea ice chemistry implications . . . . .	65
4.4.4	Conclusion . . . . .	66
<b>5</b>	<b>Optical properties of melting Arctic sea ice</b>	<b>67</b>
5.1	Introduction . . . . .	68
5.2	Methods . . . . .	71
5.2.1	Theory . . . . .	71
5.2.2	Microstructure measurements . . . . .	72
5.2.3	Reflectance measurements at 850 nm . . . . .	73

5.2.4	Two-streAm Radiative TransfEr in Snow . . . . .	74
5.3	Results . . . . .	75
5.3.1	SSL microstructure . . . . .	75
5.3.2	SSL reflectance . . . . .	77
5.4	Discussion . . . . .	83
5.5	Conclusion . . . . .	87
<b>6</b>	<b>Synthesis</b>	<b>89</b>
6.1	Conclusions, implications and future work . . . . .	89
6.2	Temporal synthesis of chapters . . . . .	91
6.3	Spatial synthesis of chapters . . . . .	92
<b>7</b>	<b>Publications</b>	<b>93</b>
<b>A</b>	<b>Responsible fieldwork</b>	<b>A-1</b>
A.1	A call for funding bodies to influence the reduction of environmental impacts in scientific fieldwork . . . . .	A-1
	<b>Bibliography</b>	<b>A-5</b>



# List of Figures

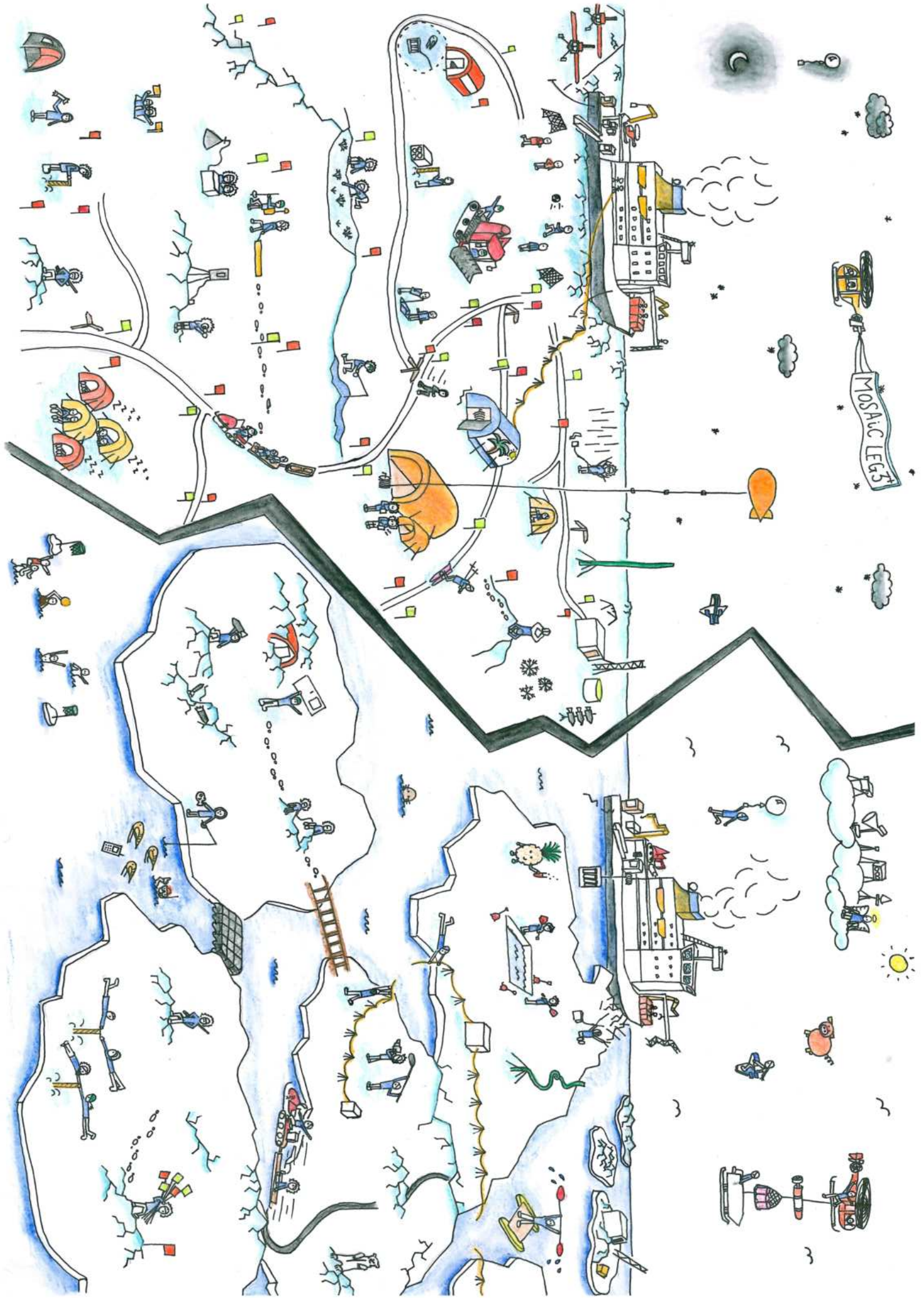
1.1	Components of the energy budget measured during the MOSAiC expedition . . .	3
1.2	The influence of snow on Arctic sea ice exchanges and processes . . . . .	5
1.3	Topographic features of Arctic sea ice in the winter season . . . . .	6
1.4	A typical Arctic sea ice winter landscape with level and ridged ice. . . . .	7
1.5	Topographic features of Arctic sea ice in summer. . . . .	8
1.6	A typical Arctic summer sea ice landscape . . . . .	9
1.7	The winter to summer sea ice transition with annotations of the chapters in this thesis. . . . .	10
2.1	Snowpit locations of each unique device operation ID. . . . .	15
2.2	Time series of snowpit measurements at each snowpit site. . . . .	16
2.3	Schematic diagram of the snowpit locations across central observatory 1. . . . .	17
2.4	Schematic diagram of the snowpit locations across central observatory 2. . . . .	18
2.5	Schematic diagram of the snowpit locations across central observatory 3. . . . .	19
2.6	A combination of the different instruments taken to the snowpit site. . . . .	22
2.7	A case study of the measurements taken during an event. . . . .	23
2.8	Time series of parameters for the entire season. . . . .	33
2.9	The snow water equivalent cross-checked for two co-located measurements. . .	34
2.10	Comparison of co-located SMP and micro-CT measurements. . . . .	35
3.1	Samples of effective thermal conductivity plotted against time. . . . .	40
3.2	The sub-samples density plotted against effective thermal conductivity . . . . .	41
3.3	Density plot of effective thermal conductivity. . . . .	45
3.4	Different parametrisations of effective thermal conductivity . . . . .	46
3.5	A box plot showing spatial and temporal trends for measured snow parameters	48
3.6	Time series of density using three independent instruments . . . . .	49
3.7	A heatmap of winter snow micro-penetrometer profiles on level ice. . . . .	50
4.1	Winter isotopic overview of the snow samples . . . . .	59
4.2	A time series heatmap of the oxygen-18 to oxygen-16 ratio and deuterium-excess	60
4.3	Profiles of the oxygen-18 to oxygen-16 ratio and deuterium-excess . . . . .	60
4.4	A schematic showing sublimation of the snow-sea ice interface . . . . .	62
4.5	Sample salinity values plotted against deuterium-excess . . . . .	63

5.1	Schematic of the formation of the surface scattering layer . . . . .	70
5.2	Methods for in situ measurements of the surface scattering layer. . . . .	72
5.3	A model reconstruction of the surface scattering layer and corresponding microstructural profiles. . . . .	73
5.4	Micro-computed tomography profiles of the surface scattering layer . . . . .	77
5.5	Time series of microstructural parameters for surface scattering layer samples. .	78
5.6	A selection of NIRbox images with their corresponding histograms . . . . .	79
5.7	A time series of reflectance measurements at 850 nm . . . . .	80
5.8	Changes in the microstructure and their influence on the reflectance at 850 nm	81
5.9	The relationship between specific surface area and reflectance at 850 nm . . . .	82
5.10	Probability density functions of the three methods used to determine reflectance at 850 nm. . . . .	83
5.11	Co-located measurements from the three methods used to determine reflectance at 850 nm. . . . .	84
5.12	A test of the influence of the asymmetry factor on the modelled output albedo.	85
6.1	A schematic to summarise the synthesis of the chapters. . . . .	91

# List of Tables

2.1	Information about each device taken into the field. . . . .	21
2.2	Details of the three snowpit protocols. . . . .	24
3.1	An overview of the thermal conductivity parameterisations. . . . .	42
3.2	Snow depth, density, thermal conductivity and resistance for each ice type . . .	47





# Introduction

---

Sea ice plays a critical role in the Arctic and Antarctic by providing habitats, buttressing tidewater glaciers, stabilising ocean currents and regulating the Earth's climate by reflecting solar radiation, all of which have a ripple effect on global weather patterns. In recent years, there has been a significant decline in sea ice in the Arctic due to climate change, causing concern among scientists and policymakers [3]. We are currently observing a "new" Arctic, which consists of younger (more first-year ice; sea ice of not more than one winter's growth, and less multi-year ice; ice that has survived at least one melt season) [4, 5], faster (the drift of the sea ice is increasing) [6], thinner [7], weaker and more saline ice [8]. This has implications throughout the entire Arctic ecosystem. As a result, we are observing more ice deformation [9], habitat loss [10], atmospheric instability [11], ocean current instability [12] and changed biogeochemical fluxes [13]. The increased ice deformation combined with sea ice decline brought about more areas of open water, an increasing amount of evaporation from the ocean, and increased precipitation in the new Arctic [14]. The consequence of the increased precipitation could result in either a) more snowfall events (providing more insulation, higher albedo and an increased likelihood of flooding of the sea ice surface causing saline snow [15]), or b) more rainfall (drastically altering the snow microstructure and decreasing albedo of the sea ice system [16]). Recent studies are identifying an increasing amount of rain on snow events [16] and the onset of rain earlier in the season. Additionally, modelling studies show a projected shift in the seasonal snowfall cycle with a decrease in snow depth associated with sea ice loss [17, 18], and monitoring of Arctic snow conditions show that some regions have exhibited a decrease in snow depth due to later sea-ice formation in autumn [19].

Heterogeneity of snow depth and density contributes a) up to 70 % of the total uncertainty in Arctic sea ice thickness retrievals from airborne and spaceborne measurements and b) uncertainty in the heat transfer from the Arctic Ocean to the atmosphere due to its spatially varying insulating properties [20]. As a result, it is measured to be one of the most significant uncertainties in global climate models [21, 22, 23]. To reduce these uncertainties and improve monitoring and modelling techniques, we must first understand the small-scale processes influencing the energy budget in this delicate region. The lack of ground-truth measurements has been a primary source of uncertainty in this region. Models often have to estimate input parameters based on very little data. Due to the rapid changes in this region, previous expeditions and in situ measurements are also becoming outdated.

## 1.1 The Arctic energy budget

The Arctic energy budget is the total of all energy flows into and out of the Arctic from all sources and is an essential factor in the Arctic climate system. Snow is the interface between the ice and the atmosphere, and as a result, it significantly influences the fluxes across the Arctic sea ice-atmosphere boundary. The total heat energy stored in this snow surface layer is the combination of a) the net surface energy, or net radiation (seasonality is shown in Figure 1.1c), b) ground heat flux, c) sensible heat flux and d) latent heat flux [24]. Net solar radiation is the difference between the absorption and reflection of shortwave and longwave radiation. Sensible heat flux is the heat transfer from the surface to the atmosphere, and latent heat flux is the heat transfer from the atmosphere to the surface. These two components are known as turbulent heat fluxes. Finally, the ground heat flux is energy loss by heat conduction. These components interact in complex ways, and depending on the season, we have different contributions from each component to the overall energy budget. The downward shortwave radiation, downward longwave radiation, net radiation and surface energy budget for one year is presented in Figure 1.1c for the MOSAiC expedition (details given in Section 1.3.2). In the winter months, we have no incoming (downward) solar shortwave radiation due to polar night (Figure 1.1a), so the downward longwave (Figure 1.1b) is dominating the net radiation component. This thesis investigates the impact of snow microstructure on the other three major energy budget components whilst studying this surface layer's seasonal, regional and general variability.

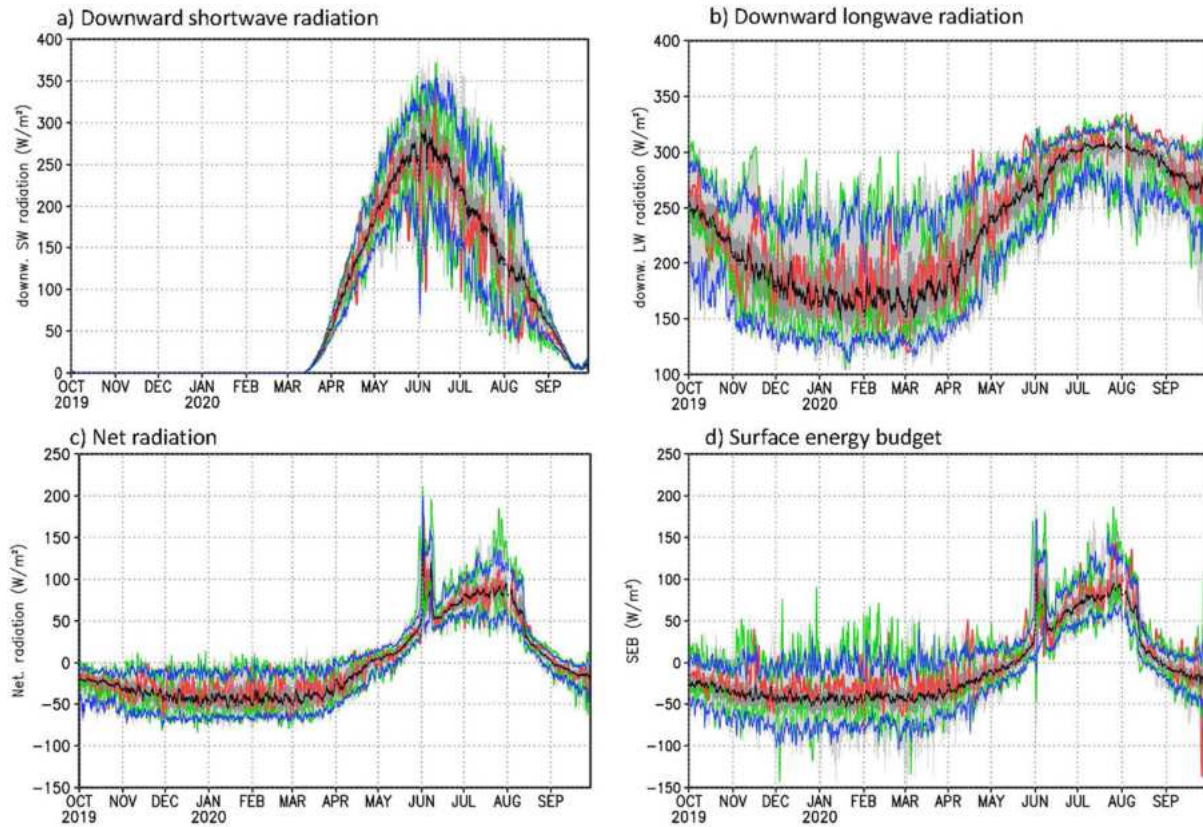


Figure 1.1: The energy budget measured from the MOSAiC expedition 2019–2020. Figure adapted from: [25] “Comparison between Multidisciplinary drifting Observatory for the Study of Arctic Climate (MOSAiC) and climatological surface energy fluxes. The comparison presents time series of surface fluxes ( $\text{W m}^{-2}$ ) of (a) downward shortwave radiation, (b) downward longwave radiation, (c) net [solar] radiation, and (d) surface energy budget (SEB) at Polarstern position and based on ERA5 (average over the four nearest grid points). Red line: MOSAiC year, black line: median over 1979–2019, dark grey shading: interquartile range, blue lines: 5<sup>th</sup> and 95<sup>th</sup> percentiles, and light grey shading: minimum–maximum range from 1979 to 2019 data. The 5<sup>th</sup> and 95<sup>th</sup> percentiles from the recent 2010–2019 period are shown with green lines and indicate the full range of this period’s data. Based on hourly data, 24-h running means are plotted. The abrupt increase of net radiation (and thus SEB) at the beginning of June is associated with the parking of Polarstern in the ice-free fjord of Svalbard between MOSAiC Leg 3 and Leg 4. The abrupt decrease of SEB at the end of September is associated with a temporary reduction of sea-ice concentration near the ice edge in the Fram Strait and large upward turbulent heat fluxes.” <https://doi.org/10.1525/elementa.2021.00023.f2>

### 1.1.1 Ground heat flux

As mentioned above, ground heat flux is energy loss by heat conduction. The thermal properties of snow play an essential role in the Arctic sea ice system by acting as an insulating layer and reducing sea ice growth. The thermal conductivity of a material is a measure of its ability to conduct heat. The thermal conductivity of snow is highly dependent on the (highly variable) microstructure (discussed in Section 1.2). There are three potential processes of heat transfer through the snow: i) conduction through the ice grains, ii) conduction, convection, and radiation across air spaces, and iii) water vapour diffusion between the ice grains [26]. Conduction occurs

when heat is transferred through direct contact between two objects. In the case of snow on sea ice, the ice grains act as the conductor, transferring the heat from the sea ice below to the atmosphere above. Convection occurs when heat is transmitted through the movement of vapour or air between the snow crystals. In the case of snow on sea ice, the warmer sea ice surface often results in vapour moving upwards through the snow, transferring heat from the warm ocean to the atmosphere. Thermal conductivity is a function of snow density and spatial heterogeneity. As a result, snow accumulation and snow stratigraphy in winter directly influence the mass balance and, consequentially, the energy balance of sea ice. Various measurements and parametrisations of thermal properties exist, but an assessment of the entire seasonal evolution of thermal conductivity and snow resistance is hitherto lacking. This is a critical assessment to understand how a “new” Arctic with younger ice and more precipitation will influence future sea ice growth in winter.

In summer, heat transfer through the ice via conduction is less prominent as the atmosphere above the sea ice surface is close to 0 °C and the underlying ocean is -1.8 °C, and as a result, the sea ice has a very low-temperature gradient or even experiences an isothermal state. The summer season energy budget is discussed in more detail below.

### 1.1.2 Latent heat

Snow is a dynamic material and, when a temperature gradient is applied, undergoes a process called metamorphism. Metamorphism is the sublimation of the ice and deposition on the opposing surface. Latent heat is a substance’s energy released or absorbed during a state change. As snow undergoes metamorphism, it changes from solid to vapour and takes latent heat from its surroundings. This energy breaks the bonds between the ice molecules and converts them from solid to gas, producing vapour and mass fluxes in the snow cover. In the Arctic, we have extreme temperature gradients in the snowpack in the range of  $100 \pm 50 \text{ K m}^{-1}$  [27] between the sea ice surface and the atmosphere, with typical atmospheric temperatures between  $-20 \text{ °C}$  to  $-40 \text{ °C}$  and stable ocean temperatures at approximately  $-1.8 \text{ °C}$ . Warm air intrusions in spring temporarily reverse the temperature gradient. Still, generally, there is a constant temperature gradient direction in winter where the sea ice interface is warmer than the atmosphere. Typical depth hoar has been reported to form from the metamorphism of snow subjected to temperature gradients of  $>20 \text{ K m}^{-1}$  [28, 29, 30], so these extreme temperature gradients on Arctic sea ice produce perfect conditions for snow metamorphism. Stable water isotopes can be used to understand the origin and changes within a snowpack caused by sublimation and deposition [31, 32, 33, 34, 35, 36]. However, isotope analysis has never been conducted for snow on sea ice in the high Arctic during winter. Consequently, we know little about the internal processes occurring in the snow cover.

As we transition into summer, latent heat also results in snow and ice melt. The amount of latent heat released in summer is a result of the net positive surface radiation, which leads to the final component of this thesis:

### 1.1.3 Net surface radiation

Radiation occurs when heat is transferred through electromagnetic waves, such as the sun’s rays. For half of the year, during the polar night, there is no shortwave radiation in the Arctic. In the other half, shortwave radiation is the dominant energy source for 24 hours of the day. As we transition from winter into summer, snow on sea ice reflects solar energy instead of allowing it to be absorbed by the underlying sea ice. This reflection prevents sea ice from melting during

the early summer months. Albedo measures how much incoming solar radiation is reflected on a scale from 0 to 1. The albedo of snow, melting sea ice and melt ponds are essential input parameters for large-scale modelling of sea ice melt. This modelling is critical in estimating the Arctic’s freshwater source (pivotal to the Arctic ecosystems).

Snow on sea ice has a much higher albedo (0.70 to 0.90) than the underlying sea ice (which ranges from 0.60 to 0.75). This higher albedo of snow helps to slow the melting of sea ice and allows the sea ice environment to remain cooler and more stable. A thicker snow layer can reduce the amount of solar radiation absorbed by the ice, resulting in a cooler surface temperature and slower melting. However, snow on Arctic sea ice is seasonal, meaning that after each winter, all the snow on level ice melts away to reveal the underlying ice. As a result, the incoming shortwave radiation directly melts the sea ice in summer. An exciting feature of sea ice is its internal brine channels that form during the ice’s freezing process in the winter. As we transition to summer and all the snow melts away, these internal brine channels undergo preferential melt, and we observe a highly porous surface appearing. The landscape looks like snow, but on closer inspection of the microstructure, we have a pillared structure originating from the melting sea ice (Chapter 5). This porous, melting sea ice is called the surface scattering layer (SSL) throughout this thesis. We have a good understanding of the SSL’s albedo and optical properties over the seasonal sea ice melt cycle [37, 38]. However, we have not measured the detailed microstructure of the SSL. We present a first study of the microstructure’s influence on the SSL’s optical properties. As sea ice is getting younger and more saline, we seek to understand the influence of these microstructural changes on the sea ice albedo.

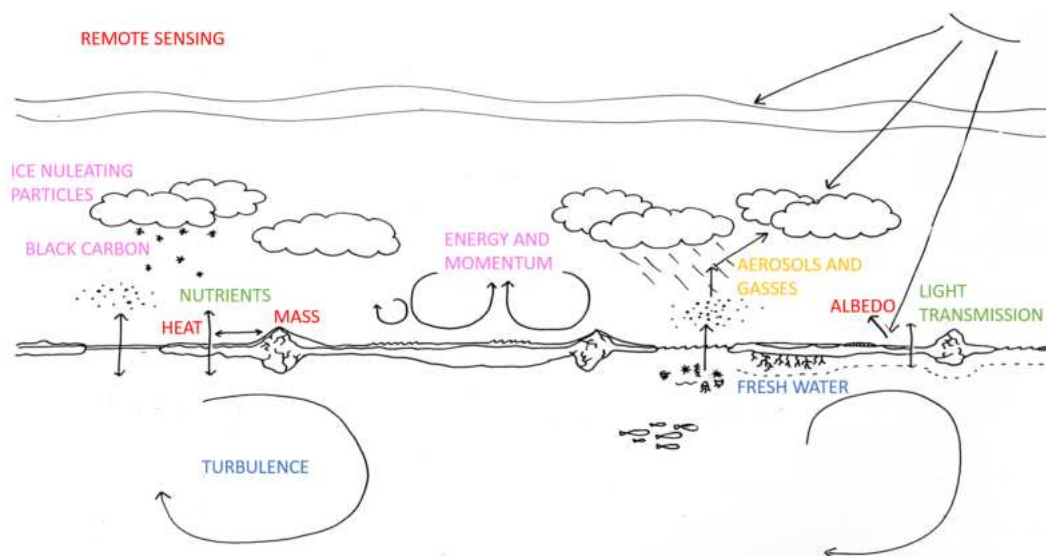


Figure 1.2: A schematic of the influence of snow on Arctic sea ice exchanges and processes. The names in red indicate processes measured from a physical ice perspective, pink indicates atmospheric processes, blue indicates ocean processes, and green indicates biogeochemical processes. This figure is not drawn to scale.

In summary, the above outline covers a) heat fluxes and b) mass exchange in the snow cover. These processes are shown in red in Figure 1.2. When we look at the overview of fluxes in the

Arctic sea ice system, we start to piece together the importance of snow in all of these aspects. The snow cover has repercussions for many fields, such as sea ice hydrology (as a source of fresh water), a source of sea salt aerosols, a sink for black carbon, and is highly influential on light transmission (relevant for sub-ice species and algae [3, 24]). Summarising the fluxes that are influenced by, or influence, the snow cover is shown in the schematic in Figure 1.2 where the colours of each component indicate a field of research.

## 1.2 Spatial heterogeneity and temporal changes of snow on sea ice

Sea ice is not a flat landscape, and modelling and ship navigation rely on information about the sea ice surface topography [39]. Mechanical forces deform sea ice due to wind stress, ocean currents, and blocking effects of land, which cause spatial variations of the ice drift velocity. Deformation can be in the form of compression of the ice (forming ridges) or separation/cracking of the ice (creating leads or polynya). These features have extreme consequences for the snow conditions resting above and the mass and energy balance of the Arctic environment. A schematic of these features is illustrated in Figure 1.3.

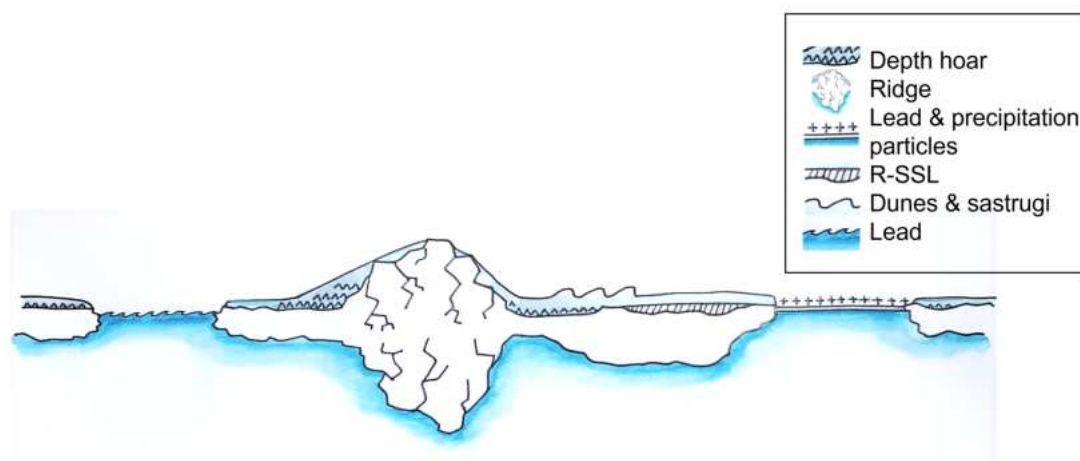


Figure 1.3: Topographic features of Arctic sea ice in the winter. First-year and second-year ice are labelled FYI and SYI, respectively. This schematic is not drawn to scale.

Un-deformed Arctic sea ice is called "level ice" throughout this article. The seasonal snow on this level ice is relatively thin (average 130 mm with a standard deviation of 99 mm [40]) and is predominantly defined by features of deposition and erosion. The typical level sea ice features can be seen in the foreground of Figure 1.4; dunes and sastrugi are dominant features. If we were to dig a snowpit in the foreground, we would see that the snowpack stratigraphy is defined by precipitation particles, rounded wind-packed grains, wind crusts (both at the surface and buried within the snowpack) and depth hoar (predominantly at the lower levels) [41].

Storms and "blowing-snow" events are common with the high wind velocities in the central Arctic. These often result in large snow re-distribution and complete snow cover mixing, making the stratigraphy extremely complex and horizontally variable. Properties of the snowpack measured just 10 cm apart show significantly different stratigraphic features. Unlike land-based

studies, the drifting sea ice and the rotating wind directions mean that snow erosion and re-distribution are not uniform. Identifying persistent layers within the snowpack is challenging, meaning accurate modelling of stratigraphy is a near-impossible task. The metamorphism of the snow and re-arrangement of the ice crystals in the snowpack produce depth hoar, a cup-shaped snow crystal. Depth hoar often forms at the lower levels of the snowpack [42, 30] and is a prominent feature of Arctic sea ice snow stratigraphy. Depth hoar influences heat flux due to the orientation of the snow crystals (anisotropy), and is a source of uncertainty in microwave backscatter from satellite remote sensing [43], hence an important feature to measure. We do not know the amount of metamorphism of snow on sea ice, and current large-scale models do not introduce complex snow stratigraphy features.

Pressure ridges, produced by the convergence between two ice floes, constitute a significant accumulation area for snow, and the stratigraphy of snow in ridges is predominantly wind-packed rounded grains. The large snow depths adjacent to the ridged areas have higher thermal resistance than level ice (Chapter 3).



Figure 1.4: A typical sea ice landscape with erosion and deformation features on the level ice in the foreground and a heavily ridged site in the background. Photo credit: M. Gutsche.

Deformation events resulting in the ice separating cause leads or polynya to form. These features can be treated as a "reset" for snow processes, and as new ice forms over the lead, there is the possibility to study the initial freeze-up and snow accumulation on young ice. Once sea ice starts to form on leads, wind re-distribution of snow ensures that no sea ice older than a few days is without a covering of snow. The snow that accumulates is primarily wind-blown and has a simple stratigraphy. Yet, the Arctic conditions (low temperature and high wind velocities) highly influence snow accumulation and the underlying ice growth. Snow can also be lost into leads if no ice forms before the snow accumulation event. A final feature of leads is "frost flowers", also seen in Figure 1.3. Frost flowers form if there is no snow re-distribution/accumulation, calm conditions and high-temperature gradients between the young sea ice and the atmosphere. When cold, moist air above the sea ice becomes saturated, imperfections on the icy surface cause frost to form and initiate the frost flower growth. The growth happens as moisture is wicked from the frozen young ice surface, capturing salt, possibly supplying bromine compounds to the atmosphere and capturing marine bacteria [44]. As snow falls on top or is re-distributed onto the frost flowers, we may measure saline snow at the sea ice-snow interface. The other processes resulting in saline snow and the implications of this are given in Chapter 4.



Transitioning into summer, on average, have 24h daylight and stable atmospheric temperatures of approximately  $0^{\circ}\text{C}$  at the sea ice surface. Occasional weather events occur in summer, which causes considerable fluctuations in the temperature and surface conditions. The sea ice is saturated with freshwater from the melted snow, and melt ponds form on the sea ice surface. This paper focuses on the un-ponded areas, including ice of different ages and topographies. The schematic in Figure 1.5 shows the typical summer sea ice landscape features.

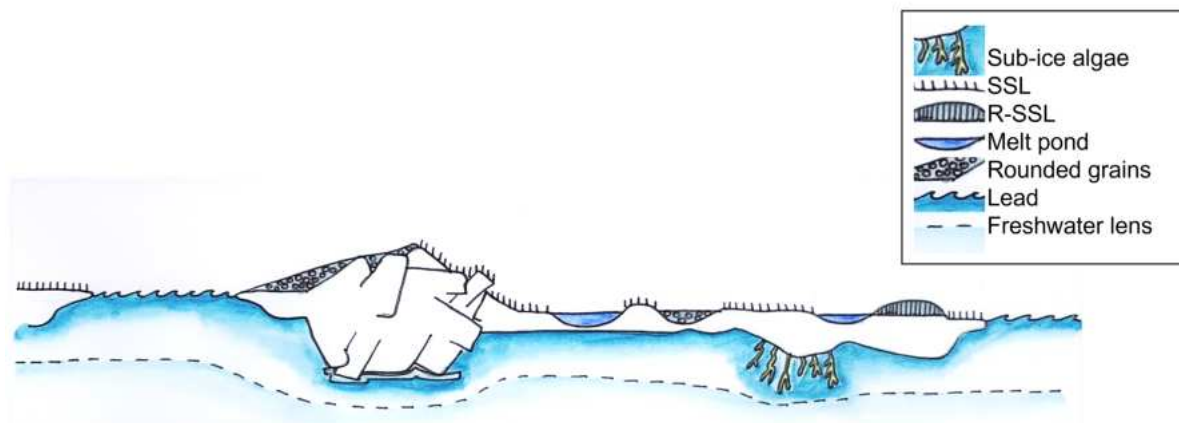


Figure 1.5: Topographic features of Arctic sea ice in the summer. This schematic is not drawn to scale.

The past decade has seen an advancement in snow measurement techniques. Tools developed in the snow research community were adapted to measure the structure of melting sea ice in the summer in this thesis. In spring, snowmelt sets the timing for ice melt [23]. If present, the snow can protect the ice from the sun’s rays in spring and summer or, if it has melted away, leave the ice exposed and vulnerable to melt [23]. As the sea ice undergoes melt, a porous, highly reflective, snow-like surface appears (named the surface scattering layer; SSL, in this paper). This snow-like appearance is explained further in Chapter 5 and visualised in Figure 1.6. The physical and optical properties of the SSL are influenced by preferential melt at the grain boundaries. We observed a large spatial variability in the microstructure of the sea ice surface, with different surface types both in the field and in our measurements. The SSL is just one of many categories of surface structures appearing on melting sea ice. We found that this spatial variability of the microstructure of the sea ice surface is high when ice has different histories or freezing processes, which leads to an array of surface melt patterns and structures caused by the ice having different grain boundaries. These different surface types provide an extensive range of albedo values. In previous studies, the surface of sea ice was categorised as early autumn snow, melting snow, bare ice (known in this study as the SSL), thin ice, sediment-laden ice and (various) ponded ice types[38]. The schematic in Figure 1.5 shows the range of different processes and features on summer sea ice. The albedo variability can be seen in Figure 1.6, where the white sea ice surface is the SSL, with local roughness varying the albedo. However, this thesis focuses on level ice with a homogeneous SSL without previous ridging, ponding (Figure 1.6) or complex freezing history.



Figure 1.6: A typical Arctic summer sea ice landscape showing melt ponds, a ridged area in the background and the surface scattering layer. Photo credit: A. Macfarlane

## 1.3 Scope of the thesis

### 1.3.1 Research gap

Spatial heterogeneity of the snow depth and vertical variability of the snow density, realised from laboratory and in situ field measurements [45], are the dominant uncertainties in estimates of Arctic sea ice thickness retrievals from airborne and spaceborne measurements [20]. Current modelling and process understanding of snow on sea ice is limited due to a lack of ground-based measurement. As a reference for models, scientists rely on the limited expeditions [46, 45] in the central Arctic for test datasets. However, these measurements may quickly become outdated due to the rapidly changing Arctic. We better understand the influential processes occurring by measuring sea ice’s thickness, extent, and concentration and the snow’s microstructural properties. This understanding can be implemented into the regional models to better monitor the sea ice through satellite remote sensing or better predict the future Arctic sea ice conditions in the changing climate.

Until now, it has not been feasible to measure the microstructure of the snow and SSL in situ in such a high resolution, and microstructural properties have been inferred through alternative methods. Through lack of measurements, many processes in the Arctic climate system are poorly represented in climate models. And this thesis presents unprecedented year-round measurements of snow and melting sea ice in the high Arctic.

### 1.3.2 Outline

This thesis studies the annual evolution of the microstructural properties of Arctic sea ice. The objective is to understand better the snow cover’s internal processes and the interaction between the snow’s microstructure and the energy budget. We identify significant uncertainties in current regional models and provide solutions to reduce this uncertainty. The thesis begins with a data paper in Chapter 2 outlining the data collection methods, giving an overview of the datasets used in this thesis, parameter coverage of the dataset and any initial technical validation. The remainder of the thesis is separated into three chapters, each improving our understanding of a component of the Arctic energy budget. Chapter 3 investigates the thermal conductivity of the snow and, therefore, the ground heat flux. Chapter 4 researches the sublimation of the sea

ice surface, deposition of water vapour in the snow, and hence the latent heat during the phase change from ice to vapour. Finally, Chapter 5 investigates the influence of the surface scattering layer’s microstructure on the albedo in summer, which is included in net surface radiation. A schematic showing each Chapter’s focus can be seen in Figure 1.7.

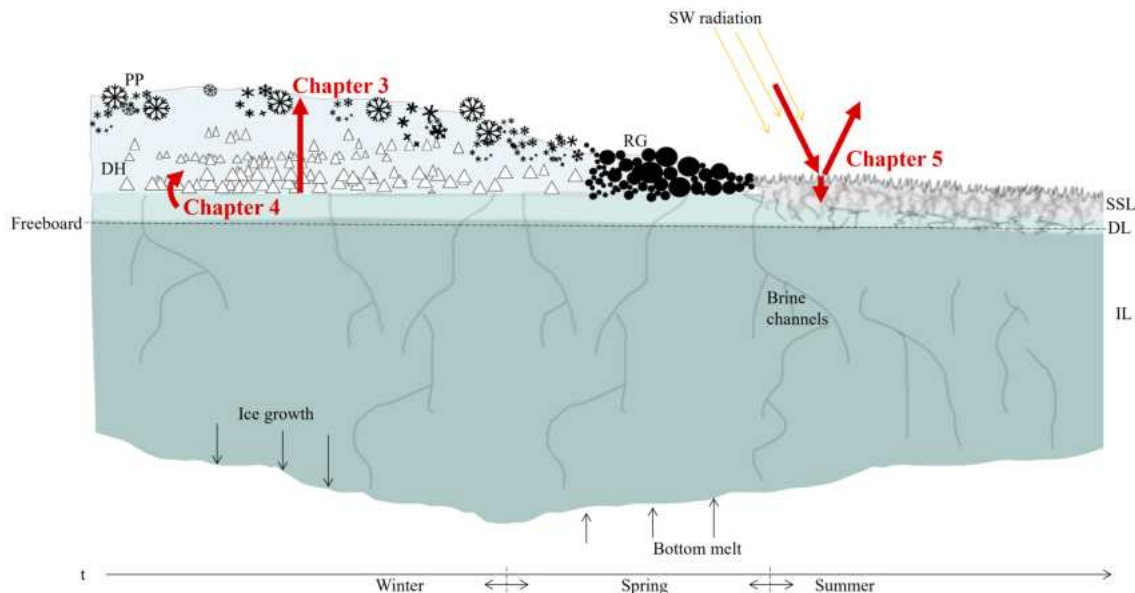


Figure 1.7: A schematic of the winter to summer sea ice transition highlighting the chapters in this thesis. Chapter 3 analyses the thermal conductivity of the snow, Chapter 4 researches the sublimation of the sea ice surface, and Chapter 5 researches the influence of the surface scattering layer’s microstructure on the albedo in summer. The acronyms are as follows: PP = precipitation particles, DH = depth hoar, RG = rounded grains, SSL = Surface scattering layer, DL = drained layer, IL = interior layer, and SW radiation = shortwave radiation. This image is not to scale.

In 2019-2020 an expedition to the Arctic provided opportunities for international scientists to conduct measurements on sea ice and contribute to large-scale process understanding. The MOSAiC expedition is the thread throughout this entire thesis. This expedition was a one-of-a-kind opportunity to collect in situ samples of the microstructure of the snow/ SSL from the high Arctic. As a result, many properties of the Arctic sea ice system were measured for the first time. It was necessary to develop new measurement methods that were efficient, accurate and easy to use in harsh measuring conditions. X-ray microcomputer tomography ( $\mu$ -CT) has advanced our understanding of micro-structural changes in the snow in the past decade. This instrument is pivotal throughout the thesis. By installing the  $\mu$ -CT in a cold laboratory on board Polarstern [1] during the MOSAiC expedition, we could measure (for the first time) the exact microstructure alongside snowpits with the standard density, temperature, reflectance and snow micro penetrometer measurements. By collecting over 300  $\mu$ -CT snow samples, the amount of snow microstructural data collected in this region is unprecedented. Consequentially, we have been able to investigate the influence of the microstructure on the different energy components (outlined at the start of the introduction). This allowed three novel studies which dive into three critical questions when solving the energy budget in the Arctic. This thesis outlines the findings of these studies. We have been able to i) develop new parameterisations of Arctic sea ice snow’s thermal conductivity and compare them to current parameterisations used in large-scale

models, ii) collect high-resolution isotopic analysis in parallel to microstructural measurements, which allowed us to identify the role of post-depositional processes within the snowpack, and finally iii) measure the microstructure of the SSL for the first time and test this as a radiative transfer model input.



# Measuring snow on Arctic sea ice

---

Macfarlane, A. R., Schneebeli, M., Dadic, R., Tavri, A., Immerz, A., Polashenski, C., Krampe, D., Clemens-Sewall, D., Wagner, D. N., Perovich, D. K., Henna-Reetta, H., Raphael, I., Matero, I., Regnery, J., Smith, M. M., Nicolaus, M., Jaggi, M., Oggier, M., Webster, M. A., Lehning, M., Kolabutin, N., Itkin, P., Naderpour, R., Pirazzini, R., Hämmerle, S., Arndt, S., Fons, S.

Published in: Scientific Data (2023).

## Abstract

Snow plays an essential role in the Arctic as the interface between the sea ice and the atmosphere. Optical properties, thermal conductivity and mass distribution are essential to understanding the complex Arctic sea ice system's energy balance and mass distribution. By conducting measurements from October 2019 to September 2020 on the Multidisciplinary drifting Observatory for the Study of Arctic Climate (MOSAiC) expedition, we have produced a dataset capturing the year-long evolution of the physical properties of the snow and surface scattering layer, a highly porous surface layer on Arctic sea ice that evolves due to preferential melt at the ice grain boundaries. The dataset includes measurements of snow during MOSAiC. Measurements included profiles of depth, density, temperature, snow water equivalent, penetration resistance, stable water isotope, salinity and microcomputer tomography samples. Most snowpit sites were visited and measured weekly to capture the temporal evolution of the physical properties of snow. The compiled dataset includes 576 snowpits and describes snow conditions during the MOSAiC expedition.

## 2.1 Background & Summary

Snow cover modulates the thermal and optical properties of the sea ice surface and the energy fluxes between the ocean and the atmosphere, directly impacting the amount of ice growth in the winter and ice melt in the summer [47, 48, 49, 50, 51, 23, 52, 53, 54, 55]. Despite its importance, measurements of the physical properties of snow on sea ice throughout the annual cycle are limited to just a few expeditions (e.g. SHEBA [45], N-ICE [56], TARA [57], Russian drifting stations [46]) and the Canadian Arctic (See Table \*1 in [58]). Due to the rapid changes in the Arctic, data in this region quickly becomes outdated. As a result, this MOSAiC dataset has increased value due to its recent collection (compared to SHEBA), and as a result, is likely more representative of the new Arctic stricken by climate change. This lack of up-to-date regional data causes significant biases in model representations of sea ice variables [59] and significant uncertainty in how sea ice influences the global energy budget. The IPCC 2019 Special Report on the Ocean and Cryosphere in a Changing Climate [60] identifies snow on sea ice as one of the "key knowledge gaps and uncertainties" limiting predictive climate models. In addition to its major implications on the physical properties of sea ice in winter, the snowmelt in summer acts as a freshwater source affecting melt ponds and upper ocean stratification and determines light and nutrient availability for polar marine ecosystems [61]. As the snow melts, bare ice is exposed. Preferential melting of grain boundaries in columnar ice produces the surface scattering layer (SSL): a granular, snow-like material that behaves similarly to meteoric snow in certain respects [37]. Understanding the physical properties of the SSL is key to understanding sea ice albedo and surface ablation.

This dataset documents the stratigraphy and microstructure of the snow cover and, in the absence of snow, the microstructure of the SSL and ice surface throughout the Multidisciplinary drifting Observatory for the Study of Arctic Climate (MOSAiC) expedition [62]. This dataset and data paper detail all measurements categorised as "snowpit events" during MOSAiC. Each snowpit "event" corresponds to one visit to a snowpit location and has an assigned unique device operation ID. The dataset documents the temporal and spatial evolution of the physical properties of the snow/ice surface layer. Expected applications of these data include snow-focused and interdisciplinary research areas, such as (1) thermal conductivity of snow on sea ice and thermal transfer across the ocean-ice-atmosphere system; (2) surface energy budget and radiative transfer through the snow and ice column into the upper ocean; (3) satellite retrievals of snow and ice thickness; (4) the freshwater budget. We used 16 different instruments to characterise the physical properties of snow and the SSL during MOSAiC.

## 2.2 Methods

The study area was on drifting sea ice, originally located 85.44 degrees North. The locations of the snowpit sites are shown in Figure 2.1. This dataset's difficult-to-access latitudinal range, unprecedented detail and wide range of parameters measured make it a unique dataset for studying the role of snow in the Arctic sea ice system. Observations were conducted in two primary modes to account for temporal and spatial heterogeneity. The first mode aimed to collect a time series of measurements at points of interest by setting up designated, undisturbed areas in the central observatories (CO), approximately 0.01 - 0.05 km<sup>2</sup>, as "clean" snow areas, where we measured adjacent snowpits at least weekly at snow pit sites to create a time series of the metamorphosing snowpack. The snowpit time series can be seen in Figure 2.2. The second mode consisted of linear transects on multiple ice types and topographies for sampling snow heterogeneity. More information can be found in section 3.4. Occasionally we conducted

one-time measurements at sites of specific interest, such as newly-formed leads, refrozen ponds, and with remote sensing or albedo transects.

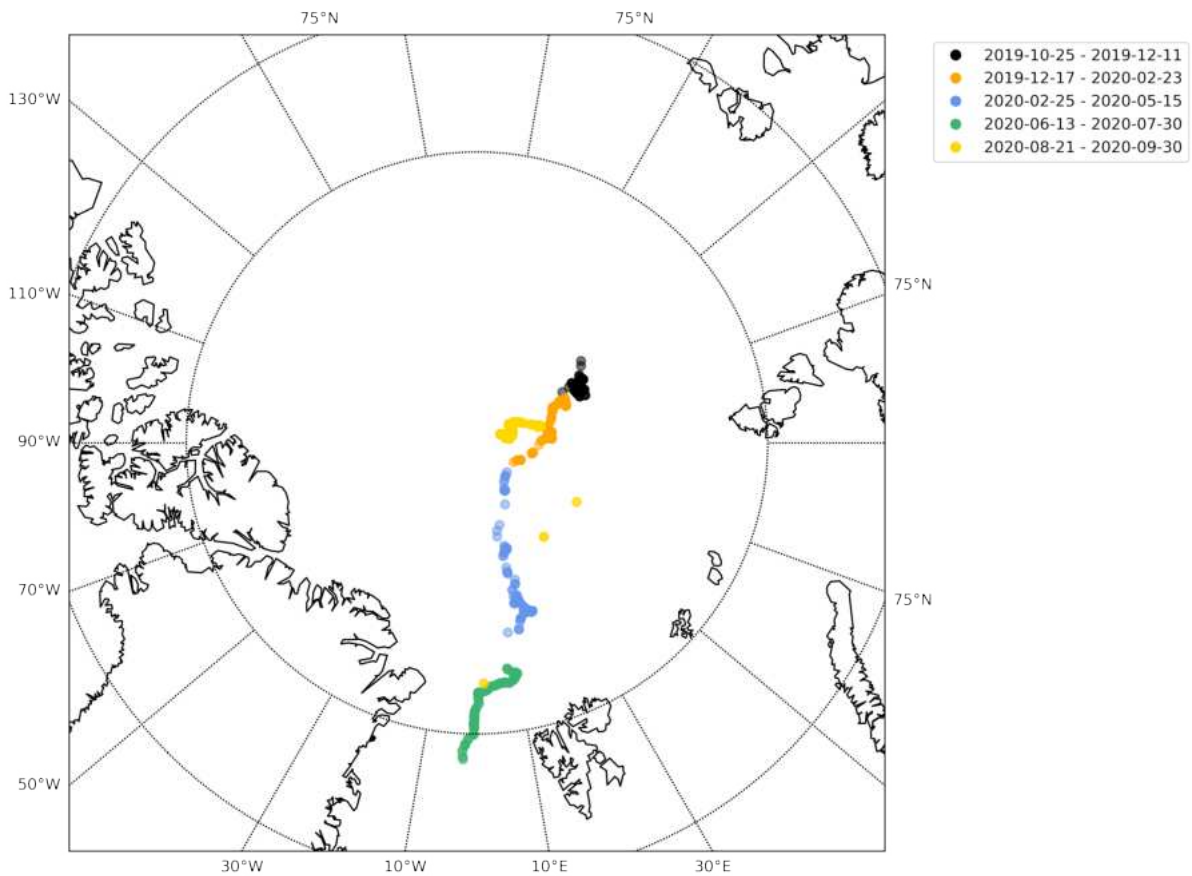


Figure 2.1: A map showing the latitude and longitude of each snowpit visit from 2019-10-25 to 2020-09-30. Each device operation ID is indicated by one mark on the figure and the colours represent the time period for each device operation ID beginning with PS122/1, PS122/2, PS122/3, PS122/4 and PS122/5 respectively. Refer to the usage notes to relate the device operation ID to the dates of interest and the contact person. The marks have transparency so the darker marks represent multiple measurements in one coordinate region.



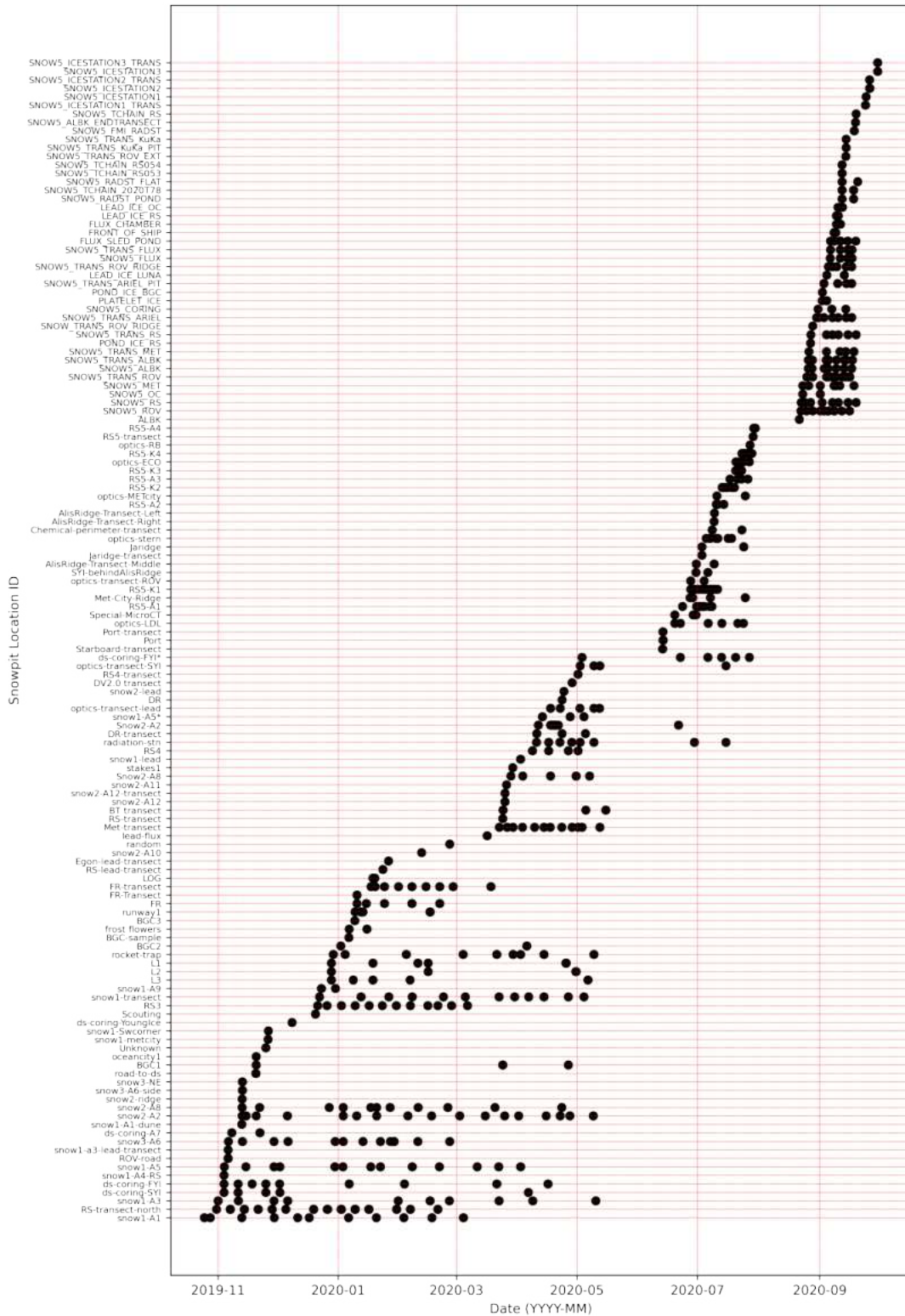


Figure 2.2: Time series of snowpit measurements at each snowpit site. A black mark indicates one visit to the snowpit site. The name of the snowpit site is indicated on the y-axis. The relocation of the central observatory and ice dynamics can be seen through the discontinuation of certain time series. This figure is to visualise the overall snowpit time series. However, due to the limited font size, please refer to the metadata publication [63] for detailed information on specific dates of the snowpit site visits.

The MOSAiC expedition transitioned between three ice floes[62] (CO1, CO2 and CO3). Figures 2.3, 2.4 and 2.5 show locations of snowpit sites on these ice floes during the MOSAiC expedition. Having three separate floes produced a discontinuity in the snowpit time series; more details can be found in section 3.4. Further discontinuity in time series was due to the highly dynamic nature of sea ice, and we often had to relocate some snowpit sites. Despite this, we could obtain measurements of the ice surface and snow stratigraphy throughout the year. The time series of visits to each snowpit site can be seen in Figure 2.2.

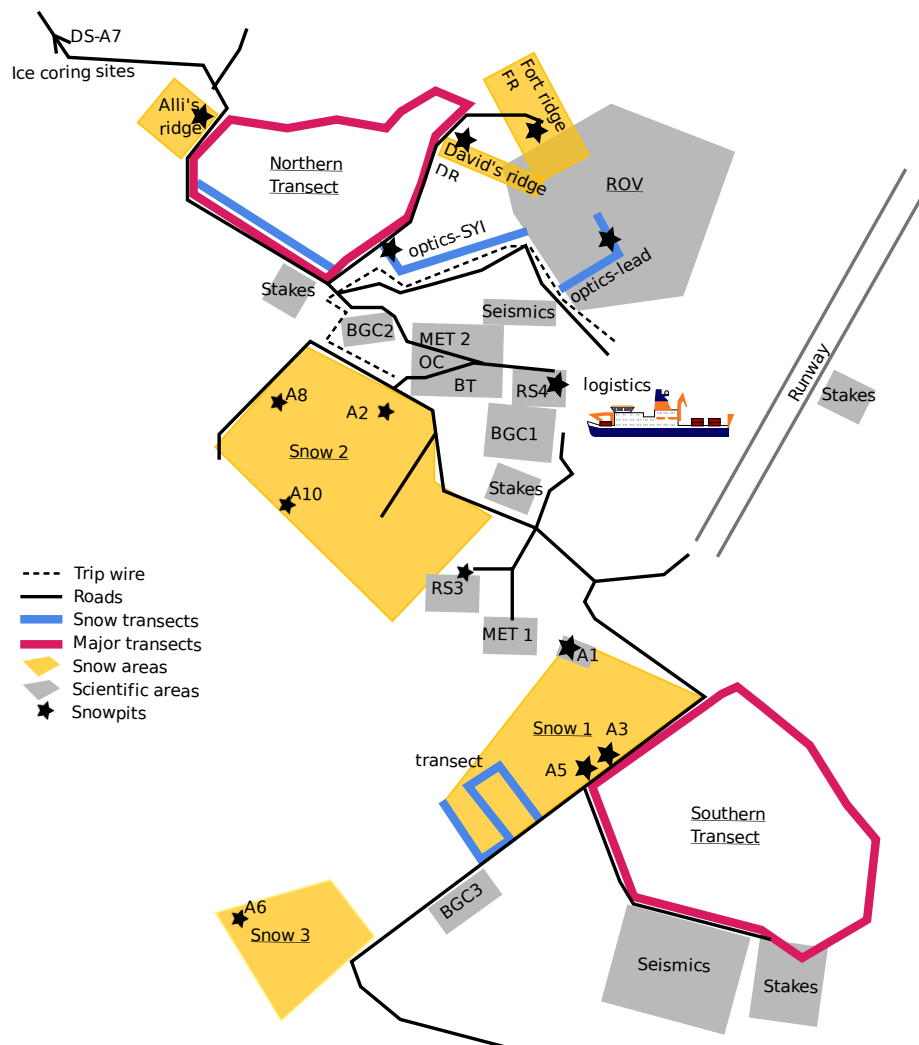


Figure 2.3: Schematic diagram of central observatory 1 (CO1) adapted from the maps used during the expedition from 2019-10-25 - 2020-07-30. For detailed information on location acronyms, please refer to the snow and ice overview manuscript [62].

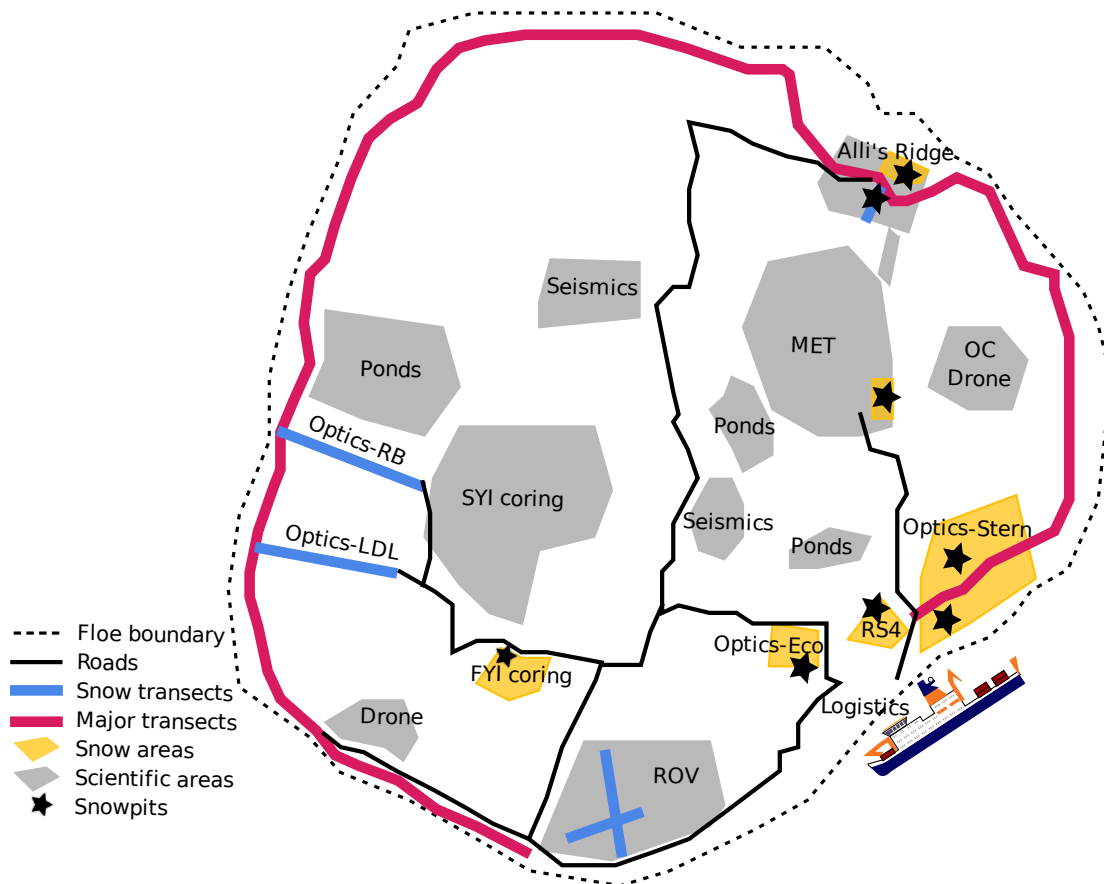


Figure 2.4: Schematic diagram of central observatory 2 (CO2) adapted from the maps used during the expedition from 2020-02-25 - 2020-07-30. For detailed information on location acronyms, please refer to the snow and ice overview manuscript [62].

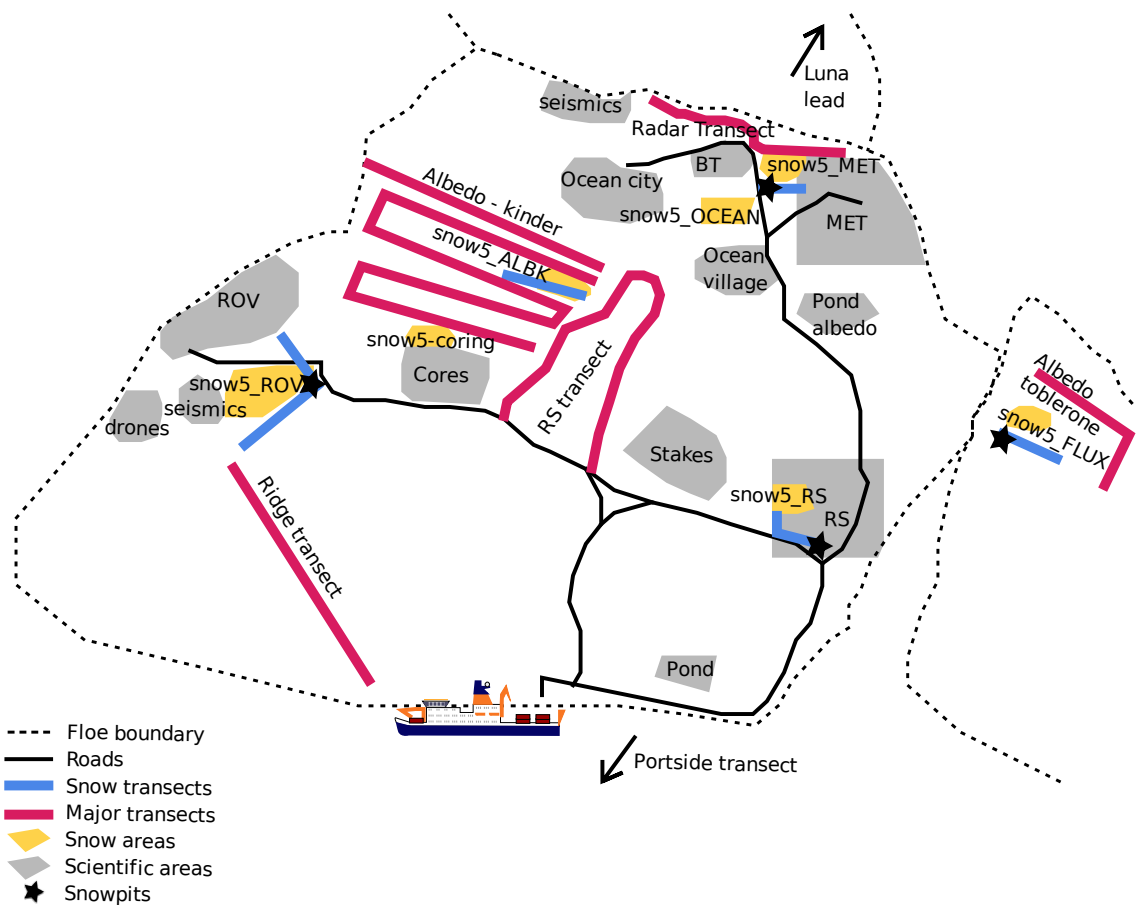


Figure 2.5: Schematic diagram of central observatory 3 (CO3) adapted from the maps used during the expedition from 2020-08-21 - 2020-09-30 after the relocation of Polarstern. For detailed information on location acronyms, please refer to the snow and ice overview manuscript [62].

A total of 16 different instruments were used at the snowpit sites during MOSAiC (details of these instruments can be found in Table 2.1 and images of each instrument can be seen in Figure 2.6). A standard operating procedure manual (SOP) for each instrument was written to increase continuity between operators (see supplementary material). We created standardised field protocols for three types of snowpits (from protocol A, including all possible observations, to protocol C, which should be followed when there were time (or other) limitations). The protocols indicated the order of measurements at each snowpit. Table 2.2 provides details of each device used for protocols A, B and C. However, it is important to note that the A, B, and C protocols were not strictly followed throughout the expedition. The final set of instruments depended on the time and ice conditions on the given day. Figure 2.7a shows an example of the snowpit layout, and details of each measurement are given in section 3.1. Orientation of the snowpit was wind dependent in the winter when there was high wind/induced mixing of the snow cover. The snowpit was dug with the operator facing the wind to reduce snow accumulation in the pit and reduce contamination of the chemical samples. When the sun appeared over the horizon, the snowpit was dug towards the sun to keep the snowpit wall in the shade.

Table 2.1: Information about each device taken into the field can be found in this table. It gives details on the device type, the published dataset related to this instrument (Ref), the number of devices used in the field, where the measurement took place, the parameters obtained directly from the raw dataset and the possible parameters that can be extracted from this dataset.

Instruments	Device Type	Number of devices	Measurement location	Measurement Parameters Raw	Extracted Parameters after processing	Ref
General observations	Protocol sheets	1	In-situ	Snow height, weather conditions, surface type	snow height (cm), weather conditions, surface type	[64, 65, 63]
Micro-CT	X-ray computer tomograph	1	Cold lab on Polarstern	3-D geometry	Stratigraphy, Microstructure: Porosity, Density ( $\text{kg m}^{-3}$ ), Connectivity, SSA ( $\text{m}^2 \text{kg}^{-1}$ ), Anisotropy, Thermal conductivity ( $\text{W m}^{-1} \text{K}^{-1}$ )	[66]
Micro-CT	DEP Snow Casting Sampler	1	In-situ for later processing	sample extraction for 3-D geometry	Stratigraphy, Microstructure: Porosity, Density ( $\text{kg m}^{-3}$ ), Connectivity, SSA ( $\text{m}^2 \text{kg}^{-1}$ ), Anisotropy, Thermal conductivity ( $\text{W m}^{-1} \text{K}^{-1}$ )	[66]
snow micro penetrometer (SMP)	snow micro penetrometer 49, 43, 31	3	In-situ	Hardness	Density ( $\text{kg m}^{-3}$ ), SSA ( $\text{m}^2 \text{kg}^{-1}$ ), grain type [67], stratigraphy	[68]
NIR camera	Box with Near-Infrared camera at 850 + 950 nm	1	In-situ	Images of NIR reflectance at 850 + 940 nm	SSA ( $\text{m}^2 \text{kg}^{-1}$ ), stratigraphy	[69]
SWE ETH-tube	SWE ETH-tube	1	In-situ	SWE	SWE (mm)	[70]
Temperature	Snow Temperature 1, 2, 3, 4, 6	5	In-situ	Temperature	Temperature ( $^{\circ}\text{C}$ )	[27]
Density cutter	Emerald500 electronic scales 1-4 and 100 $\text{cm}^3$ density cutter	4	In-situ	Weight of density cutter + snow	Density ( $\text{kg m}^{-3}$ )	[71]
GPS	Garmin GPS	1	In-situ	GPS coordinates	GPS coordinates (lat/ion)	[72]
Stable water isotopes	Stable water isotopes, vials	NaN	In-situ sampling, WSL laboratory processing	sample extraction (melted)	DeltaO18, Deuterium (ratio)	[73]
Overview pictures	Overview pictures, Olympus GP-5	1	In-situ	Images	Overview Images	[74]
SfM pictures	SfM picture sets, Olympus GP-5 + targets	1	In-situ	Image sets	Small scale DEMs, surface roughness	[75]
Ruler	Ruler	1	In-situ	Snow height + position of other measurements	Snow height + position of other measurements (cm)	[40]
Salinity	YSI 30 Salinity, Conductivity, Temperature	1	Polarstern dry laboratory	Salinity, Temperature	Salinity (ppt)	[76]
Permittivity	POGO portable soil sensor, Permittivity	1	In-situ	Dielectric permittivity (real + imaginary)	Liquid water content	[77]

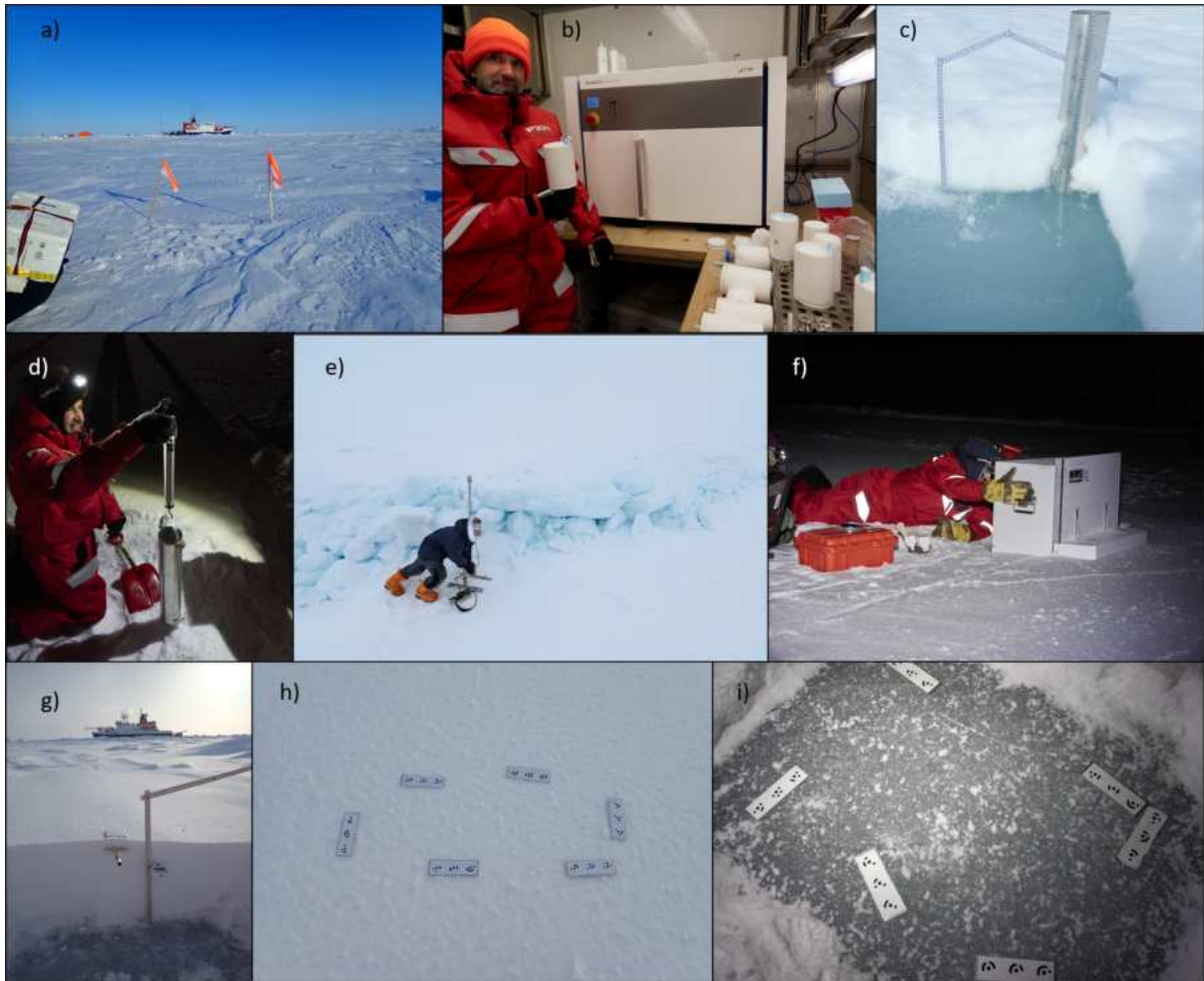


Figure 2.6: A combination of the different instruments taken to the snowpit site, showing a) An example overview picture[74], photo credits with publishing permission: A. Macfarlane. b) The micro-CT[66] mounted in the cold laboratory on Polarstern. A snow sample is being held in the white sample holder of 88 mm diameter; other sizes of samples can be seen in the table on the right side of the image, photo credits with publishing permission M. Jaggi. c) The SWE tube[70] and the ruler[40] in the snowpit in the spring season, photo credits with publishing permission: A. Macfarlane. d) The SWE tube[70] in action in the field, photo credits with publishing permission: M. Jaggi. e) The SMP[68] measuring penetration resistance in front of an ice ridge. photo credits with publishing permission: D. Ruché. f) The NIRbox [69] taking an image of the snowpit wall, photo credits with publishing permission: M. Jaggi. g) A density cutter[71] (left of the ruler) and thermometer[27] (right of the ruler) inserted in the snowpit wall, photo credits with publishing permission: A. Macfarlane. h) An SfM example image[75] showing the SfM targets placed on the naturally illuminated snow surface, photo credits with publishing permission: A. Macfarlane. i) An SfM example image[75] showing the SfM targets placed on the snow-ice interface; this image is illuminated using a head torch in the field, photo credits with publishing permission: M. Schneebeli.

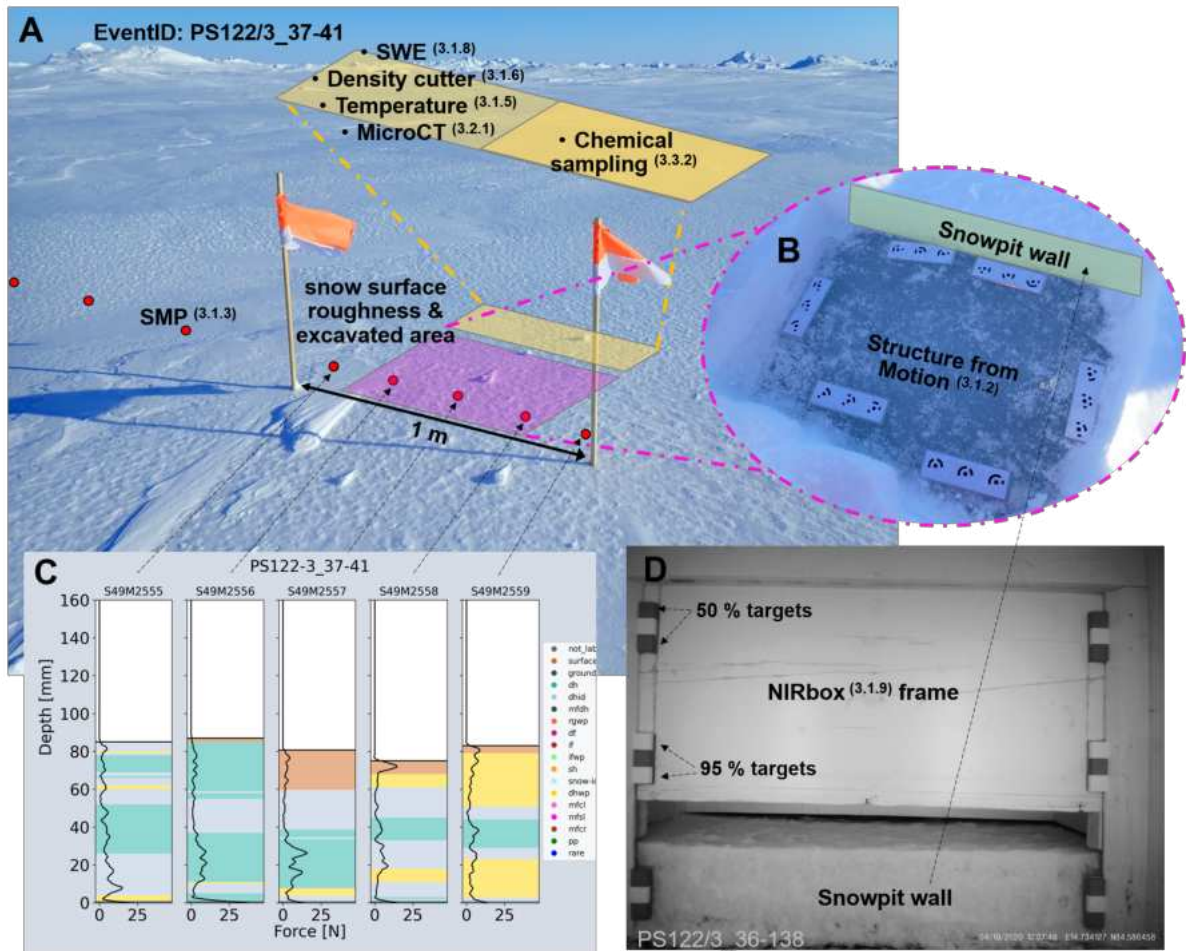


Figure 2.7: A case study of the measurements taken during event ID PS122/3\_37-41. The overview image in the background of Figure a) gives an example of the conditions upon arrival at the snowpit. Annotations to this image show the different measurement locations and their relation to each other. The pink highlighted box shows the surface roughness measurement (SfM) location and the snowpit excavation area to allow access to the snowpit wall. Once excavated, the yellow box shows where the core measurements are taken, listed as bullet points. Figure b) shows the excavated pit revealing the underlying sea ice surface, also measured for roughness using SfM. The red points indicate the SMP measurements. The five central SMP measurements are located in the snowpit, and to capture spatial heterogeneity, sometimes additional measurements were conducted to the left and right of the snowpit. Figure c) shows the SMP force signals over depth with the categorised grain types [67]. This gives an indication of the spatial heterogeneity within the snowpit. The image in Figure d) is from the NIRbox during device operation ID PS122/3\_36-138. The annotations of this figure show the reference targets (95 and 50%) and the NIRbox frame above the excavated snowpit wall.

Each snowpit "event" corresponds to one site visit and has an assigned unique device operation ID. The equipment needed for the snowpit measurements was taken in a sledge to the snowpit site marked with flags. The flags allowed us to return to the exact location of the previous measurement. Most measurements were conducted in situ (see Table 2.1). Other measurements were conducted in laboratories onboard Polarstern or shipped to laboratories after



Table 2.2: This table lists the instruments taken to each of the snowpit types; "A", "B" and "C". This was not always followed directly due to time, conditions and other limitations.

Protocol A (Complete sampling of physical and chemical properties)	Protocol B (Typically only the physical measurements taken)	Protocol C (Quick measurements)
*All protocol B and C measurements Chemical Sampling	*All protocol C measurements Overview pictures of the site Pictures for airborne structure from motion (SfM) GPS waypoint Snow height SWE (ETH-tube) Density (volumetric) Snow temperature micro-CT samples/ casting Salinity and stable water isotope samples Permittivity	Metadata collection Snow Micro Penetrometer profiles (SMP) Near infrared pictures (850 nm and 940 nm)

the expedition ended. For in-situ measurements, the first step when arriving at the snowpit site was to take an overview image, as seen in Figure 2.6a and Figure 2.7a, which provides information on the general conditions. Annotations on Figure 2.7a show the different measurement locations and their relation to each other. The second step was to conduct the nondestructive measurements that require an undisturbed state of the snow at the snowpit site, including the snow surface structure from motion images (SfM, see Figure 2.6h) and the snow micro penetrometer (SMP) measurements (Figure 2.6e). The five central SMP measurements are located in the snowpit (the red-filled circles, Figure 2.7a) and additional SMP measurements were conducted on both sides of the snowpit to capture spatial heterogeneity. After the SMP measurements, the pit was then excavated (area highlighted in pink in Figure 2.7a), allowing access to the snowpit wall and the sea ice surface. Once the snowpit wall was exposed, a near-infrared (NIR) camera mounted in a light-proof box (NIRbox) was used to image the flat snowpit wall (the NIRbox is seen in Figure 2.6f and an example of a NIRbox image is seen in Figure 2.7b), and the height of the snowpit was recorded with the ruler (Figure 2.6c). The relief of the sea ice surface was also measured using SfM (Figure 2.6i). The measurements which were “destructive” could then commence. The yellow highlighted box in Figure 2.7a shows where the core destructive measurements were taken, listed as bullet points in Figure 2.7a and details can be found in section 3.1. Images of these measurements can be seen in Figures 2.6b, 2.6c, 2.6d, and 2.6g.

Throughout this data paper, a depth of 0 mm represents the snow-ice interface. When measuring the SSL in the melt season, a depth of 0 mm represents the ice surface.

## 2.2.1 In situ measurements

### Overview pictures

We used a standard digital camera (Olympus tough TG-5) to document the surface conditions and larger area for each snowpit site visit on arrival. Figure 2.6a shows an example image.

### Structure from Motion images (SfM)

The millimetre-scale surface roughness is important for the scattering of shortwave visible [78], near-infrared and higher-frequency microwave radiation. We used a standard digital camera (Olympus Tough TG-5) and a set of unique reference targets to take sets of images. These images are processed using the structure-from-motion method (SfM) [79] into high-resolution, small-scale (approximately  $0.5 \text{ m} \times 0.7 \text{ m}$ ) digital elevation models (DEMs) to estimate the roughness of the snow surface and the snow-ice interface. The unique reference targets were printed on never tear paper and glued onto metal plates. We distributed the reference targets around a small (Approximately  $0.6 \text{ m} \times 0.6 \text{ m}$ ) area and took pictures from different angles. We included all targets in each image, ideally overlapping by at least 80%. We took pictures with the maximum wide angle of the camera. We used a headlamp to illuminate the scene during the polar night. The illumination was kept constant during the measurement. We took two sets of images; the first of the surface before excavating the snowpit (Figure 2.6h) and the second of the snow-ice interface after the snowpit excavation and using a fine-haired brush, to remove all the remaining snow off the snow-ice interface. (Figure 2.6i).

## Snow micro penetrometer

The snow micro penetrometer (SMP) is a portable device for measuring high-resolution vertical profiles of snow penetration resistance in the field. The penetration resistance can be correlated to snow microstructure [80, 81]. The penetration force is measured using a piezo-electric sensor and digitally recorded every 4 micrometres. The SMP signal can be analysed to infer stratigraphy, snow type, and snow microstructure at 1-4 millimetres vertical resolution. Snow density [82] and specific surface area (SSA) [80] can be estimated from the force signal. Through repeated measurements along transects, the SMP can help relate detailed point-scale snow profiles to a more extensive sampling area and provide information about the spatial heterogeneity of snow stratigraphy and physical snow properties. We used the SMP in snowpits and along the transects before excavating the profile wall. The SMP was taken to 389 snowpits and transects. This dataset consists of 6837 penetration resistance profiles. Figure 2.6e shows the SMP measuring a ridge, and the inset in the bottom left of Figure 2.7 shows the SMP force signals with the categorised snow grain types [67].

## Snowpit height

This parameter is measured in centimetres. We used a foldable wooden ruler to measure the height of the snow and the depth of the SSL. We used the ruler to reference the height of temperature measurements, density measurements, salinity profiles and chemical sampling. The set-up of the ruler can be seen in Figure 2.6c and g.

## Temperature

The snow temperature was measured using a waterproof thermometer with a needle probe using a ruler to determine the measurement height. Every snowpit included a surface and snow-interface temperature measurement. More measurements are taken at 5-cm intervals, starting at the bottom. Multiple thermometers were used throughout the expedition and calibrated before departure to ensure they were measuring accurately. The thermometer can be seen in Figure 2.6g after inserting it into the snowpit wall.

## Density cutter

We used a density cutter of fixed volume ( $100 \text{ cm}^3$ ) and known weight to measure the density of snow/SSL in 3 cm intervals [83]. We recorded the height of the sampled volume with a ruler and the combined weight of the density cutter and the snow inside with digital scales. The resulting density is the weight of snow/volume. The snow from the density cutter was collected in plastic containers and used for subsequent salinity and stable water isotope measurements.

## Complex dielectric permittivity $\epsilon$ (real and imaginary components)

Dielectric permittivity ( $\epsilon'$ ) and dielectric loss ( $\epsilon''$ ) measurements were made of discrete snow layers and at fixed vertical intervals at the remote sensing site during the summer months (2020-06 - 2020-09). We measured variables using the Stevens Water Monitoring Systems Hydra Probe (a.k.a. hydraprobe) [84]. The hydraprobe consists of a central waveguide and three outer rods, each 4.5 cm in length and 3 mm wide, to measure the sample's impedance at 50 MHz over a cylindrical area of 5.7 cm in length by 3 cm in diameter [84]. The sensor was calibrated using

isopropyl alcohol for  $\epsilon(\pm 0.6 \%)$  and a saline solution of known conductivity for  $\epsilon(\pm 0.7 \%)$  [85]. Other examples of the use of this sensor in snow and sea ice studies include Backstrom and Eicken (2006)[86] and Scharien et al. (2010)[87]. Measurements were obtained by horizontally inserting the probe into the snow, at a given layer/interval (every 3 cm), to their maximum depth.

### Snow water equivalent

We measured the weight and volume of a snow sample using an aluminium SWE ETH-tube to calculate the snow water equivalent (SWE). SWE is the amount of water contained within the snowpack and hence the water depth that would theoretically result if the entire snowpack melted instantaneously. Snow height (HS) is related to SWE by the local bulk density of snow ( $\rho_b$ ) using the equation  $SWE = HS \rho_b / \rho_w$ , where HS is in millimetres, ( $\rho_b$  is in  $\text{kg m}^{-3}$ ,  $\rho_w$  is the density of water ( $1000 \text{ kg m}^{-3}$ ), and SWE is in millimetres of water. At each snowpit site, the SWE ETH-tube of length 55 cm and inside surface area of  $70 \text{ cm}^2$  was inserted into the snow vertically and then closed off at the bottom. The weight of the cylindrical tube was then measured with a spring scale that was calibrated specifically for the cross-section and weight of this tube. The spring in the spring scale was not affected by cold temperatures. If the snow cover was deeper than 0.45 m (height of the tube), then the SWE was measured in several steps, using a ruler to note the snow height range from which the sample was taken. This was often the case for snowpits in ridged areas. The total water equivalent of the snow cover was then calculated as the sum of the water equivalent (WE) of the vertically aligned samples. We also measured the height of snow in each measurement, so we could back-calculate the snow density using an independent method.

### Near infrared reflectance images

This instrument measures the snow/SSL surface and snow profile wall's near-infrared (NIR) reflectivity. A NIR MAPIR camera (Survey3N Camera)[88] was built into a lightproof box and triggered by an external button. We named this instrument the NIRbox, and it can be used horizontally looking at the snowpit wall or vertically looking down at the snow/ice surface. The processing of the NIRbox images must consider the sensitivity of the different colour pixels. The setup of the reference targets, the flat field and the diffuse illumination are crucial to getting high-quality images. A geometrically corrected NIR photo objectively measures the snow stratigraphy and is observer-independent. This efficient measurement has been adapted for polar night and day by blocking out external sunlight and packaging the camera and the illuminating infrared lights into a wooden box. The length and height of the inside of the box are  $500 \text{ mm} \times 675 \text{ mm}$ . We used a blanket during polar summer to prevent light entering the box. As an extra precaution, a dark image (without any lamps) was taken for each image set, followed by images with each of the two lamps (using external light switches) to account for potential light leaks. Lambertian reflectance targets of 95 % and 50 % were mounted inside the box to account for irregular light conditions. Lamps with two different wavelengths, 850 nm and 940 nm, were mounted inside the box. We can use the images obtained horizontally by the MAPIR camera in an excavated snowpit to identify layers of snow grains with different SSA with a spatial resolution of about 1 mm [89]. This approach can highlight the snow stratigraphy's vertical and horizontal spatial heterogeneity. If the snowpit depth exceeded the NIRbox height, measurements were repeated for different heights, using an object or feature as a reference. NIR was also used vertically facing down to take images of the surface to account for the small-scale spatial heterogeneity of the SSA of the snow or SSL surface.

## 2.2.2 Ship-based measurements

### Micro Computer Tomography

Cylindrical snow and ice samples of radii 44 mm, 68 mm, 88 mm and a maximum height of 110 mm were taken from the field using a cylindrical drill and transported to the ship in an insulated container. We scanned the samples within 24 hours using a desktop cone-beam micro-CT90 (Micro-CT) [90] set-up in a -15°C cold laboratory.

### Salinity

The salinity of melted snow samples was measured using the YSI 30 Salinity, Conductivity and Temperature sensor [91]. The snow was collected using the density cutter in the field and then melted and measured in the laboratory on Polarstern. The transport containers, as well as the YSI tip, were cleaned using milli-Q water. Salinity was measured at the same vertical intervals as density.

## 2.2.3 Shore-based lab measurements

### Oxygen and hydrogen isotopes

After the salinity measurement, a small glass vial was filled with the melted snow water and transported to the Swiss Federal Institute for Forest, Snow and Landscape Research, WSL, to analyse the stable water isotope ratios.

## 2.2.4 Sampling strategy

The winter snow accumulation on sea ice is highly heterogeneous due to 1) wind-driven snow redistribution, 2) dynamic local topography and 3) differences in underlying ice types and thicknesses. Changes in local topography are mainly caused by dynamic processes like ridge and lead formation and existing refrozen ponds. Topography influences snow accumulation by modifying local wind fields, which can affect snow erosion and deposition. Differences in underlying ice type/thickness are caused by sea ice history (e.g. seasonal ice vs multiyear ice or melt pond history), dynamic processes of ridge formation, and the refreezing of leads. The physical properties and thickness of the underlying ice, in addition to atmospheric conditions, alter the temperature gradients across the snowpack, which impact the evolution of snow microstructure and snow physical properties in return. The combination of spatially variable snow deposition and erosion with spatially variable metamorphism led to high spatial heterogeneity over small horizontal scales. Two snowpit sites just decimeters apart often show significant differences in stratigraphic sequence and microstructure. Therefore, a single vertical profile is not necessarily representative of the snowpack, and the time series of snowpit observations taken adjacent to one another conflate spatial heterogeneity and temporal variability, making it challenging to assess the evolution of the snowpack. We chose a range of sites for snow measurements to understand the spatial heterogeneity of snow and the SSL. The locations of the snowpit sites included level seasonal ice, level multiyear ice, ridged areas, and refrozen leads. To account for spatial heterogeneity in the winter season, we collected high-resolution vertical profiles of penetration resistance along short transects (1.5 - 5 m) on either side of the snowpit site (see the coloured red circles in Figure 2.7), to upscale the detailed snow profile measurements from

within the snowpit itself. These measurements were part of snowpit protocols A, B and C. See Table 2.2 for more details. In certain instances, we also collected additional extended transects to account for larger-scale spatial heterogeneity on multiple ice types and topographies. These larger transects often consisted of snow micro penetrometer (SMP) measurements but were also co-located with magnaprobe transects. Magnaprobe transects are excluded from this data paper, but further details can be found at Itkin (2020)[92], alongside the table where individual snow pit events can be related to the individual Magnaprobe transect events named "mosaic-transect-actionlog-updated.xlsx" [92]. Snow and magnaprobe transects covered a larger area than the snowpit sites, sampling at predefined intervals depending on the area of interest and the study. In summer, the spatial heterogeneity of the surface layer was caused by different ice types and topographic features and winter wind-driven snow redistribution to the ridges persisting into the summer season. Sampling strategies for summer and winter were similar.

Ice deformation during the expedition cut off access to some snowpit sites and disrupted the snowpit time series. We accounted for these time-series disruptions by sampling more snowpit sites at the start of the expedition in case some of them became inaccessible. It is also important to mention that documenting the snow distribution around these dynamic events is valuable information, so these topographic features were also a focus when choosing the sampling sites. For example;

- The occurrence of leads in the field site can obstruct an existing site and prevent further measurements. However, once they refreeze, such leads allow the investigation of the snowpack over a newly formed lead, where snow metamorphism occurs more rapidly due to the relatively higher heat flux through thinner ice. By studying leads, we can follow the accumulation process from the start of sea ice formation.
- Ridging of the ice in the vicinity of a snowpit site often caused the site to become inaccessible and drastically changed the snowpack in the surrounding area. The snowpack near ridges was deeper due to wind-driven snow redistribution into drifts around ridges. Ridges add roughness to the topography, decreasing local wind speed and increasing local snow accumulation. Unless the ridge obstructed the snowpit site, measurements continued and showed how ridges affect the evolution of snowpack.

More snow-relevant events which are captured in this dataset include:

- Snow redistribution by wind
- Rain on snow
- Warm air intrusions
- Snowfall
- Melt-freeze cycles
- Surface hoar
- Melt ponds

Detailed information on the drift tracks[93] and the different COs can be found in the ICE overview publication[62]. Information on the time series continuity between CO1, CO2 and CO3 is as follows (each period corresponds to a different group of scientists on board):

- **2019-10-25 - 2019-12-11-** The setup of the CO1 and choosing snowpit sites for the start of many snowpit time series.

- **2019-12-17 - 2020-02-23**- The start of many time series and continuation of time series on CO1.
- **2020-02-25 - 2020-05-15**- Large ice dynamics resulted in the discontinuity of some time series.
- **2020-06-13 - 2020-07-30**- Re-location of the research vessel to CO2. On the way to CO2, two measurements were conducted en route. Start of many time series and the continuation of one time series at first-year ice (FYI) coring site until the end of CO2's life cycle.
- **2020-08-21 - 2020-09-30**- Re-location north to CO3. This is the start of many time series with no continuation of previous time series. Measurements in 3 locations were conducted on the way back to Bremerhaven.

## 2.3 Data Records

### 2.3.1 Overview of datasets

The corresponding data to this publication can be found in the snowpit raw dataset bundle [63]. The bundle includes all data collected from instruments taken to the snowpit sites and all metadata linked to the device operation ID. Within the snowpit dataset bundle are the following datasets:

- Snowpit metadata TXT files[65]. Each event contains a text file in the metadata dataset, which explains the event, attendees, weather conditions, instruments used and samples taken. The metadata file details what is not easily visible in the data. It gives an overview of conditions at the snowpit site, who worked on it, features of the surrounding landscape, and conducted measurements and samples. It makes it much easier to reconstruct the circumstances during the measurements.
- Snowpit SMP force profiles[68]. The measurements in this data publication are grouped by event. One event corresponds to one trip to the ice and often includes multiple SMP measurements; see Figure 2.7. The Location column gives information about where the trip took place. See the maps in Figures 2.3, 2.4 and 2.5 for details. The ID column gives an internal location of each measurement with respect to the snowpit. See "Further details: SnowMicroPen raw data: details and explanations of acronyms" in the Pangaea publication[68]. This can also be accessed using the link: <https://download.pangaea.de/reference/109819/attachments/details.pdf>.
- Snowpit near-infrared (NIR) images[69]. Uploaded photos from the MAPIR NIR camera in both jpeg and raw format. The MAPIR software can be used to create TIFF files for further analysis. Details of the wavelength and location of each NIR image can be found in the published table alongside the dataset.
- Snowpit surface type[64]. This table provides information about the snow surface on arrival at the snowpit site; it contains several possible snow surface types. It is important to note that the different observers throughout the expedition completed this table subjectively. This table should not be used for detailed analysis, only to obtain an idea of the conditions at the time of the event.

- Snowpit snow water equivalent[70]. The SWE and snow height are recorded in the meta-data spreadsheet for SWE measurements. The column MeanRho is calculated automatically. If the snowpit was variable or there was a lot of snow, there would be several SWE measurements for one snowpit visit. These measurements are listed in the table with the same device operation ID. Please see the comments to see if the whole snow profile or only a specific layer, like new snow, was measured.
- Snowpit temperature profiles[27]. The temperature device operation ID can be found in the first column alongside the corresponding snow height at which the temperature was measured. Temperature is recorded in Celsius in the column "Temperature". The last column holds the information about the sensor used.
- Snowpit overview photos[74]. All photos taken with the Olympus camera (and other digital cameras) are uploaded in jpeg format.
- Snowpit SfM images[75]. The multi-image photogrammetry images are all in jpeg format. The targets can be used to measure the relief of the ice and snow surfaces.
- Snow permittivity[77]. The permittivity, temperature and density measurements are stored in an easy-to-read Excel file.
- Snowpit snow density cutter profiles[71]. Measurements taken with the density cutter are saved in an Excel file. The first three columns give information on the event. The column "Snow weight (cutter)" contains the weight measured when putting the filled cutter on top of the scale (0 g = Empty cutter on the scale). The snow density is recorded in  $\text{kg m}^{-3}$ . The sensor cutter used (in  $\text{cm}^3$  is specified in the "Sensor cutter" column. The scale used is noted in the column "Sensor scale". The last column is again for comments.
- Snowpit height measurements[40]. The snow height table contains the device operation ID and total snow height. If total snow height differs locally in one pit, adding several snow heights by repeating the Device ID and putting several snow heights from the same pit under each other is possible. Comments go into the last column.
- Snowpit GPS locations[72]. Waypoints GPX file can be found for most events directly uploaded from the GPS device.
- Snowpit salinity profiles[76]. The salinity was taken alongside the density cutter; therefore, the height of the samples should be comparable. First, the sample was taken and measured for density. The same snow sample was then stored in a plastic container, melted and later analysed for salinity and isotopes. The salinity containers were all labelled. The label goes into the column "Containment". Salinity is only measured in ppt. Therefore, the red-marked columns were only used for the events labelled PS122/1. Column "Temperature" contains the temperature by which salinity was measured. After measuring salinity from the A-pits, the melted snow is stored in vials for stable water isotope measurements.
- Snowpit stable water (oxygen and hydrogen) isotope samples[73]. Oxygen  $\delta^{18}\text{O}$  and Hydrogen  $\delta^2\text{H}$  isotopes taken from the snowpits were analysed at the WSL laboratory in Switzerland.
- Snowpit Micro-Computer Tomograph (Micro-CT) scans[66]. Profiles of density and SSA are published for each sample collected at the snowpit site. The corresponding event ID (or device operation ID) for each sample can be used to construct complete profiles of density and SSA for each snowpit site visit.



### 2.3.2 Parameter coverage

**Specific surface area:** Micro-CT, SMP, NIR camera

**Density:** Micro-CT, manual density cutter, SMP

**Wetness:** denoth probe, dielectric permittivity

**Snow water equivalent:** SWE ETH-tube, density cutter, SMP, Micro-CT

**Temperature:** Thermometer 1,2,3,4,5

$\delta^{18}\text{O}$ ,  $\delta^2\text{H}$ : Samples collected in the field and analysed at the WSL laboratory at the Swiss Federal Institute for Forest, Snow and Landscape Research.

**Salinity:** Conductivity probe.

**Chemical sampling:** Parameters are not included in this publication.

NOTE: The "Additional metadata" provided in the snowpit metadata publication [63] can be used to identify which measurement instruments are associated with each snowpit device operation ID.

## 2.4 Technical Validation

Throughout the expedition, instruments were calibrated and the data was quality controlled. Post-processing is not something that is required for many of the variables collected. Figures plotting the temperatures density, SWE and snow height can be used to get a quick overview of the conditions throughout the year. These plots can be seen in Figure 2.8, where one point indicates one measurement in the snowpit. These graphs are a combination of multiple snowpit site locations.

A SWE comparison of two different methods can be seen in Figure 2.9. In this figure, we can see the SWE parameter cross-checked against ETH-tube measurement and bulk density cutter measurements. The ETH-tube's values can be seen in the y-axis, and the SWE measured with a density cutter can be seen in the x-axis. The average of all density cutter measurements in one profile was multiplied by the corresponding height in the SWE ETH-tube to obtain the SWE for the density cutter. The SWE ETH-tube values were taken directly from the dataset[70]. The average was taken if there were multiple SWE ETH-tube measurements for one profile. The variability in this figure is due to the different volumes being measured. The ETH-tube measures the whole snowpack, whereas the density cutter takes the snowpack in 3 cm intervals and therefore has different errors associated with it. Due to the complex nature of the snowpack on sea ice, the layering can be locally highly variable. This may also produce variability in Figure 2.9.

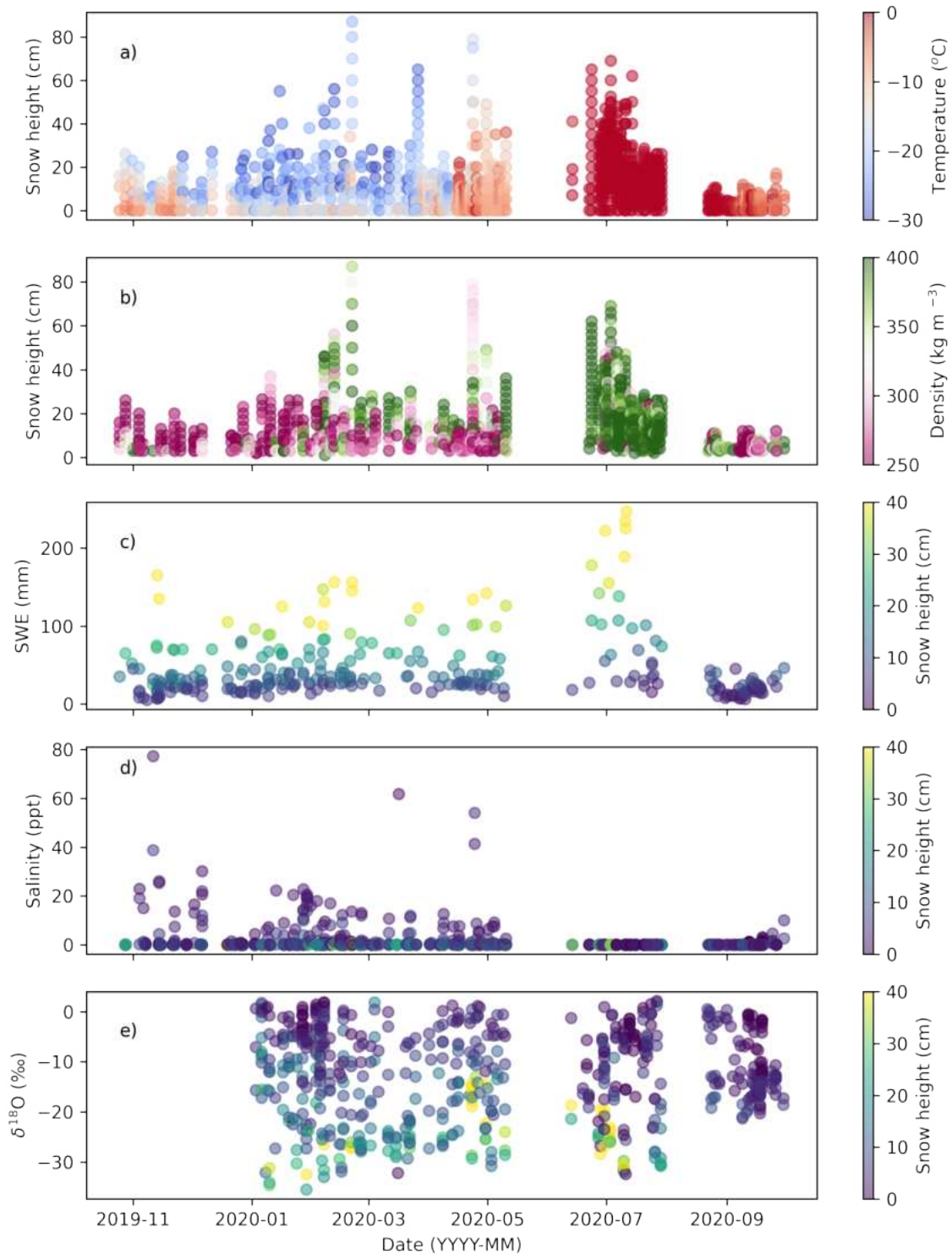


Figure 2.8: This figure gives an overview of the published datasets on Pangaea covering the entire season and collected on all three central observatories (CO1, CO2 and CO3). One marker in these graphs indicates one measurement. The marks have transparency so the darker marks represent multiple measurements at one timestamp. a) and c) show a temperature time series taken at different heights in the snowpack. Figure b) and d) show measurements of snow density using the density cutter, where one point represents one cutter measurement. Figure e) shows the SWE tube time series, Figure f) shows the salinity time series, and finally, Figure g) shows the stable water isotope  $\delta^{18}\text{O}$  time series.

Figure 2.10 illustrates how the SMP parameterisations of density and SSA need to be carefully used. Figure 2.10a shows the full snowpit profiles for density measured using micro-CT samples and SMP density parameterisations[80, 82, 94]. Figure 2.10b shows the full snowpit profile for SSA measured by four micro-CT samples taken for device operation ID PS122/3\_38-94 and one co-located SMP profile. The SMP penetration resistance profile is used alongside parameterisations[94, 80] to obtain SSA values. The difference between micro-CT and SSA profiles is also influenced by both spatial heterogeneity and the different parameterisations[95].

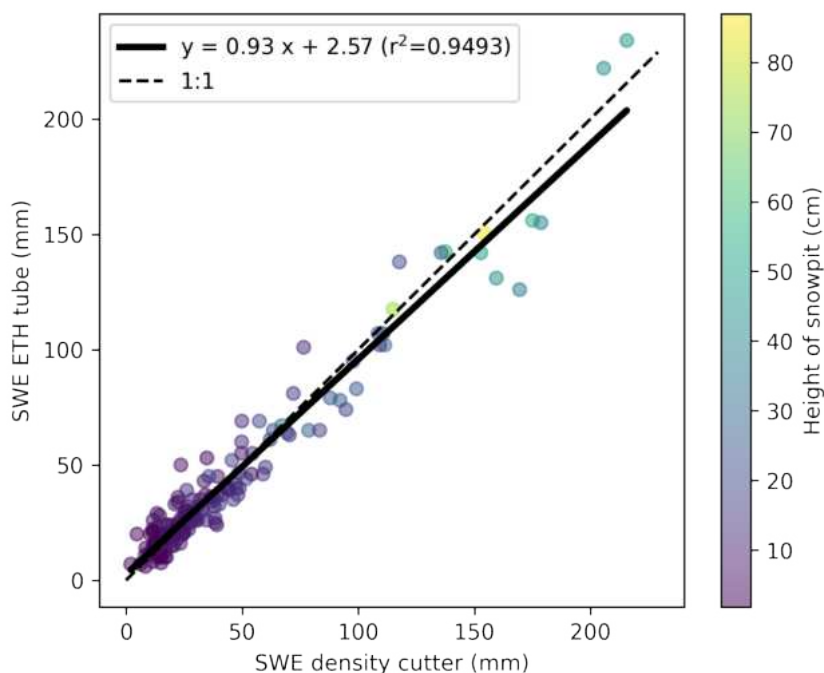


Figure 2.9: The snow water equivalent (SWE) cross-checked against the SWE ETH-tube measurement and density cutter measurements. At each snowpit, it was common to take measurements of SWE using the aluminium SWE ETH-tube and density using the density cutter. By using the equation linking SWE to the density and volume of snow, we are able to compare the two instruments. This figure presents a SWE comparison of the SWE ETH-tube to the SWE calculated using the density cutter covering measurements of the entire season and collected on all three central observatories (CO1, CO2 and CO3). The average of all density cutter measurements in one profile was multiplied by the corresponding height in the SWE ETH-tube to obtain the SWE for the density cutter. The SWE ETH-tube values were taken directly from the dataset. If there were multiple measurements for one profile.

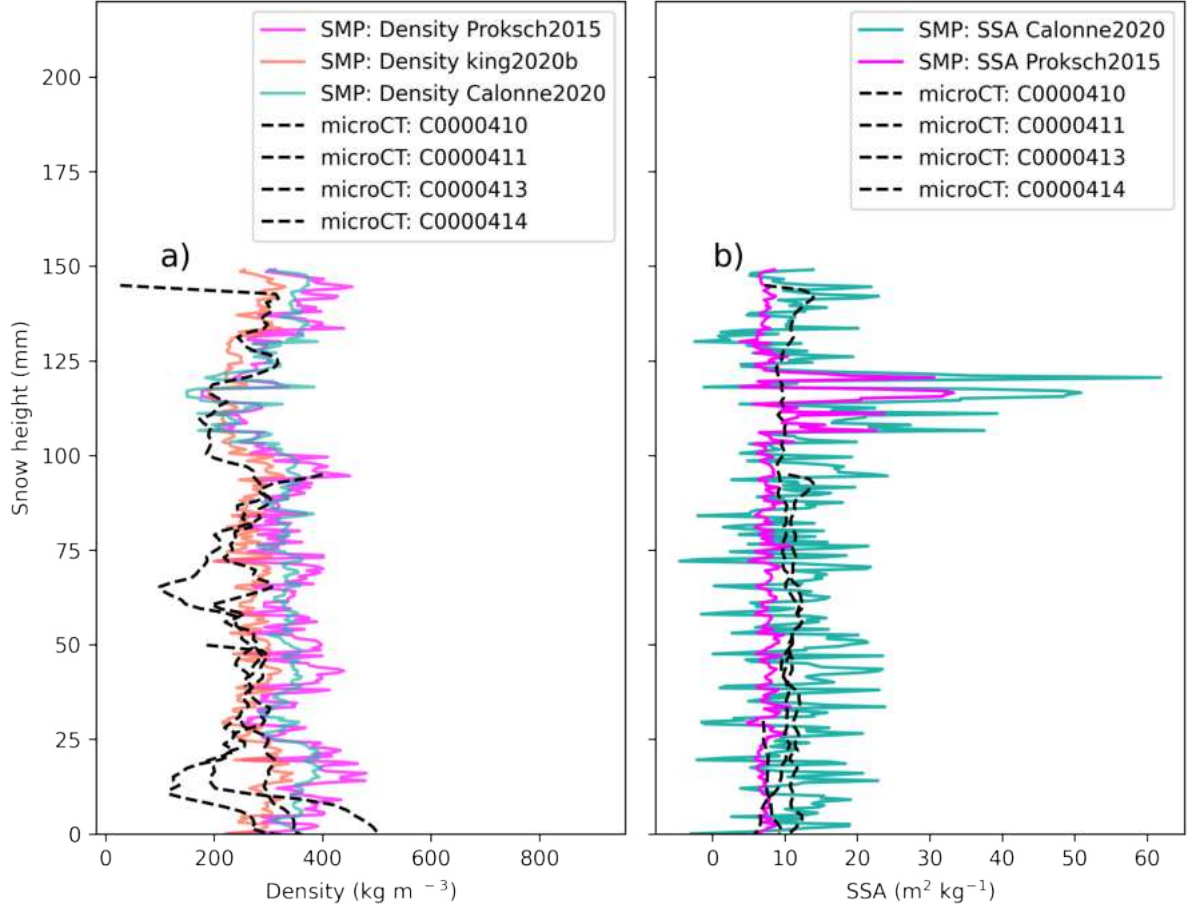


Figure 2.10: Comparing co-located SMP and micro-CT measurements for device operation ID PS122/3\_38-94. a) Shows density derived from the micro-CT and SMP parameterisations; Proksch2015[80], King2020b[82] and Calonne2020[94]. b) shows SSA derived from the micro-CT and SMP parameterisations; Calonne2020[94] and Proksch2015[80]. This figure highlights the importance of taking care when choosing the density and SSA parameterisations in all future analyses of this dataset.

## 2.5 Conclusion

This section outlines the recent collection of snow ground truth measurements conducted in the high Arctic during the MOSAiC expedition. Ground truth measurements provide empirical evidence and serve as a basis for testing models [96], training machine learning algorithms [67], improving statistical models, calibration of remote-sensing data, and aiding in the interpretation and analysis of what is being remotely sensed. This data paper outlines the methods of data collection and the consequential obtained parameters. It provides an overview of the datasets used throughout this thesis to answer pressing questions on the energy budget of the Arctic sea ice system. We hope that providing this data paper assists the future use of these datasets, and the three chapters below conclude by highlighting critical areas where more research is needed, and where this dataset can be used for future studies



# Thermal conductivity of snow on Arctic sea ice

---

Macfarlane, A. R., Löwe, H., Gimenes, L., Wagner, D. N., Dadic, R., Ottersberg, R., Hämmerle, S., and Schneebeli, M.

Published in: EGU sphere (2023)

## Abstract

Snow significantly impacts the seasonal growth of Arctic sea ice due to its thermally insulating properties. Various measurements and parametrisations of thermal properties exist, but an assessment of the entire seasonal evolution of thermal conductivity and snow resistance is hitherto lacking. Using the comprehensive snow data set from the MOSAiC expedition, we have evaluated for the first time the seasonal evolution of the snow's thermal conductivity and thermal resistance on different ice ages (refrozen leads, first and second-year ice) and topographic features (ridges). Combining different measurement parametrisations and assessing the robustness against spatial heterogeneity, we infer and quantify a hitherto undocumented feature in the seasonal variation of snow on sea ice. We observed an increase in thermal conductivity up to March and a decrease thereafter, both on first-year and second-year ice, before the melt period started. Since a similar non-monotonic behaviour is extracted for the snow depth, the average thermal resistance of snow on level sea ice remains approximately constant with substantial variability with values of  $515 \pm 404 \text{ m}^2 \text{ K W}^{-1}$  on first-year ice and  $660 \pm 475 \text{ m}^2 \text{ K W}^{-1}$  on second-year ice. We found approximately three times higher average thermal resistance on ridges ( $1411 \text{ m}^2 \text{ K W}^{-1}$ ) with large spatial variability ( $\pm 910 \text{ m}^2 \text{ K W}^{-1}$ ). Our findings are that the micro penetrometer-derived thermal conductivities give accurate values and confirm that the spatial heterogeneity of snow cover is vertically and horizontally large.

### 3.1 Introduction

Snow’s thermal conductivity and insulating properties directly impact heat transfer from the underlying sea ice to the atmosphere and directly inhibit ice growth in the winter season [23]. Due to this, snow accumulation and snow stratigraphy in winter directly influence the mass balance and, consequentially, the energy balance of sea ice [47, 97, 45]. Variability of snow’s thermal conductivity stems from the texture, e.g., specific surface area, anisotropy, connectivity and density [98, 99, 45]. Understanding this relationship and heterogeneity requires detailed and numerous microstructural measurements of snow on Arctic sea ice. The lack of these, due to the inaccessibility of this area in the winter season and shortfalls in the methods [100], has limited research on the spatial and temporal variability of heat transfer through the snow. Consequentially, accurately calculating the energy balance variability of sea ice in the high Arctic has considerable shortcomings [101].

Snow depth and microstructural properties on sea ice are spatially heterogeneous on the metre scale, meaning heat transfer through the snow cover is highly variable. There are three potential processes of heat transfer through the snow: 1) conduction through the ice skeleton, 2) conduction, convection, and radiation across air spaces, and 3) phase change and vapour diffusion between the snow grains [26]. Conduction across the air spaces and radiation heat transfer is negligible [45] compared to the conduction of heat across the ice skeleton due to the high thermal conductivity of ice. Convection and vapour diffusion depend on the permeability and hence the ice volume fraction of the snow. Due to this, the high ice volume fraction of snow wind slabs on sea ice reduces convection and vapour diffusion. As a result, conduction through the ice skeleton is the foremost process influencing heat transfer through the snow cover.

X-ray micro-computed tomography ( $\mu$ -CT) has enabled snow research to advance by measuring the exact ice skeleton without damaging it [102, 103], which allows calculations of the microstructure’s textural properties. Direct numerical simulations of heat conduction through the ice skeleton and the pore space using the finite element method (FEM) [104, 105, 106, 107] is currently the most reliable method to calculate the thermal conductivity of snow [100]. This opens new opportunities to investigate the relationship between textural properties and heat transport.

Density is used to parametrise thermal conductivity because of the first-order dependency between thermal conductivity and density. Additionally, it is a simple, low cost and quick measurement in the field [108, 109, 110, 46, 99, 111, 45, 112, 82, 113]. However, we are now aware of shortcomings when excluding other necessary textural properties from thermal conductivity parametrisations. [95] highlights that the samples’ anisotropy plays a significant role in the heat transfer through the snowpack. A parametrisation for thermal conductivity is presented using density and anisotropy for snow, specifically for densities below  $500 \text{ kg m}^{-3}$ . However, this parametrisation is not adapted to high snow densities. [114, 110, 115, 116, 117] realised the influence of temperature on the thermal conductivity. [117] created upper bounds to ensure that the thermal conductivity is in agreement with the thermal conductivity of ice at specific temperatures in the higher density ranges. However, their parametrisation does not include anisotropy. In summary, significantly few thermal conductivity measurements are simulated from the high Arctic [118]; therefore, the influence of anisotropy is unknown.

The study of spatial heterogeneity of the snow on sea ice requires a very high number of measurements, which can not only be realized by  $\mu$ -CT. A faster method is needed (the  $\mu$ -CT on MOSAiC took 7 hours to measure 10 cm of snow). For this reason, we used high-resolution penetrometry using a SnowMicroPen to improve spatial coverage. [45] and [82] studied the spatial heterogeneity of snow on Arctic sea ice. Very few studies have investigated temporal changes in

contrast to the snow on Arctic tundra [119, 120]. Thermal conductivity measured from thermistor strings installed in the snow and ice [121, 122, 123] measures temporal changes in thermal conductivity. They are also destructive measurements and disturb the snow cover during and after installation. Therefore it is challenging to accurately capture the snow’s effective thermal conductivity using this method.

Given the importance of snow in the sea ice system, we work towards advancing our understanding of both spatial and temporal heterogeneity of the thermal conductivity of snow on sea ice in the high Arctic. We present two new parametrisations, with and without anisotropy, for the complete range of possible snow/firn densities, developed using FEM using snow samples collected during the MOSAiC expedition (Section 3.2.1). We up-scaled (related individual point measurements to a larger area by increasing the sample size) individual  $\mu$ -CT profiles (Section 3.2.2) by using snow micro penetrometer (SMP) density profiles (Section 3.2.3) to identify both spatial and temporal trends in the data set (Section 3.3.3). Our measurement concept considered the spatial heterogeneity of sea ice [62]. As a result, we can draw new conclusions about the thermal conductivity and resistance of the snow cover on different ice types over the entire winter. This is relevant for calculating the Arctic sea ice’s energy budget [124] and allows us to better understand sea ice growth in the winter. We finally compare our data set to the average snow thermal conductivity value of 0.31 to 0.33 W K<sup>-1</sup> m<sup>-1</sup>, used in the modelling community [45, 125, 126].

## 3.2 Data and methods

### 3.2.1 MOSAiC expedition

Field measurements used in this study were conducted during the MOSAiC expedition in the winter months from November 2019 to April 2020. The field measurements were located on drifting Arctic sea ice, with the first measurement at 86.3 degrees North, 123.0 degrees East reaching a maximum latitude of 88.9 degrees North, and then drifting South until 83.7 degrees North, 13.0 degrees East. A single ice floe was studied in this period. We set up snowpit sites on the sea ice to understand the snow conditions, where we took weekly measurements. These were marked with flags so we could relocate the same snowpit site on the next visit and create time series of measurements at that location. The snowpit sites were randomly distributed across the ice floe to sample different ice types (e.g. first-year ice (FYI), second-year ice (SYI) and refrozen leads) and topographic features (e.g. ridges). However, the exact location cannot be sampled twice due to the destructive nature of most measurements within the snowpit. The snowpit operator measured consecutive snowpits approximately 1 meter apart to continue a time series at one snowpit site. Locations of each snowpit site are indicated alongside the data set paper [63]. A snowpit is a collection of measurements measuring the physical properties of the snowpack at the same snowpit site at one point in time. The snowpit analysis used in this study focused on the physical properties of the snowpack, including depth, density, anisotropy and thermal conductivity. In this study, we analyse the MOSAiC snowpit data set [63], of which three key instruments were the focus of this study. The instruments included i)  $\mu$ -CT, ii) SMP, and iii) density cutter. Details of these instruments are given below.

### 3.2.2 $\mu$ -CT Samples

The data set evaluated for this manuscript includes 138  $\mu$ -CT samples (approximately 10 cm high and 6.6 to 7.8 cm diameter) collected during 69 individual trips to the sea ice, known



as 'Events'. More than one  $\mu$ -CT sample was often collected during an event to sample the complete snow profile. An overview of the samples taken at specific dates and their heights can be seen in Fig. 3.1. The EventID (a unique labelling system representing one trip to the ice) can be used to identify co-located  $\mu$ -CT samples. The snow samples were extracted using an electric cylindrical drill, carefully placed in a sample holder, and transported back to the laboratory on *Polarstern* [1]. By installing a desktop cone-beam  $\mu$ -CT90 in a laboratory onboard, we could measure the microstructure of the snow semi-in situ. The laboratory was cooled to  $-15^\circ\text{C}$ , and the  $\mu$ -CT had a custom ventilation system meaning the sample remained at  $-12^\circ\text{C}$  during the scanning process. Once the snow samples were scanned, the data was analysed by dividing each snow sample into sub-samples of volume  $5.83\text{ cm}^3$  in order to calculate the density and the geometrical anisotropy  $A_g = 2\xi_z/(\xi_x + \xi_y)$  from the correlation lengths  $\xi$  in different coordinate directions [95] and the effective thermal conductivity using FEM and the thermal anisotropy (given in Equation (3.2)).

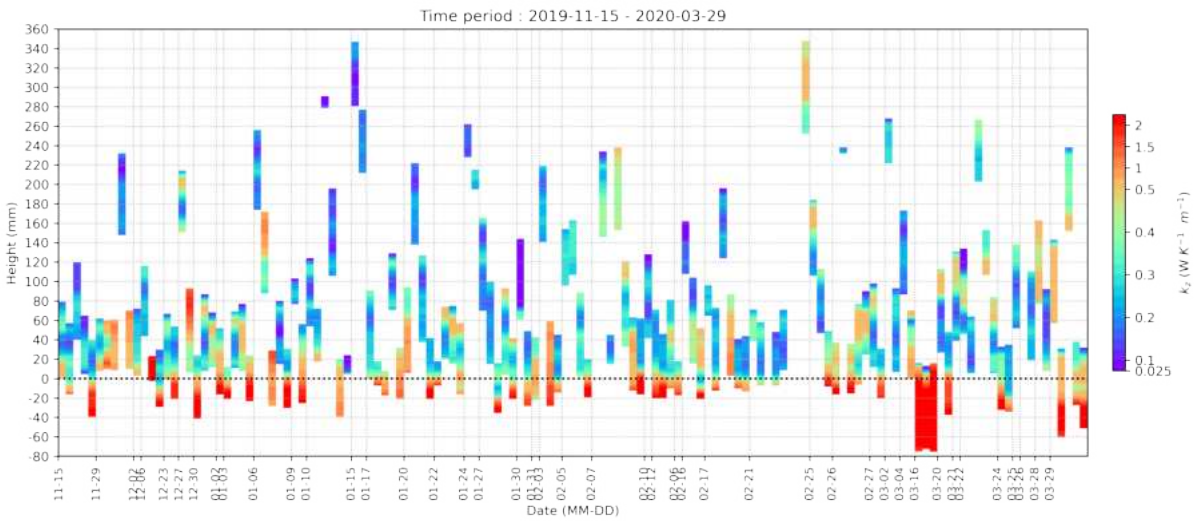


Figure 3.1: Snow samples were collected during the winter to be measured using micro-computed tomography. We simulated effective thermal conductivity across these samples using FEM. Here we see each sample plotted at the height taken in the snowpack against the collection date. Negative heights correspond to samples of the sea ice beneath the snowpack. This figure highlights the vertical variability within the samples.

### Direct numerical simulations using FEM, $k_{\text{eff}}^{\text{FEM}}$

FEM is an approximation that subdivides the complex snow microstructure into several small and finite pieces whose thermal conductivity can be easily calculated. We can then use these as an approximation of the thermal conductivity of the structure as a whole.  $\mu$ -CT samples and FEM were used to obtain the effective thermal conductivity of the snow. The effective thermal conductivity ( $k_{\text{eff}}$ ) characterises the steady-state heat flow through a unit area of a homogeneous material induced by a unit temperature gradient in a direction perpendicular to that unit area ( $\text{W K}^{-1} \text{m}^{-1}$ ). We take the vertical temperature gradient ( $z$ -direction) and discard any lateral heat flow. The relationship is shown in Equation (3.1), where  $h$  is the sample thickness (m),  $T$  represents the temperature (K), and  $q$  represents the volume averaged heat flux ( $\text{W m}^{-2}$ ).

$$k_{\text{eff}} = q \frac{h}{\Delta T} \quad (3.1)$$

The simulated thermal conductivities  $k_{\text{eff}}$  can be used to characterise the thermal anisotropy ( $A_k$ ) of the samples in the x, y and z direction, as seen in Equation (3.2).

$$A_k = \frac{2k_{\text{eff}(z)}}{k_{\text{eff}(x)} + k_{\text{eff}(y)}}, \quad (3.2)$$

The thermal conductivity of the  $\mu$ -CT sub-samples, calculated using FEM ( $k_{\text{eff}}^{\text{FEM}}$ ), were compared to the density and  $A_k$  of the sub-samples, seen in Fig. 3.2 to identify sources of variability. The numerical simulation uses the code from [127] and precisely follows the procedures described by [95, 118]. For the thermal conductivity of ice ( $k_{\text{ice}}$ ) and air ( $k_{\text{air}}$ ), we used their values at  $T = -20$  °C, namely  $k_{\text{ice}} = 2.34 \text{ W K}^{-1} \text{ m}^{-1}$ , [128] and  $k_{\text{air}} = 0.024 \text{ W K}^{-1} \text{ m}^{-1}$ . Based on the simulated heat flux and the prescribed temperature gradient,  $k_{\text{eff}}^{\text{FEM}}$  is calculated using Equation (3.1).

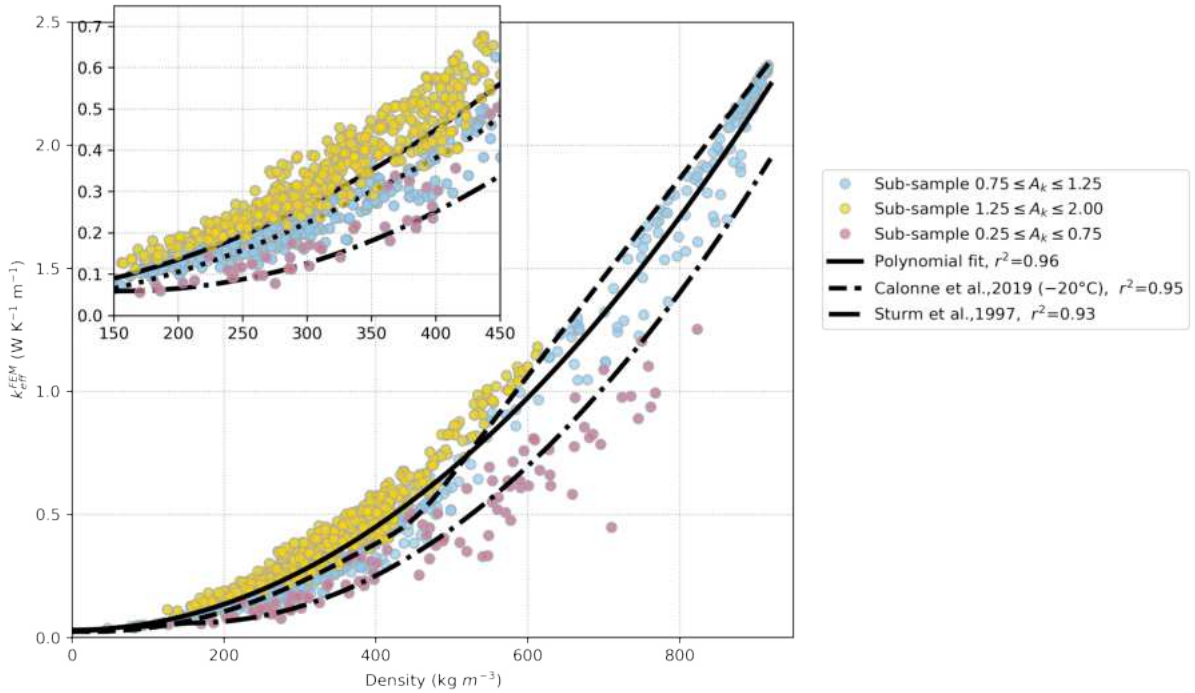


Figure 3.2: Direct numerical simulations of the effective thermal conductivity using finite element method (FEM) for the sub-samples are compared to the sub-sample density. A polynomial fit of the data is shown in the solid line. This relationship between effective thermal conductivity and density has been tested in previous studies. This figure includes two current parametrisations [117, 99]. Anisotropy values are indicated in different colours with details given in the legend, and the figure shows how anisotropy influences the effective thermal conductivity of the sub-samples.

### Parametrisations of thermal conductivity

X in  $k_{\text{eff}}^{\text{X}}$  represents the different parametrisations of thermal conductivity used in this manuscript. For details on the difference between each parameterisation, please refer to Table 3.1, adapted from Table ~1 [117].

X	Formula	Density	Temperature	Anisotropy
Yen	$k_{\text{eff}}^{\text{Yen}} = 2.22362 \left(\frac{\rho}{1000}\right)^{1.885}$	80 – 600	Undefined	No
Stm	$k_{\text{eff}}^{\text{Stm}} = 0.023 + 0.234 \frac{\rho}{1000}$ $= 0.138 - 1.01 \frac{\rho}{1000} + 3.233 \left(\frac{\rho}{1000}\right)^2$	for $\rho < 156$ for $156 < \rho < 600$	Average $-15$ °C	No No
Cal3, Cal20, Cal60	See [117]	102 – 888	$-3^\circ\text{C}$ , $-20^\circ\text{C}$ and $-60^\circ\text{C}$	No
Löwe	See [95]	Approx. 91.6 – 460	$-20^\circ\text{C}$	Yes

Table 3.1: An overview of the thermal conductivity parameterisations used throughout this manuscript.

$k_{\text{eff}}^{\text{X}}$  parameterisations tested in this study used a) density from [109, 45], where  $\text{X} = \text{Yen, Stm}$  respectively, b) density and temperature from [117], where  $\text{X} = \text{Cal3, Cal20, Cal60}$  for different temperature parameterisations, and c) density and  $A_k$  from [95], where  $\text{X} = \text{Löwe}$ . An overview is given in Table 3.1. By comparing these parameterisations to the values of  $k_{\text{eff}}^{\text{FEM}}$ , we could identify which parameters are optimal for measuring  $k_{\text{eff}}^{\text{X}}$  for snow on Arctic sea ice. After conducting this analysis, we calculated the second-order polynomial fit for this data set to obtain a density parameterisation specific for snow on sea ice, as seen in Equation (3.3), where  $\rho$  represents the density of the sub-samples,  $a = 2.62 \times 10^{-6}$ ,  $b = 1.54 \times 10^{-33}$  and  $c = 3.04 \times 10^{-2}$

$$k_{\text{eff}}^{\text{Mac(I)}} = a\rho^2 + b\rho + c \quad (3.3)$$

When allowing for anisotropy in the parameterisation, it is straightforward to generalise the empirical correction [95] to obtain an accurate parameterisation as a function of density and  $A_g$  in the entire density range. To this end, we use the empirical transformation as a function of the lower bound values  $k^{(\text{L})}$ , which are given in Eq. 2 in [95] through density and  $A_g$ . However, instead of using the linear empirical tweak from [95], we used a similar empirical adjustment (Equations 11 and 12) as suggested in [129] for the elasticity tensor to cover the entire range of densities.  $\Omega, \beta, k_0$  are adjustable parameters obtained by minimising the differences between Equation (3.4) and FEM estimates.

$$k_{\text{eff}}^{\text{Mac(II)}} = k_0 + \left( \frac{k^{(\text{L})\beta}}{\Omega(1 - k^{(\text{L})}) + k^{(\text{L})}(\beta-1)} \right) \quad (3.4)$$

### 3.2.3 SMP profiles

The snow micro penetrometer (SMP) instrument measures the penetration force resistance of a snow profile at 0.3 mm vertical resolution. Five SMP force profiles were obtained within one snowpit, approximately 0.25 meters apart. Additional measurements were often taken on both sides of the snowpit to capture the spatial heterogeneity of the snow in the surrounding area. These additional SMP measurements were taken at intervals of one meter (more details of the measurement protocol can be found alongside the published dataset and datapaper [68]). This reduced operator bias when selecting an area to measure. Further details can be found alongside the published SMP data [68] set within the snowpit bundle [63]. 3266 SMP profiles are used in this study. The SMP penetration force profile can be used to obtain density and, in combination with parameterisations listed in the previous Section, estimates of the thermal conductivity. We used the density parameterisation from [82]. The seasonal comparison of the density obtained by these instruments can be seen in Fig. 3.6. This parameterisation was chosen because the data set used was also collected on sea ice in the high Arctic. When comparing the density of the snow using a) a density cutter to b) density derived from the SMP and

[82]’s parameterisation we experienced difficulties using the field data. The field measurements include the high spatial heterogeneity of the snow-sea ice landscape. To derive an uncertainty, further laboratory work (by using similar methods to [100]) is needed to better understand uncertainties of the SMP-density derived method.

### The effective thermal conductivity’s harmonic mean

For the purpose of this analysis, we assume the thermal gradient in a snowpack is vertical. For a layered material, such as snow, the average thermal conductivity is represented in analogy to Ohm’s law by conduction resistances in series [130]. In our case, as all sub-samples have the same dimension, this simplifies the harmonic mean. The harmonic mean of a snow profile’s thermal resistance ( $\overline{k_{\text{eff}}^X}$ ) is calculated using Equation (3.5). Where  $n$  is the number of sub-samples in a profile, and  $k_i$  is the effective thermal conductivity of individual sub-samples, as all sub-samples have the same dimension.

$$\overline{k_{\text{eff}}^X} = \left( \frac{\sum_{i=1}^n k_i^{-1}}{n} \right)^{-1} \quad (3.5)$$

After testing the listed parameterizations in Table 3.1, we used the parameterisation with the highest  $r^2$  in relation to this dataset to upscale the single snowpits. The harmonically averaged  $\overline{k_{\text{eff}}^X}$  of all the SMP profiles in winter were then grouped depending on the snowpit site’s underlying ice type (e.g. FYI areas, SYI areas, or refrozen leads), topographic features (e.g. ridges), and month to better understand spatial heterogeneity.

### Average effective thermal Resistance

The SMP measurements of thermal conductivity and snow depth were used to investigate the snow’s thermal resistance ( $R$ ) on the ice floe using the  $k_{\text{eff}}^{\text{Mac(1)}}$  parameterisation. The snowpack’s  $R$ -value is the temperature difference, at steady state, between the ice-snow interface and ice-atmosphere interface, given a unit heat flow rate through a unit area ( $\text{m}^2 \text{K W}^{-1}$ ). By combining this definition and Equation (3.1), the snowpack’s  $R$  can be found by dividing the snow depth (HS) by the profile’s  $\overline{k_{\text{eff}}^X}$ , as seen in Equation (3.6). The thermal resistance is a useful parameter for modelling heat transfer in the sea ice system as it is including snow conductivity and depth in one parameter.

$$R = \frac{\Delta T}{q} = \frac{\text{HS}}{\overline{k_{\text{eff}}^X}} \quad (3.6)$$

The measurements were grouped as mentioned in Section 3.2.3.

### 3.2.4 Density profiles

We further investigated the reduction in density in April by using all density measurements available. The instruments that are used to measure density include a density cutter ( $\rho^{\text{Cutter}}$ ), a SWE tube ( $\rho^{\text{SWE}}$ ; measuring snow water equivalent) and the SMP measurements ( $\rho^{\text{SMP}}$ ), using the parameterisation from [82], as indicated in Section 3.2.3.

### 3.2.5 Atmospheric data

Using three independent instruments, we identified a density reduction, and to better explain this, we used shortwave radiation data [131] from up and down radiometer systems, temperature and wind data measured at 2 m [132] from a meteorological flux tower. These instruments were deployed at Met City (a station approximately 200 m away from the snowpit measurements). This additional atmospheric data helped us understand and explain the conditions that might have caused the density reduction.

## 3.3 Results

### 3.3.1 Direct numerical simulations using FEM

Individual vertical snow profiles showed high vertical variability in a) the density profiles, b)  $A_k$ , and as a result of this, high variability in  $k_{\text{eff}}^{\text{FEM}}$ . Icy layers within the snow profile, crusts on the surface and a 'remnant surface scattering layer' at the snow-ice interface (a granular layer at the top of the melting summer sea ice [133]) were of high density and low  $A_k$ , in contrast to the low-density precipitated snow and high values of  $A_k$  for depth hoar. The vertical profiles of  $k_{\text{eff}}^{\text{FEM}}$  in Fig. 3.1 highlight the large variability amongst samples, showing that snow stratigraphy highly influences thermal conductivity. The commonly occurring layers of depth hoar and rounded, wind-blown snow are of similar densities of approximately  $300 \text{ kg m}^{-3}$ . Due to these two grain types being dominant on Arctic sea ice, we see a large proportion of our sub-samples densities in the range of  $200$  to  $400 \text{ kg m}^{-3}$ , seen in the high point concentration in this density range in Fig. 3.2. The colour in this figure shows the range of  $A_k$  values and the influence of  $A_k$  on  $k_{\text{eff}}^{\text{FEM}}$ .  $A_k$  values ranged between  $0.25$  and  $2$ , indicated in the legend in Fig. 3.2. Extreme values of anisotropy in the lower range show icy layers and high values are depth hoar samples. The density distribution of the  $k_{\text{eff}}^{\text{FEM}}$  values are shown in Fig. 3.3, after a  $550 \text{ kg m}^{-3}$  density cut-off is applied to exclude ice samples [134]. The average  $k_{\text{eff}}^{\text{FEM}}$  value is  $0.27 \pm 0.17 \text{ W K}^{-1} \text{ m}^{-1}$ . The errors given throughout this manuscript are one standard deviation ( $\pm 1\sigma$ ).

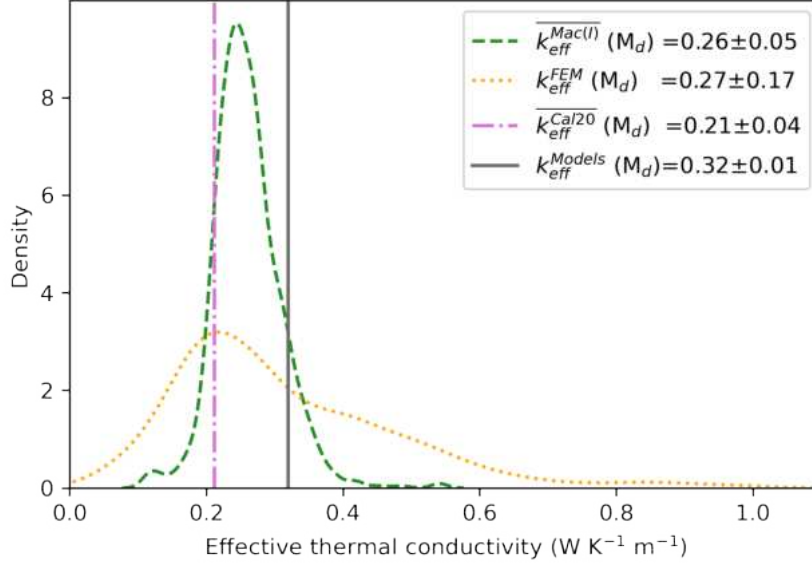


Figure 3.3: The density distribution of  $k_{\text{eff}}^{\text{FEM}}$  for all  $\mu$ -CT sub-samples with densities below 500  $\text{kg m}^{-3}$  and the harmonic mean of the SMP profiles ( $\overline{k_{\text{eff}}^{\text{Mac(I)}}}$ ) from January to March 2020. The median values are indicated with the symbol  $M_d$  in the legend. The error given in the legend represents one standard deviation.

### 3.3.2 Parametrisations of thermal conductivity

The high variability amongst samples allowed our data set to cover density values of approximately 50 to 950  $\text{kg m}^{-3}$  and anisotropy values between 0.25 and 1.25. This allowed us to test each  $k_{\text{eff}}^{\text{X}}$  parametrisation currently presented in this field.

When comparing  $k_{\text{eff}}^{\text{X}}$  to  $k_{\text{eff}}^{\text{FEM}}$  for all sub-samples, Fig. 3.4 shows the relationship for current parametrisations for the full range of possible snow densities. The  $r^2$  values for each parametrisation can be found in Fig. 3.4. Using the parametrisation  $k_{\text{eff}}^{\text{L\"owe}}$  results in a low  $r^2$  value since in the original work [95] the adjustable coefficients were optimised only in the density range below 500  $\text{kg m}^{-3}$ ). Adapting the work from [95] using Equation 3.4 results in a correlation coefficient of  $r^2 = 0.99$ . This  $k_{\text{eff}}^{\text{Mac(II)}}$  relationship to  $k_{\text{eff}}^{\text{FEM}}$  is shown in Fig. 3.4.

Without including anisotropy in the parameterisation,  $k_{\text{eff}}^{\text{Mac(I)}}$  is the best representation of  $k_{\text{eff}}$ , as it has the highest  $r^2$  value compared to this dataset. We use this parametrisation and introduce the SMP to upscale our measurements of  $k_{\text{eff}}$ , of which we do not have corresponding  $A_k$  or  $A_g$  measurements.

The harmonic mean reduces any profile outliers. The  $\overline{k_{\text{eff}}^{\text{X}}}$  profiles, therefore, have a smaller range of values in the histogram in Fig. 3.3. Despite the reduction in the range, the median value of  $\overline{k_{\text{eff}}^{\text{Mac(I)}}}$  ( $M_d = 0.25 \pm 0.05 \text{ W K}^{-1} \text{ m}^{-1}$ ) aligns with the median value of  $k_{\text{eff}}^{\text{FEM}}$ .

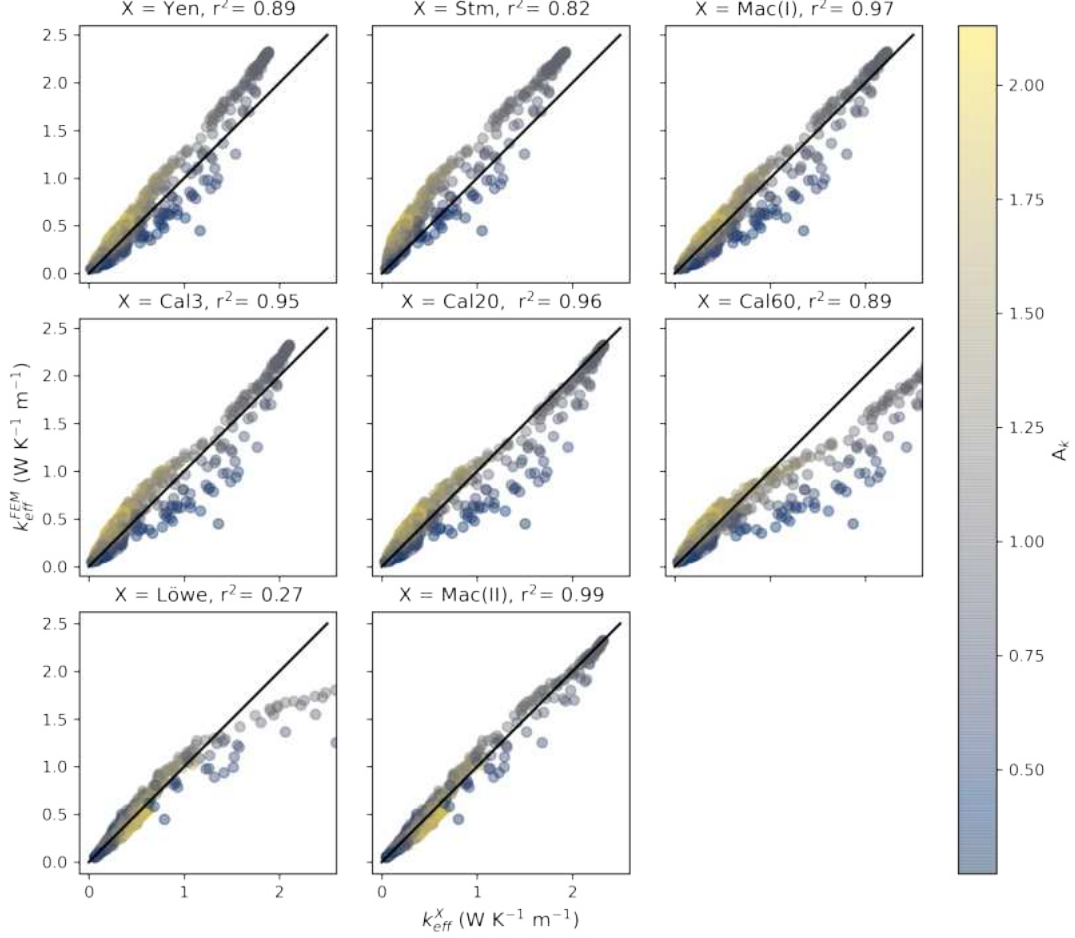


Figure 3.4: Parametrisations of effective thermal conductivity plotted against effective thermal conductivity measured using FEM. Each sub-sample was used to measure effective thermal conductivity using i) direct numerical simulations on a finite element method (FEM) and ii) different parametrisations using density, anisotropy and temperature. The top row shows the performance of density parametrisations ([109, 99]), and the polynomial fit of this data set,  $k_{\text{eff}}^{\text{Mac(I)}}$ . The middle row shows the performance of density and temperature parametrisations [117] for  $-3^\circ\text{C}$ ,  $-20^\circ\text{C}$  and  $-60^\circ\text{C}$ . The bottom row shows parametrisations using anisotropy [95] and the new parametrisation as an outcome of this study ( $k_{\text{eff}}^{\text{Mac(II)}}$ ).

### 3.3.3 Spatial heterogeneity and temporal changes

For the rest of the study, we use SMP profiles and the effective thermal conductivity's harmonic mean,  $\overline{k_{\text{eff}}^{\text{Mac(I)}}}$ , using the density of the SMP profiles ( $\rho^{\text{SMP}}$ ) calculated using [82] parametrisation of density to investigate spatial heterogeneity and temporal changes of the snow cover on Arctic sea ice.

To understand the heterogeneity of the snow depth (HS), we categorised the snowpits in situ into ice type and ridged areas. Fig. 3.5 shows the snow heights, snow density (measured using the SMP and the [82] parameterization), thermal conductivity and thermal resistance for each ice type and for ridge areas. This can be seen in the grey box plots in the background of Fig. 3.5. Table 3.2 shows that more snow is found on Ridges with  $\text{HS} = 335$  mm and less on leads (as this ice type is when thin ice has formed and snow has just started to accumulate) with 84

mm on average. A breakdown of this dataset to investigate the average of each parameter for individual months can be seen in the coloured bar charts in Fig. 3.5. The snow depth is highly variable on all ice types, with standard deviations between 109 mm on FYI and 278 mm on ridges. The range of snow depth on ridges (0 to > 1000 mm) shows consistently high spatial heterogeneity throughout the winter season; therefore, temporal changes are less discernible than in FYI and SYI areas.

Ice type	HS (mm)	$\rho^{\text{SMP}}$ (kg m <sup>-3</sup> )	$\overline{k_{\text{eff}}^{\text{Mac(I)}}}$ (W K <sup>-1</sup> m <sup>-1</sup> )	$R$ (m <sup>2</sup> K W <sup>-1</sup> )
Refrozen leads	84 ± 124	301 ± 41	0.25 ± 0.06	350 ± 469
FYI	129 ± 109	294 ± 32	0.24 ± 0.05	515 ± 404
SYI	144 ± 113	277 ± 26	0.22 ± 0.04	660 ± 475
Ridges	335 ± 278	304 ± 30	0.26 ± 0.05	1411 ± 910

Table 3.2: The median ( $\pm 1 \sigma$ ) of snow depth (HS), density ( $\rho^{\text{SMP}}$ ), harmonically averaged effective thermal conductivity using the Mac(I) parametrisation ( $\overline{k_{\text{eff}}^{\text{Mac(I)}}}$ ), and thermal resistance ( $R$ ) for each ice type.

The snow density ( $\rho^{\text{SMP}}$ ) median is slightly higher on refrozen leads, FYI and ridges, compared to snow densities on SYI (values are given in Table 3.2). Snow density has a similar monthly trend on all ice types (shown in the coloured boxplots in Fig. 3.5), increasing until February/March and then decreasing in April. Looking at the median density values for this season in Fig. 3.6 shows this feature in multiple data sets, not just the SMP. Fig. 3.6 shows a density increase from November to March ( $\rho^{\text{SMP}}$  increases by 43 kg m<sup>-3</sup>,  $\rho^{\text{Cutter}}$  increases by 78 kg m<sup>-3</sup> and  $\rho^{\text{SWE}}$  increases by 96 kg m<sup>-3</sup>) and a decrease after that (average  $\rho$  decrease in April is 24.3 kg m<sup>-3</sup>). The SMP penetration resistance was normalised for the snow depth (Fig. 3.7) to see changes throughout the season to better understand the reason for this density decrease. Fig. 3.7 shows a density reduction in April at the surface and lower depths of the snow cover. This is further discussed in Section 3.4.3.

$\overline{k_{\text{eff}}^{\text{Mac(I)}}}$  has a standard deviation between 0.04 and 0.06 W K<sup>-1</sup> m<sup>-1</sup> for all ice types the difference between the median  $\overline{k_{\text{eff}}^{\text{Mac(I)}}}$  of these ice types is 0.04 W K<sup>-1</sup> m<sup>-1</sup>, meaning the values are very close and are not significantly different. This data can be found in Table 3.2. We see an increase in  $\overline{k_{\text{eff}}^{\text{Mac(I)}}}$  of snow on all ice types until March 2020. After March  $\overline{k_{\text{eff}}^{\text{Mac(I)}}}$  decreases. This is especially prominent on FYI and SYI areas.

The average  $R$  for the winter is lowest on refrozen leads and FYI areas, increasing slightly on SYI and highest on ridged areas.  $R$  remained constant through the season on FYI and SYI. Refrozen leads and ridges had high variability between months.



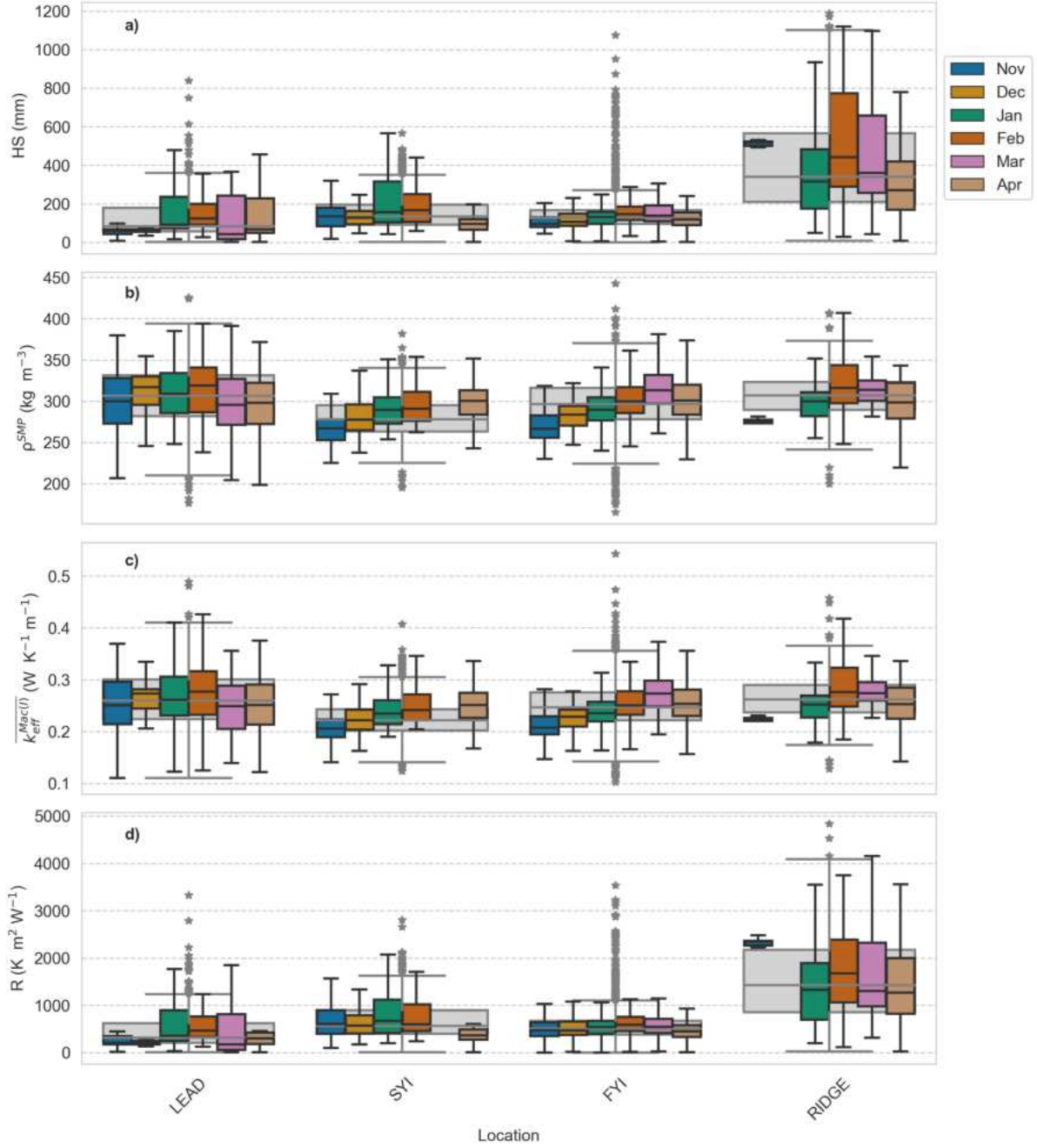


Figure 3.5: Snow depth (HS), density ( $\rho^{\text{SMP}}$ ), harmonically averaged thermal conductivity ( $\overline{k_{\text{eff}}^{\text{Mac(I)}}$ ) and resistance (R) were all measured using a snow micro-penetrometer and plotted against underlying ice type and month. A snow micro penetrometer was used to measure vertical profiles of penetration resistance. These profiles can be used to extract snow depth, density (using [82]), harmonically averaged effective thermal conductivity using the Mac(I) parametrisation, given in Equation (3.3), with the [82] derived density as an input, and, finally, the resistance of the snowpack (R). These profiles are grouped by underlying ice type, topographic feature (seen in the grey bar charts in the background of the figure, with grey stars indicating the outliers), and month (seen in the coloured bar charts, of which the outliers are not shown).

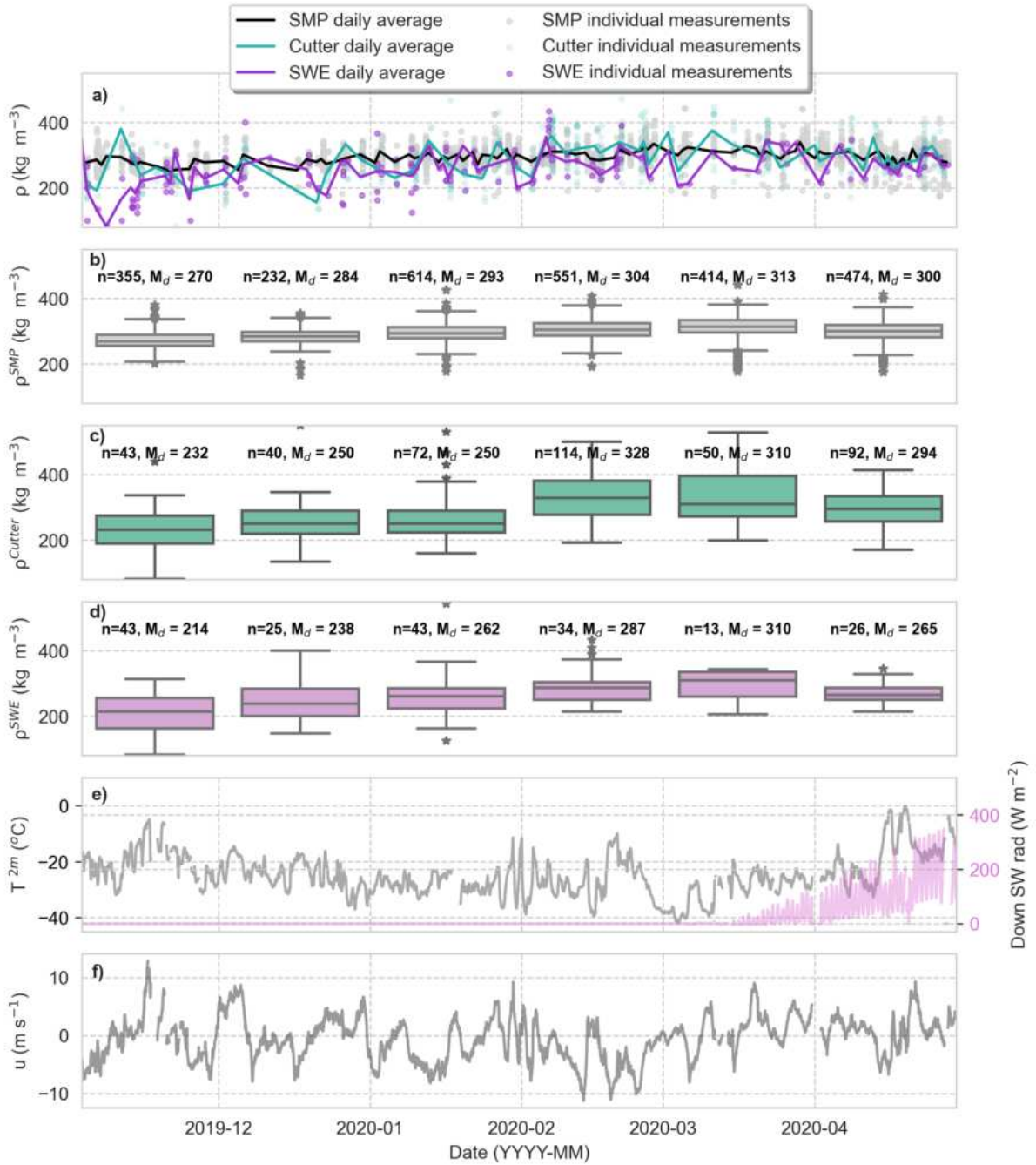


Figure 3.6: a) Time series of density using three independent instruments. The lines show the daily average and the points show the individual measurements. b) a box plot grouping the snow micro penetrometer measurements of density by month. c) a box plot grouping the density cutter measurements of density by month. d) a box plot grouping the snow water equivalent measurements of density by month. All box plots show the temporal change in the medians ( $M_d$ ) and the number of data points in each box plot ( $n$ ). e) the local air temperature at 2 meters above the snow surface ( $T^{2m}$ ) and downward shortwave (SW) radiation. f) time series of wind speeds ( $u$ ). Density measurements from different instruments within the snowpit are compared in the upper plot against time.

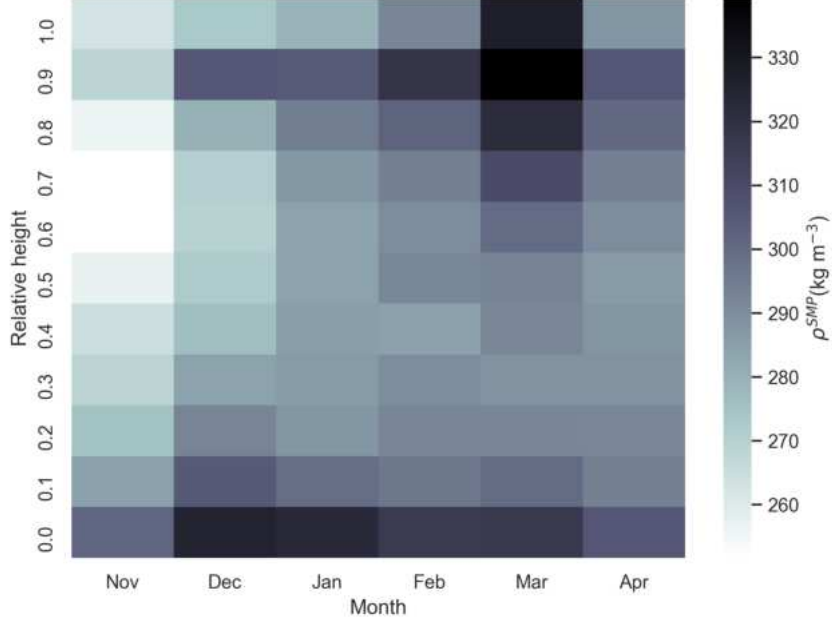


Figure 3.7: A heatmap of winter snow micro-penetrometer profiles on level FYI and SYI. All snow micro penetrometer profiles are concatenated, and their depths are normalised. The normalised SMP density signals averaged for all profiles within one month are displayed throughout the winter to show seasonal changes in the snow cover. A relative height of 0 represents the snow-ice interface, and 1 represents the snow-air interface.

## 3.4 Discussion

Before advancing our understanding of the snow’s thermal conductivity heterogeneity and temporal trends, we must assess the performance of existing parametrisations on samples of snow measured on sea ice in the high Arctic. The  $\mu$ -CT simulations allowed us to assess the current parametrisations for the complete ranges of density and anisotropy values. Following this, we introduced two new parametrisations, with and without anisotropy. To investigate the spatial variability of the snow cover, the  $\mu$ -CT is not an ideal method due to the time required for one measurement. We, therefore, introduced the SMP to have a larger sampling density. The SMP does not have anisotropy measurements in parallel; therefore, a density parametrisation ( $k_{\text{eff}}^{\text{Mac(I)}}$ , given in Equation (3.3)) was used for this up-scaling, as it had the highest  $r^2$  value for this data set when compared to the  $k_{\text{eff}}^{\text{FEM}}$  values. This approach ensured that the measured variability within the data set directly results from spatial heterogeneity and temporal variability, and imprecise parametrisations do not influence the results. The implications of our findings are discussed below.

### 3.4.1 Assessing existing parametrisations

A large range of the sub-samples density and anisotropy values allowed us to create parametrisations of thermal conductivity (and test existing parametrisations) for all ranges of density (from  $50 \text{ kg m}^{-3}$  to  $900 \text{ kg m}^{-3}$ ) and anisotropy (from 0.25 to 2). The relationship between density and  $k_{\text{eff}}^{\text{FEM}}$  in Fig. 3.2 was compared to the parametrisations from [117] at  $-20 \text{ }^\circ\text{C}$  and [99]. Through this comparison, we can see that the anisotropy heavily influences the  $k_{\text{eff}}^{\text{FEM}}$

values. A snow sub-sample with a density of  $400 \text{ kg m}^{-3}$  can have a thermal conductivity value ranging from  $0.2 \text{ W K}^{-1}\text{m}^{-1}$  to  $0.6 \text{ W K}^{-1}\text{m}^{-1}$  if the snow is isotropic or anisotropic in the vertical direction, respectively.

Comparing parametrisations of  $k_{\text{eff}}^{\text{X}}$  and  $k_{\text{eff}}^{\text{FEM}}$ , seen in Fig. 3.4, allows us to analyse which parametrisations represent the simulated  $k_{\text{eff}}^{\text{FEM}}$  most accurately. Fig. 3.4 shows that  $k_{\text{eff}}^{\text{Yen}}$  and  $k_{\text{eff}}^{\text{Stm}}$  align on the 1:1 line at low effective thermal conductivity values. However, for the upper range of  $k_{\text{eff}}$  values, there is an underestimation when compared to  $k_{\text{eff}}^{\text{FEM}}$  resulting in the  $r^2$  value being 0.89 and 0.82 respectively.  $k_{\text{eff}}^{\text{Cal3}}$ ,  $k_{\text{eff}}^{\text{Cal20}}$ , and  $k_{\text{eff}}^{\text{Cal60}}$  appear to underestimate (overestimate) samples with high (low) anisotropy at lower  $k_{\text{eff}}^{\text{FEM}}$  values. Despite this,  $k_{\text{eff}}^{\text{Cal20}}$  has a very similar  $r^2$  value (0.96) to the polynomial fit of this data set ( $k_{\text{eff}}^{\text{Mac(I)}}$ ). The thermal conductivity of our samples at higher densities correspond to the [117] predictions at  $-20^\circ\text{C}$ ; this is a result of our simulations using  $k_{\text{ice}}$  at  $-20^\circ\text{C} = 2.34 \text{ W K}^{-1} \text{ m}^{-1}$ . When introducing an anisotropy parameter,  $X = \text{Löwe}$  [95] is well suited for low densities, below  $500 \text{ kg m}^{-3}$ , but start underestimating for sub-samples with densities higher than  $500 \text{ kg m}^{-3}$ . This was expected as the parametrisation was not built for higher densities. We correct this parametrisation for higher densities (outlined in Section 3.2.2, resulting in the  $k_{\text{eff}}^{\text{Mac(II)}}$  parametrisation with an  $r^2$  of 0.99.

In summary, we have introduced two new thermal conductivity parametrisations; see Equations (3.3) and (3.4). The latter requires an anisotropy factor, which can, for now, only be measured in the laboratory using  $\mu$ -CT. We recommend using Equation (3.3) when measuring the thermal conductivity of snow on Arctic sea ice when only density measurements or approximations are available.  $k_{\text{eff}}^{\text{Mac(I)}}$  is used throughout this study when there were no co-measured anisotropy values, for example, when using the SMP. It is important to mention that calculations of  $k_{\text{eff}}^{\text{FEM}}$  excludes convection, which would increase the thermal conductivity values. However, the convection is negligible compared to the conduction through the ice skeleton.

### 3.4.2 Spatial heterogeneity

Due to the high heterogeneity of the snow cover on Arctic sea ice, the highly time-consuming  $\mu$ -CT measurements could not represent the wide spatial heterogeneity. For this reason, we could up-scale using the SMP after analysing suitable parametrisations from the  $\mu$ -CT data set. As previously mentioned, the SMP does not have simultaneous anisotropy measurements, so the parametrisation  $k_{\text{eff}}^{\text{Mac(I)}}$  was used. The SMP data set consisted of 3266 profiles taken during this study period. This is highly representative of the landscape due to the spatial scale of the measurements taken over a variety of conditions and a large measurement sample size.

This is the first time we have been able to group a dataset of thermal conductivity measurements by underlying ice type (FYI, SYI and refrozen leads) and topographic feature (ridges) for one winter period. This has allowed us to analyse different features of importance for heat transfer. Fig. 3.5 highlights that snow depth is highly dependent on the ridging of the ice, as known from other studies on sea ice ridging [111, 135, 136].  $\rho^{\text{SMP}}$  is slightly higher for refrozen leads, likely due to the inclusion of brine in the snow on refrozen leads during formation, which lowers the freezing temperature and increases the density. The same is for  $\rho^{\text{SMP}}$  measured at ridged sites, which is likely due to wind densification. However, the standard deviation is large enough for these variations not to appear significant.  $k_{\text{eff}}^{\text{Mac(I)}}$  is derived from the  $\rho^{\text{SMP}}$ ; therefore, we see similar dependencies in the groups, as explained above.

The average  $k_{\text{eff}}^{\text{FEM}}$  for all sub-samples of this dataset had the value of  $0.27 \pm 0.17 \text{ W K}^{-1} \text{ m}^{-1}$  and the 1623 SMP profiles harmonically averaged between January and March profiles of

$\overline{k_{\text{eff}}^{\text{Mac(I)}}}$  had an average value of  $0.25 \pm 0.05 \text{ W K}^{-1} \text{ m}^{-1}$ , seen in Fig. 3.3. Including spatial heterogeneity in models is critical for improving heat transfer through the snow cover. Fig. 3.3 compares the range of values of  $\overline{k_{\text{eff}}^{\text{Mac(I)}}$  and  $\overline{k_{\text{eff}}^{\text{FEM}}}$  to the constant average value of  $\overline{k_{\text{eff}}^{\text{Cal20}}}$  and  $\overline{k_{\text{eff}}^{\text{Models}}}$  (also represented as  $k_s$ ) =  $0.30\text{--}0.33 \text{ W K}^{-1} \text{ m}^{-1}$  proposed by [137] and [138]. This snow thermal conductivity value is inferred from thermodynamic ice growth and is widely used in the modelling community [45, 125, 126]. The breakdown of  $\overline{k_{\text{eff}}^{\text{Mac(I)}}$  for each ice type can be seen in Table 3.2. We propose that large-scale sea ice models test a lower average ( $k_s$ ) value of  $0.25 \pm 0.05 \text{ W K}^{-1} \text{ m}^{-1}$  for snow on sea ice. We have calculated this using independent methods. We need to answer the question: what would happen in Arctic sea ice models if the established value of  $k_{\text{eff}}$  was too high?

The snowpack’s thermal resistance  $R$  on sea ice heavily depends on topography. Ridged areas showed approximately three times the thermal resistance compared to level ice areas. SYI and FYI areas have similar  $R$  medians, with SYI areas having more significant heterogeneity than FYI areas. Finally, refrozen leads have the lowest  $R$  and have a significant standard deviation. Sampling bias is likely one reason for these large standard deviations (especially on ridged and lead areas). Refrozen leads can not be measured until there is sufficient ice thickness to walk on. However, different ages and seasons produce highly varying conditions on the leads [139], and our sampling was not focused on measuring different ages of refrozen leads throughout the season. This means that our sampling was likely not representative of the many different conditions of refrozen leads and cannot be used to draw concrete conclusions about snow thickness and thermal resistance. The high variability in the ridge’s  $R$  values is due to the varying snow distribution. SMP measurements were taken adjacent and perpendicular to the ridges to try and capture this heterogeneity.

### 3.4.3 Temporal change

The time component of this study shows that HS is highly variable, but the monthly median of SYI and lead areas remain consistent throughout the season. These ice-type categories were defined in situ. Snow depth on FYI increased until March, thereafter showing a decrease. This decrease in snow depth is likely due to the significant wind speeds during the storm event described by [140]. HS in ridged areas is highly heterogeneous and is likely due to the blocks within the ridges causing an uneven sea ice topography causing high heterogeneity in snow accumulation. Temporal variability of the ridged sites could also be due to the operator selecting different ridge areas to measure or the sudden inaccessibility of different snowpit sites due to ice dynamics.

By conducting this analysis, we have seen that there is an increase of  $\rho^{\text{SMP}}$  on all ice types (and therefore also an increase of  $\overline{k_{\text{eff}}^{\text{Mac(I)}}$ ) until Feb/March 2020, followed by a decrease in both  $\rho^{\text{SMP}}$  and  $\overline{k_{\text{eff}}^{\text{Mac(I)}}$ . This seasonal trend in  $\rho^{\text{SMP}}$  can be seen in Fig. 3.5 where  $\rho^{\text{SMP}}$  decreases from 312 to 299  $\text{kg m}^{-3}$ ,  $\rho^{\text{Cutter}}$  decreases from 310 to 296  $\text{kg m}^{-3}$  and  $\rho^{\text{SWE}}$  decreases from 310 to 264  $\text{kg m}^{-3}$ . Fig. 3.6 confirms this seasonal trend by comparing multiple-density data sets. The air temperature at 2 meters, the downward shortwave (SW) radiation and the wind speed are plotted in Fig. 3.6. After March, we see an increase in SW radiation and two warm air intrusions in April. Wind speed variability remains high from November to April. Taking the atmospheric conditions into account, a density reduction at the surface (relative height = 1) in Fig. 3.7 could result from:

- Snowfall precipitation would lower the average density. A layer with low thermal conduc-

tivity  $\overline{k_{\text{eff}}^{\text{Mac(I)}}$  leads to a drastic decrease in the average thermal conductivity. We can see in [140] that we had snowfall during this period; however this is not apparent in the snow height data in Figure 3.5 on level (FYI and SYI) or ridged areas, but we saw an increase in snow height on refrozen leads.

The reduction in SMP density the lower depths could be a combined effect of the below three points:

- Erosion of the snow surface due to high wind speeds. [140] showed a reduction in SWE during this period and concluded that the erosion of the snow drove this. Erosion of the surface snow would leave behind a less dense lower snowpack, resulting in an overall reduction in density. This process would also explain the reduction in snow depth.
- Vapour diffusion within the snowpack and sublimation of the snow surface produces a density reduction at the bottom due to depth hoar formation. [141]’s simulations showed significant density reductions upon including diffusive water vapour transport within SNOWPACK. They showed that diffusive vapour transport could result in cumulative density changes of  $-62$  to  $-66 \text{ kg m}^{-3}$  for the bottom layer in a shallow Arctic snowpack and snow on sea ice. More work on implementing SNOWPACK with vapour diffusion and studying this period would be required to confirm if this is a dominant process causing a density reduction.
- Penetration of the hard density layers at the snow-ice interface (named the ‘remnant surface scattering layer’ in Section 3.3.1) changed due to sublimation within the snowpack, contributing less to the overall statistics of high densities at the interface. A reduction in measured densities at the lower depths would also reduce the SMP-derived SWE. Therefore, this would also apply to the transect analysis in [140]. More work investigating this snow-ice interface layer is required to form a conclusion.

Due to the combination of I) this seasonal trend in  $\overline{k_{\text{eff}}^{\text{Mac(I)}}$  and ii) snow depths, we see no seasonal trend in  $R$  values on level ice, with a value of  $R = 515 \pm 404 \text{ m}^2 \text{ K W}^{-1}$  on first-year ice and  $660 \pm 475 \text{ m}^2 \text{ K W}^{-1}$  on second-year ice. Therefore, we can conclude that the calculated values of  $R$  remain consistent during winter but include high spatial heterogeneity due to snow depth variability. Ridged areas show a high heterogeneity throughout the season but no significant change in the average  $R$  from January to April.

## 3.5 Conclusions

Using measurements of snow microstructure on different ice types and topographic features on Arctic sea ice for a seven-month winter period in the high Arctic, we have built upon previous work analysing the seasonal evolution of snow’s thermal conductivity [45, 117] using a method that has not previously been used on snow on sea ice. By evaluating the seasonal evolution and spatial heterogeneity of the snow’s thermal conductivity and thermal resistance, we assessed the current thermal conductivity parametrisations and their performance for the range of possible snow densities. We present two new parametrisations, with and without anisotropy.

Field measurements highlighted the need for a high sampling density to represent spatial heterogeneity of thermal conductivity due to snow’s high heterogeneity in the Arctic sea ice system. We conclude that the SMP data set used in this study can be used to measure the

thermal conductivity’s heterogeneity as it had a large sampling size over a wide variety of conditions. However, excluding anisotropy and convection are the limitations of this approach. We propose testing lower values of snow thermal conductivities in large-scale sea ice models. The average of  $\overline{k_{\text{eff}}^{\text{Mac(I)}}}$  for all SMP winter measurements was  $0.25 \pm 0.05 \text{ W K}^{-1} \text{ m}^{-1}$  for snow on sea ice. This indicates that  $0.32 \pm 0.01 \text{ W K}^{-1} \text{ m}^{-1}$ , currently used in sea ice modelling, may largely overestimate thermal conductivity. We also provide a breakdown of snow’s thermal conductivity values per ice type and found the averages ranged from 0.22 to 0.26  $\text{W K}^{-1} \text{ m}^{-1}$  (the overview can be seen in Table 3.2).

By studying the temporal variability of snow density in Fig. 3.6, we infer and quantify from three independent density measurements an increase in the snow’s density from November to March ( $\rho^{\text{SMP}}$  increases by  $43 \text{ kg m}^{-3}$ ,  $\rho^{\text{Cutter}}$  increases by  $78 \text{ kg m}^{-3}$  and  $\rho^{\text{SWE}}$  increases by  $96 \text{ kg m}^{-3}$ ) and a decrease after that (average  $\rho$  decrease in April is  $24.3 \text{ kg m}^{-3}$ ). It was found that a combination of precipitation, high wind speeds causing erosion and re-deposition, vapour diffusion within the snow and changes at the snow-ice interface, could all result in a density reduction across the snow profile. This density trend projected the thermal conductivity on first-year and second-year ice before the melt period started. Since a similar non-monotonic behaviour is extracted for the snow depth, the thermal resistance of snow on level sea ice remains approximately constant with a value of  $R = 515 \pm 404 \text{ m}^2 \text{ K W}^{-1}$  on first-year ice and  $660 \pm 475 \text{ m}^2 \text{ K W}^{-1}$  on second-year ice. Although the  $\overline{k_{\text{eff}}^{\text{Mac(I)}}}$  on ridged areas did not vary significantly in comparison to level areas, we found approximately three times higher thermal resistance on ridges ( $1411 \pm 910 \text{ m}^2 \text{ K W}^{-1}$ ), with extremely high spatial heterogeneity due to snow depth. We conclude that ridged and level areas need to be treated separately in modelling, as thermal resistance is almost three times higher in ridged areas. High spatial heterogeneity of thermal resistance is apparent, but temporal changes in the snow cover are minimal during this period.

# Ocean-sourced snow on Arctic sea ice

---

Macfarlane, A. R., Mellat, M., Meyer, H., Werner, M., Brunello, C. F., Arndt, S., Wagner, D. N., Jaggi, M., Krampe, D., Dadic, R., and Schneebeli, M.

In preparation for submission.

## Abstract

The role of snow on Arctic sea ice is vast; it insulates and decreases sea ice growth in winter, reduces surface sea ice melt due to its high albedo, provides fresh water in summer, is a source of ions and sea salt aerosols, and currently causes a 70 % uncertainty in sea ice thickness estimations from altimetry methods. Despite its importance, snow on sea ice is relatively understudied due to the inaccessibility of the high Arctic. Here we use stable water isotope and salinity analysis of the winter snow cover in the high Arctic to find that sublimation of the sea ice surface is directly producing snow at the snow-ice interface. We call this "ocean-sourced" snow throughout the manuscript. This results from the high-temperature gradients in the snowpack producing large water vapour fluxes in the Arctic snowpack. We found that sublimation of the sea ice surface and deposition of the water vapour in the snowpack contributes to up to 51–54 mm of the snow depth equivalent. This finding has identified a source of uncertainty when comparing snow water equivalent values between snow depths and snowfall, the heat transfer through the ice and snow (as a highly-conductive material is being replaced by a highly-insulating material), and the chemical composition of snow on sea ice (through better understanding the source of sea salt aerosols and the contribution of a snowpack molecular iodine source to Arctic ozone destruction). This new understanding highlights the need to include vapour flux modelling in larger sea ice models and conduct further tests on sea ice surface sublimation with the Community Earth System Model (CESM), which incorporates CICE and has coupled fluxes.



## 4.1 Introduction

The reduction in Arctic sea ice impacts mid-latitude winters [142], and the relatively thin layer of snow resting on top is the most significant uncertainty in future predictions of Arctic sea ice [20]. In the "new" Arctic, we are predicting faster and larger increases in precipitation than previously projected [143], which means more snowfall in winter and early-onset rain-on-snow events. The quantitative link between precipitation and sea ice extent is poorly constrained [144]. A better understanding of the response of increased precipitation on the Arctic sea ice energy balance is needed to assess the sensitivity and better predict future Arctic sea ice conditions.

Snow is the insulating barrier between the sea ice and the atmosphere [145], a key element in the mass balance [146] and a source of aerosols [147] and other chemical compounds [148]. Accurate estimations of the snow depth and internal processes within the snow cover on Arctic sea ice are critical for many components of the sea ice system.

High wind speeds on Arctic sea ice produce large layers of wind-blown snow in the snow cover. Once the blowing snow has settled and undergone wind compaction on sea ice, it is exposed to extreme internal temperature gradients in the range of  $100 \pm 50 \text{ K m}^{-1}$  between the sea ice surface and the atmosphere [27]. This produces perfect conditions for snow metamorphism and causes vapour fluxes in the snow [149]. These internal processes, including re-crystallisation through metamorphism (sublimation and deposition) and vapour exchange, alter the snow's chemical and physical composition, making this layer a complex piece of the puzzle. This study focuses on temperature gradient metamorphism, where temperature differences drive the vapour diffusion within the snow. The equilibrium vapour pressure is higher above warm ice surfaces, causing sublimation and deposition onto the colder surface. This re-crystallisation of the snow produces a highly dynamic snowpack, which is not yet accounted for in current large-scale climate models [150]. Most of the current detailed snow models, such as [151] and [152], do not include the upward water vapour flux. We try to answer (through stable-water isotopes) whether internal, post-depositional processes occurring in this small but highly dynamic layer are critical processes that should be included in large-scale sea ice models.

Stable water isotopes can be used as a process tracer in the water cycle. The isotopic fractionation of stable water isotopes in a snow cover is the preferential partitioning of heavier and lighter isotopes during a phase change. Fractionation can be either i) equilibrium or ii) kinetic, reflecting differences in i) equilibrium constants or ii) rate constants for isotopic species [153]. As a result, isotopic signals can be used to understand the origin and changes of snow's isotopic signature caused by sublimation and deposition [31, 32, 33, 34, 35, 36]. Sublimation and deposition occur on all ice surfaces in the snow cover subjected to a temperature gradient. As a result, snow in the sea ice system is often undergoing large amounts of sublimation and deposition (due to the high temperature gradients), in parallel to other processes (e.g. flooding, wind redistribution etc.) resulting in complex isotopic signatures of the snowpack [154].

Through the MOSAiC campaign, we collected samples of snow on sea ice in high-resolution (3 cm) vertical profiles. These samples were collected for stable water isotope and salinity analysis. We present our findings which have the ability to correct discrepancies in snow depth and snowfall measured in situ and identify a significant sea salt aerosol source in the sea ice system [155].

## 4.2 Methods

### 4.2.1 The MOSAiC expedition

This manuscript studies snow on sea ice in the winter months from January 2020 to May 2020 in the high Arctic between 83.4°N and 88.6°N. The research vessel Polarstern was drifting alongside a single ice floe as part of the MOSAiC expedition. To describe the evolution of the snowpack conditions over time, we set up "snowpit sites" on the ice floe. We returned to these snowpit sites weekly unless ice dynamics meant they were inaccessible. The snowpit sites included FYI areas, SYI areas, leads and ridges. The set-up of these snowpit sites on the ice allowed for in-situ measurements of snow properties [62]. One "snowpit event" is one visit to the ice and includes a library of different physical, chemical, isotopic and conductivity measurements of the snow, measured simultaneously [63]. The snowpit research used in this study focuses on microstructural and chemical analysis of snow, including salinity and stable water isotope measurements. Snow samples were taken in the field and analysed after returning to onshore laboratories.

### 4.2.2 Stable water isotope and snow salinity profiles

Designated areas were assigned to snow measurements on the MOSAiC winter floe and named "snowpits". The snowpit sites were chosen randomly and were a collection of measurements taken within one "Event". One Event represents one trip to the ice. Within these snowpits, isotope samples were collected in profiles. In total, 514 isotope samples were collected and analysed in two laboratories (The Swiss Federal Research Institute WSL and The Alfred Wegener Institute) for this study period. Both datasets contribute to this study. The first dataset [73] took vertical profiles of snow samples (each 100 cm<sup>3</sup>). These samples were measured for density in the field and then transported to the ship in sealed plastic cups. The vertical resolution of these samples was every 3 cm in the vertical. After the samples were transported to Polarstern, the samples were melted for salinity measurements (using the YSI 30 Salinity, Conductivity and Temperature sensor, [76]) and sealed into glass jars onboard Polarstern. As a result of this sampling protocol,  $\delta^{18}\text{O}$  and  $\delta\text{D}$  isotope composition were measured at the same intervals as density and salinity profiles. Each sample in this dataset was transported to Switzerland and measured for stable water isotopic composition at WSL, Zurich, using a Los Gatos Research (LGR) Isotopic Water Analyzer (model IWA-45EP) instrument. Each sample was measured five times in this dataset [73] with a resulting measurement uncertainty of  $\delta^{18}\text{O} \pm 1 \text{ ‰}$  and  $\delta\text{D} \pm 2 \text{ ‰}$ , and accuracy of  $\delta^{18}\text{O} \pm 0.5 \text{ ‰}$  and  $\delta\text{D} \pm 1 \text{ ‰}$ . The second dataset [156] was collected in the snowpit at three layers: top, middle, and bottom. A plastic shovel was used to sample the snow in these three layers directly into plastic bags. These samples were transported to Polarstern and remained frozen onboard as they were stored at  $-4^\circ\text{C}$ . After the expedition, this second dataset was sent to AWI, Germany, thawed at room temperature, poured into 20 ml glass vials, sealed with parafilm tape and stored at  $4^\circ\text{C}$ . This dataset was measured for stable water isotopes using mass spectrometers (DELTA-S Finnigan MAT, USA) to an accuracy of 0.1 ‰ for  $\delta^{18}\text{O}$  and 1.0 ‰ for  $\delta\text{D}$ . The measurement protocol was the same in this second dataset, which also took an average of five measurements for each sample. Both datasets are published with open access in Pangaea, where more details can be found. A comparison was conducted between the two laboratories by measuring 50 samples twice to show continuity between the datasets. It was found that the WSL-measured samples needed a correction due to evaporative fractionation during sample storage. The correction was done by calculating the mean of this dataset to the mean of the parallel dataset and correcting for the difference. This was possible

as the histograms for both datasets were of a similar shape but appeared to have a shift. As a result, the  $\delta^{18}\text{O}$  was corrected by  $-6.4\text{‰}$ , the  $\delta\text{D}$  was corrected by  $-36.4\text{‰}$ .

Isotopic profiles were normalised, and the term "relative height" was used in this study to account for the heterogeneity of the snow cover. By analysing normalised profiles (where 0 is the snow-ice interface and 1 is the snow-atmosphere interface), we can identify seasonal and vertical profile trends without addressing the complex spatial variability and redistribution of snow across the ice floe.

## 4.3 Results

### 4.3.1 Stable water isotopes as a tracer

Throughout this article, the stable water isotopes  $\delta\text{D}$  and  $\delta^{18}\text{O}$  denote the ratio of stable isotopes protium ( $^1\text{H}$ ) / deuterium ( $^2\text{H}$ ) and oxygen-18 ( $^{18}\text{O}$ ) / oxygen-16 ( $^{16}\text{O}$ ) relative to the Vienna Standard Mean Ocean Water (VSMOW). This manuscript gives the ratios in parts per thousand (‰). We know that kinetic fractionation through metamorphism causes enrichment in the heavier isotopes within the snowpack and modifies the original vapour and snowfall isotope signal [157]. The temperature differences in the pore spaces lead to a difference in water-vapour concentration, hence diffusion within the pore spaces. This leads to local vapour-pressure deviations (compared to equilibrium vapour pressure), causing snow sublimation. Sublimation is where the snow undergoes a phase change from a solid to a vapour state, preferentially evaporating the lighter isotopes from a warmer surface. This vapour then deposits on a colder surface [158]. However, few studies investigate the implications of this [159, 160, 161]. The large vapour fluxes within the Arctic snowpack, as mentioned in the previous paragraph, are a result of the temperature gradients causing sublimation of i) surface snow into the atmosphere (and removed just after [162]) or ii) in the interstitial air within the snowpack (available to re-exchange and deposit on the ice crystals). These vapour fluxes are expected to highly alter the isotopic signature of the thin snowpack on sea ice. The gradient in Figure 4.1a of the relationship between  $\delta\text{D}$  plotted against  $\delta^{18}\text{O}$  for the two datasets can be an indication of internal processes in the snow. We found the average surface snow sample is less enriched in  $\delta^{18}\text{O}$  and  $\delta\text{D}$  than a snow sample at the snow-ice interface, seen in Figures 4.1a and 4.1c.

To investigate temporal changes of the isotopic signature of the snow cover, the heatmap is demonstrated in Figure 4.2, which presents the  $\delta^{18}\text{O}$  profiles. This figure shows that  $\delta^{18}\text{O}$  values are more enriched at the snow-sea ice interface. Figures 4.1 and 4.2 indicate a consistent isotopic gradient throughout the season. The snow enrichment at the sea-ice interface suggests the sublimation processes occurring. However, the amount of enrichment shown in the lower snowpack compared to the surface snow implies another process occurring. Due to the  $\delta^{18}\text{O}$  values being comparable to the sea ice surface (Figure 4.3), we hypothesise that the water-vapour saturated air at the snow-sea ice interface is highly enriched due to the sea-ice surface sublimation. When this enriched vapour deposits in the snowpack, we have an isotopic signal of the snow similar to the sea ice (see the schematic in Figure 4.4 to explain this process). [161] and [163] showed a strong enrichment in  $\delta^{18}\text{O}$  between snow and water-vapour-saturated air within the snowpack. We support this hypothesis with other tracer measurements outlined below.

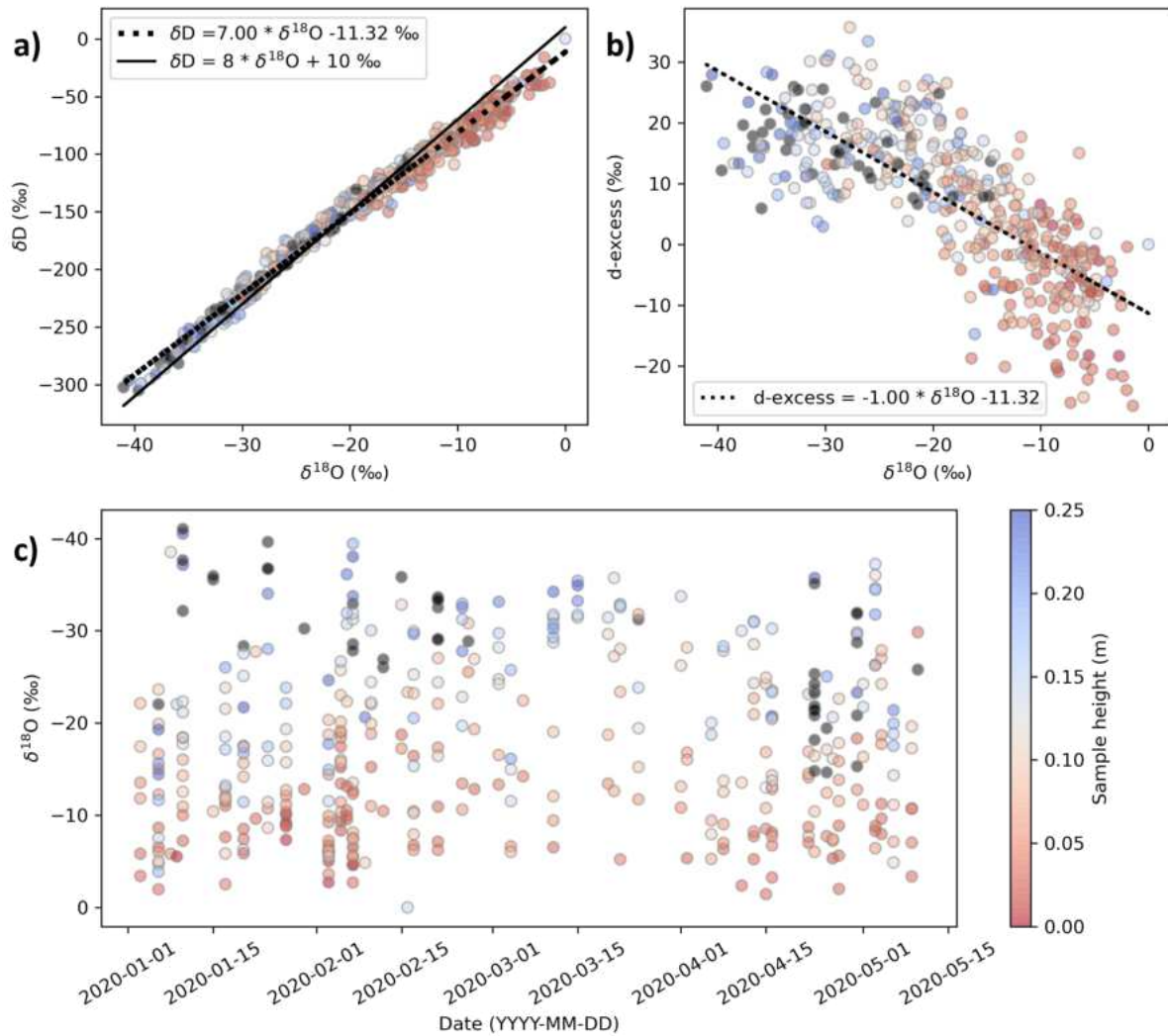


Figure 4.1: Stable water isotope analysis for the snow samples collected within the snowpits on the MOSAiC expedition a) the relationship between the oxygen-18 to oxygen-16 ratio ( $\delta^{18}\text{O}$ ) and the protium (1H) to deuterium (2H) ratio ( $\delta\text{D}$ ), b) the oxygen-18 to oxygen-16 ratio ( $\delta^{18}\text{O}$ ) plotted against deuterium-excess, and c) the time series of the oxygen-18 to oxygen-16 ratio ( $\delta^{18}\text{O}$ ). In all three plots, colour represents the height of the top of the sample from the sea ice surface. The black points represent samples collected above 0.25 m snow height, indicating samples collected at ridged ice areas.

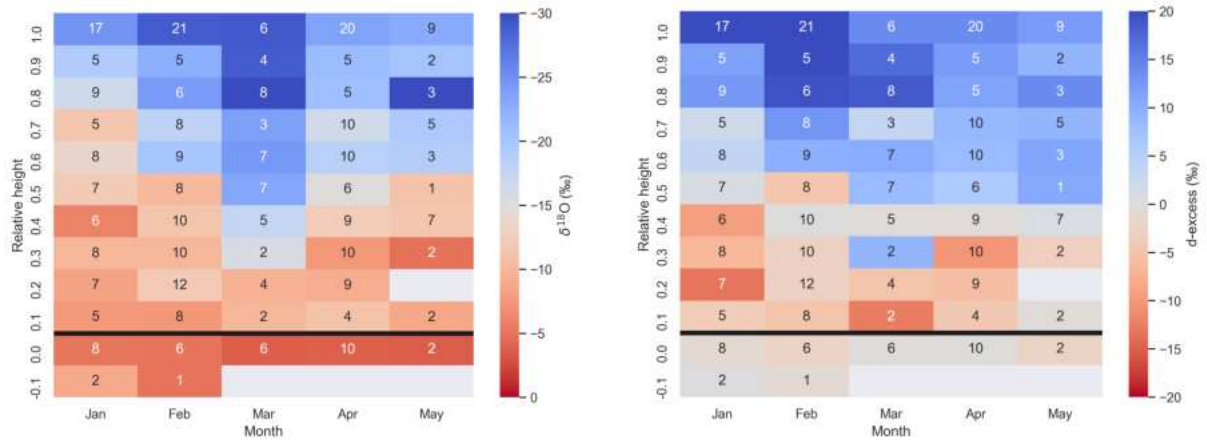


Figure 4.2: A time series heatmap of average  $\delta^{18}\text{O}$  (left) and d-excess (right) sample values averaged by relative height from the sea ice surface of the top of the sample. The values in the boxes indicate the number of samples in the dataset at the relevant height for the indicated month (the different colours are for visual purposes only). The black horizontal line indicates the snow-ice interface.

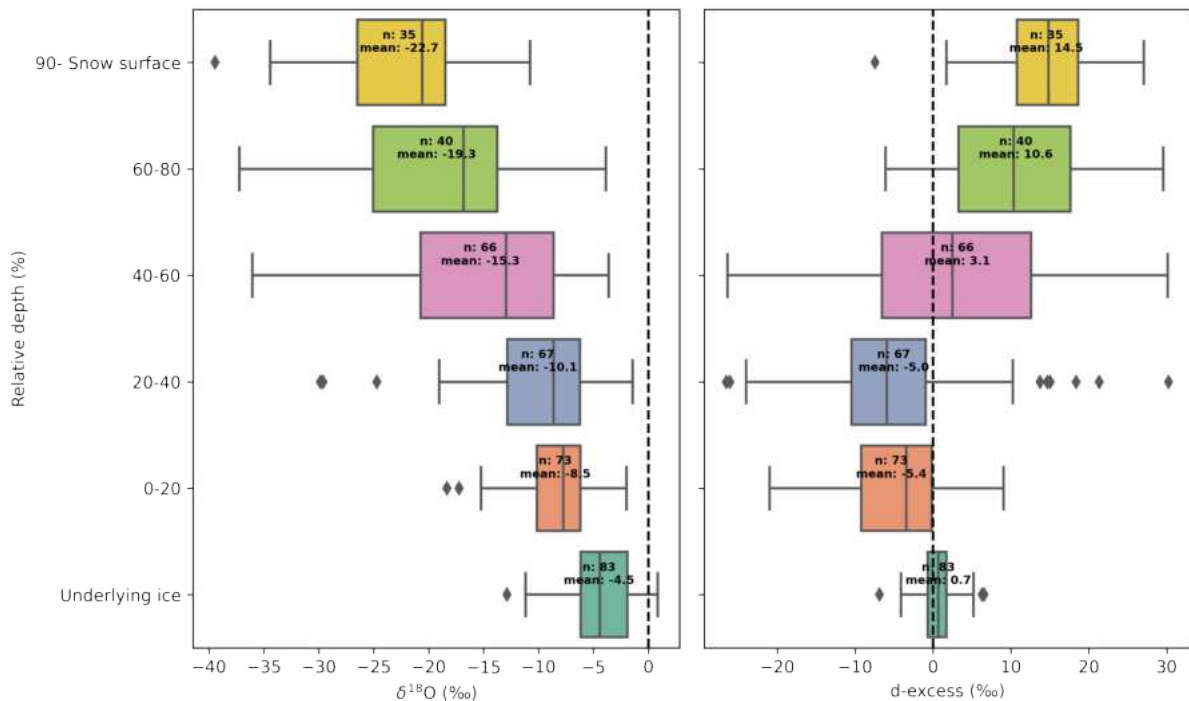


Figure 4.3: The relative height profiles of the oxygen-18 to oxygen-16 ratio (left) and deuterium-excess (right) from January to May 2020. The number of samples (n) and the means are annotated for each layer.

### 4.3.2 Salinity and d-excess as tracers

The Arctic snowpack is known to contain salinity which has previously been thought to result from three processes: i) frost flowers (ice vapourising into the dry air and then refreezing, often above a highly saline brine layer due to expulsion from the ice surface), ii) sea spray (from nearby open water during an event with high wind velocities), and iii) capillary effect within the snow cover where brine from the sea ice is conveyed into the snow by capillary action. [164] explains these three processes in detail. The conductivity of each snow sample (Figure 4.5) shows that NaCl was present in 58 % of the samples taken in the snowpits during this study period. The majority of saline samples have a negative d-excess. Previous studies assumed capillary action [164], and capillary rise in the snow was tested by [165, 166].

The snow-sea ice interface temperature was, on average,  $-13.3 \pm 4.2$  °C during this study period. Salt does not sublimate at these low temperatures but undergoes crystallisation under high concentrations producing different minerals [167].

The deuterium excess (d-excess) is a second-order isotope parameter ( $\text{d-excess} = \delta^2\text{D} - 8 \times \delta^{18}\text{O}$ ) that is specifically sensitive to the conditions during evaporation and sublimation [168]. D-excess depends mainly on temperature and humidity conditions during evaporation [168, 169, 170]. For example, negative d-excess values were observed in water vapour from ocean water in high humidity and low-temperature conditions. Sublimation reduces d-excess in the snowpack, with the water vapour having a relatively high d-excess [171, 34, 172, 36, 173]. D-excess is also affected by ice crystal formation under supersaturated conditions. (this process is lowering both  $\delta^{18}\text{O}$  and d-excess of the remaining vapour, leading sometimes to negative d-excess values. In the Arctic, typical snow d-excess values range from approximately 0 ‰ to 15 ‰, and 5 to 20 ‰ when the samples were from multiple taiga and tundra Arctic snow profiles (Alaska and Finland) [35], and central Greenland respectively [174]. [175] observed "exceptionally low" d-excess values of  $-5$  ‰ in the McMurdo Dry Valleys in Antarctica. An important feature of the datasets analysed in this study saw d-excess values as low as  $-25$  ‰ in snow samples that are taken close to the sea-ice interface.

The d-excess heatmap in Figure 4.2 shows a contrast between the underlying sea ice with an average d-excess of  $0.7 \pm 2.2$  ‰ and the lower fifth of the snow cover with an average d-excess of  $-5.4 \pm 8.4$  ‰. A hypothesis for this difference is due to the lower half of the snow being composed of sea ice with an enriched  $\delta^{18}\text{O}$  and  $\delta\text{D}$  isotopic signal, the two stable water isotopes have a hypothetically infinite source of stable isotopes throughout the underlying ice, whereas in the above snow cover, we are getting extremely negative d-excess values meaning that the  $\delta\text{D}$  ratio is changing at a different rate than the  $\delta^{18}\text{O}$ . This could mean either a)  $\delta\text{D}$  is relatively more depleted (compared to a d-excess of zero), or  $\delta^{18}\text{O}$  is relatively more enriched (compared to a d-excess of zero), both of these results in a negative d-excess. However, when looking at the  $\delta^{18}\text{O}$  profile, there is no difference between the sea ice and underlying snow, so a process within the lower layers of the snowpack is causing  $\delta\text{D}$  to be relatively more depleted. In short, the underlying snow has experienced extreme sublimation and deposition, which lowers the d-excess. Unlike the underlying ice, the d-excess signal cannot recover to a typical zero value due to the limited source of stable water isotopes; therefore,  $\delta\text{D}$  is relatively more depleted in the bottom of the snowpack. As a result, we can use d-excess as a tracer for highly metamorphosed "snow" originating from sea ice.

We compare our snow samples' d-excess and salinity values and highlight two independent features of snow on sea ice. 1) Saline samples with a positive d-excess occur in samples collected on snow above refrozen leads (see Figure 4.5), likely a result of wind-blown snow accumulating on the leads and wicking. 2) The majority of saline samples on first-year ice (FYI) have a

negative d-excess (see Figure 4.5). This supports our conclusions on sea ice sublimation as upward vapour fluxes would leave behind salty pockets.

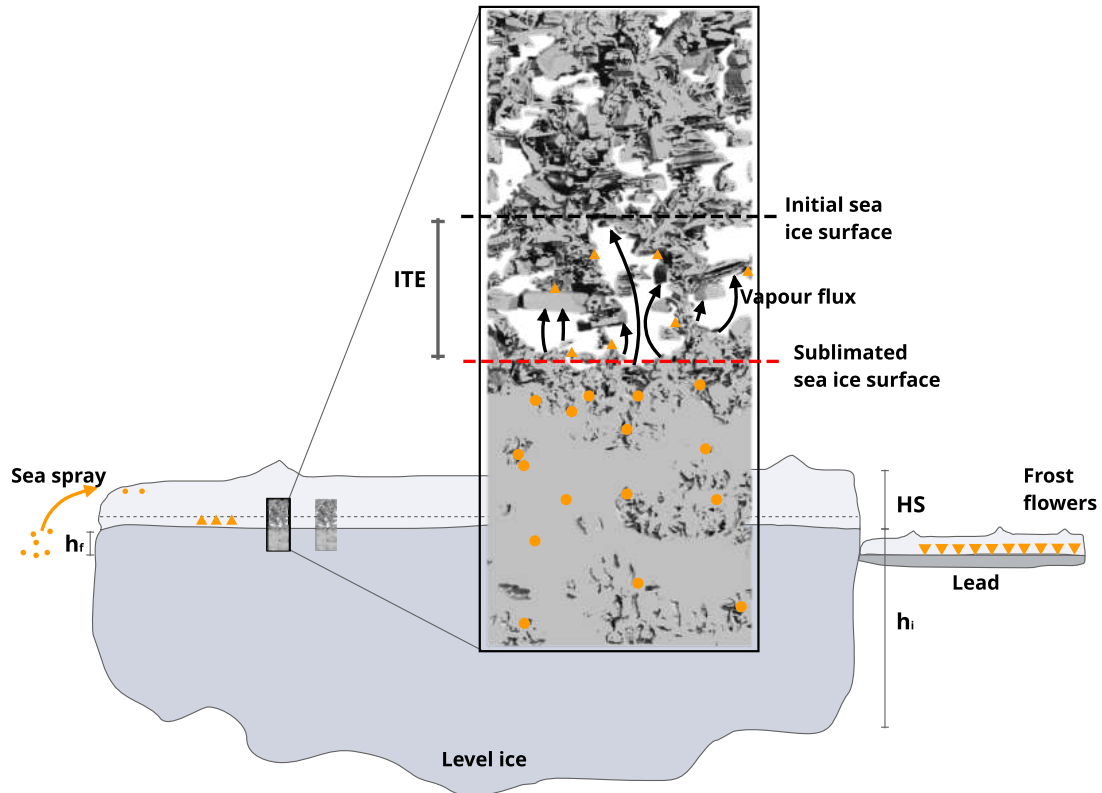


Figure 4.4: A schematic with a  $\mu$ -CT image overlaid to show the sublimation of the snow-sea ice interface. The background schematic shows different processes which could contribute to the salty snow above sea ice (adapted from [164]), where the orange represents locations of the saline pockets, the black arrows represent vapour fluxes from the sea ice surface and deposition and formation of depth hoar crystals. ITE represents the height of sublimation of the sea ice surface, HS is the snow height,  $h_i$  is the ice thickness, and  $h_f$  is the freeboard. Saline ice is commonly a feature of first-year ice. Therefore, this schematic only shows an example of first-year ice processes. This diagram is not drawn to scale

In late summer/early autumn, the first snowfall often creates a thin skim of slushy snow on the sea ice surface. In this skim, snow and briny water become mixed and eventually freeze into a layer of ice; this ice has both atmospheric and oceanic sources. This mixed-ice layer may

be an additional contributing source to the isotope signatures within the basal snowpack and a source of saline snow.

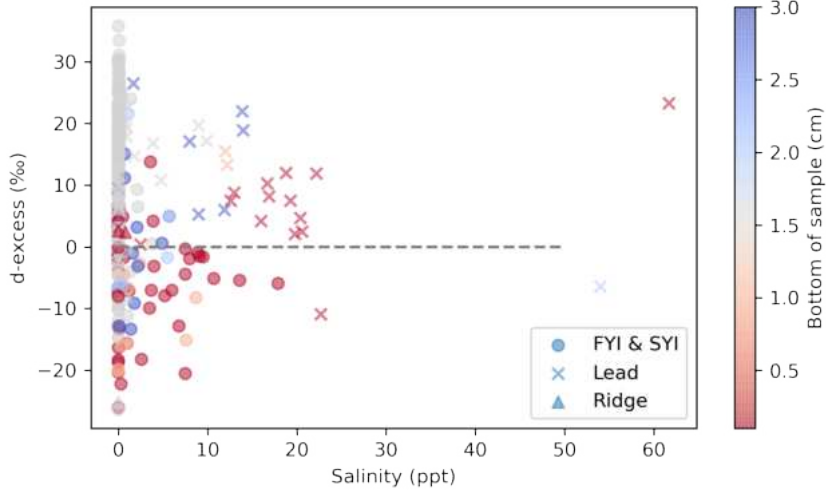


Figure 4.5: Sample salinity values plotted against deuterium-excess. The colour indicates the height of the sample above the snow-ice interface. The different markers indicate the ice types under the snowpit. The legend indicates the snow samples collected on first-year level ice (FYI) and second-year level ice (SYI), leads and ridges. One point in this figure is one snow sample. The sample collection period is between January and May 2020.

### 4.3.3 The rate of the sea ice sublimation

#### a) Controlled laboratory conditions

[42] investigated the sublimation rate of an ice surface under a temperature gradient in controlled laboratory conditions. A temperature gradient of  $100 \text{ K m}^{-1}$  was applied to a snow sample (with a surface temperature of  $-40$ , and a ground temperature of  $-5 \text{ }^\circ\text{C}$  over a snow sample of height  $100 \text{ mm}$ ), with a higher temperature at the bottom for 21 days (with the snow density,  $\rho_s = 201 \text{ kg m}^{-3}$  and  $\text{SSA} = 15.4 \text{ m}^2 \text{ kg}^{-3}$ ) on top of an ice lens. This snow density is marginally lower than the conditions found on sea ice in the Arctic [176]. However, a temperature gradient of  $100 \text{ K m}^{-1}$  is typical for this study region. [42] calculated the apparent movement of the ice lens from the ice-voxel fraction profile (where the ice-voxel fraction was equal to 1 in the ice lens). The linear fit of the ice lens surface movement is given in Equation 4.1, where  $t$  corresponds to the time in days, and  $z_{il} - z_{il,0}$  represents the height of sublimation of the sea ice surface (named ice thickness equivalent, ITE, in this study).

$$z_{il} - z_{il,0} = 0.11 \times t + 0.07 \quad (4.1)$$

Sublimation of the ice surface between January and May 2020 (150 days) has an  $\text{ITE}_a$  of  $16.57 \text{ mm}$ .  $\text{ITE}$  can be converted to Snow Depth Equivalent ( $\text{SDE}$ ) by taking the average density of snow and ice as  $\rho_s = 291 \text{ kg m}^{-3}$  (from average density snow micro-penetrometer measurements in [176]), and  $\rho_i = 900 \text{ kg m}^{-3}$ , respectively [177], and then applying Equation 4.2. This results in a snow depth equivalent,  $\text{SDE}_a = 51.25 \text{ mm}$ , using this method.

$$\text{SDE} = \text{ITE} \times \frac{\rho_i}{\rho_s} \quad (4.2)$$



[42] also concluded that the rate of ice mass flux ( $j_a$ ) from the sublimating ice lens into the snow was  $j_a = v_i \rho_i = 1.2 \times 10^{-6} \text{ kg m}^2 \text{ s}^{-1}$ , where  $v_i$  is the rate that the ice lens sublimated. In 150 days this amounts to  $15.55 \text{ kg m}^2$  of sublimated ice mass.

## b) Isotope composition

In the sea ice environment, we have a clear differentiation of atmospheric sourced snow (with values of  $\delta^{18}\text{O}$  between approximately  $-15 \text{ ‰}$  to  $-35 \text{ ‰}$  [35] and sea ice frozen from the ocean water (with second-year ice (SYI) having average  $\delta^{18}\text{O}$  values of  $-3.1 \text{ ‰}$  and first-year ice with average  $\delta^{18}\text{O}$  values of  $-0.7 \text{ ‰}$  [178]). This allows us to calculate the percentage of our snowpack originating from "atmospheric-sourced" snow and sublimated sea ice, which we name "ocean-sourced" snow throughout this article. Figure 4.3 shows our surface snow samples  $\delta^{18}\text{O}$  values have an average of  $-22.7 \pm 6.2 \text{ ‰}$  ( $n = 35$ ) between January and May 2020. For the same period, the underlying sea ice has  $\delta^{18}\text{O}$  values of  $-4.5 \pm 3.1 \text{ ‰}$  ( $n = 83$ ). The average snowpack for this season has a mean  $\delta^{18}\text{O}$  of  $-17.9 \pm 8.9$ . A simple ratio calculation between these values showed a 28 % enrichment of the  $\delta^{18}\text{O}$  snowpack. If our average snow height is  $192 \text{ mm} \pm 158$  [179] this is an  $\text{SDE}_b = 54 \text{ mm}$  of ocean-sourced snow. This results in  $\text{ITE}_b = 17.5 \text{ mm}$ .

SDE calculated from isotope analysis ( $\text{SDE}_a$ ) is seven per cent smaller than  $\text{SDE}_b$  calculated from ice surface sublimation. These independent methods have a large variability individually, producing snow depth equivalent values in a similar range. The calculated range of estimated sublimated ice has the ice thickness equivalent of  $51 - 54 \text{ mm}$ .

## 4.4 Discussion

The simultaneous measurements of chemical and physical properties allow us to advance our understanding of internal post-depositional processes within the snowpack on Arctic sea ice. Stable water isotopes and microstructural measurements of the snow and underlying sea ice were collected in parallel to investigate the role of sublimation and evaporation under extreme temperature gradients. We found that sea ice sublimation produces 28 % of the snowpack. We call this "ocean-sourced" snow throughout this manuscript. The resulting vapour flux in the snowpack is a key driver in the snow's isotopic signature. We present calculations of the sea ice surface sublimation rate using a) sublimation rates of an ice surface and b) isotope analysis. Finally, salinity measurements of the snow cover are presented alongside d-excess values.

Sublimation of snow enriches the  $\delta^{18}\text{O}$  signal of the snow. Previous laboratory and field studies have found that  $\delta^{18}\text{O}$  enrichment during sublimation causes a difference of  $1-5 \text{ ‰}$  [175, 171]. However, it is important to mention that these studies have a smaller timescale. We agree that the sublimation of the snow alone contributes to our enrichment signal, but this does not explain the enrichment of  $\delta^{18}\text{O}$  to near-ice  $\delta^{18}\text{O}$  values. Another explanation must be given for the near-ice  $\delta^{18}\text{O}$  values of the snow close to the snow-sea ice interface. We use  $\delta^{18}\text{O}$ , d-excess and salinity as tracers within the snowpack to understand the source of the snow. It is uncommon for d-excess to have negative values with sublimation alone [180, 181]. The d-excess value of the underlying sea ice has an average value of  $0.2 \text{ ‰}$  (Figure 4.3). The contrasting snow d-excess values imply different processes occurring in the snow and the underlying ice. We hypothesise that the snow and sea ice are both sublimating, but the resulting vapour from the sea ice sublimation is undergoing deposition and producing enriched snow at the sea ice interface. The combined analysis of  $\delta^{18}\text{O}$  and d-excess prove that ocean-sourced snow, due to

the sublimation of sea ice, is a major influence on the isotopic signature of the snowpack on sea ice. Using isotopes, we estimate that 28 % of the snow on sea ice is from the sublimation of the sea ice surface. This result puts an emphasis on testing the current inclusions of vapour fluxes in large-scale sea ice models (e.g. CICE [18]).

#### 4.4.1 Precipitation estimates

When precipitation is modelled throughout the Arctic, we often compared it to in situ snow water equivalent measurements for validation [140]. If 28 % of the snow on sea ice is from the sublimation of the sea ice surface, we are underestimating the snow water equivalent of snow on Arctic sea ice if measuring remotely (e.g. reanalysis precipitation estimates), and precipitation could be overestimated by 28 % when comparing to in situ snow depth measurements. This has major implications on our estimations of snow mass in the Arctic, which in turn introduces uncertainties in the amount of snow deposited into leads and accumulating around ridges, further influencing heat flux through the Arctic snowpack. With more precipitation predicted in the Arctic region due to climate change, a current difference of 28 % could be detrimental to reducing uncertainties of the future Arctic conditions.

#### 4.4.2 Heat transfer

The sublimation of the sea ice surface and the density reduction of snow on sea ice has implications for the thermal conductivity of the snow cover. We now understand that approximately 20 mm of sea ice is producing approximately 50 mm of snow depth equivalent on sea ice. This process is transforming a highly conductive material (with thermal conductivity of  $2.34 \text{ W K}^{-1} \text{ m}^{-1}$ ) into a low conductivity material (with a thermal conductivity of  $0.27 \pm 0.17 \text{ W K}^{-1} \text{ m}^{-1}$ ; [176]). This could have significant consequences when calculating ice growth rates. Vapour fluxes are now known to be an essential part of the snow-on-sea ice system, and future work needs to test vapour fluxes in large-scale sea ice and climate models, for example, CICE in CESM [18].

#### 4.4.3 Sea ice chemistry implications

Vapour flux within the snowpack has significant implications for other gasses and could indicate a larger process understanding in the biogeochemistry community. We now understand that an additional process (sea ice surface sublimation) could produce saline snow on level ice. The saline snow on level ice in this analysis also had a majority of negative d-excess (see Figure 4.5). This is in contrast to saline lead samples which have a positive d-excess. This indicates that there are two independent processes creating saline snow.

FYI is more saline than SYI, and in the "new" Arctic (with more first-year sea ice), we predict a larger proportion of the snow cover to include NaCl. This is important information when i) modelling future Arctic freshwater sources (essential for ecological communities), ii) microwave remote sensing backscatter signals (influenced by salinity in the snowpack), iii) modelling and understanding sources of sea salt aerosols and their role in polar climate [155], iv) better constraining the origin of bromine and iodine on Arctic sea ice, hence understanding the contribution of a snowpack molecular iodine source [182] to Arctic ozone destruction [183]. Models including vapour fluxes through the snow are necessary for modelling gas exchanges through the Arctic sea ice and snow.

#### 4.4.4 Conclusion

Sublimation of the sea ice surface is the dominant process affecting the isotopic signature of snow on sea ice and creates a mix of atmospheric and ocean-sourced snow. The sublimation of approximately 20 mm of the sea ice surface results in saline snow and mineral deposition in the snowpack. 58 % of samples taken in this study between January and May 2020 contain NaCl, and most of these samples taken on level ice have a negative d-excess value. Using two independent calculations, we estimate that 50–54 mm of snow on sea ice is ocean-sourced. This new understanding explains the negative d-excess values reaching as low as  $-30\text{‰}$ , in combination with saline samples. These findings have wide-reaching implications in sea ice research; from identifying uncertainty in precipitation estimates (when comparisons are made to in situ SWE measurements), the heat transfer through the ice and snow (as the highly-conductive ice is being replaced by the highly-insulating snow), the chemical composition of snow on sea ice (through better understanding the source of sea salt aerosols and the contribution of a snowpack molecular iodine source to Arctic ozone destruction). This new understanding and the suggestion to include vapour flux modelling in larger sea ice models have the opportunity to reduce major uncertainties in this field.

# Optical properties of melting Arctic sea ice

---

Macfarlane, A. R., Dadic, R., Smith, M. M., Light, B., Nicolaus, M., Henna-Reetta, H., Webster, M., Linhardt, F., Hämmerle, S., and Schneebeli, M.

Published in: *Elementa*, Science of the Anthropocene (2023).

## Abstract

The microstructure of the uppermost portions of a melting Arctic sea ice cover has a disproportionately large influence on how incident sunlight is reflected and absorbed in the ice/ocean system. The surface scattering layer (SSL) effectively backscatters solar radiation and keeps the surface albedo of melting ice relatively high compared to the ice with the SSL manually removed. Albedo measurements provide information on how incoming shortwave radiation is partitioned by the SSL and have been pivotal to improving climate model parameterisations. However, the relationship between the physical and optical properties of the SSL is still poorly constrained. Until now, radiative transfer models have been the only way to infer the microstructure of the SSL. During the MOSAiC expedition of 2019–2020, we took samples and, for the first time, directly measured the microstructure of the SSL on bare sea ice using X-ray micro-computed tomography. We show that the SSL has a highly anisotropic, coarse, and porous structure, with a small optical diameter and density at the surface, increasing with depth. As the melting surface ablates, the SSL regenerates, maintaining some aspects of its microstructure throughout the melt season. We used the microstructure measurements with a radiative transfer model to improve our understanding of the relationship between physical and optical properties at 850 nm wavelength. When the microstructure is used as model input, we see a 10–15 % overestimation of the reflectance at 850 nm. This comparison suggests that either a) spatial variability at the meter scale is important for the two in situ optical measurements and therefore a larger sample size is needed to represent the microstructure or b) future work should investigate either i) using a ray-tracing approach instead of explicitly solving the radiative transfer equation, or ii) using a more appropriate radiative transfer model.

## 5.1 Introduction

The 2019 IPCC special report on the ocean and cryosphere in a changing climate states that sea-ice albedo feedback is a key driver of sea-ice loss [184, 185]. However, a lack of process understanding makes differentiating between anthropogenic and natural drivers of summer Arctic sea ice variability a challenge [186, 187, 188]. We currently understand that the high reflectivity of sea ice exerts a large cooling influence on the Arctic system [189]. Nevertheless, global climate models have highly variable representations of the sea-ice albedo feedback [190, 191, 192], which contributes to uncertainty in climate projections. These variabilities come from spatial and temporal heterogeneity in surface conditions (including sea-ice properties, snow cover, and albedo [193]). Our understanding of Arctic sea-ice melt processes needs to advance to improve projections of sea-ice conditions.

The sea-ice extent at the end of the summer of 2020 was the second lowest in the satellite record [194], continuing the trend in the recent sea-ice decline. A Siberian heat wave in the spring of 2020 initiated an early Arctic sea-ice melt [195], resulting in the melt season lasting more than a month longer than usual, with July and August 2020 being, on average, the all-time warmest and wettest months [25]. During the same year, the Multidisciplinary drifting Observatory for the Study of Arctic Climate (MOSAiC) expedition was moored alongside an ice floe in the transpolar drift stream collecting measurements [196, 62]. The interdisciplinary approach allowed for the comparison of many measurement techniques and for experts in various research fields to work simultaneously on sea ice. This holistic approach allowed novel combinations of instruments to be installed and used on sea ice to better understand the influence of changes in the Arctic on sea-ice processes.

In the Arctic, the melt season conditions cause the highly reflective snow to melt, exposing bare sea ice to solar radiation. As a result of the absorption of this solar radiation, a porous, granular, and highly fragile pillared structure begins to form at the top of the melting sea ice. Here we refer to this surface structure as the surface scattering layer (SSL). The surface type is known as melting "bare ice", "white ice", or "loose, large ice grain layer" in the literature [197, 137, 198, 37, 199, 200, 38, 201]. Unlike snow, the origin of the SSL is not atmospheric but melting sea ice. The SSL governs the optical properties of summer sea ice due to its effective backscattering of solar radiation, which keeps the surface albedo relatively high [137]. As a result, the SSL plays a vital role in the energy budget of melting sea ice and determines the surface melt of Arctic sea ice during summer [201]. Despite the importance of the SSL for optical properties, there is no quantitative description of the evolution of the pore microstructure during melt [202], as the microstructure of the SSL has been challenging to measure in detail.

Measurements of the SSL microstructure previously relied on transporting the ice sample from its area of origin to a suitable laboratory to study its properties without structural change. Light et al. (2008) [37] describe the SSL as an "intricate skeletal structure of fragile ice crystals". Because the SSL exhibits such a fragile structure, transporting it without structural change is difficult. Therefore, due to its high porosity and fragility, the microstructure of the SSL has not previously been measured in situ. Measuring the SSL in situ has previously been impossible without implementing an adopted method of casting [203].

Prior measurements were focused primarily on thickness and images of the surface. We know that the thickness of the SSL varies spatially between approximately 0.01 and 0.10 m [37, 200]. For this study, we define the SSL as the surface structure with densities below  $700 \text{ kg m}^{-3}$ . This threshold slightly exceeds the threshold for firn [134]. Due to the vertical structural arrangement and increase in density, using a ruler to penetrate the structure to lower depths and measure the complete thickness of the SSL is challenging. Without manually removing the

SSL, the thickness is often underestimated [201]. Future work to obtain a better measurement of the SSL thickness would benefit from using a shovel to remove the surface layer to the greatest depth that is physically feasible. Through ice cores, we know that a large proportion of the volume of Arctic sea ice is composed of granular and columnar ice. The latter has pore space elongated along the vertical [204, 205, 206], which informs our understanding of the surface microstructure during the melt season. During the melt, a liquid film grows along the grain boundaries, which then causes more melt in these areas. This process is nicely visualised in Figure ~2 in Dash (2006) [207]. The elongated pore space, gravity drainage of surface water, and internal melt along the vertically elongated grain boundaries [208, 209, 210] likely explain the pillared structure of the SSL.

Below the SSL lies the drained layer (DL). DL thickness is limited to the difference between the freeboard height and the SSL thickness. Perovich (2017) [200] notes a DL thickness ranging from 5 to 30 cm. Densities of the DL lie within the range of densities for the underlying interior ice (IL), 700–900 kg m<sup>-3</sup>. The only difference between these two categories (DL and IL) is that the DL depends on the freeboard height, and the meltwater drains away by gravity, leaving airspace and higher scattering. As the surface undergoes melt, the SSL is ablated, and the DL undergoes preferential crystal boundary melt, which causes the porosity to increase and the DL to transition into the new SSL. The seasonal evolution of these layers is shown in the schematic in Figure 5.1. The porosity of these layers is due to different internal processes: the SSL has a high porosity (density range of approximately 0–700 kg m<sup>-3</sup>) due to preferential grain boundary melt [207]. The DL porosity is due to brine channel drainage and pathways forming for brine and meltwater [211]. Finally, the IL porosity is due to brine channels within the columnar ice (with IL density of approximately 700–900 kg m<sup>-3</sup>, which decreases throughout the summer [212]). During the melt season, wet snow metamorphism and surface ablation cause freshwater infiltration through the SSL and DL pore spaces. We can assume that shortwave radiation is producing grain boundary melt at the surface and causing an increase in porosity. However, because shortwave radiation intensity decreases at lower levels within the ice structure, another mechanism must cause an increase in porosity. At these lower levels, the increased porosity is therefore attributed to brine channel conditions.

The high light scattering of the SSL is responsible for the consistently high albedo and relatively low transmittance of bare, melting sea ice [37, 213]. Surface melt and constant regeneration of the SSL layer produce a consistently high albedo during the Arctic summer [214, 215, 216]. Therefore, the SSL plays a crucial role in the energy balance of sea ice during the melt season. Light et al. (2022) [38], in comparing data from MOSAiC and the Surface Heat Budget of the Arctic Ocean (SHEBA) expedition, confirmed that "the spectral albedo for bare, melting sea ice also appears invariant with respect to the ice age (first-year, second-year, multi-year). We suggest that the principal reason for this invariance is the ubiquitous presence of surface scattering layers". This suggestion notably excludes sedimented areas. Throughout this manuscript, albedo represents the integrated hemispherical spectral albedo, and reflectance refers to the reflectivity of an artificially illuminated surface. Measurements of sea ice albedo and reflectance are most informative when combined with observations of the physical properties of the SSL and not simply its thickness, as the thickness is often underestimated when measured by a ruler (as previously explained). Light et al. (2022) [38] advised that observations should include surface type description, snow and ice thickness, snow grain size and density, ice freeboard, temperature, and texture.

Until now, measurements of the microstructure of the SSL have not been made. Radiative transfer models (RTMs) have been used to infer the microstructure of the ice surface from optical measurements [217, 209, 37, 213, 199, 200]. Inherent optical properties (IOPs) are

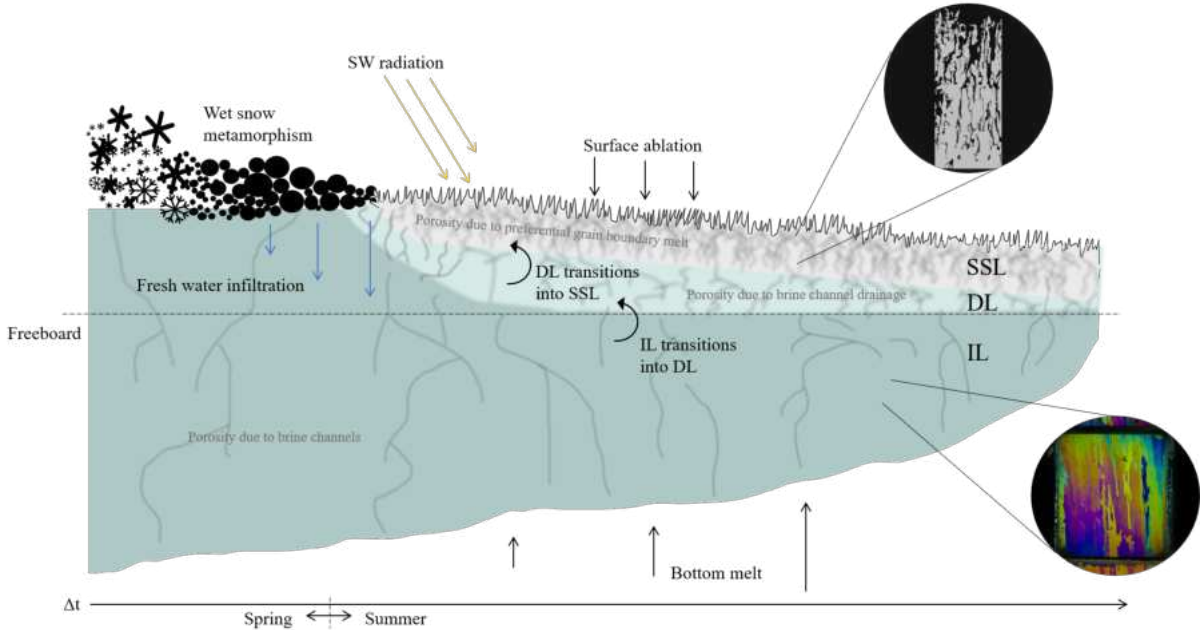


Figure 5.1: This schematic represents the surface scattering layer (SSL) formation from the beginning of the snowmelt in spring through the end of summer, with time ( $\Delta t$ ) represented along the x-axis. Wet snow metamorphism and surface ablation cause freshwater infiltration through the pore spaces of the SSL, drained layer (DL) and interior layer (IL) during the melt. Once the snow melts and drains away, surface ablation maintains the SSL thickness. The SSL persists because of two processes: 1) surface ablation due to incoming shortwave (SW) radiation (reducing SSL thickness), and 2) the transition of IL to DL to SSL (increasing SSL thickness). DL thickness is the freeboard minus SSL thickness. This schematic shows the changing freeboard due to a reduction in the ice thickness. A thin section of columnar ice taken on the MOSAiC expedition (bottom) and a  $\mu$ -CT SSL microstructure (top) can be seen in the circular insets. This figure is not drawn to scale.

fundamental to modelling the ice-albedo: scattering and absorption coefficients and scattering phase functions. Previously IOPs of melting sea ice have been inferred or measured in the laboratory [218, 219]. Our limited knowledge of the geometrical structure and impurity content of the ice and snow means that RTMs are limited by the knowledge of the IOPs [37].

In this study, we investigated the evolution of the microstructure and reflectance of the SSL on melting, level Arctic sea ice. We addressed the questions: What are the geometrical properties of the SSL? How does the SSL vary spatially and temporally? What are the optical properties of the SSL? How does the spatial and temporal variability affect the optical properties? To answer these questions, we have made the first microstructural measurements of the SSL for the summer melt season. We introduced and used a novel instrument that houses a near-infrared camera (NIRbox) to measure reflectance under standardised conditions. We compared results to the commonly used analytical spectral device (ASD). We combined the microstructural information with albedo and reflectance to test if spatial variability of the

surface structure influences reflectance. By using microstructural measurements as inputs to a radiative transfer model, we could directly compare measured and modelled reflectance at 850 nm.

## 5.2 Methods

Measurements of SSL density, specific surface area (SSA, total surface area of a material per unit of mass), spectral albedo and reflectance at 850 nm (NIRbox; see Section 5.2.3) were taken during the MOSAiC expedition [62] using techniques applied to the study of snowpits in winter [63]. We used the same suite of measurements for the SSL analysis as used for the snowpits in winter. This study is focused on the summer months, but as it represents a continuation of the winter measurements, we continue to use terminology such as snowpit. Between June and July 2020 (Leg 4), remnant coarse snow was adjacent to the ridges, but the ice level became snow-free, and only the SSL was present. For this study, we define the surface of melting sea ice as the origin ( $z = 0$ ). All of the measurements in this study were made within the Central Observatory of the expedition ice camp, a designated floe area close to the research vessel Polarstern [1], with a diameter of approximately 1 km and a mixture of level seasonal and level second-year ice. We focused this study on level ice and excluded ridged or heavily sedimented areas of the floe. These heavily sedimented areas were in noticeable patches with clean areas in between. Areas with impurities that were not visible were not influencing the absorption of the wavelength used in this study (850 nm). We chose the measurement locations on arrival at the floe, set up undisturbed areas and repeatedly measured the SSL at snowpit sites (location details in Figure 2.4). Additional measurements were made along transects to quantify spatial variability, which the dedicated undisturbed areas did not necessarily represent. The frequency of SSL measurements was weekly or twice a week. The X-ray micro-computed tomography ( $\mu$ -CT) samples and the reflectance measurements from the near-infrared camera (NIRbox) were collected as part of the "snowpit" dataset [63]. Measurements of spectral albedo using the ASD (optics-RB/LDL/Eco/Stern; Figure 2.4) were co-located both along part of the transects and at individual snowpits within the undisturbed areas ([220]; Figure 5.2c). Co-located samples were taken at the same time. However, due to the destructive sampling of the  $\mu$ -CT, the locations were not precisely aligned but side by side. Samples that were not co-located were taken at different times and areas within the Central Observatory.

### 5.2.1 Theory

The backscattering of near-infrared radiation depends on the SSA of snow and the SSL [221, 222]. At 850 nm wavelength, the microstructure of different snowpacks and SSL can be distinguished because the absorption of near-infrared radiation within the ice is higher than that of visible radiation within the ice [89]. As a result, 850 nm is sensitive to the SSL and the underlying DL, explaining why it is the optimal wavelength for this study and previous studies on snow microstructure [89]. Impurities at low concentrations do not influence the reflectance of snow/SSL in the near-infrared spectrum [221, 223]; therefore, we do not model impurities in this study. The radiative transfer equation is composed of scattering and absorption coefficients. We kept the absorption term constant by focusing on the 850 nm wavelength. We only varied the scattering term when we investigated how the geometrical input parameters influence albedo. These input parameters included the density, SSA and thickness calculated from each  $\mu$ -CT sample. Using 850 nm albedo as an output allowed for intercomparison between the measured (ASD and NIRbox) and modelled reflectance ( $\mu$ -CT/TARTES).



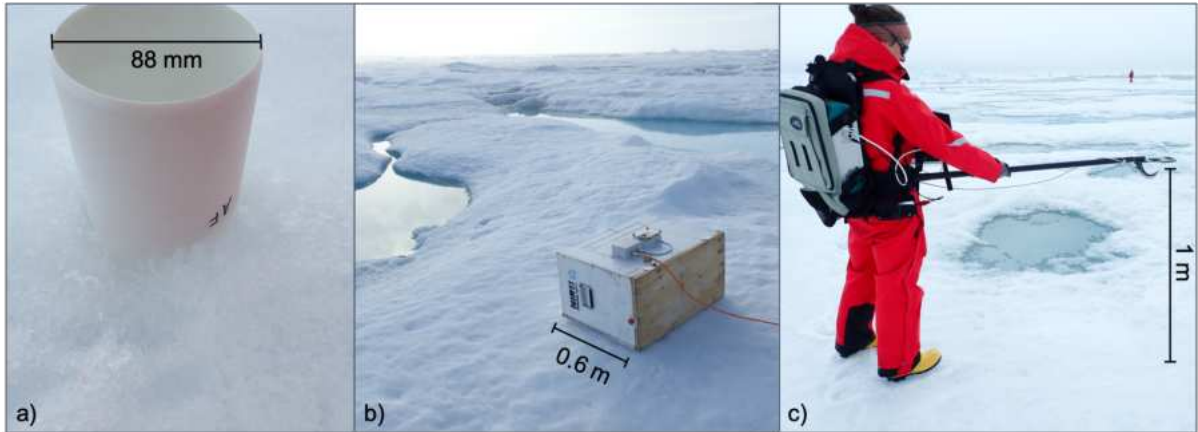


Figure 5.2: The three instruments used throughout the summer months of the MOSAiC expedition to document the geometric and optical properties of the surface scattering layer (SSL): a) an X-ray micro-computed tomography ( $\mu$ -CT) sample measuring the geometry; b) a novel, near-infrared instrument (NIRbox) pointing down to image the SSL at 850 nm; and c) an analytical spectral device (ASD) taking spectral albedo measurements of the SSL. Scale bars indicate the different footprints of each instrument ( $\mu$ -CT =  $5.03 \times 10^{-3} \text{ m}^2$ , ASD = approximately  $1.77 \text{ m}^2$ , NIRbox =  $0.12 \text{ m}^2$ ). Images from [69]

### 5.2.2 Microstructure measurements

Fifty-four cylindrical SSL samples of 55 to 80 mm in diameter and a height of 100 mm were collected in the field using a hollow drill bit (Figure 5.2a). This method allowed us to keep the microstructure intact while also sampling the underlying DL. To account for any microstructural damage at the edges of the samples, we analysed a sub-sample of volume commonly  $20 \times 20 \text{ mm}$  in width. A sub-sample volume is reconstructed in Figure 5.3. The samples were drained to the irreducible water content during extraction and transferred to a sample holder. The samples were immediately transported to a cold laboratory at  $-15^\circ\text{C}$  to prevent structural changes to the SSL before measuring it. The SSA was not affected when the sample was frozen, as any liquid water had percolated out of the sample. Freezing of the pore water was unlikely due to the melting state of the sea ice reflected in its large pore sizes. The average salinities of the samples in July were 0 ppm [63], and the average temperature at the time of sample collection in July was  $0.3^\circ\text{C}$  [63].

The microstructure of the SSL was measured on-site by installing a  $\mu$ -CT in the cold laboratory onboard the Polarstern and scanning the samples within 24 hours of collection. Micro-computed tomography is a 3-D imaging technique using X-rays to image cross-sections of an object and to reconstruct a 3-D model of that object [90]; in our case, an SSL sample. The  $-15^\circ\text{C}$  cold laboratory and an actively ventilated  $\mu$ -CT meant that the temperature inside the  $\mu$ -CT was consistently  $-12^\circ\text{C}$  during the scan. This consistency was due to the good ventilation system. The internal temperature of the  $\mu$ -CT was displayed during the scan and checked often. The samples were scanned, and using this sampling collection method, we could measure the microstructure to a resolution of  $26\text{--}42 \mu\text{m}$  in an approximate  $20 \times 20 \text{ mm}$  footprint, depending on the sample diameter. Because a sample maintains its microstructure at  $-12^\circ\text{C}$ , a second scan of the same sample would have shown no change. After scanning the samples and producing the 3-D model reconstruction, we segmented the voxels of ice and air within the 3-D structure and used the segmented images to calculate the geometrical parameters of the SSL. We used IPL Version 5.42 [90] to evaluate density, SSA, and optical equivalent diameter ( $d_{\text{eff}}$ ) using a

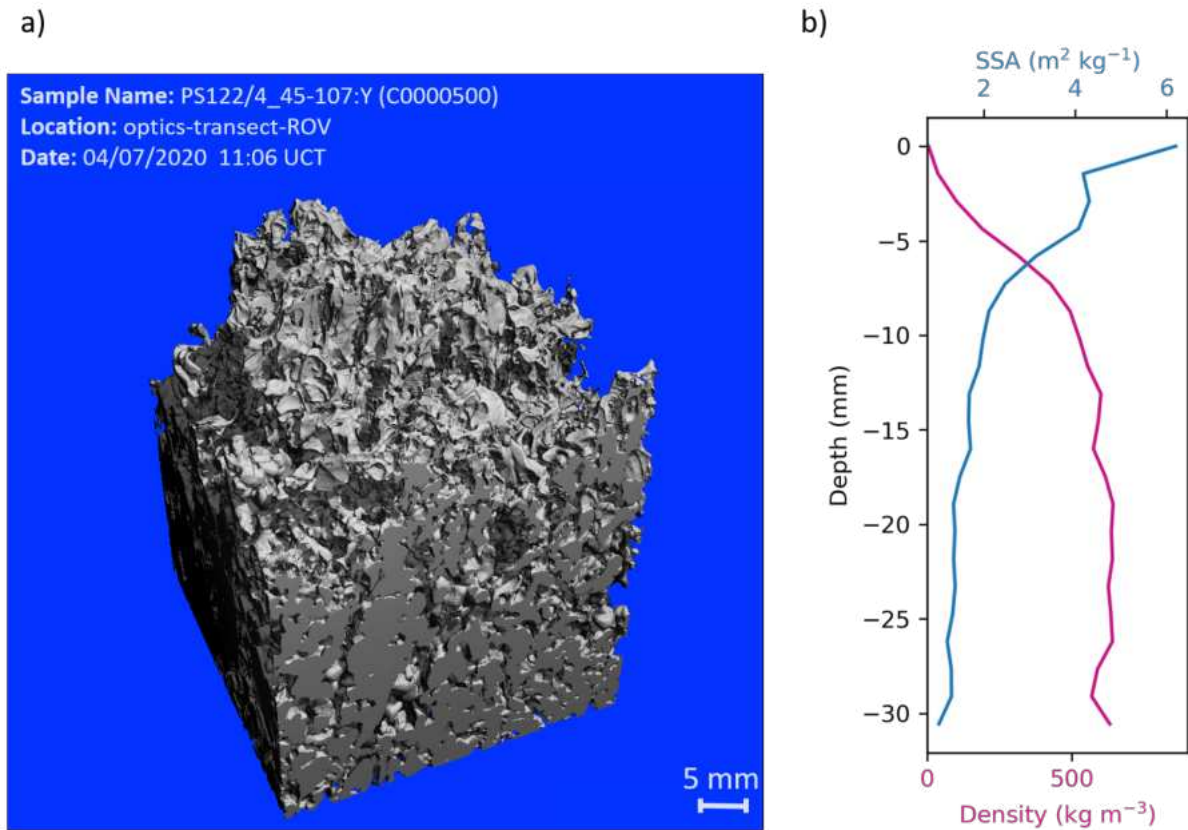


Figure 5.3: a) 3-D model reconstruction from a micro-computed tomography sample taken on July 4, 2020, at the Central Observatory optics-transect-ROV site. b) Profiles of the corresponding microstructural density and specific surface area (SSA).

triangulation-based estimate from the  $\mu$ -CT samples [224]. The term  $d_{\text{eff}}$  is the diameter of a sphere of equivalent volume to that of the irregular-shaped ice grains and was calculated as  $d_{\text{eff}} = \frac{6}{\rho_{\text{ice}} \text{SSA}}$ , where  $\rho_{\text{ice}}$  is the density of ice, and SSA has units of  $\text{mm}^{-1}$ . These three parameters were chosen, as the density and SSA or  $d_{\text{eff}}$  are necessary inputs into RTMs. SSA and  $d_{\text{eff}}$  can be used interchangeably due to their inverse relationship; for the rest of this manuscript, we focus on SSA. The amount of reflected and absorbed visible and near-infrared solar radiation depends strongly on the SSA, a parameter essential for remote sensing applications [225]. A typical sample is shown in Figure 5.3.

### 5.2.3 Reflectance measurements at 850 nm

Near-infrared photography is a method of determining the SSA of snow and the stratigraphy of alpine snowpacks [89]. The new NIRbox is a modification of the method developed by Matzl and Schneebeli (2006) [89] by artificially illuminating the surface with two LED lamps at 850 nm wavelength in a lightproof box (Figure 5.2b) and using a MAPIR camera (Survey3N MAPIR Camera: Near Infrared [88]) to image the snow surface. It is a low-cost, accurate measurement made at wavelengths relevant to microstructure. In this study, we used the NIRbox to measure the surface reflectance at 850 nm, obtaining 78 surface reflectance images of the SSL. We placed the lightproof box facing down on the ice surface so that the camera could capture the surface reflectance of the lights with no outside influence from incoming radiation, cloud cover, surface

inclination or azimuth angle due to its ease of use. This setup allowed the NIRbox to be used throughout the expedition during the polar day and night. For measurements taken during the polar day, a picture without the illumination of the lights inside the box was taken before each measurement and used as a reference to ensure that no external light was entering the box from the underlying ice or the edges of the box. The NIRbox images have a footprint of 0.12 m<sup>2</sup> and a resolution of 0.18 mm to capture the macro-scale variability of the surface microstructure. The TIFF images [69] were calibrated against targets with reflectances of 95 % and 50 % inside the box and corrected for inhomogeneous illumination. The camera was not monochrome and had RGB channels. The red channel was used for this study, but any RGB channel could have been chosen. The correction was done by dividing the image’s red channel by the normalized red channel of the reference plate image. The greyscale of this image was smoothed with a 2D Gaussian mask. From the smoothed image, the target reflectance values of 95 % and 50 % reflectance were identified. After selecting the targets manually and identifying the reflective values of the targets of known reflectance, images were calibrated by multiplying the corrected image by  $0.5\left(\frac{0.95}{\text{mean}(ref95)} + \frac{0.5}{\text{mean}(ref50)}\right)$ , where *ref95* and *ref50* are the reflectances of the 95 % and 50 % targets, respectively. These calibrated images were saved, and the mean surface reflectance of each NIRbox image (NIR<sub>850</sub>) was measured by averaging the reflectance of each pixel within a sub-volume. The sub-volume of these images excludes the frame and targets. These output images are an aggregation of the small-scale variability in reflectance in the images resulting from the microstructure. This study uses mean surface reflectance only. Figure 5.6 shows examples of the NIRbox images of the SSL alongside the histograms of the reflectance values.

Spectral albedo was measured using an Analytical Spectral Device FieldSpec3 spectroradiometer [220, 38]. We calculated the albedo using the incident-to-reflected flux ratio for wavelengths 350–2500 nm. This study focuses on the 850 nm wavelength to compare ASD and NIRbox reflectance. ASD albedo measurements have a footprint of approximately 1.77 m<sup>2</sup>. The measured reflectance of the ASD at 850 nm is represented by ASD<sub>850</sub>. More details about the ASD instrument, collection methods and quality control process can be found alongside the published dataset [220]. By comparing the two methods (NIR and ASD), we could test the novel NIRbox measurement device.

#### 5.2.4 Two-streAm Radiative TransfEr in Snow

Geometry (SSA, density, and layer thickness) from the  $\mu$ -CT SSL samples [66] were used as input into the Two-streAm Radiative TransfEr in Snow model (TARTES 1.0; [226, 227]). TARTES is based on the delta-Eddington approximation [228] and uses measured physical properties in a multi-layer snowpack to compute the spectral albedo and irradiance profiles. Instead of a multi-layered snowpack, we used the layered SSL and the DL, where each horizontal layer is assumed to have homogeneous physical characteristics. TARTES was chosen due to its ease of use and well-documented code. We tested different layer segmentation of the  $\mu$ -CT samples of the SSL to find the optimal layering. The layering setup ranged from one layer, three layers of equal thicknesses, weighted three layers with varying thicknesses, and five layers of equal thicknesses. Layers were weighted by taking the sum of the total SSA of the sample and dividing it by the required layers (for this study, three layers were chosen). This approach meant that each layer had equal sums of the SSA, as seen in Equation 5.1. The number of slices corresponding to a given layer is represented by *n* in Equations 5.1 and 5.2. The number of slices was multiplied by the slice height ( $\Delta z$ ) to give the height of each layer ( $h_{L1} = n_{L1}\Delta z$ ). Where *h* is the sample

height.

$$\frac{1}{3} \sum_{n=1}^{n_{\text{tot}}} \text{SSA}_{\text{tot}} = \sum_{n=1}^{n_{\text{L1}}} \text{SSA}_{\text{L1}} = \sum_{n=1}^{n_{\text{L2}}} \text{SSA}_{\text{L2}} = \sum_{n=1}^{n_{\text{L3}}} \text{SSA}_{\text{L3}} \quad (5.1)$$

$$h = n_{\text{tot}} \Delta z = n_{\text{L1}} \Delta z + n_{\text{L2}} \Delta z + n_{\text{L3}} \Delta z \quad (5.2)$$

This approach of weighting the layers ensured that if there were higher SSA values at the surface, we would use a smaller layer to avoid missing the details in the model, and the vertical distribution of the observed SSA would be better represented. We tested multiple layers and found that one layer produces a higher albedo than a weighted three-layer. A five-layered approach with equal layer thickness and a weighted three-layer approach had the same albedo values. For the remainder of this study, the weighted three-layer approach was used, as less computational power is needed to model fewer layers.

The DL is located beneath the SSL. Some samples included some underlying DL due to the drilling collection method. A density of  $700 \text{ kg m}^{-3}$  was applied to the samples as the cut-off between the SSL and the DL to account for the inconsistent inclusion of the DL in the samples. An artificial layer representing the DL was added beneath the model SSL layers. Details of this layer are given below. Although the SSL and DL are described and modelled as distinct layers in this study, the transition is likely gradual in reality, as mentioned by Smith et al. (2022) [201]. This transition could be better represented in a different model setup, as explained in the discussion. Different thicknesses of the DL were tested in the model at the start of this study. However, thicknesses beyond 300 mm had no influence on the output spectral albedo due to negligible transmission at 850 nm due to reflection at the surface and absorption in the DL. Therefore, the artificial DL layer in this study was 300 mm thick (to account for an approximate DL thickness relating to the freeboard of 2-m thick ice) and had an SSA of  $0.1 \text{ m}^2 \text{ kg}^{-1}$  and a density of  $700 \text{ kg m}^{-3}$ .  $\text{TARTES}_{850}$  represents the TARTES 850 nm output with a weighted three-layered microstructural input, an underlying artificial DL, and a subsurface albedo of 0.1. In the model, this subsurface is called "soil albedo".

An overestimation of radiative transfer models was also found by Dadic et al. (2013) [229] when using RTMs in Antarctic blue ice areas. The bias increased with increasing SSA. The possible reasons were summarised, and the asymmetry factor  $g$  in the model was found to be the most plausible answer [229]. Throughout this study, we used a spherical shape with an asymmetric factor,  $g = 0.895$ , and an absorption enhancement parameter,  $B = 1.25$ . These parameters are explained further in Libois et al. (2014) [227]. We conducted a test to understand the influence of changing the asymmetry factor on the TARTES model output. The input layers for this test were simply a three-layered input, where layer one was the average of all SSL profiles of 0–20 mm ( $0.02 \text{ m}$ ,  $332 \text{ kg m}^{-3}$ ,  $4.08 \text{ m}^2 \text{ kg}^{-1}$ ), layer two was the average of all profiles above 20 mm ( $0.05 \text{ m}$ ,  $578 \text{ kg m}^{-3}$ ,  $2.09 \text{ m}^2 \text{ kg}^{-1}$ ), and the third layer was the modelled DL ( $1 \text{ m}$ ,  $700 \text{ kg m}^{-3}$ ,  $0.1 \text{ m}^2 \text{ kg}^{-1}$ ) used earlier in this study.

## 5.3 Results

### 5.3.1 SSL microstructure

$\mu$ -CT microstructural measurements taken from the end of June through July within the MO-SAiC Central Observatory were used to understand the properties of the SSL. The stable oxygen isotope signal of the SSL on level ice and excluding ridged areas in July 2022 was  $-7.3\% \pm$

6.4‰ (one standard deviation,  $\sigma$ ; [73], indicating that we were measuring the SSL during this period and excluding melting snow. The SSL’s average stable oxygen isotope signal had a more negative value than ocean water. This result was expected, as we measured some second-year ice with possible re-frozen melted snow from the previous winter. The average winter snowpack had an average of  $-18.5 \text{ ‰} \pm 9.6 \text{ ‰} (\sigma)$ . Therefore, we were outside one deviation of the isotopic signal of snow. A typical SSL structure can be seen in Figure 5.3. We took this SSL sample on July 4, 2020, at the optics-transect-ROV site (location can be seen in Figure 2.4). The SSA is highest at the surface and decreases with depth. The pillar-looking structures are visible in Figure 5.3.

Common patterns can be seen in the SSL microstructure. Figure 5.4 shows all  $\mu$ -CT SSL profiles plotted for density, SSA and optically equivalent diameter ( $d_{\text{eff}}$ ). All profiles have a low (high) density and  $d_{\text{eff}}$  (SSA) at the surface, which increases (decreases) with depth. After a gradual density increase in the top 20 mm, the density is highly variable between samples; in the lower depths, it varies between 300 and 700  $\text{kg m}^{-3}$ . This pattern and variability are also seen when we plotted the depth where the density threshold (700  $\text{kg m}^{-3}$ ) was reached (left scatter plot in Figure 5.4). This scatter plot shows variability in the thickness of the samples ranging from 20 mm to 100 mm before the threshold is reached. The top 0–20 mm has a density of  $332 \pm 84 \text{ kg m}^{-3}$  ( $\sigma$ ,  $n = 51$ ). After 20 mm, the gradient of the density profile appears to reduce to an average density of  $579 \pm 109 \text{ kg m}^{-3}$  ( $\sigma$ ,  $n = 51$ ), which is the upper limit of the density of snow (Muskett, 2012). The SSA (middle) plot in Figure 5.4 also shows high variability at the surface, with an average SSA at 0–20 mm of  $4.08 \pm 1.18 \text{ m}^2 \text{ kg}^{-1}$  ( $\sigma$ ,  $n = 51$ ) and a reduction of the gradient below 20 mm, where the average SSA is  $2.09 \pm 0.68 \text{ m}^2 \text{ kg}^{-1}$  ( $\sigma$ ,  $n = 51$ ).

The microstructure (density, SSA, depth) of the SSL, determined from  $\mu$ -CT samples, showed no change over the time period of sample collection (Figure 5.5). The full sample was split into three layers to better understand the evolution of the structure over the time period; they were later used for the TARTES model input. Figure 5.5 shows that layer one has highly variable SSA and density, but their averages do not change over time. Values of the gradients of the layer two trendlines (provided in Figure 5.5) indicate that the depth of this layer increases by 0.16 mm per day, the density increases by 2  $\text{kg m}^{-3}$  per day, and the SSA decreases by 0.008  $\text{m}^2 \text{ kg}^{-1}$  per day. A unit root test was conducted to determine if the time series variable is non-stationary and possesses a unit root. This test, called the Augmented Dickey-Fuller (ADF) test [230], was performed on the dataset to determine how strongly the time series is defined by the trend. The null hypothesis is that this dataset is not stationary. The results of this test include the following ADF statistic for the layer two time series:  $-5.28$  (depth),  $-5.17$  (density),  $-4.45$  (SSA), with corresponding p-values of 0.000006 (depth), 0.00001 (density), 0.0002 (SSA). The critical values for layer two at 1 % are  $-3.58$  (depth),  $-3.58$  (density), and  $-3.58$  (SSA). The more negative the ADF statistic, the more likely to reject the null hypothesis. For all three parameter time series, the ADF statistic is less than the value at 1 %. This result suggests rejection of the null hypothesis with a significance level of less than 1 % (i.e., a low probability that the result is a statistical fluke). Rejecting the null hypothesis means that the process has no unit root, and in turn, all three time series are stationary and do not have a time-dependent structure. This lack of temporal variability can be seen in the low gradients of the trendlines (Figure 5.5). To conclude, we can confidently state that the microstructure shows no temporal change in layer two.

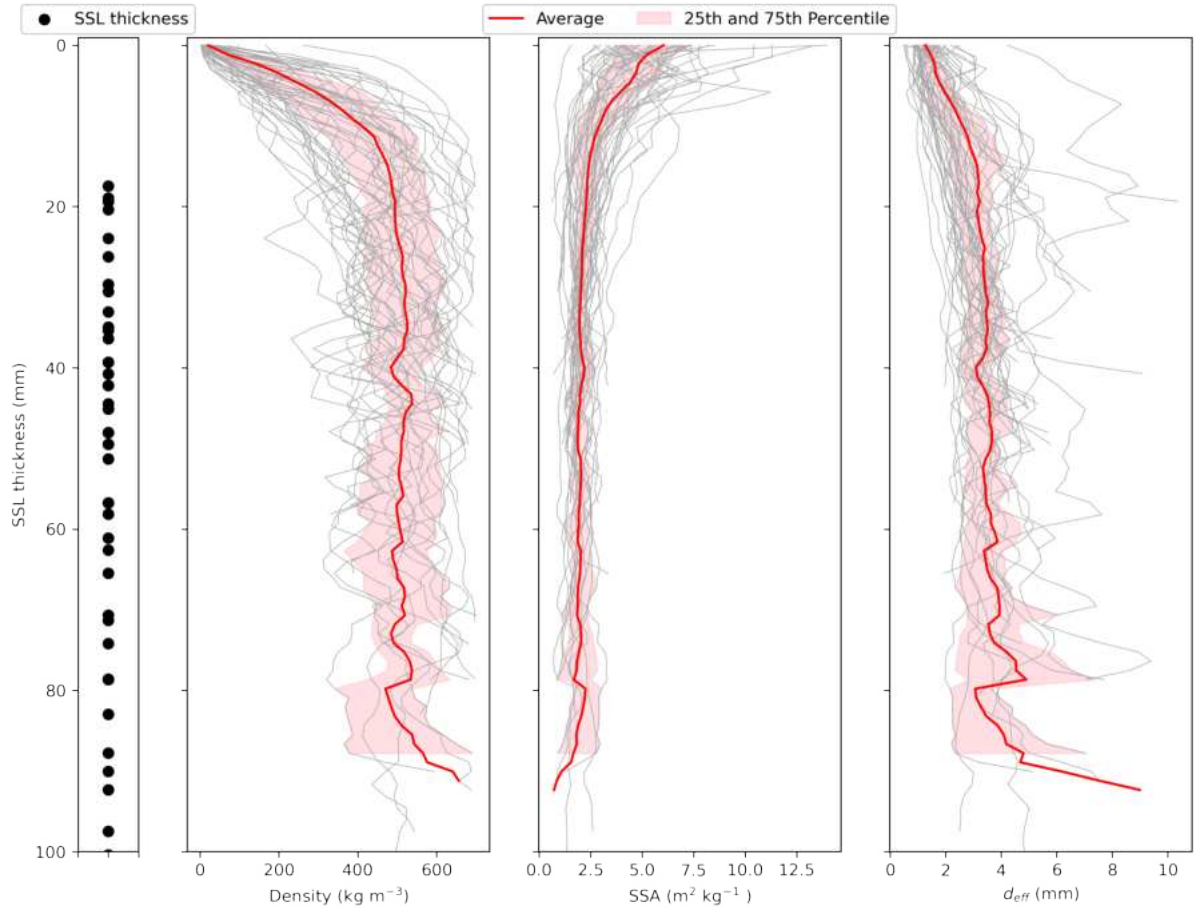


Figure 5.4: Profiles of density, specific surface area (SSA) and optically equivalent diameter ( $d_{\text{eff}}$ ) for individual micro-computed tomography samples of the surface scattering layer (SSL) taken in June and July are plotted in grey. The average profile (red line) and the 25th and 75th percentiles (red-shaded areas) are displayed for each parameter. A cut-off density threshold of  $700 \text{ kg m}^{-3}$  was applied to account for the inconsistent sampling of the underlying drained layer. The depths of the SSL after applying this threshold are plotted as black circles in the panel on the left.

### 5.3.2 SSL reflectance

Figure 5.6 shows examples of NIRbox images of  $0.12 \text{ m}^2$  areas, taken in July 2020, alongside histograms of the SSL surface reflectance. The mean  $\text{NIR}_{850}$  and one standard deviation ( $\sigma$ ) are displayed in the histograms. These images have been corrected for inhomogeneous illumination and calibrated against the targets, as described in the methods section. The images can be used to visualise the spatial distribution of the SSL on level ice within the CO and to give an indication of the spatial variability within the NIRbox footprint. However, for this study, the means of images are used later to compare to the ASD. In the figure, the images with darker spots caused by drainage channels within the ice can be seen to lower the average mean reflectance and increase the standard deviation.

The reflectance of the ice surface shows no temporal change over the time period shown in Figure 5.7a, which compares the daily mean and one standard deviation of all ASD spectral albedo ( $\text{ASD}_{850}$ ), and NIRbox measurements of the SSL at 850 nm ( $\text{NIR}_{850}$ ) in July 2020. The

error bars plotted with the  $\text{NIR}_{850}$  data points (one standard deviation of all the pixels in the NIRbox image) allow for a quantification of the spatial variability within the image. The  $\text{NIR}_{850}$  mean over this time period of  $0.60 \pm 0.04$  ( $\sigma$ ) is comparable to the  $\text{ASD}_{850}$  mean of  $0.63 \pm 0.09$  ( $\sigma$ ). The reflectance of the NIRbox images increases by 0.008 per day. As for Figure 5.5, the ADF unit root test was performed on this dataset to determine how strongly the time series is defined by the trend. The results for this test include the ADF statistic of  $-3.69$ , with a p-value of 0.004, and the critical value at 1 % of  $-3.47$ . Because the ADF statistic is less than the value at 1 %, we can reject the null hypothesis with a significance level of less than 1 % (i.e., a low probability that the result is a statistical fluke) and conclude that the time series does not have a time-dependent structure.

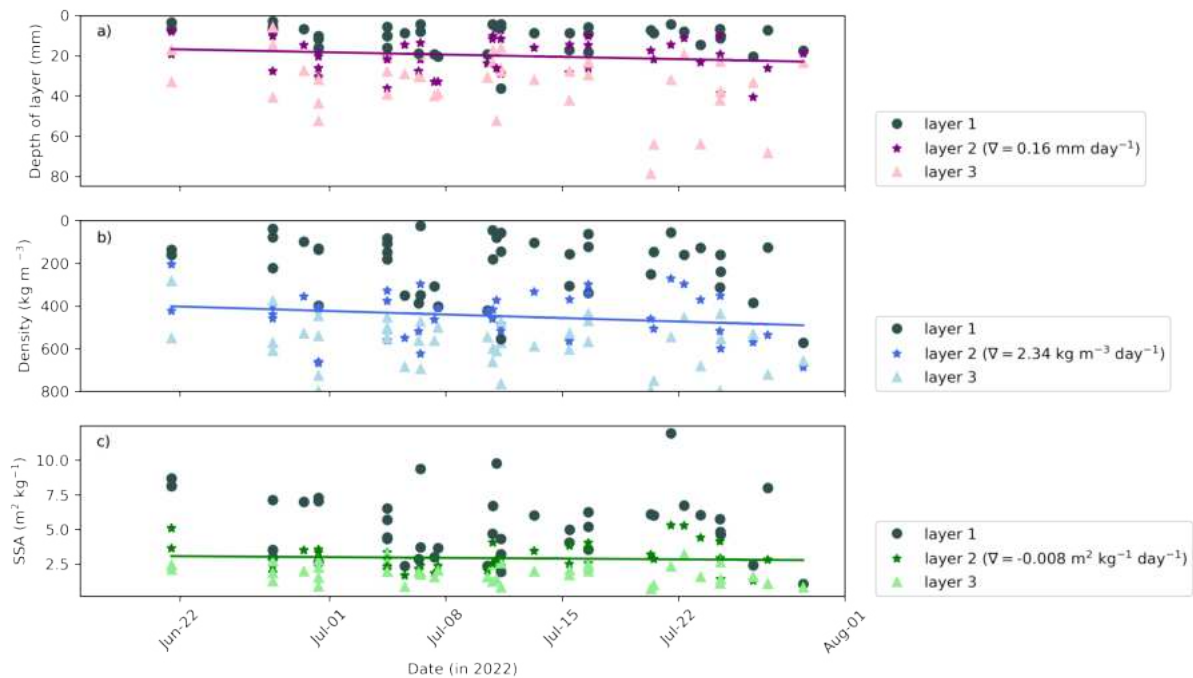


Figure 5.5: Individual micro-computed tomography samples of the surface scattering layer (SSL) were collected in the field. Once the profiles of density and specific surface area (SSA) were obtained for each sample, the sample profiles were separated into three weighted layers, as described in the methods section. For each layer, a) depth, b) density and c) SSA are plotted against the time the samples were collected. The lines of best fit are given for layer 2 in each panel. Gradients of these best-fit lines are indicated in the inset legends. The surface of melting sea ice is defined as the origin ( $z = 0$ ). Due to low density and high SSA at the surface of the SSL samples, the y-axis is inverted in (b) to better visualise the properties of the three layers.

Having returned to the same locations for measurements with the NIRbox allowed us to determine if there were any temporal changes in the  $\text{NIR}_{850}$  values for SSL reflectance. Figure 5.7b shows the same data as in Figure 5.7a but the data are grouped by location. The majority of locations showed no change during July 2020. However, the location designated Optics-LDL60 showed an increase in reflectance from 0.46 to 0.64 within 15 days. This increase could be due to drainage of surface water, although wetness was not measured in this study, or to changes in the microstructure.

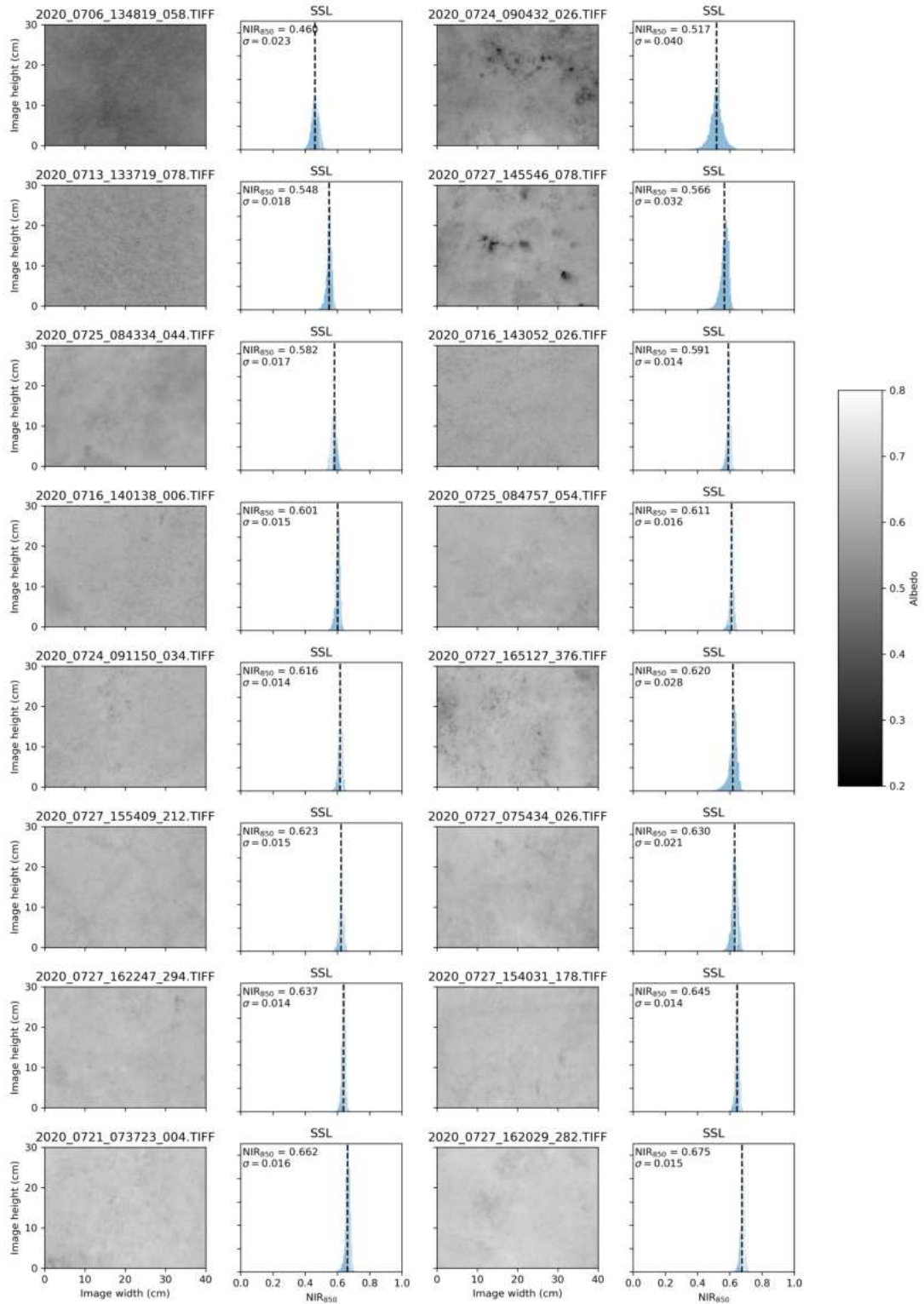


Figure 5.6: Spatial variability of the sea ice surface is shown in the near-infrared reflectance range at 850 nm ( $NIR_{850}$ ). All images were taken in July 2020 within the Central Observatory. The date of each image appears in the filename; e.g., "2020\_0713\_" is July 13, 2020. Histograms of the reflectances can be seen to the right of the NIRbox image.  $NIR_{850}$  and  $\sigma$  indicate the mean and standard deviation, respectively, of the reflectance of the area shown in the image (number of pixels =  $1700 \times 2250$ ). TIFF images are available in [69]



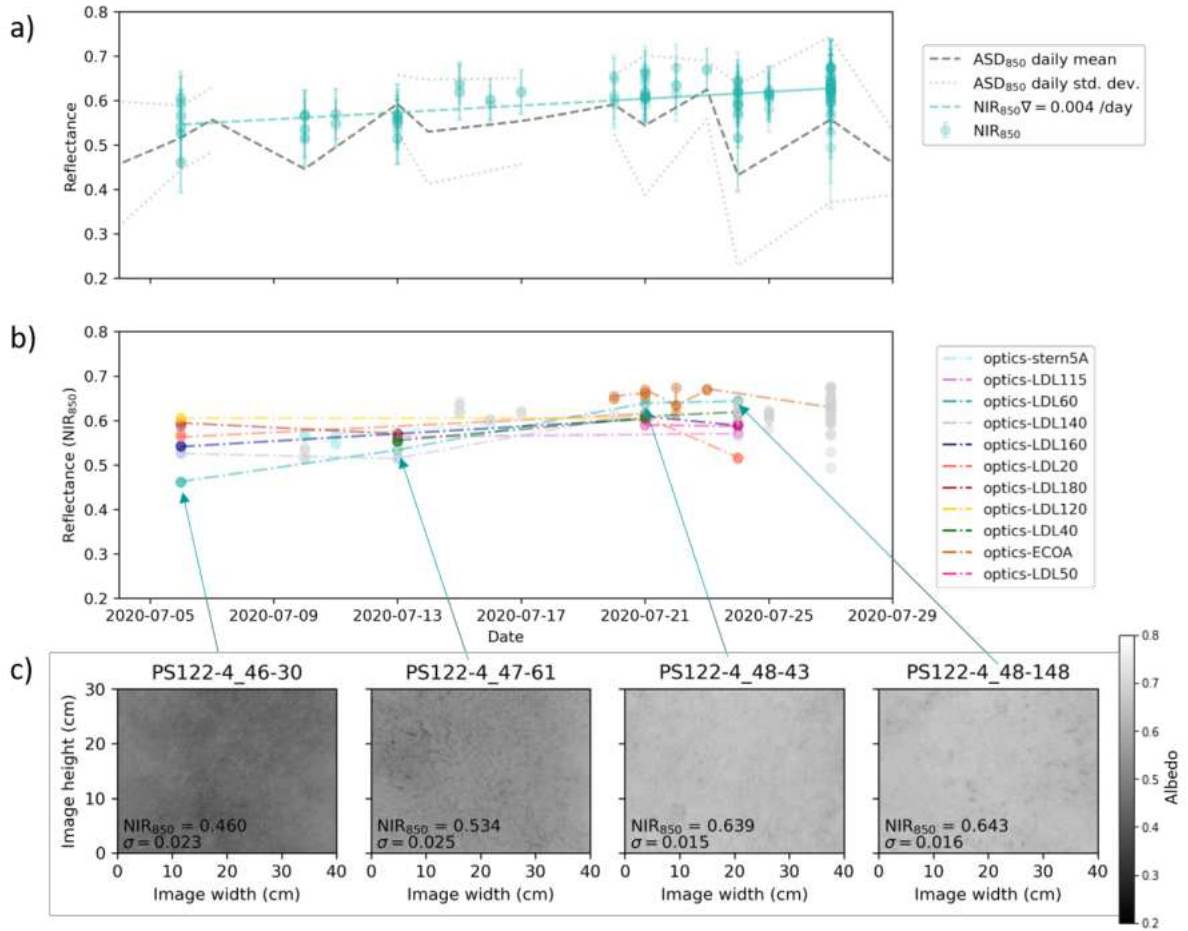


Figure 5.7: Reflectance measurements at 850 nm from the analytical spectral device ( $ASD_{850}$ ) and the NIRbox images ( $NIR_{850}$ ) over the month of July. In a), a time series of the mean ASD (dark grey line) with one standard deviation is indicated by the light grey lines plotted alongside the average reflectance of the NIRbox image pixel values. The  $ASD_{850}$  daily mean does not show a continuous line, as the spectral albedo was not measured every day. Error bars plotted with the  $NIR_{850}$  data points are one standard deviation of all the pixels in the NIRbox image. All of these measurements were taken in the Central Observatory on a mixture of second-year and seasonal ice. The NIRbox and ASD were often measured in the same location; however, this figure also includes measurements that were not co-located. In b), the time series of these NIRbox images for the month of July are grouped by location. Each colour shown in the inset legend indicates a unique location with lines connecting measurements at the same location. Grey points indicate one-off measurements that are not part of a time series. In c), a collection of four NIRbox images is shown from Optics-LDL60, the location in b) showing the largest increase in reflectance over the period. The dates in 2020 (and file names) of the images, left to right, are July 6 (2020\_0706\_134819\_058.TIFF), July 13 (2020\_0713\_131206\_016.TIFF), July 21 (2020\_0721\_140144\_094.TIFF) and July 24 (2020\_0724\_091952\_054.TIFF). These TIFF images are available in [74].

Figure 5.8 displays this increase in reflectance in more detail. The NIRbox images in Figure 5.8a are co-located with the  $\mu$ -CT samples shown in Figure 5.8c, where the images appear to become more pillared over time. The SSA and density profiles shown in Figure 5.8b are almost identical for each sample, implying that simple density and SSA profiles are not documenting the visually changing microstructure seen in Figure 5.8c. Figure 5.8d is discussed at the end of the results section.

The correlation between the microstructure and the reflectivity at 850 nm is visualised in Figure 5.9a and 5.9b. The relationship between the average SSA (Figure 5.9a) and SSA multiplied by density (Figure 5.9b) of different layers of the  $\mu$ -CT sample and the co-located NIR<sub>850</sub> measurement was plotted. The  $r^2$  value for each layer was calculated to identify the layers of higher interest, i.e., those with the higher  $r^2$  values and the top 0–20 mm with a very low  $r^2$  value.

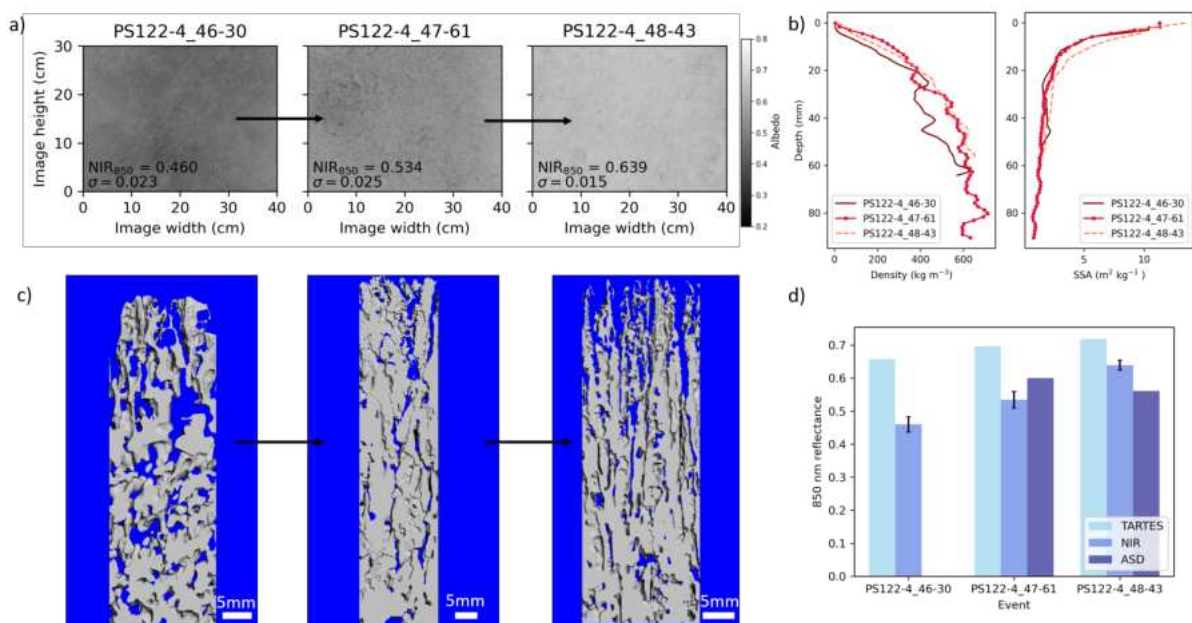


Figure 5.8: This figure is to aid in visualising the influence of microstructure on the NIR<sub>850</sub> reflectance at the sampling location designated optics-LDL (see Figure 5.7b). The panels show: a) the first three NIRbox images (as shown in Figure 5.7c) taken on the 2020 dates (and file names) of July 6 (2020\_0706\_134819\_058.TIFF), July 13 (2020\_0713\_131206\_016.TIFF), and July 21 (2020\_0721\_140144\_094.TIFF); b) the almost identical co-located density and specific surface area (SSA) profiles of the three microcomputer tomograph ( $\mu$ -CT) samples; c) visualisation of the three  $\mu$ -CT samples; and d) comparison of the three types of reflectance measurements, TARTES<sub>850</sub> from the  $\mu$ -CT samples, NIR<sub>850</sub> from the NIRbox images, and ASD<sub>850</sub> from the analytical spectral device at 850 nm.

Figure 5.10a shows probability density functions (PDFs) of the complete datasets of NIR<sub>850</sub>, ASD<sub>850</sub> and TARTES<sub>850</sub> and for the co-located samples only (Figure 5.10b). The "NIR<sub>850</sub> All" has a mode of 0.596, comparable to the "ASD<sub>850</sub> All" mode at 0.597. This close similarity indicates that the NIRbox is a reliable instrument to measure reflectance at 850 nm and can be used to better understand the spatial and temporal variability of sea ice. The "TARTES<sub>850</sub> All" mode is 0.69, which is the first indication of the overestimation of the RTM model. An Anderson-Darling normality test was conducted to determine if the data samples had a Gaussian distribution. The NIR<sub>850</sub> and ASD<sub>850</sub> co-located data samples were Gaussian at the 1–15 %

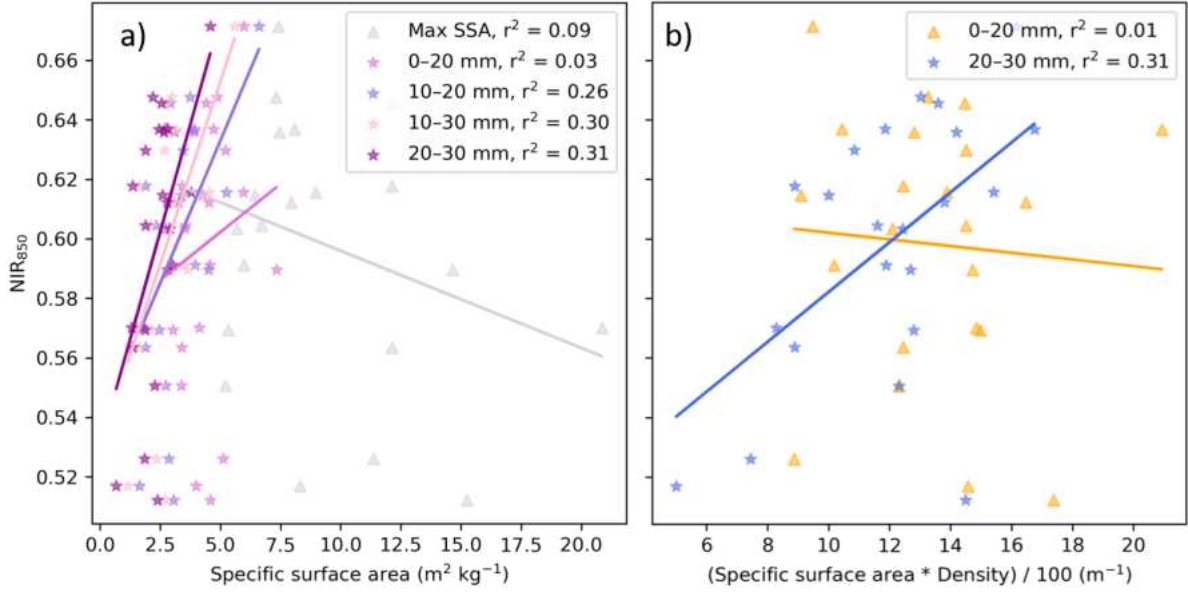


Figure 5.9: Having acquired co-located NIRbox images and micro-computed tomography ( $\mu$ -CT) samples allowed us to compare the microstructural parameters of the surface scattering layer (SSL) to the reflectance of the SSL at 850 nm. The  $\mu$ -CT samples were divided into 10 to 50 mm layers and tested for the highest  $r^2$  value in relation to the corresponding NIR<sub>850</sub> value; the layers of higher interest are plotted here. In a), the average specific surface area (SSA) of the layers is plotted against co-located NIR<sub>850</sub> values, with layer depth and  $r^2$  value provided in the inset legend. The maximum SSA (max SSA) measured for the sample was often at the surface. In b), the same samples are shown as in a), but the SSA and density have been multiplied to show the combined relationship of these two parameters with the reflectance at 850 nm.

level. The TARTES<sub>850</sub> co-located data samples were Gaussian at the 1–5 % level. The range of each dataset is 0.71 for "ASD<sub>850</sub> All", 0.16 for "NIR<sub>850</sub> All", and 0.27 for "TARTES<sub>850</sub> All". The spread of values in the "ASD<sub>850</sub> All" dataset could be due to a wrongly classified surface (we tried to analyse only ASD measurements indicated as SSL samples, but misclassifications may have been likely) or external influences on the spectral albedo, such as changes in azimuth angle or influence from adjacent surfaces (e.g., neighbouring melt ponds). Working through each ASD measurement and its corresponding overview image would have helped to understand these lower values; however, that objective was not the focus of this study. Our focus here is on the co-located datasets (Figures 5.10b and 5.11).

Figure 5.11 compares all co-located samples of NIR<sub>850</sub> and ASD<sub>850</sub> against TARTES<sub>850</sub>. The overestimation of TARTES<sub>850</sub> values is apparent, with all the points lying below the 1:1 line. The difference in albedo values of the co-located ASD<sub>850</sub> (mean = 0.58;  $\sigma^2$  = 0.003, n = 7), NIR<sub>850</sub> (mean = 0.60;  $\sigma^2$  = 0.002, n = 7) and TARTES<sub>850</sub> datasets (mean = 0.66;  $\sigma^2$  = 0.004, n = 4) was not significant for ASD<sub>850</sub> NIR<sub>850</sub> (t (16) = 0.5; p > 0.05). However, it was significant for NIR<sub>850</sub> TARTES<sub>850</sub> (t (32) = 0.001; p < 0.05) and ASD<sub>850</sub> TARTES<sub>850</sub> (t (24) = 0.003; p < 0.05).  $\sigma^2$  represents variance, t (16) represents the t-test (assuming unequal variances) value with 16 degrees of freedom, and 0.05 is the significance level. If the p-value is less than the significance level, the hypothesis that the two means of the two datasets are equal can be rejected.

Returning to Figure 5.8, which shows three different visits to one snowpit site. The overes-

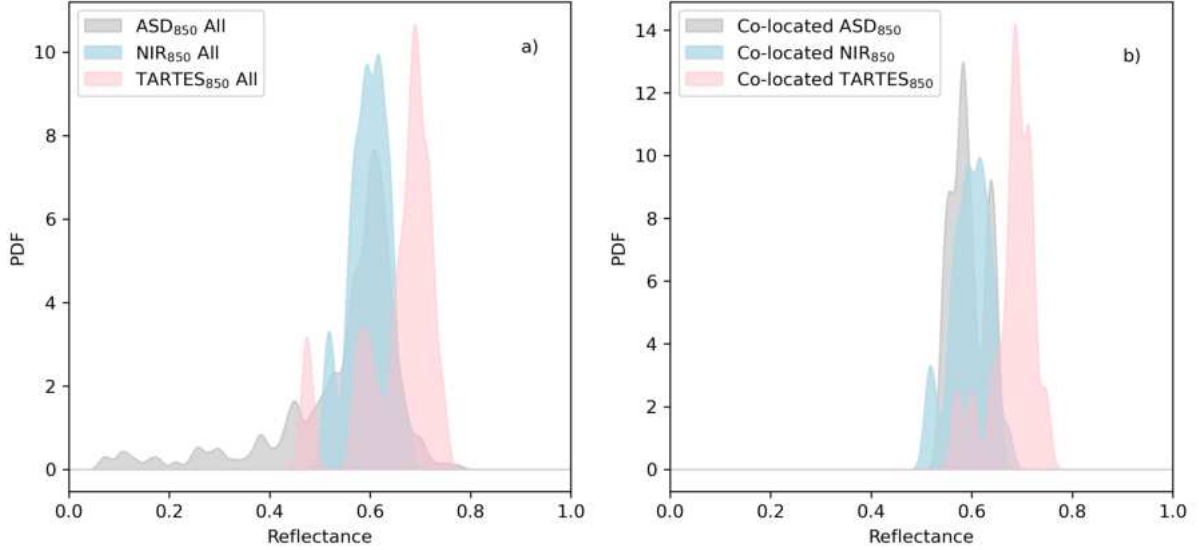


Figure 5.10: This figure compares colour-coded datasets from the three methods used to determine reflectance at 850 nm: near-infrared imaging from the NIRbox (NIR<sub>850</sub>), data from the analytical spectral device (ASD<sub>850</sub>), and micro-computed tomography data input to a radiative transfer model (TARTES<sub>850</sub>). In a), all measurements throughout July and the beginning of August are shown for ASD<sub>850</sub>, NIR<sub>850</sub> and TARTES<sub>850</sub>. In b), only co-located measurements are shown when the three instruments were deployed simultaneously in the same place.

timination of the TARTES/ $\mu$ -CT approach with respect to the NIRbox image and the ASD can be seen (Figure 5.8d). The TARTES<sub>850</sub> values show an increasing trend similar to the NIR<sub>850</sub> values. However, for the three snowpit site visits, TARTES overestimates by 0.20, 0.16 and 0.08, respectively. The TARTES<sub>850</sub> value does not lie within one standard deviation of the NIR values (indicated by the black error bars in Figure 5.8d).

The TARTES overestimation is significant, as seen in the p-test values (given above). A test was conducted to understand the influence of changing the asymmetry factor on the TARTES model output. Figure 5.12 shows the output of this test at different wavelengths. At 850 nm, the resulting albedo was 0.783 for a cube ( $g = 0.77$ ,  $B = 1.56$ ) and 0.696 for a sphere. Therefore, the results would increase in albedo if a different asymmetry factor was used, indicating that another factor within the model causes the overestimation.

## 5.4 Discussion

Previous studies on the reflective properties of the melting sea ice surface did not include the influence of SSL geometry on the albedo due to a lack of measurements. This study is the first to measure the micro- and macrostructure of the SSL and establish the link between the SSL microstructure and reflectance at 850 nm. In the  $\mu$ -CT measurements, we observed a coarse and porous structure with a small SSA at the surface that increases with depth. Figure 5.4 shows that density was highly variable between all samples and at the surface of the SSA profiles in the top layer, where it ranged between 5 and 10 m<sup>2</sup> kg<sup>-1</sup>. In the lower layers, the SSA profiles are more consistent between samples. In the surface layer (layer one), SSA was highly variable, with a thickness varying around 10–20 mm. However, due to the low density of layer one, its influence on the optical properties is minimal, as light can penetrate deeper layers.

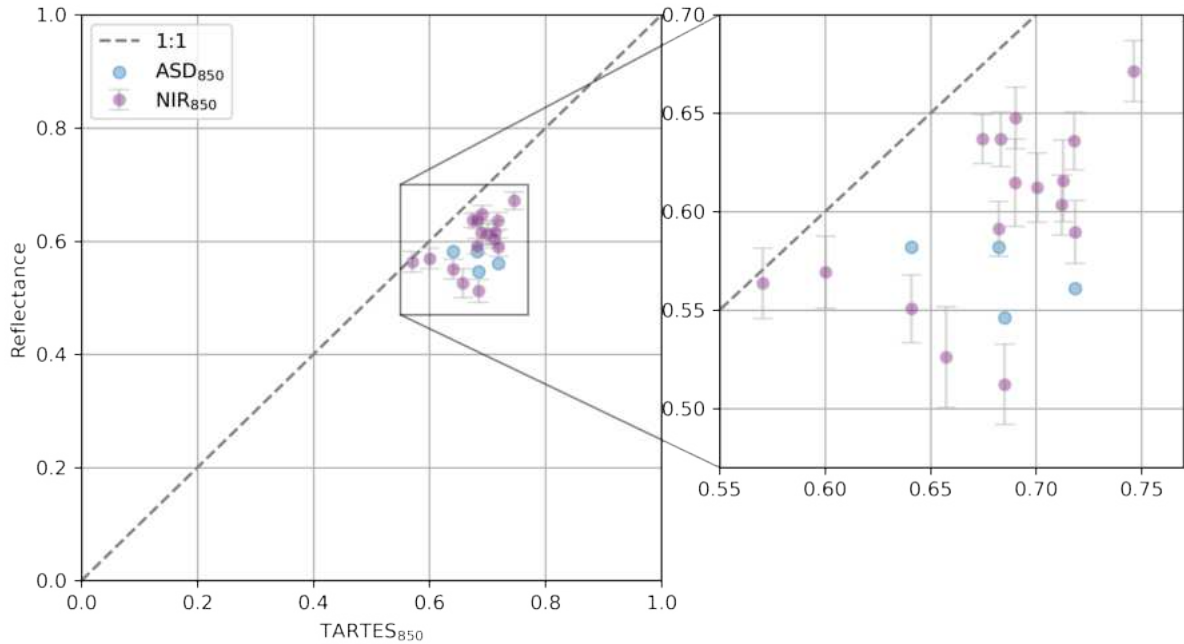


Figure 5.11: This figure shows the reflectance at 850 nm, calculated from the micro-computed tomography data input to a radiative transfer model (TARTES<sub>850</sub>), compared to measurements of reflectivity by near-infrared imaging from the NIRbox (NIR<sub>850</sub>) and by the analytical spectral device (ASD<sub>850</sub>). It uses the same data as the co-located measurements in Figure 5.10b. The NIR<sub>850</sub> error bars represent one standard deviation of the NIRbox image pixel values. The dark grey line denotes the 1:1 line.

Unlike wet snow metamorphism, which coarsens with age [231], the SSL did not coarsen, maintaining its density and SSA in the lower layers throughout the melt season. This lack of coarsening and consistency in the density and SSA is due to the different processes. In contrast to coarsening and porosity reduction when snow undergoes melt, the SSL acts in the opposite direction: the porosity increases as it goes from a solid ice structure to a porous SSL. As a result of surface ablation and the DL becoming more porous as it melts preferentially at the grain boundaries, the SSL regenerates and maintains a consistent microstructural profile throughout the melt season. In the time series in Figure 5.5, the gradient of the density and SSA line of best fit for layer two does not vary temporally over the study period. As mentioned in the introduction, the sea ice extent at the end of summer 2020 was the second lowest in the satellite record [194], and the melt season lasted more than a month longer than usual [25]. In this study, we found that the SSL remained constant over time. Therefore, a longer melt season does not influence the SSL microstructure. We can conclude that this study represents the typical optical and microstructural properties of the surface scattering layer in the high Arctic on first and second-year level ice.

Figure 5.6 shows examples of NIR<sub>850</sub> from NIRbox images which, when compared against ASD<sub>850</sub> in Figure 5.7, remained within one standard deviation of the ASD<sub>850</sub> daily mean. This close correspondence indicates that the new NIRbox measurement technique can accurately measure surface reflectance at 850 nm. This novel method is not influenced by incoming radiation, cloud cover, surface inclination or azimuth angle, which may influence the ASD measurements. Reference images taken prior to each measurement show no influence from external light.

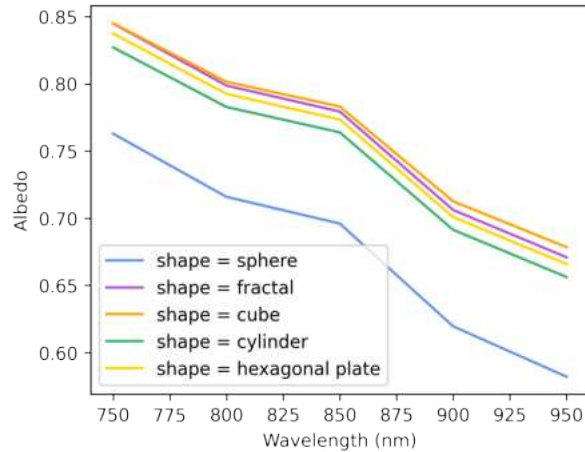


Figure 5.12: This figure shows the results of a test of the influence of different asymmetric factors ( $g$ ) and absorption enhancement parameters ( $B$ ) on output from the radiative transfer model (TARTES) with data input from micro-computed tomography. The different shapes in the inset legend represent different combinations of  $g$  and  $B$ . A two-layer surface scattering layer structure and a drained layer were inputs for this test. The density and specific surface area were taken from the average of all profiles in this study (see more information in the methods section). For this study, the 850 nm wavelength is of interest.

After confirming that the NIRbox is a reliable instrument to assess the albedo of the ice surface at 850 nm, we used the  $NIR_{850}$  values to investigate the spatial and temporal variability of the SSL reflectance at 850 nm. Figure 5.6 shows the large spatial variability in the month of July. The  $NIR_{850}$  values show a minimum of 0.46 and a maximum of 0.675. At this wavelength, the spatial variability in the optical properties could be a result of the microstructure. We are aware that the microstructure of the SSL plays a significant role in the optical properties and reflectance of the surface [37]. In the rest of this study, we tried to understand how the microstructure influences optical properties through investigations of co-located measurements and radiative transfer modelling.

Most locations had little to no change in reflectivity over the period examined. However, one location showed a consistent increase in reflectivity. Figure 5.7 shows a time series grouped by location, with the NIRbox images at this specific location (opticsLDL) showing a consistent increase in reflectivity (Figure 5.7c). Figure 5.8 provides more measurement detail at opticsLDL: the microstructure is observed to change visually and become more pillared, but the density and SSA profiles remain largely unchanged (Figure 5.8c). These results imply that another optical analysis is needed, not based on the density and SSA of spheres used in TARTES. The microstructure in the third image in Figure 5.8c is likely to have more internal scattering compared to the first two microstructures. In an attempt to understand the influence of the microstructural properties on the reflectance values and to see if a specific depth range influences the overall reflectance, we conducted a layered study on all the co-located samples, visualised in Figure 5.9. The results show a low correlation of the average SSA of the upper layers (0–20 mm) of the  $\mu$ -CT sample to the  $NIR_{850}$  values and a higher correlation to the lower layers (10–30 mm, with the highest  $r^2$  value of 0.31). They imply that lower layers affect overall reflectance more than surface layers, but the low  $r^2$  values of all trends in Figure 5.9 mean that all layers have an important effect. The low density and pillared structure combined with an  $r^2$  value of 0.09 at the surface indicates that the underlying layer of the SSL below 20 mm is more relevant for the reflectance.

Aware that the microstructure is influencing the reflectance at 850 nm, we then assessed directly, by introducing an RTM (TARTES), how the models represent these changes in microstructure and the influence on the optical properties. By comparing the three measurement approaches, we searched for any discrepancies between them. The probability density functions in Figure 5.10 introduce TARTES and compare the reflectance of the SSL on level ice for NIR<sub>850</sub>, ASD<sub>850</sub> and TARTES<sub>850</sub>. Figure 5.10a compares the reflectance for all measurements on Leg 4. Figure 5.10b shows the co-located measurements, representing the same dataset as Figure 5.11. The comparable mean values of the NIR<sub>850</sub> and ASD<sub>850</sub> are another indication that the NIRbox is a reliable instrument to assess the albedo of the ice surface at 850 nm. We conclude that the NIRbox is an excellent way to get information that can be used to determine the SSA of the SSL. However, the t-test results show significant differences in the mean of the TARTES<sub>850</sub> dataset compared to ASD<sub>850</sub> and NIR<sub>850</sub>. We find that using the microstructure (density, SSA and layer thickness) as an input into the TARTES RTM produces a 10–15 % overestimation of the reflectance at 850 nm. This overestimation was not due to the asymmetry factor, as tested in Figure 5.11, as changing this factor increased the output and did not explain the overestimation. Alternative reasons for the overestimation could be:

- a) The footprints differ between the three measurement techniques ( $\mu$ -CT =  $5.03 \times 10^{-3} \text{ m}^2$ , ASD approximately  $1.77 \text{ m}^2$ , and NIRbox =  $0.12 \text{ m}^2$ ). The NIRbox and the ASD include more spatial variability in the measurements. As seen in Figure 5.6, there are darker patches that increase the standard deviation of the NIR<sub>850</sub> pixel values. The  $\mu$ -CT sample size may be too small to capture the meter scale spatial variability, and these darker patches would not be sampled. However, this scaling problem would not influence all co-located measurement points, as many NIR<sub>850</sub> images did not include the dark patches seen in Figure 5.6. The different footprints between techniques are thus likely to explain a few of the underestimated values but not the general underestimation of the TARTES model.
- b) In TARTES, we are averaging the extremely intricate and complex aspects of microstructure. The NIR<sub>850</sub> image and the  $\mu$ -CT-image clearly show vertical air gaps with a width of many wavelengths and depth of several millimeters to centimeters (Figure 5.3). Such a geometry resembles a scaled-down vegetation canopy structure [232]. The low density and pillared structure at the surface before averaging into layers means that the underlying layer two is more relevant for the reflectance. However, when we average this structure into layers, we increase the density, decrease the SSA at the very surface in layer one and produce an artificial grain size in a homogeneous layer. This averaging may thus result in an overestimation of the reflectance as less radiation penetrates to the lower depths of the SSL, compared to a pillared structure with a low density at the surface and vertical air gaps. We suggest that this structure is too complex to average into layers. An RTM assuming horizontally homogeneous layers, as used in this study, cannot account for the pillared microstructure and is not appropriate for this type of structure. This microstructure complexity is also visible in Figure 5.8, where the microstructure changes visibly, but the density and SSA profiles remain the same, indicating that a different analysis is needed. Future work could benefit from using either a ray tracing approach, instead of explicitly solving the RT equation, or a more appropriate RTM, possibly based on a stochastic Beer-Lambert-Bouguer law commonly used for vegetation canopy structures (as represented in Figure ~3 of Shabanov and Gastellu-Etchegorry, 2018 [232]) to better represent the intricate structures on melting sea ice.

The physical and optical properties of the melting sea ice surface are influenced by preferen-

tial melt at the grain boundaries. We observed a large spatial variability in the microstructure of the sea ice surface, with different surface types both in the field and in our measurements. The SSL is just one of many categories of surface structures appearing on melting sea ice. We found that spatial variability of the microstructure of the sea ice surface is high when ice has different histories or freezing processes, which leads to an array of surface melt patterns and structures caused by the ice having different grain boundaries. These different surface types provide an extensive range of reflectance values. In previous studies, the surface of sea ice was categorised as ponded or bare ice/SSL. We support the idea that the spatial variability of sea ice needs to be incorporated when modelling the microstructure and reflectance of the sea ice surface. We propose that ice surface history, expressed in the macrostructure, is a key parameter to understanding the microstructural spatial variability of the ice. However, macrostructure was not the focus of this study, and we used only level ice with no previous ridging, ponding or freezing history that would have created different grain boundaries. We focused on level ice with a homogeneous SSL. A future study, beyond the scope of this one, could profitably investigate the influence of freeboard on microstructure and reflectance.

## 5.5 Conclusion

For the first time, this paper shows measurements of the SSL microstructure and its relation to optical properties in the near-infrared wavelength of 850 nm. By co-locating microstructural measurements with reflectance measurements, we could better understand the SSL temporal and spatial variability. The findings are as follows:

- The average SSL profile consisted of a vertical pillared structure with a high average SSA of  $4.08 \pm 1.18 \text{ m}^2 \text{ kg}^{-1}$  ( $\sigma$ ) and a low density of  $332 \pm 84 \text{ kg m}^{-3}$  ( $\sigma$ ) at the surface. We observed consistent patterns in the microstructure profile across spatial and temporal sampling. Most of the variability was focused in the top 0–20 mm (Figure 5.2). This variability in the microstructure introduced spatial variability in the optical properties of the melting sea ice.
- Unlike snow, where wet snow metamorphism causes a coarsening of grains and albedo decreases with age, the SSL regenerated and maintained its microstructure over the season. The SSL low density and pillared structure observed at the surface mean that the underlying layer below 20 mm is more relevant for reflectance. The microstructure below 20 mm was consistent through the melt season, and, at most locations, no temporal variability was observed in the optical properties of the SSL. We obtained a distribution of melting sea ice reflectance and concluded that temporal evolution was small. We do not have a multimodal distribution (in Figure 5.10) that would have resulted from different ice ages or changes in the freeboard. The influence of these parameters was smaller than the standard deviation of all samples and within the limits of the observed distribution. The melt rate may have varied, but the SSL always regenerated in the same manner. Future large-scale changes in the surface reflectance of the sea ice cannot be ascribed to a changing SSL. Therefore, future work could benefit from a focus on the melt pond fraction, ridges and changes in melt pond optical properties.
- The new NIRbox method was shown to be a low-cost, easy-to-use method for measuring reflectance at wavelengths sensitive to snow and SSL microstructure. In this study, the NIRbox was used to measure the surface reflectance at 850 nm without any influence from incoming radiation (as shown through the reference images taken at each event),



cloud cover, surface inclination or azimuth angle. The NIRbox contributes considerable knowledge to research on the surface reflectance of sea ice and can be used to answer critical questions on the variability of albedo.

- For the first time, we calculated albedo using  $\mu$ -CT-derived SSA, thickness, and density in the TARTES model. We observed a 10–15 % overestimation when using this approach. Reasons for the overestimation could include: a) insufficient sample size to represent the microstructure, as spatial variability at the meter scale is important for the two in situ optical measurements, or b) insufficient model representation in TARTES (which uses the Mie solution to Maxwell’s equation). TARTES does not consider anisotropy and estimates the structure as spheres in discrete layers. We calculated geometrical anisotropy for the samples, but this parameter is not useful when calculating optical properties. Full structural anisotropy and star volume would be interesting geometrical measures to make in a future study. Future work could benefit from using either a ray tracing approach instead of explicitly solving the RT equation or a more appropriate RTM. This RTM could be based on a stochastic Beer-Lambert-Bouguer law, which considers anisotropy and is commonly used for vegetation canopy structures (as represented in Figure ~3 in Shabanov and Gastellu-Etchegorry, 2018 [232]), to better represent the intricate structures on melting sea ice.

# Synthesis

---

This thesis investigated three components of the Arctic sea ice energy balance and presents the first analysis of a library of in situ ground-based measurements of snow’s physical and isotopic properties and the SSL on sea ice in the high Arctic. We conducted a complete annual overview of the major processes occurring in the snow and SSL on sea ice in the summer and winter. Throughout the thesis, we have outlined how snow is an integral part of the entire sea-ice energy balance and how its microstructure and physical properties influence energy exchange from the Arctic sea ice to the atmosphere. Chapter 3 focused on the snow properties in winter, investigating thermal conductivity and resistance concerning spatial heterogeneity and temporal changes. We were able to give the average thermal resistance of different landscape features to better model sea ice growth. Chapter 4 studied the influence of extreme temperature gradients on the sublimation of the sea ice surface causing ocean-sourced snow. We identified a significant source of uncertainty in precipitation estimates due to the sublimation of the sea ice surface. Finally, Chapter 5 investigated the summer melting sea ice surface properties and the relationship between the SSL’s microstructural properties and its influence on the albedo. We found an overestimation when using the three-layered microstructure as an input for radiative transfer modelling to determine albedo. As a result, we suggested alternative approaches for future tests. The synthesis of these chapters, the detailed conclusions and the importance of each chapter in the Arctic sea ice system are outlined below.

## 6.1 Conclusions, implications and future work

Using measurements of snow microstructure on different ice types and topographic features on Arctic sea ice for a seven-month winter period in the high Arctic, we evaluated for the first time the seasonal evolution and spatial heterogeneity of the snow’s thermal conductivity and thermal resistance. We assessed the current thermal conductivity parametrisations and their performance for the range of possible snow and firn densities. We present two new parametrisations, with and without anisotropy, which have implications for future studies to optimise the modelling of ice growth in the high-Arctic winter. Field measurements highlighted the need for a high sampling density to represent spatial heterogeneity of the snow’s thermal conductivity in the Arctic sea ice system. The average thermal conductivity of all snow micro-penetrator measurements collected throughout winter in this study was  $0.25 \pm 0.05 \text{ W K}^{-1} \text{ m}^{-1}$  for snow on sea ice. This indicates that  $0.32 \pm 0.01 \text{ W K}^{-1} \text{ m}^{-1}$ , currently used in sea ice modelling, vastly overestimates thermal conductivity. Future work needs to test the sensitivity of large-scale sea ice models to lower thermal conductivity values as input. By studying the temporal variability, we infer and quantify (from three independent density measurements) an increase in the snow’s density up to March and a decrease after that. We propose four processes which could result

in density reduction and future work is needed to decipher which process is dominant. This density trend projected the thermal conductivity on first-year and second-year ice before the melt period started. Since a similar non-monotonic behaviour is extracted for the snow depth, the thermal resistance of snow on level sea ice remains constant. We found approximately three times higher thermal resistance on ridges, with extremely high spatial heterogeneity due to snow depth. We conclude that ridged and level areas must be treated separately in modelling heat flux in the central Arctic. High spatial variability of thermal resistance is apparent, but temporal changes in the snow cover are minimal during this period.

Sublimation of the sea ice surface is the dominant process affecting the isotopic signature of snow on sea ice. It creates a mix of atmospheric and ocean-sourced snow (originating from the sublimation of the sea ice surface). This new understanding explains the negative d-excess values reaching as low as  $-30\text{ ‰}$  in combination with saline samples. The sublimation of approximately 17 mm (ice thickness equivalent) of the sea ice surface results in saline snow and mineral deposition in the snowpack. 58 % of samples taken in this study between January and May 2020 are electrically conductive (in melted form), and most of these samples taken on level ice have a negative d-excess value. Using two independent calculations, we estimate that 50–54 mm of snow on sea ice is ocean-sourced (approximately 28 % of the snowpack). These findings have wide-reaching implications in sea ice research, from identifying uncertainties in: a) precipitation estimates, when comparisons are made to in situ SWE measurements, b) the heat transfer through the ice and snow, as the highly-conductive ice is replaced by highly-insulating snow, and c) the chemical composition of snow on sea ice, through a better understanding of the source of sea salt aerosols and the contribution of a snowpack molecular iodine source to Arctic ozone destruction. This new understanding and the suggestion to include vapour fluxes in larger sea ice models have the opportunity to reduce significant uncertainties in this field.

For the first time, this paper presents measurements of the SSL microstructure and its relation to optical properties in the near-infrared wavelength of 850 nm. We could better understand the SSL temporal and spatial variability by co-locating microstructural and reflectance measurements. We found that the average SSL profile consisted of a vertical pillared structure with a high(low) average SSA(density) at the surface. We observed consistent patterns in the microstructure profile across spatial and temporal sampling. Most of the variability was focused in the top 1–20 mm. Unlike snow, where wet snow metamorphism causes a coarsening of grains and albedo decreases with age, the SSL regenerated and maintained its microstructure over the season. Future large-scale changes in the surface reflectance of the sea ice cannot be ascribed to a changing SSL. Therefore, future work could focus on the melt pond fraction, ridges and changes in melt pond optical properties. We introduced a new measurement method to measure the reflectance of the SSL: the NIRbox method was shown to be a low-cost, easy-to-use method for measuring reflectance at wavelengths sensitive to snow and SSL microstructure. In this study, the NIRbox operates at 850 nm without any influence from incoming radiation (as shown through the reference images taken at each event), cloud cover, surface inclination or azimuth angle. The NIRbox contributes considerable knowledge to research on the surface reflectance of sea ice and can be used to answer critical questions on albedo variability. For the first time, we calculated the albedo of the SSL using  $\mu$ -CT-derived SSA, thickness, and density in the TARTES model. We observed a 10–15 % overestimation when using this approach. We concluded that this overestimation could be a result of a) insufficient sample size to represent the microstructure, as spatial variability at the meter scale is essential for the two in situ optical measurements, or b) insufficient model representation in TARTES (which uses the Mie solution to Maxwell’s equation). TARTES does not consider anisotropy and estimates the structure as spheres in discrete layers. Future work could benefit from using either a ray

tracing approach instead of explicitly solving the radiative transfer equation or a more appropriate radiative transfer model. This radiative transfer model could be based on a stochastic Beer-Lambert-Bouguer law, which considers anisotropy and is commonly used for vegetation canopy structures and is likely better to represent the intricate structures of melting sea ice.

## 6.2 Temporal synthesis of chapters

By studying the annual evolution of the sea ice landscape from winter to summer, we have investigated temporal changes in the snow and the surface scattering layer (SSL). One significant temporal synthesis is the transformation of the SSL (Chapter 5) into the remnant surface scattering layer (R-SSL), visualised in Figure 6.1. As the summer ice experiences re-freeze and the SSL is covered by fresh snowfall, the first-year ice (that has survived summer) transitions into multi-year ice. Snowpits on this multi-year ice reveal the R-SSL at the sea ice-snow interface. It is important to stress that this is only a feature on multi-year ice. This R-SSL has an extremely high density compared to the other strata in the winter snowpack and, as a result, influences the heat flux through the snowpack. In Chapter 3, we investigated the thermal conductivity properties of the snow cover. Our high-density measurements show that we occasionally included an R-SSL with a higher thermal conductivity than the rest of the snowpack. This temporal evolution links Chapter 3 to Chapter 5. This synthesis is annotated on the right in Figure 6.1.

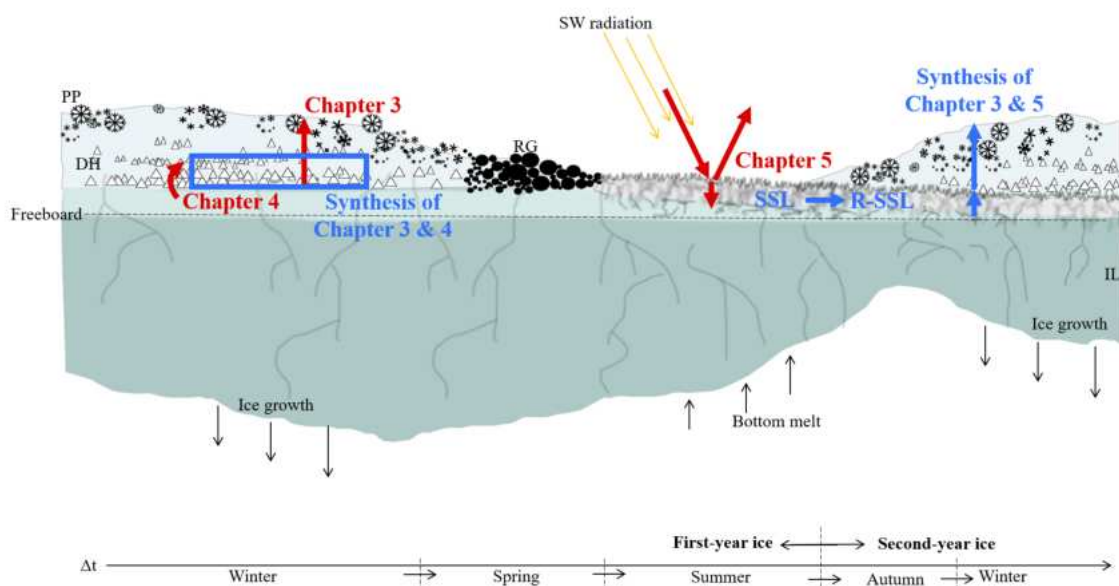


Figure 6.1: A schematic to summarise the synthesis of the three major chapters included in this thesis. The temporal connection between the chapters is shown through the transition from a first-year ice floe in winter to a second-year ice floe after surviving a summer melt season. The acronyms are PP = precipitation particles, DH = depth hoar, RG = rounded grains, SSL = Surface scattering layer, R-SSL = remnant surface scattering layer, DL = drained layer, IL = interior layer, and SW radiation = shortwave radiation. This is adapted from Figure 1.7 and is not drawn to scale.

This temporal evolution and the R-SSL, shown in the schematic in Figure 6.1, is not only a heat flux uncertainty, as explained above, but also a source of uncertainty for ground-based snow thickness measurements. The density of this layer lies between sea ice and extremely

hard snow, so we need to decide whether this should be included in measurements as it will have an influence on calculations of heat transfer and mass balance in the Arctic. In addition, we have identified a possible source of underestimation of snow thickness compared to in situ precipitation measurements in Chapter 4 due to the snow originating from the sublimating sea ice. These two sources of snow thickness uncertainties synthesise chapters 4 and 5. Methods to measure snow thickness in situ (e.g. magnaprobe and SMP: predominantly penetrometers) have a new uncertainty as we are unsure if the R-SSL is being measured. The density and penetration of the R-SSL change depending on the season and the metamorphism conditions. This is explained in Chapter 3 and shown in Figure 3.7 by a heatmap of the density profile obtained from penetration resistance; at lower relative depths (in the snow above the sea ice surface), we see that the resistance changes throughout the year, and we hypothesise that this could be a result of including or excluding the R-SSL in the measurement. This would influence comparisons of the precipitation snow estimates to the ground-measured snow thickness.

### 6.3 Spatial synthesis of chapters

Spatial heterogeneity is also a central element of this thesis. All chapters investigate the spatial heterogeneity of the snow/SSL microstructural parameters of interest and the influence on the energy budget component. An example is the spatial heterogeneity of the thermal conductivity and thermal resistance in Chapter 3, which is visualised in Figure 3.5. The spatial heterogeneity of the density of the snow cover results in thermal resistance variability. The consequence is a changing heat flux change through the snow and the sea ice surface's sublimation rate, resulting in more or less ocean snow formation (Chapter 4). In addition, the high rate of sublimation of the sea ice surface and extreme metamorphism in the snow is also a crucial driver of the microstructural properties of the snow directly above the sea ice interface. As a result, we often find low-density, highly anisotropic depth hoar at the snow-sea ice interface (originating from sea ice). The depth hoar's high anisotropy influences the snow cover's thermal conductivity. We introduce anisotropy and density parameterisation in Chapter 3 and show how snow's textural properties (density and anisotropy) influence thermal conductivity. Hence the synthesis of the extreme metamorphism explained in Chapter 4, and thermal conductivity (Chapter 3).

In summary, this thesis advances our understanding of the role of snow in this complex system and identifies primary sources of uncertainties in our regional and global models. The uncertainties highlighted in this thesis need further investigation to improve our understanding of their importance in the sea ice system. Future work should be to i) test lower thermal conductivity values of snow in mass balance modelling, ii) test the influence of including vapour fluxes into sea ice models to understand the precipitation uncertainty introduced above, iii) test alternative radiative transfer models to represent the albedo of the SSL better, or use a ray tracing approach instead of explicitly solving the radiative transfer equation.

# Publications

---

Publications used for this doctoral thesis:

**Chapter 2:** Macfarlane, A. R., Schneebeli, M., Dadic, R., Tavri, A., Immerz, A., Polashenski, C., Krampe, D., Clemens-Sewall, D., Wagner, D. N., Perovich, D. K., Henna-Reetta, H., Raphael, I., Matero, I., Regnery, J., Smith, M. M., Nicolaus, M., Jaggi, M., Oggier, M., Webster, M. A., Lehning, M., Kolabutin, N., Itkin, P., Naderpour, R., Pirazzini, R., Hämmerle, S., Arndt, S., and Fons, S. (2023). A Database of Snow on Sea Ice in the Central Arctic: Collected during the MOSAiC expedition, [Data paper]. *Scientific Data*.

**Chapter 3:** Macfarlane, A. R., Löwe, H., Gimenes, L., Wagner, D. N., Dadic, R., Ottersberg, R., Hämmerle, S., and Schneebeli, M., (2023). Thermal Conductivity of Snow on Arctic Sea Ice, *EGUsphere* [preprint], DOI: <https://doi.org/10.5194/egusphere-2023-83>.

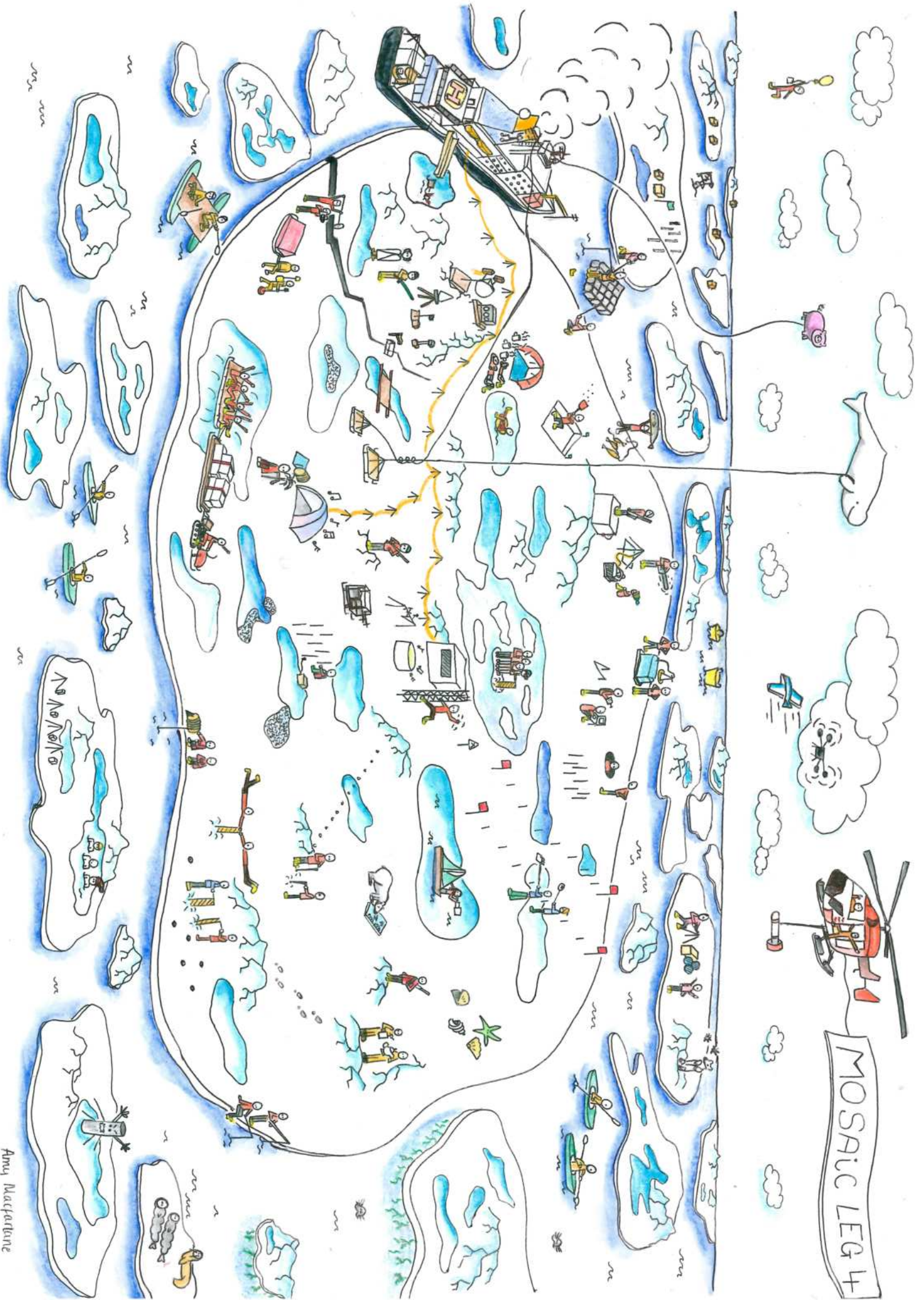
**Chapter 4:** Macfarlane, A. R., Mellat, M., Meyer, H., Werner, M., Brunello, C. F., Arndt, S., Wagner, D. N., Jaggi, M., Krampe, D., Dadic, R., and Schneebeli, M. Ocean sourced snow on Arctic sea ice. *In preparation for submission to Nature Geoscience*.

**Chapter 5:** Macfarlane, A. R., Dadic, R., Smith, M. M., Light, B., Nicolaus, M., Henna-Reetta, H., Webster, M., Linhardt, F., Hämmerle, S., and Schneebeli, M., (2023). Evolution of the microstructure and reflectance of the surface scattering layer on melting, level Arctic sea ice. *Elementa: Science of the Anthropocene* 11(1). DOI: <https://doi.org/10.1525/elementa.2022.00103>.

Additional publications:

**A.1:** Macfarlane, A. R., Ben-Ari, T., Blanc, G., Bozzato, D., Calmer, R., Haslett, S., Holste, S., Jardé, E., Rixen, C., Ruché, D., Schneebeli, M., Smith, M. M., Thielke, L., Vandavelde, S., and Wheeler, H. C. A call for funding bodies to influence the reduction of environmental impacts in scientific fieldwork [Comment Article]. *Submitted to Science*.

Macfarlane, A. R., Smith, M. M., Thielke, L., Calmer, R., and Mohaupt, V. The MOSAiC expedition environmental impact assessment. [Environmental Impact Assessment] *In preparation for submission to Nature Sustainability*.



MOSAIC LEG 4

# Responsible fieldwork

---

Macfarlane, A. R., Ben-Ari, T., Blanc, G., Bozzato, D., Calmer, R., Haslett, S., Holste, S., Jardé, E., Rixen, C., Ruché, D., Schneebeli, M., Smith, M. M., Thielke, L., Vandavelde, S., and Wheeler, H. C.

Submitted to: Science.

## Introduction

A vital component of this thesis was fieldwork, which required working in a sensitive environment, far away from research laboratories. As the Earth's average temperature rises and IPCC reports warn of the consequences of climate change [3], scientists are driven to understand the implications of these changes better and improve the monitoring and modelling of these regions. This requires ground-truth measurements, which are key drivers of regional and global models. Policymakers are highly dependent on these models for accurate predictions. As a result, scientists have the responsibility to conduct fieldwork in these environments, which has become a paradox for a number of researchers. This is due to the environmental cost of this work and many researchers believe a focus should be on conducting this fieldwork in a responsible manner. We avoid using the phrase "sustainable science" in this context as this implies that the only requirement for scientific practices is that it is maintained at a certain rate or level. In contrast, we believe scientists should feel the obligation to minimize their environmental footprint, hence "responsible science" is preferred. Scientists often experience the problem of filtering their data and samples to prevent measuring their anthropogenic signal. In this direction, it is often in their interest to reduce the environmental impact of their work. Recent large-scale expeditions have led to increased awareness of the environmental costs of this research and the need to think about less impactful fieldwork. This chapter highlights the steps that funding agencies could take to reduce anthropogenic impacts with high environmental pollution whilst suggesting steps to assess and improve fieldwork practices.

## A.1 A call for funding bodies to influence the reduction of environmental impacts in scientific fieldwork

There is a growing consensus in the scientific community that there is a need to reduce the environmental impacts of scientific research, including the observations conducted in the field [233]. Scientists conduct fieldwork in various disciplines (natural, human and social sciences). Without fieldwork, there is no primary data to build knowledge for these disciplines. Even



though fieldwork is fundamental for research, more and more scientists are gaining awareness of the problems associated with the environmental footprint of their work. Still, they need more effective resources or adequate incentives to assess or reduce it. Researchers' initiatives to quantify, understand and reduce their environmental footprint are growing rapidly in research labs (see, for example, the French Labos 1point5 initiative born in 2019 [234]), but these initiatives are carried by the research staff themselves without a framework by the funders. There is a need for the rapid construction of appropriate incentives by funders to implement mitigation measures. The nature of scientific fieldwork often requires working in sensitive environments, far away from the scientists' research laboratories, to understand the changes in the natural environment. Science needs to start prioritizing the reduction of the scientific impact of such fieldwork. This article is a direct call for international, national and local funding bodies to expand their considerations in funding decisions and support researchers in reducing the impact of science on sensitive environments. We propose that this can be achieved in three steps: a) by requiring environmental impact assessments in the initial grant proposal and considering the relative scientific and environmental impact as well as the adequacy of mitigation measures as additional criteria in funding decisions, b) by giving researchers the means to finance these measures (e.g. finance the train which can be more expensive than the plane, finance better quality equipment with a longer life-use expectancy, etc.), and c) by following up on the status of the project after the fieldwork and evaluating the impact assessment. Regular surveys of the impact of the specific expeditions will further enhance our knowledge and improve the implementation of best practices in the field.

Gathering knowledge and data to improve our global understanding, whatever the research domain, is the first objective of any fieldwork. The quality of science and research should not be compromised. Nonetheless, new practices that do not affect science, such as those listed above, should be considered. Including an impact assessment in funding applications and taking this assessment into account in funding decisions will bring more attention to reducing the deleterious impact of science on the environment. Such impact assessments should also support local governments in assessing and reducing environmental impacts. Indeed, in some regions, some Indigenous organizations already require environmental risk assessments through their permitting process [235]. These initiatives from local governance (to support mechanisms to evaluate and examine environmental impacts locally) should be supported by funding agencies and not overlooked regarding these issues. In this effort of environmental commitment, it is essential to ensure that no top-down decision is imposed from outside the communities they affect. The methodology and tools for such impact assessments need to be open source, free and standardized across disciplines for it to be possible to compare different proposals. Choosing which projects to fund requires considering that low-impact research can be less competitive (often taking more time, sometimes collecting fewer data but optimizing their use) than high-impact research. However, prioritizing a project with a more considerable relative reduction of the environmental impact over a project which has not attempted to reduce impact will encourage projects to implement scientific best practices to reduce their impact in fieldwork. Projects are more likely to invest in research and development to improve the sustainability of instruments through the design and use of biodegradable materials. It will allow funding agencies to compare the emissions from various projects, promote low environmental impact initiatives, and likely increase the funding of existing dataset analysis. By implementing impact assessments, funding agencies will consequently be able to base funding decisions on both scientific and environmental impact and abandon projects with too high of an environmental impact.

Of course, all funding cannot go towards reductions of the environmental footprint of projects. Indeed, taking the train rather than the plane or buying reusable, higher quality,

longer life-expectancy equipment incurs substantial costs. Therefore, we propose that funding agencies establish a double counting of projects with an "environmental cost accounting" parallel to "financial accounting". Thus, a virtuous project that reduces its environmental impact (decreasing its debit balance in the "environmental accounting") would see its financial credit increase, making it possible to finance these reductions. Another option could be to release an additional financial envelope for environmentally sustainable projects. By giving researchers the means to fund their environmental impact reductions in the field, funding agencies will thus be able to encourage and take an active part in transforming research to make it more sustainable.

The funding agencies should conduct a post-funding calculation of the environmental footprint weighted by the primary scientific outcomes prioritized by each agency. This would prevent additional reporting burdens to the scientists and streamline the process by having one individual at funding agencies who is an expert assessing the impact of funded projects. Alternatively, one could develop an understandable and easy-to-use open-source software for the researchers to conduct this analysis. Following up and making this assessment after the grant completion could have two benefits: 1) it will give the opportunity to provide feedback on if the impact value was feasible/achievable and allow for projects to provide recommendations to future expeditions/campaigns, and 2) it encourages scientists to refine their research to maximize the scientific return for each unit of environmental impact. This encourages interdisciplinary science and science of opportunity and will optimize networking and collaborations of groups working on similar datasets in similar areas. It will encourage optimising time in the field by collecting/measuring for multiple teams, involving more projects, and consequently having a more significant scientific impact.

More consistent quantification of fieldwork impacts will ultimately allow for evaluation of the impacts and critical areas for improvement on a community scale. We hope that funding agencies will play a key role in pushing for quantifying environmental impact analysis before the field work and, ultimately, the requirement to make improvements in critical areas. But it also requires providing financial means to the researchers committed to this effort.

The purpose of research funding agencies is to support research. Today there is a unique opportunity to be part of a historic and necessary shift by supporting all those researchers calling for a transformation of research, by changing the evaluation and funding criteria based on more quality rather than quantity, towards more ethics, more meaning and more sustainability.



# Bibliography

- [1] Rainer Knust. Polar research and supply vessel POLARSTERN operated by the Alfred-Wegener-Institute. *Journal of large-scale research facilities JLSRF*, 3:A119–A119, 2017.
- [2] Uwe Nixdorf, Klaus Dethloff, Markus Rex, Matthew Shupe, Anja Sommerfeld, Donald K Perovich, Marcel Nicolaus, Céline Heuzé, Benjamin Rabe, Brice Loose, et al. MOSAiC extended acknowledgement. 2021.
- [3] M Meredith, M Sommerkorn, S Cassotta, C Derksen, A Ekaykin, A Hollowed, G Kofinas, A Mackintosh, J Melbourne-Thomas, MMC Muelbert, et al. Chapter 3: polar regions. *IPCC special report on the ocean and cryosphere in a changing climate*, 5, 2019.
- [4] Julienne C Stroeve, Vladimir Kattsov, Andrew Barrett, Mark Serreze, Tatiana Pavlova, Marika Holland, and Walter N Meier. Trends in arctic sea ice extent from cmip5, cmip3 and observations. *Geophysical Research Letters*, 39(16), 2012.
- [5] Jennifer E Kay, Marika M Holland, and Alexandra Jahn. Inter-annual to multi-decadal arctic sea ice extent trends in a warming world. *Geophysical Research Letters*, 38(15), 2011.
- [6] Ron Kwok, G Spreen, and S Pang. Arctic sea ice circulation and drift speed: Decadal trends and ocean currents. *Journal of Geophysical Research: Oceans*, 118(5):2408–2425, 2013.
- [7] James Maslanik, Julienne Stroeve, Charles Fowler, and William Emery. Distribution and trends in arctic sea ice age through spring 2011. *Geophysical Research Letters*, 38(13), 2011.
- [8] Gordon FN Cox and Wilford F Weeks. Salinity variations in sea ice. *Journal of Glaciology*, 13(67):109–120, 1974.
- [9] Pierre Rampal, Jérôme Weiss, and David Marsan. Positive trend in the mean speed and deformation rate of arctic sea ice, 1979–2007. *Journal of Geophysical Research: Oceans*, 114(C5), 2009.
- [10] Kristin L Laidre, Harry Stern, Kit M Kovacs, Lloyd Lowry, Sue E Moore, Eric V Regehr, Steven H Ferguson, Øystein Wiig, Peter Boveng, Robyn P Angliss, et al. Arctic marine mammal population status, sea ice habitat loss, and conservation recommendations for the 21st century. *Conservation Biology*, 29(3):724–737, 2015.
- [11] Timo Vihma. Effects of arctic sea ice decline on weather and climate: A review. *Surveys in Geophysics*, 35:1175–1214, 2014.
- [12] Mary-Louise Timmermans and John Marshall. Understanding arctic ocean circulation: A review of ocean dynamics in a changing climate. *Journal of Geophysical Research: Oceans*, 125(4):e2018JC014378, 2020.

- [13] Martin Vancoppenolle, Klaus M Meiners, Christine Michel, Laurent Bopp, Frédéric Brabant, Gauthier Carnat, Bruno Delille, Delphine Lannuzel, Gurvan Madec, Sébastien Moreau, et al. Role of sea ice in global biogeochemical cycles: emerging views and challenges. *Quaternary science reviews*, 79:207–230, 2013.
- [14] Matthew L Druckenmiller, RL Thoman, and TA Moon. Arctic report card 2022: Executive summary. 2022.
- [15] Ioanna Merkouriadi, Bin Cheng, Robert M Graham, Anja Rösel, and Mats A Granskog. Critical role of snow on sea ice growth in the atlantic sector of the arctic ocean. *Geophysical Research Letters*, 44(20):10–479, 2017.
- [16] Julienne Stroeve, Vishnu Nandan, Rosemary Willatt, Ruzica Dadic, Philip Rostosky, Michael Gallagher, Robbie Mallett, Andrew Barrett, Stefan Hendricks, Rasmus Tonboe, et al. Rain on snow (ros) understudied in sea ice remote sensing: a multi-sensor analysis of ros during mosaic (multidisciplinary drifting observatory for the study of arctic climate). *The Cryosphere*, 16(10):4223–4250, 2022.
- [17] PJ Hezel, X Zhang, CM Bitz, BP Kelly, and François Massonnet. Projected decline in spring snow depth on arctic sea ice caused by progressively later autumn open ocean freeze-up this century. *Geophysical Research Letters*, 39(17), 2012.
- [18] MA Webster, AK DuVivier, MM Holland, and DA Bailey. Snow on arctic sea ice in a warming climate as simulated in cesm. *Journal of Geophysical Research: Oceans*, 126(1):e2020JC016308, 2021.
- [19] Melinda A Webster, Ignatius G Rigor, Son V Nghiem, Nathan T Kurtz, Sinead L Farrell, Donald K Perovich, and Matthew Sturm. Interdecadal changes in snow depth on arctic sea ice. *Journal of Geophysical Research: Oceans*, 119(8):5395–5406, 2014.
- [20] Marta Zygmuntowska, Pierre Rampal, Natalia Ivanova, and Lars Henrik Smedsrud. Uncertainties in arctic sea ice thickness and volume: new estimates and implications for trends. *The Cryosphere*, 8(2):705–720, 2014.
- [21] H Douville, J-F Royer, and J-F Mahfouf. A new snow parameterization for the météofrance climate model: Part i: validation in stand-alone experiments. *Climate Dynamics*, 12(1):21–35, 1995.
- [22] Christian Steger, Sven Kotlarski, Tobias Jonas, and Christoph Schär. Alpine snow cover in a changing climate: a regional climate model perspective. *Climate dynamics*, 41:735–754, 2013.
- [23] Matthew Sturm and Robert A Massom. Snow in the sea ice system: Friend or foe. *Sea ice*, pages 65–109, 2017.
- [24] Georg Lackner, Florent Domine, Daniel F Nadeau, Annie-Claude Parent, François Anctil, Matthieu Lafaysse, and Marie Dumont. On the energy budget of a low-arctic snowpack. *The Cryosphere*, 16(1):127–142, 2022.
- [25] Annette Rinke, John J Cassano, Elizabeth N Cassano, Ralf Jaiser, and Dörthe Handorf. Meteorological conditions during the mosaic expedition: Normal or anomalous? *Elem Sci Anth*, 9(1):00023, 2021.
- [26] Ym-Chao Yen, K Cheng, and S Fukusako. A review of intrinsic thermophysical properties of snow, ice, sea ice, and frost. *The Northern Engineer*, 24:53–74, 1991.

- [27] Amy R Macfarlane, Martin Schneebeli, Ruzica Dadic, David N Wagner, Stefanie Arndt, David Clemens-Sewall, Stefan Hämmerle, Henna-Reetta Hannula, Matthias Jaggi, Nikolai Kolabutin, Daniela Krampe, Michael Lehning, Ilkka Matero, Marcel Nicolaus, Marc Oggier, Roberta Pirazzini, Chris Polashenski, Ian Raphael, Julia Regnery, Egor Shimanuchuk, Madison M Smith, and Aikaterini Tavri. Snowpit temperature profiles measured during the MOSAiC expedition. *PANGAEA*, 2022.
- [28] Eizi Akitaya. Studies on depth hoar. *Contributions from the Institute of Low Temperature Science*, 26:1–67, 1974.
- [29] Bernd R Pinzer and Martin Schneebeli. Snow metamorphism under alternating temperature gradients: Morphology and recrystallization in surface snow. *Geophysical research letters*, 36(23), 2009.
- [30] Florent Domine, Maria Belke-Brea, Denis Sarrazin, Laurent Arnaud, Mathieu Barrere, and Mathilde Poirier. Soil moisture, wind speed and depth hoar formation in the arctic snowpack. *Journal of Glaciology*, 64(248):990–1002, 2018.
- [31] Sam Earman, Andrew R Campbell, Fred M Phillips, and Brent D Newman. Isotopic exchange between snow and atmospheric water vapor: Estimation of the snowmelt component of groundwater recharge in the southwestern united states. *Journal of Geophysical Research: Atmospheres*, 111(D9), 2006.
- [32] Alex R Lechler and Nathan A Niemi. The influence of snow sublimation on the isotopic composition of spring and surface waters in the southwestern united states: Implications for stable isotope-based paleoaltimetry and hydrologic studies. *Bulletin*, 124(3-4):318–334, 2012.
- [33] Martin Vindbæk Madsen, Hans Christian Steen-Larsen, Maria Hörhold, J Box, Sarah Miche Patricia Berben, Emilie Capron, A-K Faber, Alun Hubbard, Mari Fjalstad Jensen, TR Jones, et al. Evidence of isotopic fractionation during vapor exchange between the atmosphere and the snow surface in greenland. *Journal of Geophysical Research: Atmospheres*, 124(6):2932–2945, 2019.
- [34] Ben G Kopec, Pete D Akers, Eric S Klein, and Jeffery M Welker. Significant water vapor fluxes from the greenland ice sheet detected through water vapor isotopic ( $\delta^{18}\text{O}$ ,  $\delta\text{D}$ , deuterium excess) measurements. *The Cryosphere Discussions*, pages 1–38, 2020.
- [35] Pertti Ala-aho, Jeffrey M. Welker, Hannah Bailey, Stine Højlund Pedersen, Ben Kopec, Eric Klein, Moein Mellat, Kaisa-Riikka Mustonen, Kashif Noor, and Hannu Marttila. Arctic snow isotope hydrology: A comparative snow-water vapor study. *Atmosphere*, 12(2), 2021.
- [36] Sonja Wahl, Hans Christian Steen-Larsen, Joachim Reuder, and Maria Hörhold. Quantifying the stable water isotopologue exchange between the snow surface and lower atmosphere by direct flux measurements. *Journal of Geophysical Research: Atmospheres*, 126(13):e2020JD034400, 2021.
- [37] Bonnie Light, Thomas C Grenfell, and Donald K Perovich. Transmission and absorption of solar radiation by Arctic sea ice during the melt season. *Journal of Geophysical Research: Oceans*, 113(C3), 2008.

- [38] Bonnie Light, Madison M Smith, Donald K Perovich, Melinda A Webster, Marika M Holland, Felix Linhardt, Ian A Raphael, David Clemens-Sewall, Amy R Macfarlane, Philipp Anhaus, et al. Arctic sea ice albedo: Spectral composition, spatial heterogeneity, and temporal evolution observed during the mosaic drift. *Elem Sci Anth*, 10(1):000103, 2022.
- [39] R. Ricker, S. Fons, A. Jutila, N. Hutter, K. Duncan, S. L. Farrell, N. T. Kurtz, and R. M. Fredensborg Hansen. Linking scales of sea ice surface topography: evaluation of icesat-2 measurements with coincident helicopter laser scanning during mosaic. *EGU sphere*, 2022:1–27, 2022.
- [40] Amy R Macfarlane, Martin Schneebeli, Ruzica Dadic, David N Wagner, Stefanie Arndt, David Clemens-Sewall, Stefan Hämmerle, Henna-Reetta Hannula, Matthias Jaggi, Nikolai Kolabutin, Daniela Krampe, Michael Lehning, Ilkka Matero, Marcel Nicolaus, Marc Oggier, Roberta Pirazzini, Chris Polashenski, Ian Raphael, Julia Regnery, Egor Shimanuchuk, Madison M Smith, and Aikaterini Tavri. Snowpit height measurements during the MOSAiC expedition. *PANGAEA*, 2022.
- [41] CRLA Fierz, Richard L Armstrong, Yves Durand, Pierre Etchevers, Ethan Greene, David M McClung, Kouichi Nishimura, Pramod K Satyawali, and Sergey A Sokratov. The international classification for seasonal snow on the ground. 2009.
- [42] Mareike Wiese. *Time-lapse tomography of mass fluxes and microstructural changes in snow*. PhD thesis, ETH-Zurich, 2017. unpublished thesis.
- [43] Ghislain Picard, Henning Löwe, Florent Domine, Laurent Arnaud, Fanny Larue, Vincent Favier, Emmanuel Le Meur, Eric Lefebvre, Joel Savarino, and Alain Royer. The microwave snow grain size: A new concept to predict satellite observations over snow-covered regions. *AGU Advances*, 3(4):e2021AV000630, 2022.
- [44] Florent Domine, Anne Sophie Taillandier, William R Simpson, and Ken Severin. Specific surface area, density and microstructure of frost flowers. *Geophysical Research Letters*, 32(13), 2005.
- [45] Matthew Sturm, Jon Holmgren, and Don K Perovich. Winter snow cover on the sea ice of the Arctic Ocean at the Surface Heat Budget of the Arctic Ocean (SHEBA): Temporal evolution and spatial variability. *Journal of Geophysical Research: Oceans*, 107(C10):SHE–23, 2002.
- [46] Vladimir Fyodorovich Radionov, Nicolay Nikolaevich Bryazgin, and Evgeniy Ivanovich Alexandrov. The snow cover of the Arctic basin. Technical report, WASHINGTON UNIV SEATTLE APPLIED PHYSICS LAB, 1997.
- [47] Hajo Eicken, Holger Fischer, and Peter Lemke. Effects of the snow cover on Antarctic sea ice and potential modulation of its response to climate change. *Annals of Glaciology*, 21:369–376, 1995.
- [48] Thierry Fichefet and MA Maqueda. Modelling the influence of snow accumulation and snow-ice formation on the seasonal cycle of the Antarctic sea-ice cover. *Climate Dynamics*, 15(4):251–268, 1999.
- [49] Robert A Massom, Hajo Eicken, Christian Hass, Martin O Jeffries, Mark R Drinkwater, Matthew Sturm, Anthony P Worby, Xingren Wu, Victoria I Lytle, Shuki Ushio, et al. Snow on Antarctic sea ice. *Reviews of Geophysics*, 39(3):413–445, 2001.

- [50] Olivier Lecomte, Thierry Fichefet, Daniela Flocco, David Schroeder, and Martin Vancoppenolle. Interactions between wind-blown snow redistribution and melt ponds in a coupled ocean-sea ice model. *Ocean Modelling*, 87:67–80, 2015.
- [51] Olivier Lecomte, Thierry Fichefet, Martin Vancoppenolle, Florent Dominé, François Massonnet, Pierre Mathiot, Samuel Morin, and Pierre-Yves Barriat. On the formulation of snow thermal conductivity in large-scale sea ice models. *Journal of Advances in Modeling Earth Systems*, 5(3):542–557, 2013.
- [52] Mats A Granskog, Anja Rösel, Paul A Dodd, Dmitry Divine, Sebastian Gerland, Tõnu Martma, and Melanie J Leng. Snow contribution to first-year and second-year Arctic sea ice mass balance north of svalbard. *Journal of Geophysical Research: Oceans*, 122(3):2539–2549, 2017.
- [53] Stefanie Arndt, Klaus M Meiners, Robert Ricker, Thomas Krumpfen, Christian Katlein, and Marcel Nicolaus. Influence of snow depth and surface flooding on light transmission through Antarctic pack ice. *Journal of Geophysical Research: Oceans*, 122(3):2108–2119, 2017.
- [54] Alek A Petty, Melinda Webster, Linette Boisvert, and Thorsten Markus. The NASA eulerian snow on sea ice model (NESOSIM) v1. 0: initial model development and analysis. *Geoscientific Model Development*, 11(11):4577–4602, 2018.
- [55] Melinda Webster, Sebastian Gerland, Marika Holland, Elizabeth Hunke, Ron Kwok, Olivier Lecomte, Robert Massom, Don Perovich, and Matthew Sturm. Snow in the changing sea-ice systems. *Nature Climate Change*, 8(11):946–953, 2018.
- [56] Ioanna Merkouriadi, Bin Cheng, Stephen R Hudson, and Mats A Granskog. Effect of frequent winter warming events (storms) and snow on sea-ice growth—a case from the Atlantic sector of the Arctic Ocean during the N-ICE2015 campaign. *Annals of Glaciology*, 61(82):164–170, 2020.
- [57] Paula Sankelo, Jari Haapala, István Heiler, and Eero Rinne. Melt pond formation and temporal evolution at the drifting station tara during summer 2007. *Polar Research*, 29(3):311–321, 2010.
- [58] Vishnu Nandan, Torsten Geldsetzer, John Yackel, Mallik Mahmud, Randall Scharien, Stephen Howell, Joshua King, Robert Ricker, and Brent Else. Effect of snow salinity on cryosat-2 arctic first-year sea ice freeboard measurements. *Geophysical Research Letters*, 44(20):10–419, 2017.
- [59] Ted Maksym. Arctic and Antarctic sea ice change: contrasts, commonalities, and causes. *Annual Review of Marine Science*, 11(1):187–213, 2019.
- [60] M Meredith, M Sommerkorn, S Cassotta, C Derksen, A Ekaykin, A Hollowed, G Kofinas, A Mackintosh, J Melbourne-Thomas, MMC Muelbert, et al. Polar Regions. Chapter 3, IPCC Special Report on the Ocean and Cryosphere in a Changing Climate. *IPCC, Polar Regions*, 2019.
- [61] Kevin R Arrigo. Sea ice as a habitat for primary producers. *Sea ice*, pages 352–369, 2017.
- [62] Marcel Nicolaus, Donald K Perovich, Gunnar Spreen, Mats A Granskog, Luisa von Albedyll, Michael Angelopoulos, Philipp Anhaus, Stefanie Arndt, H Jakob Belter, Vladimir Bessonov, et al. Overview of the MOSAiC expedition: Snow and sea ice, 2022.



- [63] Amy R Macfarlane, Martin Schneebeli, Ruzica Dadic, David N Wagner, Stefanie Arndt, David Clemens-Sewall, Stefan Hämmerle, Henna-Reetta Hannula, Matthias Jaggi, Nikolai Kolabutin, Daniela Krampe, Michael Lehning, Ilkka Matero, Marcel Nicolaus, Marc Oggier, Roberta Pirazzini, Chris Polashenski, Ian Raphael, Julia Regnery, Egor Shimanuchuck, Madison M Smith, and Aikaterini Tavri. Snowpit raw data collected during the MOSAiC expedition. *PANGAEA*, 2021.
- [64] Amy R Macfarlane, Martin Schneebeli, Ruzica Dadic, David N Wagner, Stefanie Arndt, David Clemens-Sewall, Stefan Hämmerle, Henna-Reetta Hannula, Matthias Jaggi, Nikolai Kolabutin, Daniela Krampe, Michael Lehning, Ilkka Matero, Marcel Nicolaus, Marc Oggier, Roberta Pirazzini, Chris Polashenski, Ian Raphael, Julia Regnery, Egor Shimanuchuck, Madison M Smith, and Aikaterini Tavri. Snowpit surface type observed during the MOSAiC expedition. *PANGAEA*, 2022.
- [65] Amy R Macfarlane, Martin Schneebeli, Ruzica Dadic, David N Wagner, Stefanie Arndt, David Clemens-Sewall, Stefan Hämmerle, Henna-Reetta Hannula, Matthias Jaggi, Nikolai Kolabutin, Daniela Krampe, Michael Lehning, Ilkka Matero, Marcel Nicolaus, Marc Oggier, Roberta Pirazzini, Chris Polashenski, Ian Raphael, Julia Regnery, Egor Shimanuchuck, Madison M Smith, and Aikaterini Tavri. Snowpit metadata TXT files collected during the MOSAiC expedition. *PANGAEA*, 2022.
- [66] Amy R Macfarlane, Martin Schneebeli, David N Wagner, Ruzica Dadic, Matthias Jaggi, and Stefan Hämmerle. MicroCT density and specific surface area snowpit profiles during the MOSAiC expedition. *PANGAEA*, 2022.
- [67] Julia Kaltenborn, Viviane Clay, Amy R. Macfarlane, and Martin Schneebeli. Machine learning for snow stratigraphy classification. In *NeurIPS 2021 Workshop on Tackling Climate Change with Machine Learning*, 2021.
- [68] Amy R Macfarlane, Martin Schneebeli, Ruzica Dadic, David N Wagner, Stefanie Arndt, David Clemens-Sewall, Stefan Hämmerle, Henna-Reetta Hannula, Matthias Jaggi, Nikolai Kolabutin, Daniela Krampe, Michael Lehning, Ilkka Matero, Marcel Nicolaus, Marc Oggier, Roberta Pirazzini, Chris Polashenski, Ian Raphael, Julia Regnery, Egor Shimanuchuck, Madison M Smith, and Aikaterini Tavri. Snowpit SnowMicroPen (SMP) force profiles collected during the MOSAiC expedition. *PANGAEA*, 2021.
- [69] Amy R Macfarlane, Martin Schneebeli, Ruzica Dadic, David N Wagner, Stefanie Arndt, David Clemens-Sewall, Stefan Hämmerle, Henna-Reetta Hannula, Matthias Jaggi, Nikolai Kolabutin, Daniela Krampe, Michael Lehning, Ilkka Matero, Marcel Nicolaus, Marc Oggier, Roberta Pirazzini, Chris Polashenski, Ian Raphael, Julia Regnery, Egor Shimanuchuck, Madison M Smith, and Aikaterini Tavri. Snowpit near-infrared (NIR) images collected during the MOSAiC expedition. *PANGAEA*, 2022.
- [70] Amy R Macfarlane, Martin Schneebeli, Ruzica Dadic, David N Wagner, Stefanie Arndt, David Clemens-Sewall, Stefan Hämmerle, Henna-Reetta Hannula, Matthias Jaggi, Nikolai Kolabutin, Daniela Krampe, Michael Lehning, Ilkka Matero, Marcel Nicolaus, Marc Oggier, Roberta Pirazzini, Chris Polashenski, Ian Raphael, Julia Regnery, Egor Shimanuchuck, Madison M Smith, and Aikaterini Tavri. Snowpit snow water equivalent collected with an ETH tube during the MOSAiC expedition. *PANGAEA*, 2022.
- [71] Amy R Macfarlane, Martin Schneebeli, Ruzica Dadic, David N Wagner, Stefanie Arndt, David Clemens-Sewall, Stefan Hämmerle, Henna-Reetta Hannula, Matthias Jaggi, Nikolai Kolabutin, Daniela Krampe, Michael Lehning, Ilkka Matero, Marcel Nicolaus, Marc

- Oggier, Roberta Pirazzini, Chris Polashenski, Ian Raphael, Julia Regnery, Egor Shimanuchuck, Madison M Smith, and Aikaterini Tavri. Snowpit snow density cutter profiles measured during the MOSAiC expedition. *PANGAEA*, 2022.
- [72] Amy R Macfarlane, Martin Schneebeli, Ruzica Dadic, David N Wagner, Stefanie Arndt, David Clemens-Sewall, Stefan Hämmerle, Henna-Reetta Hannula, Matthias Jaggi, Nikolai Kolabutin, Daniela Krampe, Michael Lehning, Ilkka Matero, Marcel Nicolaus, Marc Oggier, Roberta Pirazzini, Chris Polashenski, Ian Raphael, Julia Regnery, Egor Shimanuchuck, Madison M Smith, and Aikaterini Tavri. Snowpit GPS locations during the MOSAiC expedition. *PANGAEA*, 2021.
- [73] Amy R Macfarlane, Martin Schneebeli, Ruzica Dadic, David N Wagner, Stefanie Arndt, David Clemens-Sewall, Stefan Hämmerle, Henna-Reetta Hannula, Matthias Jaggi, Nikolai Kolabutin, Daniela Krampe, Michael Lehning, Ilkka Matero, Marcel Nicolaus, Marc Oggier, Roberta Pirazzini, Chris Polashenski, Ian Raphael, Julia Regnery, Egor Shimanuchuck, Madison M Smith, Aikaterini Tavri, Moein Mellat, Hanno Meyer, Martin Werner, and Camilla F Brunello. Snowpit stable isotope profiles during the MOSAiC expedition. *PANGAEA*, 2022.
- [74] Amy R Macfarlane, Martin Schneebeli, Ruzica Dadic, David N Wagner, Stefanie Arndt, David Clemens-Sewall, Stefan Hämmerle, Henna-Reetta Hannula, Matthias Jaggi, Nikolai Kolabutin, Daniela Krampe, Michael Lehning, Ilkka Matero, Marcel Nicolaus, Marc Oggier, Roberta Pirazzini, Chris Polashenski, Ian Raphael, Julia Regnery, Egor Shimanuchuck, Madison M Smith, and Aikaterini Tavri. Snowpit overview photos collected during the MOSAiC expedition. *PANGAEA*, 2022.
- [75] Amy R Macfarlane, Martin Schneebeli, Ruzica Dadic, David N Wagner, Stefanie Arndt, David Clemens-Sewall, Stefan Hämmerle, Henna-Reetta Hannula, Matthias Jaggi, Nikolai Kolabutin, Daniela Krampe, Michael Lehning, Ilkka Matero, Marcel Nicolaus, Marc Oggier, Roberta Pirazzini, Chris Polashenski, Ian Raphael, Julia Regnery, Egor Shimanuchuck, Madison M Smith, and Aikaterini Tavri. Snowpit multi-image photogrammetry images collected during the MOSAiC expedition. *PANGAEA*, 2021.
- [76] Amy R Macfarlane, Martin Schneebeli, Ruzica Dadic, David N Wagner, Stefanie Arndt, David Clemens-Sewall, Stefan Hämmerle, Henna-Reetta Hannula, Matthias Jaggi, Nikolai Kolabutin, Daniela Krampe, Michael Lehning, Ilkka Matero, Marcel Nicolaus, Marc Oggier, Roberta Pirazzini, Chris Polashenski, Ian Raphael, Julia Regnery, Egor Shimanuchuck, Madison M Smith, and Aikaterini Tavri. Snowpit salinity profiles during the MOSAiC expedition. *PANGAEA*, 2022.
- [77] Amy R Macfarlane, Martin Schneebeli, Ruzica Dadic, David N Wagner, Stefanie Arndt, David Clemens-Sewall, Stefan Hämmerle, Henna-Reetta Hannula, Matthias Jaggi, Nikolai Kolabutin, Daniela Krampe, Michael Lehning, Ilkka Matero, Marcel Nicolaus, Marc Oggier, Roberta Pirazzini, Chris Polashenski, Ian Raphael, Julia Regnery, Egor Shimanuchuck, Madison M Smith, and Aikaterini Tavri. Snow permittivity measured during the MOSAiC expedition. *PANGAEA*, 2022.
- [78] Terhikki Manninen, Kati Anttila, Emmihenna Jääskeläinen, Aku Riihelä, Jouni Peltoniemi, Petri Räisänen, Panu Lahtinen, Niilo Siljamo, Laura Thölix, Outi Meinander, et al. Effect of small-scale snow surface roughness on snow albedo and reflectance. *The Cryosphere*, 15(2):793–820, 2021.

- [79] Tristram DL Irvine-Fynn, Enoc Sanz-Ablanedo, Nick Rutter, Mark W Smith, and Jim H Chandler. Measuring glacier surface roughness using plot-scale, close-range digital photogrammetry. *Journal of Glaciology*, 60(223):957–969, 2014.
- [80] Martin Proksch, Henning Löwe, and Martin Schneebeli. Density, specific surface area, and correlation length of snow measured by high-resolution penetrometry. *Journal of Geophysical Research: Earth Surface*, 120(2):346–362, 2015.
- [81] Martin Schneebeli, Christine Pielmeier, and Jerome B Johnson. Measuring snow microstructure and hardness using a high resolution penetrometer. *Cold Regions Science and Technology*, 30(1-3):101–114, 1999.
- [82] Joshua King, Stephen Howell, Mike Brady, Peter Toose, Chris Derksen, Christian Haas, and Justin Beckers. Local-scale variability of snow density on arctic sea ice. *The Cryosphere*, 14(12):4323–4339, 2020.
- [83] Steven M Conger and David M McCLUNG. Comparison of density cutters for snow profile observations. *Journal of Glaciology*, 55(189):163–169, 2009.
- [84] Stevens. Stevens ® Water Monitoring System, Inc. The Hydra Probe ® Soil Sensor Comprehensive Stevens Hydra Probe Users Manual, 2015.
- [85] Torsten Geldsetzer, Alexandre Langlois, and John Yackel. Dielectric properties of brine-wetted snow on first-year sea ice. *Cold Regions Science and Technology*, 58(1-2):47–56, 2009.
- [86] Lars GE Backstrom and Hajo Eicken. Capacitance probe measurements of brine volume and bulk salinity in first-year sea ice. *Cold regions science and technology*, 46(3):167–180, 2006.
- [87] Randall K Scharien, Torsten Geldsetzer, David G Barber, John J Yackel, and A Langlois. Physical, dielectric, and C band microwave scattering properties of first-year sea ice during advanced melt. *Journal of Geophysical Research: Oceans*, 115(C12), 2010.
- [88] Survey3N Camera - Near Infrared (NIR) - MAPIR CAMERA. <https://www.mapir.camera/products/survey3n-camera-near-infrared-nir>.
- [89] Margret Matzl and Martin Schneebeli. Measuring specific surface area of snow by near-infrared photography. *Journal of Glaciology*, 52(179):558–564, 2006.
- [90] Scanco Medical AG. µct 90 desktop microct scanner. <https://www.scanco.ch/microct90.html>, 2022. Accessed: 19-10-2022.
- [91] YSI incorporated. Ysi model 30 ysi model 30m handheld salinity, conductivity and temperature system operations manual. <https://www.ysi.com/File%20Library/Documents/Manuals%20for%20Discontinued%20Products/030136-YSI-Model-30-Operations-Manual-RevE.pdf>, 2007.
- [92] Polona Itkin, Melinda Webster, Stefan Hendricks, Marc Oggier, Matthias Jaggi, Robert Ricker, Stefanie Arndt, Dmitry V Divine, Luisa von Albedyll, Ian Raphael, Jan Rohde, and Glen E Liston. Magnaprobe snow and melt pond depth measurements from the 2019-2020 MOSAiC expedition (Pangaea) data sets. <https://doi.org/10.1594/PANGAEA.937781>, 2021.

- [93] Marcel Nicolaus, Kathrin Riemann-Campe, Angela Bliss, Jennifer K Hutchings, Mats A Granskog, Christian Haas, Mario Hoppmann, Torsten Kanzow, Richard A Krishfield, Ruibo Lei, Markus Rex, Tao Li, and Benjamin Rabe. Drift trajectories of the main sites of the Distributed Network of MOSAiC 2019/2020, 2021.
- [94] Neige Calonne, Bettina Richter, Henning Löwe, Cecilia Cetti, Judith ter Schure, Alec Van Herwijnen, Charles Fierz, Matthias Jaggi, and Martin Schneebeli. The RHOSSA campaign: multi-resolution monitoring of the seasonal evolution of the structure and mechanical stability of an alpine snowpack. *The Cryosphere*, 14(6):1829–1848, 2020.
- [95] H Löwe, F Riche, and M Schneebeli. A general treatment of snow microstructure exemplified by an improved relation for thermal conductivity. *The Cryosphere*, 7(5):1473–1480, 2013.
- [96] Amy R Macfarlane, Ruzica Dadic, Madison M Smith, Bonnie Light, Marcel Nicolaus, Hannula Henna-Reetta, Melinda Webster, Felix Linhardt, Stefan Hämmerle, and Martin Schneebeli. Evolution of the microstructure and reflectance of the surface scattering layer on melting, level arctic sea ice. *Elem Sci Anth*, 11(1):00103, 2023.
- [97] Thierry Fichefet and MA Morales Maqueda. Sensitivity of a global sea ice model to the treatment of ice thermodynamics and dynamics. *Journal of Geophysical Research: Oceans*, 102(C6):12609–12646, 1997.
- [98] Malcolm Mellor. Engineering properties of snow. *Journal of Glaciology*, 19(81):15–66, 1977.
- [99] Matthew Sturm, Jon Holmgren, Max König, and Kim Morris. The thermal conductivity of seasonal snow. *Journal of Glaciology*, 43(143):26–41, 1997.
- [100] F Riche and M Schneebeli. Thermal conductivity of snow measured by three independent methods and anisotropy considerations. *The Cryosphere*, 7(1):217–227, 2013.
- [101] Alex West, Mat Collins, and Ed Blockley. Using arctic ice mass balance buoys for evaluation of modelled ice energy fluxes. *Geoscientific Model Development*, 13(10):4845–4868, 2020.
- [102] Cecile Coleou, Bernard Lesaffre, Jean-Bruno Brzoska, Wolfgang Ludwig, and Elodie Bollor. Three-dimensional snow images by x-ray microtomography. *Annals of glaciology*, 32:75–81, 2001.
- [103] Fabienne Riche and Martin Schneebeli. Microstructural change around a needle probe to measure thermal conductivity of snow. *Journal of Glaciology*, 56(199):871–876, 2010.
- [104] Christoph H Arns, Mark A Knackstedt, M Val Pinczewski, and WB Lindquist. Accurate estimation of transport properties from microtomographic images. *Geophysical research letters*, 28(17):3361–3364, 2001.
- [105] Th U Kaempfer, M Schneebeli, and SA Sokratov. A microstructural approach to model heat transfer in snow. *Geophysical Research Letters*, 32(21), 2005.
- [106] Jörg Petrasch, Birte Schrader, Peter Wyss, and Aldo Steinfeld. Tomography-based determination of the effective thermal conductivity of fluid-saturated reticulate porous ceramics. *Journal of heat transfer*, 130(3), 2008.

- [107] Neige Calonne, Frédéric Flin, Samuel Morin, Bernard Lesaffre, S Rolland du Roscoat, and Christian Geindreau. Numerical and experimental investigations of the effective thermal conductivity of snow. *Geophysical research letters*, 38(23), 2011.
- [108] Sverre Orvig. *Climates of the polar regions*. Elsevier Pub. Co., 1970.
- [109] Yin-Chao Yen. *Review of thermal properties of snow, ice, and sea ice*, volume 81. US Army, Corps of Engineers, Cold Regions Research and Engineering Laboratory, 1981.
- [110] Shoichiro Fukusako. Thermophysical properties of ice, snow, and sea ice. *International Journal of Thermophysics*, 11(2):353–372, 1990.
- [111] Stephen G Warren, Ignatius G Rigor, Norbert Untersteiner, Vladimir F Radionov, Nikolay N Bryazgin, Yevgeniy I Aleksandrov, and Roger Colony. Snow depth on arctic sea ice. *Journal of Climate*, 12(6):1814–1829, 1999.
- [112] Florent Domine, Josué Bock, Samuel Morin, and Gérald Giraud. Linking the effective thermal conductivity of snow to its shear strength and density. *Journal of Geophysical Research: Earth Surface*, 116(F4), 2011.
- [113] Stefanie Arndt. Sensitivity of sea ice growth to snow properties in opposing regions of the weddell sea in late summer. *Geophysical Research Letters*, 49(19):e2022GL099653, 2022.
- [114] D Pitman and B Zuckerman. Effective thermal conductivity of snow at  $-88^{\circ}$ ,  $-27^{\circ}$ , and  $-5^{\circ}$  c. *Journal of Applied Physics*, 38(6):2698–2699, 1967.
- [115] AK Singh. An investigation of the thermal conductivity of snow. *Journal of Glaciology*, 45(150):346–351, 1999.
- [116] Michael Smith and Bruce Jamieson. A new set of thermal conductivity measurements. In *Proceedings of the International Snow Science Workshop*, pages 507–510, 2014.
- [117] Neige Calonne, Lucas Milliancourt, Alexis Burr, Armelle Philip, Christophe L Martin, Frédéric Flin, and Christian Geindreau. Thermal conductivity of snow, firn, and porous ice from 3-d image-based computations. *Geophysical Research Letters*, 46(22):13079–13089, 2019.
- [118] Isabelle Gouttevin, Moritz Langer, Henning Löwe, Julia Boike, Martin Proksch, and Martin Schneebeli. Observation and modelling of snow at a polygonal tundra permafrost site: spatial variability and thermal implications. *The Cryosphere*, 12(11):3693–3717, November 2018. Publisher: Copernicus Publications.
- [119] Florent Domine, Mathieu Barrere, and Denis Sarrazin. Seasonal evolution of the effective thermal conductivity of the snow and the soil in high arctic herb tundra at bylot island, canada. *The Cryosphere*, 10(6):2573–2588, 2016.
- [120] Matthew Sturm and Jerome B Johnson. Thermal conductivity measurements of depth hoar. *Journal of Geophysical Research: Solid Earth*, 97(B2):2129–2139, 1992.
- [121] H Huwald, L-B Tremblay, and H Blatter. Reconciling different observational data sets from surface heat budget of the arctic ocean (sheba) for model validation purposes. *Journal of Geophysical Research: Oceans*, 110(C5), 2005.
- [122] DJ Pringle, H Eicken, HJ Trodahl, and LGE Backstrom. Thermal conductivity of landfast antarctic and arctic sea ice. *Journal of Geophysical Research: Oceans*, 112(C4), 2007.

- [123] Sergey Marchenko, Gong Cheng, Per Lötstedt, Veijo Pohjola, Rickard Pettersson, Ward Van Pelt, and Carleen Reijmer. Thermal conductivity of firn at lomonosovfonna, svalbard, derived from subsurface temperature measurements. *The Cryosphere*, 13(7):1843–1859, 2019.
- [124] Gabriele Arduini, Sarah Keeley, Jonathan J Day, Irina Sandu, Lorenzo Zampieri, and Gianpaolo Balsamo. On the importance of representing snow over sea-ice for simulating the arctic boundary layer. *Journal of Advances in Modeling Earth Systems*, 14(7):e2021MS002777, 2022.
- [125] Olivier Lecomte, Thierry Fichet, Martin Vancoppenolle, Florent Domine, F. Massonnet, Pierre Mathiot, Samuel Morin, and P.-Y Barriat. On the formulation of snow thermal conductivity in large-scale sea ice models. *Journal of Advances in Modeling Earth Systems*, 5:542–557, 07 2013.
- [126] Marika M Holland, David Clemens-Sewall, Laura Landrum, Bonnie Light, Donald Perovich, Chris Polashenski, Madison Smith, and Melinda Webster. The influence of snow on sea ice as assessed from simulations of cesm2. *The Cryosphere*, 15(10):4981–4998, 2021.
- [127] Edward J Garboczi et al. Finite element and finite difference programs for computing the linear electric and elastic properties of digital images of random materials. 1998.
- [128] Glen A Slack. Thermal conductivity of ice. *Physical Review B*, 22(6):3065, 1980.
- [129] Kavitha Sundu, Johannes Freitag, Kévin Fourteau, and Henning Löwe. A microstructure-based parameterization of the effective, anisotropic elasticity tensor of snow, firn, and bubbly ice. *EGU sphere*, 2023:1–27, 2023.
- [130] Theodore L Bergman, Theodore L Bergman, Frank P Incropera, David P Dewitt, and Adrienne S Lavine. *Fundamentals of heat and mass transfer*. John Wiley & Sons, 2011.
- [131] L Riihimaki. Radiation instruments on ice (iceradriihimaki). *Atmospheric Radiation Measurement (ARM) user facility*. DOI: <http://dx.doi.org/10.5439/1608608>, 2021.
- [132] C Cox, M Gallagher, M Shupe, O Persson, A Solomon, B Blomquist, I Brooks, D Costa, D Gottas, J Hutchings, et al. 10-meter (m) meteorological flux tower measurements (level 1 raw), multidisciplinary drifting observatory for the study of arctic climate (mosaic), central arctic, october 2019–september 2020. *Arctic Data Center*. DOI: <http://dx.doi.org/10.18739/A2VM42Z5F>, 2021.
- [133] Donald K Perovich et al. The optical properties of sea ice. 1996.
- [134] T Britannica. Editors of encyclopaedia, "firn". *Argon. Encyclopedia Britannica*, 2014.
- [135] Rolf Gradinger, Bodil Bluhm, and Katrin Iken. Arctic sea-ice ridges—safe heavens for sea-ice fauna during periods of extreme ice melt? *Deep Sea Research Part II: Topical Studies in Oceanography*, 57(1-2):86–95, 2010.
- [136] Océane Hames, Mahdi Jafari, David Nicholas Wagner, Ian Raphael, David Clemens-Sewall, Chris Polashenski, Matthew D Shupe, Martin Schneebeli, and Michael Lehning. Modeling the small-scale deposition of snow onto structured arctic sea ice during a mosaic storm using snowbedfoam 1.0. *Geoscientific Model Development*, 15(16):6429–6449, 2022.
- [137] Gary A Maykut and Norbert Untersteiner. Some results from a time-dependent thermodynamic model of sea ice. *Journal of Geophysical Research*, 76(6):1550–1575, 1971.

- [138] Albert J Semtner Jr. A model for the thermodynamic growth of sea ice in numerical investigations of climate. *Journal of Physical Oceanography*, 6(3):379–389, 1976.
- [139] David Clemens-Sewall, Madison M Smith, Marika M Holland, Chris Polashenski, and Don Perovich. Snow redistribution onto young sea ice: Observations and implications for climate models. *Elem Sci Anth*, 10(1):00115, 2022.
- [140] David N Wagner, Matthew D Shupe, Christopher Cox, Ola G Persson, Taneil Uttal, Markus M Frey, Amélie Kirchgaessner, Martin Schneebeli, Matthias Jaggi, Amy R Macfarlane, et al. Snowfall and snow accumulation processes during the mosaic winter and spring season. 2022.
- [141] Mahdi Jafari, Isabelle Gouttevin, Margaux Couttet, Nander Wever, Adrien Michel, Varun Sharma, Leonard Rossmann, Nina Maass, Marcel Nicolaus, and Michael Lehning. The impact of diffusive water vapor transport on snow profiles in deep and shallow snow covers and on sea ice. *Frontiers in Earth Science*, 8:249, 2020.
- [142] Hannah Bailey, Alun Hubbard, Eric S Klein, Kaisa-Riikka Mustonen, Pete D Akers, Hannu Marttila, and Jeffrey M Welker. Arctic sea-ice loss fuels extreme european snowfall. *Nature Geoscience*, 14(5):283–288, 2021.
- [143] Michelle R McCrystall, Julianne Stroeve, Mark Serreze, Bruce C Forbes, and James A Screen. New climate models reveal faster and larger increases in arctic precipitation than previously projected. *Nature communications*, 12(1):6765, 2021.
- [144] Ben G Kopec, Xiahong Feng, Fred A Michel, and Eric S Posmentier. Influence of sea ice on arctic precipitation. *Proceedings of the National Academy of Sciences*, 113(1):46–51, 2016.
- [145] Tamara Shapiro Ledley. Snow on sea ice: Competing effects in shaping climate. *Journal of Geophysical Research: Atmospheres*, 96(D9):17195–17208, 1991.
- [146] Jari Haapala, Mikko Lensu, Marie Dumont, Angelika HH Renner, Mats A Granskog, and Sebastian Gerland. Small-scale horizontal variability of snow, sea-ice thickness and freeboard in the first-year ice region north of svalbard. *Annals of Glaciology*, 54(62):261–266, 2013.
- [147] AM Grannas, Anna E Jones, J Dibb, M Ammann, Cort Anastasio, HJ Beine, M Bergin, J Bottenheim, CS Boxe, G Carver, et al. An overview of snow photochemistry: evidence, mechanisms and impacts. *Atmospheric chemistry and physics*, 7(16):4329–4373, 2007.
- [148] Louis Marelle, Jennie L Thomas, Shaddy Ahmed, Katie Tuite, Jochen Stutz, Aurélien Dommergue, William R Simpson, Markus M Frey, and Foteini Baladima. Implementation and impacts of surface and blowing snow sources of arctic bromine activation within wrf-chem 4.1. 1. *Journal of advances in modeling earth systems*, 13(8):e2020MS002391, 2021.
- [149] RA Sommerfeld and E LaChapelle. The classification of snow metamorphism. *Journal of Glaciology*, 9(55):3–18, 1970.
- [150] Matthew Sturm and Carl S Benson. Vapor transport, grain growth and depth-hoar development in the subarctic snow. *Journal of Glaciology*, 43(143):42–59, 1997.

- [151] Nander Wever, Leonard Rossmann, Nina Maaß, Katherine C Leonard, Lars Kaleschke, Marcel Nicolaus, and Michael Lehning. Version 1 of a sea ice module for the physics-based, detailed, multi-layer snowpack model. *Geoscientific Model Development*, 13(1):99–119, 2020.
- [152] Glen E Liston, Chris Polashenski, Anja Rösel, Polona Itkin, Jennifer King, Ioanna Merkouriadi, and Jari Haapala. A distributed snow-evolution model for sea-ice applications (snowmodel). *Journal of Geophysical Research: Oceans*, 123(5):3786–3810, 2018.
- [153] Manish Tiwari, Ashutosh K Singh, and Devesh K Sinha. Stable isotopes: Tools for understanding past climatic conditions and their applications in chemostratigraphy. In *Chemostratigraphy*, pages 65–92. Elsevier, 2015.
- [154] Martin O Jeffries, Raymond A Shaw, Kim Morris, Alice L Veazey, and H Roy Krouse. Crystal structure, stable isotopes ( $\delta^{18}\text{O}$ ), and development of sea ice in the ross, amundsen, and bellingshausen seas, antarctica. *Journal of Geophysical Research: Oceans*, 99(C1):985–995, 1994.
- [155] Rémy Lapere, Jennie L Thomas, Louis Marelle, Annica ML Ekman, Markus Michael Frey, Marianne Tronstad Lund, Risto Makkonen, Ananth Ranjithkumar, Matthew Edward Salter, Bjørn Hallvard Samset, et al. The representation of sea salt aerosols and their role in polar climate within cmip6. *Authorea Preprints*, 2022.
- [156] Moein Mellat, Hanno Meyer, Camilla F Brunello, Stefanie Arndt, Amy R Macfarlane, Martin Schneebeli, Maria Hörhold, Martin Werner, Mikaela Weiner, and Andreas Marent. Stable water isotopes of snow during MOSAiC expedition, 2022.
- [157] HC Steen-Larsen, Valérie Masson-Delmotte, J Sjolte, SJ Johnsen, BM Vinther, F-M Bréon, HB Clausen, D Dahl-Jensen, S Falourd, X Fettweis, et al. Understanding the climatic signal in the water stable isotope records from the neem shallow firn/ice cores in northwest greenland. *Journal of Geophysical Research: Atmospheres*, 116(D6), 2011.
- [158] Carol Kendall and Eric A Caldwell. Fundamentals of isotope geochemistry. In *Isotope tracers in catchment hydrology*, pages 51–86. Elsevier, 1998.
- [159] H Moser and W Stichler. Deuterium and oxygen-18 contents as an index of the properties of snow covers. In *Snow Mechanics Symposium*, 1975.
- [160] Harsh Beria, Joshua R Larsen, Natalie Claire Ceperley, Anthony Michelon, Torsten Venemann, and Bettina Schaefli. Understanding snow hydrological processes through the lens of stable water isotopes. *Wiley Interdisciplinary Reviews: Water*, 5(6):e1311, 2018.
- [161] Pirmin Philipp Ebner, Hans Christian Steen-Larsen, Barbara Stenni, Martin Schneebeli, and Aldo Steinfeld. Experimental observation of transient  $\delta^{18}\text{O}$  interaction between snow and advective airflow under various temperature gradient conditions. *The Cryosphere*, 11(4):1733–1743, 2017.
- [162] Mathieu Casado, Amaelle Landais, Ghislain Picard, Laurent Arnaud, Giuliano Dreossi, Barbara Stenni, and Frederic Prié. Water isotopic signature of surface snow metamorphism in antarctica. *Geophysical Research Letters*, 48(17):e2021GL093382, 2021.
- [163] Romilly Harris Stuart, Anne-Katrine Faber, Sonja Wahl, Maria Hörhold, Sepp Kipfstuhl, Kristian Vasskog, Melanie Behrens, Alexandra Zuhr, and Hans Christian Steen-Larsen. Exploring the role of snow metamorphism on the isotopic composition of the surface snow at eastgrip. *The Cryosphere Discussions*, pages 1–27, 2021.



- [164] F Domine, R Sparapani, A Ianniello, and HJ Beine. The origin of sea salt in snow on arctic sea ice and in coastal regions. *Atmospheric Chemistry and Physics*, 4(9/10):2259–2271, 2004.
- [165] Rachel E Jordan, Janet P Hardy, Frank E Perron Jr, and David J Fisk. Air permeability and capillary rise as measures of the pore structure of snow: an experimental and theoretical study. *Hydrological Processes*, 13(12-13):1733–1753, 1999.
- [166] Cécile Coléou, Ke Xu, Bernard Lesaffre, and Jean-Bruno Brzoska. Capillary rise in snow. *Hydrological processes*, 13(12-13):1721–1732, 1999.
- [167] Søren Rysgaard, Dorthe H Sogaard, M Cooper, M Pućko, Kunuk Lennert, TN Papakyriakou, F Wang, NX Geilfus, Ronnie N Glud, J Ehn, et al. Ikaite crystal distribution in winter sea ice and implications for CO<sub>2</sub> system dynamics. *The Cryosphere*, 7(2):707–718, 2013.
- [168] Harmon Craig, Louis Irwin Gordon, et al. Deuterium and oxygen 18 variations in the ocean and the marine atmosphere. 1965.
- [169] Joel R Gat and R Gonfiantini. Stable isotope hydrology: deuterium and oxygen-18 in the water cycle. technical reports series no. 210. 1981.
- [170] Joel R Gat. Oxygen and hydrogen isotopes in the hydrologic cycle. *Annual Review of Earth and Planetary Sciences*, 24(1):225–262, 1996.
- [171] W Stichler, U Schotterer, K Fröhlich, P Ginot, Ch Kull, H Gäggeler, and B Pouyaud. Influence of sublimation on stable isotope records recovered from high-altitude glaciers in the tropical andes. *Journal of Geophysical Research: Atmospheres*, 106(D19):22613–22620, 2001.
- [172] Abigail G Hughes, Sonja Wahl, Tyler R Jones, Alexandra Zuhr, Maria Hörhold, James WC White, and Hans Christian Steen-Larsen. The role of sublimation as a driver of climate signals in the water isotope content of surface snow: Laboratory and field experimental results. *The Cryosphere*, 15(10):4949–4974, 2021.
- [173] Ben G Kopec, Xiahong Feng, Erich C Osterberg, and Eric S Posmentier. Climatological significance of  $\delta d$ - $\delta^{18}O$  line slopes from precipitation, snow pits, and ice cores at summit, greenland. *Journal of Geophysical Research: Atmospheres*, 127(21):e2022JD037037, 2022.
- [174] Hans C Steen-Larsen, Valérie Masson-Delmotte, Motohiro Hirabayashi, Renato Winkler, Kazuhide Satow, F Prié, Nicolas Bayou, E Brun, KM Cuffey, D Dahl-Jensen, et al. What controls the isotopic composition of greenland surface snow? *Climate of the Past*, 10(1):377–392, 2014.
- [175] Jun Hu, Yuzhen Yan, Laurence Y Yeung, and Sylvia G Dee. Sublimation origin of negative deuterium excess observed in snow and ice samples from mcmurdo dry valleys and allan hills blue ice areas, east antarctica. *Journal of Geophysical Research: Atmospheres*, 127(11):e2021JD035950, 2022.
- [176] A. R. Macfarlane, H. Löwe, L. Gimenes, D. N. Wagner, R. Dacic, R. Ottersberg, S. Hämmerle, and M. Schneebeli. Thermal conductivity of snow on arctic sea ice. *EGU sphere*, 2023:1–22, 2023.

- [177] L Tian, Y Gao, SF Ackley, S Stammerjohn, T Maksym, and B Weissling. Stable isotope clues to the formation and evolution of refrozen melt ponds on arctic sea ice. *Journal of Geophysical Research: Oceans*, 123(12):8887–8901, 2018.
- [178] Moein Mellat, Camilla Brunello, Martin Werner, Dorothea Bauch, Ellem Damm, Daiki Nomura, Alessandra D’Angelo, and Hanno Meyer. Changes of water isotopes in arctic sea ice, ocean and atmosphere (ciasom). In *AGU Fall Meeting Abstracts*, volume 2021, pages C55C–0609, 2021.
- [179] Amy R Macfarlane, Martin Schneebeli, Ruzica Dadic, David N Wagner, Stefanie Arndt, David Clemens-Sewall, Stefan Hämmerle, Henna-Reetta Hannula, Matthias Jaggi, Nikolai Kolabutin, Daniela Krampe, Michael Lehning, Ilkka Matero, Marcel Nicolaus, Marc Oggier, Roberta Pirazzini, Chris Polashenski, Ian Raphael, Julia Regnery, Egor Shimanchuck, Madison M Smith, and Aikaterini Tavri. Snowpit height measurements during the MOSAiC expedition. PANGAEA, 2022. In: Macfarlane, AR et al. (2021): Snowpit raw data collected during the MOSAiC expedition. PANGAEA, <https://doi.org/10.1594/PANGAEA.935934>.
- [180] S. Pfahl and H. Sodemann. What controls deuterium excess in global precipitation? *Climate of the Past*, 10(2):771–781, 2014.
- [181] A. Touzeau, A. Landais, S. Morin, L. Arnaud, and G. Picard. Numerical experiments on vapor diffusion in polar snow and firn and its impact on isotopes using the multi-layer energy balance model crocus in surfex v8.0. *Geoscientific Model Development*, 11(6):2393–2418, 2018.
- [182] Angela RW Raso, Kyle D Custard, Nathaniel W May, David Tanner, Matt K Newburn, Lawrence Walker, Ronald J Moore, L Gregory Huey, Liz Alexander, Paul B Shepson, et al. Active molecular iodine photochemistry in the arctic. *Proceedings of the National Academy of Sciences*, 114(38):10053–10058, 2017.
- [183] Nuria Benavent, Anoop S Mahajan, Qinyi Li, Carlos A Cuevas, Julia Schmale, Hélène Angot, Tuija Jokinen, Lauriane LJ Quéléver, Anne-Marlene Blechschmidt, Bianca Zilker, et al. Substantial contribution of iodine to arctic ozone destruction. *Nature Geoscience*, 15(10):770–773, 2022.
- [184] Donald K Perovich and Christopher Polashenski. Albedo evolution of seasonal arctic sea ice. *Geophysical Research Letters*, 39(8), 2012.
- [185] Hans-Otto Pörtner, Debra C Roberts, Valérie Masson-Delmotte, Panmao Zhai, Melinda Tignor, Elvira Poloczanska, and N Weyer. The ocean and cryosphere in a changing climate. *IPCC special report on the ocean and cryosphere in a changing climate*, 1155, 2019.
- [186] Mark C Serreze, Alex D Crawford, Julianne C Stroeve, Andrew P Barrett, and Rebecca A Woodgate. Variability, trends, and predictability of seasonal sea ice retreat and advance in the chukchi sea. *Journal of Geophysical Research: Oceans*, 121(10):7308–7325, 2016.
- [187] Qinghua Ding, Axel Schweiger, Michelle L’Heureux, David S Battisti, Stephen Po-Chedley, Nathaniel C Johnson, Eduardo Blanchard-Wrigglesworth, Kirstin Harnos, Qin Zhang, Ryan Eastman, et al. Influence of high-latitude atmospheric circulation changes on summertime arctic sea ice. *Nature Climate Change*, 7(4):289–295, 2017.

- [188] Gerald A Meehl, Christine TY Chung, Julie M Arblaster, Marika M Holland, and Cecilia M Bitz. Tropical decadal variability and the rate of arctic sea ice decrease. *Geophysical Research Letters*, 45(20):11–326, 2018.
- [189] Chad W Thackeray and Christopher G Fletcher. Snow albedo feedback: Current knowledge, importance, outstanding issues and future directions. *Progress in Physical Geography*, 40(3):392–408, 2016.
- [190] Michael Winton. Surface albedo feedback estimates for the ar4 climate models. *Journal of Climate*, 19(3):359–365, 2006.
- [191] Mark G Flanner, Karen M Shell, Michael Barlage, Donald K Perovich, and MA Tschudi. Radiative forcing and albedo feedback from the northern hemisphere cryosphere between 1979 and 2008. *Nature Geoscience*, 4(3):151–155, 2011.
- [192] RA Colman. Surface albedo feedbacks from climate variability and change. *Journal of Geophysical Research: Atmospheres*, 118(7):2827–2834, 2013.
- [193] W Su, J Corbett, Z Eitzen, and L Liang. Next-generation angular distribution models for top-of-atmosphere radiative flux calculation from ceres instruments: Validation. *Atmospheric Measurement Techniques*, 8(8):3297–3313, 2015.
- [194] Donald Perovich, Walt Meier, M Tschudi, S Hendricks, AA Petty, D Divine, S Farrell, S Gerland, C Haas, L Kaleschke, et al. Arctic report card 2020: Sea ice. 2020.
- [195] WN Meier, D Perovich, S Farrell, C Haas, S Hendricks, AA Petty, M Webster, D Divine, S Gerland, L Kaleschke, et al. Sea ice. 2021.
- [196] Thomas Krumpfen, Luisa von Albedyll, Helge F Goessling, Stefan Hendricks, Bennet Juhls, Gunnar Spreen, Sascha Willmes, H Jakob Belter, Klaus Dethloff, Christian Haas, et al. Mosaic drift expedition from october 2019 to july 2020: Sea ice conditions from space and comparison with previous years. *The Cryosphere*, 15(8):3897–3920, 2021.
- [197] Norbert Untersteiner. On the mass and heat budget of arctic sea ice. *Archiv für Meteorologie, Geophysik und Bioklimatologie, Serie A*, 12:151–182, 1961.
- [198] Thomas C Grenfell and Gary A Maykut. The optical properties of ice and snow in the arctic basin. *Journal of Glaciology*, 18(80):445–463, 1977.
- [199] Aleksey Malinka, Eleonora Zege, Georg Heygster, and Larysa Istomina. Reflective properties of white sea ice and snow. *The Cryosphere*, 10(6):2541–2557, 2016.
- [200] Donald K Perovich. Sea ice and sunlight. *Sea ice*, pages 110–137, 2017.
- [201] Madison M Smith, Bonnie Light, Amy R Macfarlane, Don K Perovich, Marika M Holland, and Matthew D Shupe. Sensitivity of the arctic sea ice cover to the summer surface scattering layer. *Geophysical Research Letters*, 49(9):e2022GL098349, 2022.
- [202] Chris Petrich and Hajo Eicken. Growth, structure and properties of sea ice. *Sea ice*, 2:23–77, 2010.
- [203] Michael Lombardo, Martin Schneebeli, and Henning Löwe. A casting method using contrast-enhanced diethylphthalate for micro-computed tomography of snow. *Journal of Glaciology*, 67(265):847–861, 2021.

- [204] Hajo Eicken. From the microscopic, to the macroscopic, to the regional scale: growth, microstructure and properties of sea ice. *Sea ice: an introduction to its physics, chemistry, biology and geology*, 22:81, 2003.
- [205] Wenfeng Huang, Ruibo Lei, Hongwei Han, and Zhijun Li. Physical structures and interior melt of the central arctic sea ice/snow in summer 2012. *Cold Regions Science and Technology*, 124:127–137, 2016.
- [206] Marc Oggier and Hajo Eicken. Seasonal evolution of granular and columnar sea ice pore microstructure and pore network connectivity. *Journal of Glaciology*, pages 1–16, 2022.
- [207] JG Dash, AW Rempel, and JS Wettlaufer. The physics of premelted ice and its geophysical consequences. *Reviews of modern physics*, 78(3):695, 2006.
- [208] DM Cole and LH Shapiro. Observations of brine drainage networks and microstructure of first-year sea ice. *Journal of Geophysical Research: Oceans*, 103(C10):21739–21750, 1998.
- [209] JK Ehn, TN Papakyriakou, and DG Barber. Inference of optical properties from radiation profiles within melting landfast sea ice. *Journal of Geophysical Research: Oceans*, 113(C9), 2008.
- [210] Johannes Freitag and Hajo Eicken. Meltwater circulation and permeability of arctic summer sea ice derived from hydrological field experiments. *Journal of glaciology*, 49(166):349–358, 2003.
- [211] Chris Petrich and Hajo Eicken. Overview of sea ice growth and properties. *Sea ice*, pages 1–41, 2017.
- [212] Carie M Frantz, Bonnie Light, Samuel M Farley, Shelly Carpenter, Ross Lieblappen, Zoe Courville, Mónica V Orellana, and Karen Junge. Physical and optical characteristics of heavily melted “rotten” arctic sea ice. *The Cryosphere*, 13(3):775–793, 2019.
- [213] Bonnie Light, Donald K Perovich, Melinda A Webster, Christopher Polashenski, and Ruzica Dadic. Optical properties of melting first-year arctic sea ice. *Journal of Geophysical Research: Oceans*, 120(11):7657–7675, 2015.
- [214] DK Perovich, TC Grenfell, B Light, and PV Hobbs. Seasonal evolution of the albedo of multiyear arctic sea ice. *Journal of Geophysical Research: Oceans*, 107(C10):SHE–20, 2002.
- [215] Thomas C Grenfell, Bonnie Light, and Donald K Perovich. Spectral transmission and implications for the partitioning of shortwave radiation in arctic sea ice. *Annals of Glaciology*, 44:1–6, 2006.
- [216] Bonnie Light, Marika Holland, Madison Smith, Donald Perovich, Melinda Webster, David Clemens-Sewell, Felix Linhardt, Ian Raphael, and David Bailey. The mosaic sea ice albedo record: its context and role for informing improved surface radiative budgets in a climate model. In *EGU General Assembly Conference Abstracts*, pages EGU21–8585, 2021.
- [217] Thomas C Grenfell. A radiative transfer model for sea ice with vertical structure variations. *Journal of Geophysical Research: Oceans*, 96(C9):16991–17001, 1991.
- [218] Donald K Perovich and Thomas C Grenfell. Laboratory studies of the optical properties of young sea ice. *Journal of Glaciology*, 27(96):331–346, 1981.

- [219] Richard Moritz and Bonnie Light. Observing and modeling the surface scattering layer of first-year arctic sea ice. Technical report, WASHINGTON UNIV SEATTLE APPLIED PHYSICS LAB, 2007.
- [220] Madison Smith, Bonnie Light, Don Perovich, Melinda Webster, Philipp Anhaus, David Clemens-Sewall, Felix Linhardt, Amy Macfarlane, Ian Raphael, Debbie Bozzato, et al. Spectral albedo measurements of the sea ice surface during the multidisciplinary drifting observatory for the study of arctic climate (mosaic) campaign in the central arctic ocean, april–september 2020. 2021.
- [221] Warren J Wiscombe and Stephen G Warren. A model for the spectral albedo of snow. i: Pure snow. *Journal of Atmospheric Sciences*, 37(12):2712–2733, 1980.
- [222] Jeff Dozier. Remote sensing of alpine snow cover invisible and near-infrared wavelengths. In *Proceedings from the Centre for Snow Science at Alta 1991 Symposium: Online at: <http://www.avalanche.org/~moonstone/cssa91?.htm>*, 1991.
- [223] C Leroux, J Lenoble, G Brogniez, JW Hovenier, and JF De Haan. A model for the bidirectional polarized reflectance of snow. *Journal of Quantitative Spectroscopy and Radiative Transfer*, 61(3):273–285, 1999.
- [224] Tor Hildebrand and Peter Rügsegger. A new method for the model-independent assessment of thickness in three-dimensional images. *Journal of microscopy*, 185(1):67–75, 1997.
- [225] Mathias Gergely, Fabian Wolfsperger, and Martin Schneebeli. Simulation and validation of the infrasnow: an instrument to measure snow optically equivalent grain size. *IEEE transactions on geoscience and remote sensing*, 52(7):4236–4247, 2013.
- [226] Q Libois, G Picard, JL France, L Arnaud, Marie Dumont, CM Carmagnola, and MD King. Influence of grain shape on light penetration in snow. *The Cryosphere*, 7(6):1803–1818, 2013.
- [227] Quentin Libois, Ghislain Picard, Marie Dumont, Laurent Arnaud, Claude Sergent, Evelyne Pougatch, Marcel Sudul, and David Vial. Experimental determination of the absorption enhancement parameter of snow. *Journal of Glaciology*, 60(222):714–724, 2014.
- [228] J H\_ Joseph, WJ Wiscombe, and JA Weinman. The delta-eddington approximation for radiative flux transfer. *Journal of Atmospheric Sciences*, 33(12):2452–2459, 1976.
- [229] Ruzica Dadic, Peter C Mullen, Martin Schneebeli, Richard E Brandt, and Stephen G Warren. Effects of bubbles, cracks, and volcanic tephra on the spectral albedo of bare ice near the transantarctic mountains: Implications for sea glaciers on snowball earth. *Journal of Geophysical Research: Earth Surface*, 118(3):1658–1676, 2013.
- [230] Rizwan Mushtaq. Augmented dickey fuller test. 2011.
- [231] Charles F Raymond and Katsutosi Tusima. Grain coarsening of water-saturated snow. *Journal of Glaciology*, 22(86):83–105, 1979.
- [232] N Shabanov and J-P Gastellu-Etchegorry. The stochastic beer–lambert–bouguer law for discontinuous vegetation canopies. *Journal of Quantitative Spectroscopy and Radiative Transfer*, 214:18–32, 2018.

- [233] Michelle Bezanson, Rochelle Stowe, and Sean M Watts. Reducing the ecological impact of field research. *American Journal of Primatology*, 75(1):1–9, 2013.
- [234] Collectif Labos 1.5. Réduire l’empreinte de nos activités de recherche sur l’environnement [reducing the environmental footprint of our research activities]. <https://labos1point5.org/>, 2023.
- [235] Marc G Stevenson. Indigenous knowledge in environmental assessment. *Arctic*, pages 278–291, 1996.



# Curriculum Vitae

## Personal Information

Name: Amy R. Macfarlane  
Date of Birth : 20.07.1994  
Place of Birth : Rochdale, England  
ORCID ID : 0000-0002-1638-8885

## Education

Degree	Organisation	Duration
PhD: Influences of snow microstructure on the Arctic sea ice energy budget Dr. Martin Schneebeli	WSL Institute for Snow and Avalanche SLF Snow Physics Group	10.2019 – 03.2023 3 years 5 months
MSc: Arctic Glaciers and Melt Season Dynamics Prof. Dr. Andy Hodson	University Centre in Svalbard Department of Glaciology	08.2017 – 08.2017 1 month
MRes: Polar and Alpine change Prof. Dr. Grant Bigg	University of Sheffield, GB Department of Geography	09.2016 – 08.2017 1 year
BSc: Physics with placement year Prof. Dr. Philippe Blondel	University of Bath, GB Department of Physics	09.2012 – 08.2016 4 years

## Employment

Role	Organisation	Duration
Research associate / Scientific collaborator Prof (Assoc.), Dr. Bogdan Gądek	University of Silesia, PL Centre for polar studies	09.2015 – 10.2015 2 months
Internship Dr. Martin Schneebeli	WSL Institute for Snow and Avalanche SLF Research SLF, CH, Snow Physics	06.2014 – 06.2015 1 year



# Amy R. Macfarlane

ORCID ID: 0000-0002-1638-8885

Email:  
amyrmacfarlane@gmail.com

Mobile:  
+41 (0) 797873265

Address:  
Holmboevegen 10B, Tromsø, Norway

Nationality:  
British

## 1. Professional and Research Interests

*My research investigates the influence of snow microstructure on sea ice energy budget and microwave remote sensing. In addition, I use outreach, illustrations, and environmental impact assessments to improve societal understanding of the changing polar climates.*

## 2. Education

- (2019-2023) **PhD.** ETH-Zurich and WSL Institute for Snow and Avalanche Research SLF, Switzerland.  
*'Influences of snow microstructure on the Arctic sea ice energy budget'*
- (2017) **MSc** UNIS, Svalbard. *Glacier Melt Dynamics.*
- (2016- 2017) **MSc(res).** University of Sheffield, UK. Polar and Alpine Change.  
*'Upper-ocean and Atmosphere mixing induced by a Polar mesocyclone event'*
- (2012- 2016) **BSc.** University of Bath, UK. Physics with placement year.

## 3. Scientific Work Experience

- (2024-current) **Postdoc.** SNSF Postdoc Mobility. UiT Tromsø, Norway and Northumbria University, UK.  
*'Microwave signatures of snow on sea ice'*
- (2023) **Fellowship.** Institute for Marine and Antarctic studies, Hobart, Tasmania. 3 months self-obtained funding.
- (2019) **Visiting scientist.** WSL Institute for Snow and Avalanche Research SLF, Switzerland. 7 months.
- (2015) **Internship.** University of Silesia, Poland with fieldwork on the Hansbreen glacier, Svalbard.
- (2014-2015) **Internship.** WSL Institute for Snow and Avalanche Research SLF, Switzerland. 12-month internship.

## 4. Field work

- MOSAiC expedition, Arctic Sea Ice (February 2020 – September 2020: 8 months)
- SnowAPP2019 Sodankyla, Finland (2019: 2 months)
- UNIS, Svalbard (2017: 1 month)
- Polish Polar station, Svalbard (2015: 2 months)
- Laret, Davos (2014/15: 12 months)

## 5. Teaching

- (2021) **Field teaching assistant.** ETH-Zurich: Snow Physics course.
- (2016-2018) **Tutor.** Private Tuition Physics and Maths A-level/GCSE

## 6. Supervision of theses

- Marie Berger. **MSc.** The influence of temperature on the SnowMicroPen (SMP). Jan 2021-August 2021.
- Julia Kaltenborn. **MSc.** Machine Learning for Snow Stratigraphy Classification. December 2020- April 2021.
- Lucille Gimenes. **BSc.** Thermal conductivity of snow on sea ice. April 2022- July 2022

## 7. Selected professional activities

- IASC Cryosphere Working Group. Representing Switzerland (2023-current).
- Responsible science (RISE) President. This is an APECS full year project group working towards reducing the impact of scientific field work.
- Creation of the first Arctic expedition impact assessment.
- APECS Switzerland president, organising workshops, events and networking for early career researchers across Switzerland (2022-2023).
- Actively involved in outreach events hosted at schools, universities, and for the general public.
- Girls on Ice volunteer, encouraging women to continue studying STEM subjects.
- Swiss Committee for Polar and High Altitude Research (SKPH) member.
- WSL SLF PhD representative and Club Meteo Winter 2020/21 organiser.
- IASC AGCF (Action Group on Carbon Footprint) contributor.

## 8. Publications in peer-reviewed scientific journals

### First-author publications

- **Macfarlane, A.R.**, Dadic R, Smith M M., Light B., Nicolaus M, Henna-Reetta H., Webster M., Linhardt F., Hämmerle S., Schneebeli M., (2023). Evolution of the microstructure and reflectance of the surface scattering layer on melting level Arctic sea ice. *Elementa: Science of the Anthropocene* 11(1). DOI: <https://doi.org/10.1525/elementa.2022.00103>
- **Macfarlane, A.R.**, Löwe, H., Gimenes, L., Wagner, D.N., Dadic, R., Ottersberg, R., Hämmerle, S. and Schneebeli, M., (2023). Temporospacial variability of snow's thermal conductivity on Arctic sea ice. *The Cryosphere*, 17(12), pp.5417-5434. DOI: <https://doi.org/10.5194/tc-17-5417-2023>
- **Macfarlane, A.R.**, Mellat, M., Meyer, H., Wagner, D.N., Krampe, D., Jaggi, M., Arndt, S., Dadic, R., Schneebeli, M., (preprint). Ocean-Sourced Snow: Quantifying the Overlooked Contribution of Sea Ice Sublimation to the Arctic Snowpack. *Nature Geoscience*. DOI: <https://doi.org/10.21203/rs.3.rs-3572881/v1>
- **Macfarlane, A.R.**, Schneebeli, M., Dadic, R. et al. A Database of Snow on Sea Ice in the Central Arctic Collected during the MOSAiC expedition. *Sci Data* 10, 398 (2023). DOI: <https://doi.org/10.1038/s41597-023-02273-1>

### Top co-author publications

- Mellat, M., **Macfarlane, A.R.**, Brunello, C.F., Werner, M., Schneebeli, M., Dadic, R., Arndt, S., Mustonen, K.R., Welker, J.M. and Meyer, H., (2024). Arctic Surface Snow Interactions with the Atmosphere: Spatio-Temporal Isotopic Variability During the MOSAiC Expedition. *EGUsphere*, (2024), pp.1-36.
- Clemens-Sewall, D., Polashenski, C., Raphael, I.A., Parno, M., Perovich, D., Itkin, P., Jaggi, M., Jutila, A., **Macfarlane, A.R.**, Matero, I.S. and Oggier, M., (2024). High-resolution repeat topography of drifting ice floes in the Arctic Ocean from terrestrial laser scanning. *Scientific Data*, 11(1), p.70.
- Mellat, M., Brunello, C.F., Werner, M., Bauch, D., Damm, E., Angelopoulos, M., Nomura, D., Welker, J.M., Schneebeli, M., Granskog, M.A. and Hoerhold, M., **Macfarlane, A.R.**, (2024). Isotopic signatures of snow, sea ice, and surface seawater in the central Arctic Ocean during the MOSAiC expedition. *Elementa: Science of the Anthropocene*, 12(1).
- Kaltenborn, J., **Macfarlane, A.R.**, Clay, V. and Schneebeli, M., (2023). Automatic classification and segmentation of Snow Micro Penetrometer profiles with machine learning algorithms. *EGUsphere*, pp.1-30.
- Lange, B.A., Salganik, E., **Macfarlane, A.R.**, Schneebeli, M., Høyland, K.V., Gardner, J., Müller, O., Divine, D., Kohlbach, D., Kattlein, C. and Granskog, M., (2023). Snowmelt contribution to Arctic first-year ice ridge mass balance and rapid consolidation during summer melt.
- Rückert, J.E., Rostosky, P., Huntemann, M., Clemens-Sewall, D., Ebell, K., Kaleschke, L., Lemmetyinen, J., **Macfarlane, A.R.**, Naderpour, R., Stroeve, J., Walbröl, A., Spreen, G. (2023). Sea ice concentration satellite retrievals influenced by surface changes due to warm air intrusions: A case study from the MOSAiC expedition. *Elementa: Science of the Anthropocene* 11(1).
- Clemens-Sewall, D., Polashenski, C., Frey, M.M., Cox, C.J., Granskog, M.A., **Macfarlane, A.R.**, Fons, S.W., Schmale, J., Hutchings, J.K., von Albedyll, L. and Arndt, S., (2023). Snow loss into leads in Arctic sea ice: Minimal in typical wintertime conditions, but high during a warm and windy snowfall event. *Geophysical Research Letters*, 50(12), p.e2023GL102816.
- Smith, M.M., Light, B., **Macfarlane, A.R.**, Perovich, D.K., Holland, M.M. and Shupe, M.D., (2022). Sensitivity of the Arctic sea ice cover to the summer surface scattering layer. *Geophysical Research Letters*, p.e2022GL098349.
- Light, B., Smith, M.M., Perovich, D.K., Webster, M.A., Holland, M.M., Linhardt, F., Raphael, I.A., Clemens-Sewall, D., **Macfarlane, A.R.**, Anhaus, P. and Bailey, D.A., (2022). Arctic sea ice albedo: Spectral composition, spatial heterogeneity, and temporal evolution observed during the MOSAiC drift. *Elem Sci Anth*, 10(1), p.000103.
- Nicolaus, M., Perovich, D.K., Spreen, G., Granskog, M.A., von Albedyll, L., Angelopoulos, M., Anhaus, P., Arndt, S., Belter, H.J., Bessonov, V. and Birnbaum, G., **Macfarlane, A.R.**, . . . (2022). Overview of the MOSAiC expedition: Snow and sea ice. *Elem Sci Anth*, 10(1), p.000046.
- Stroeve, J., Nandan, V., Willatt, R., Dadic, R., Rostosky, P., Gallagher, M., Mallett, R., Barrett, A., Hendricks, S., Tonboe, R. and McCrystall, M., **Macfarlane, A.R.**, . . . (2022). Rain on snow (ROS) understudied in sea ice remote sensing: a multi-sensor analysis of ROS during MOSAiC (Multidisciplinary drifting Observatory for the Study of Arctic Climate). *The Cryosphere*, 16(10), pp.4223-4250.
- Nandan, V., Willatt, R., Mallett, R., Stroeve, J., Geldsetzer, T., Scharien, R., Tonboe, R., Landy, J., Clemens-Sewall, D., Jutila, A., Wagner, D.N., **Macfarlane, A.R.**, (2022). Wind Transport of Snow Impacts Ka- and Ku-band Radar Signatures on Arctic Sea Ice. *The Cryosphere Discussions*, pp.1-38.

- Wagner, D.N., Shupe, M.D., Persson, O.G., Uttal, T., Frey, M.M., Kirchgaessner, A., Schneebeli, M., Jaggi, M., **Macfarlane, A.R.**, Itkin, P. and Arndt, S., (2021). Snowfall and snow accumulation processes during the MOSAiC winter and spring season. *The Cryosphere Discussions*, pp.1-48.
- Frey, O., Werner, C.L., Schneebeli, M., **Macfarlane, A.R.** and Wiesmann, A., (2015). Enhancement of SnowScat for tomographic observation capabilities. In *Proc. FRINGE 2015*.

## 9. Peer-reviewed monographs

- **Macfarlane, A.R.**, (2023). Influences of snow microstructure on the Arctic sea ice energy budget (Doctoral dissertation, ETH Zurich).

## 10. Acquisition of funding

- **Macfarlane, A.R.** (2022) Radiative transfer modelling applied to melting Arctic and Antarctic sea ice. *SPI Mertz Fellowship 2022*. Home institution: WSL Snow and Avalanche Research SLF. Host institution: Australian Antarctic Program Partnership (AAPP).
- **Macfarlane, A.R.** (2024) Microwave signatures of snow on sea ice. *SNSF Postdoc Mobility Grant*. Host Institutions: UiT Tromsø, Norway and Northumbria University, Newcastle, UK.

## 11. Contributions to books

- Mallett, R.D.C, Nandana, V., **Macfarlane, A.R.**, Campbell, K., Stroeve, J.C., (in review). Snow on Sea Ice. Elsevier: Comprehensive Cryospheric Science.
- Wongpan, P., Fraser, A.D., Corkill, M., Dalman, L.A., **Macfarlane, A.R.**, (in review). Sea ice properties: A Practical Resource. Elsevier: Comprehensive Cryospheric Science.

## 12. General contributions to science

- **Macfarlane, A.R.**, Smith M.M., Calmer, R., Droste, E.S., Mohapt, V. (in prep). Assessing environmental impacts of Polar expeditions as a path to sustainability: the MOSAiC expedition as a case study. *Elementa*.
- **Macfarlane, A.R.**, Ben-Ari, T., Blanc, G., Bozzato, D., Calmer, R., Haslett, S., Holste, S., Jardé, E., Rixen, C., Ruché, D. and Schneebeli, M., (2024). A call for funding bodies to influence the reduction of environmental impacts in remote scientific fieldwork. *Frontiers in Sustainability*, 5, p.1338660. DOI: <https://doi.org/10.3389/frsus.2024.1338660>

## 13. Published datasets

- **Macfarlane, A.R.**; Schneebeli, M; Dacic, R; Wagner, D N; Arndt, S; Clemens-Sewall, D; Hämmerle, S; Hannula, H-R; Jaggi, M; Kolabutin, N; Krampe, D; Lehning, M; Matero, I; Nicolaus, M; Oggier, M; Pirazzini, R; Polashenski, C; Raphael, I; Regnery, J; Shimanchuck, E; Smith, M M; Tavri, A (2021): Snowpit raw data collected during the MOSAiC expedition. PANGAEA, <https://doi.org/10.1594/PANGAEA.935934>.

## 14. Unpublished work

- **Macfarlane, A.R.** and Bigg G.R. (2017). The impact of polar mesocyclone events on the upper ocean in the North Atlantic: Two case studies. *MSc Thesis*
- **Macfarlane, A.R.** and Ilie A. (2016). Defects in transition metal dichalcogenides. *BSc Thesis*